博士論文

Experimental Study on Loading Rate Dependent Mechanical Behavior of Artificially Bounded Geomaterials

(人工的に固結させた地盤材料の載荷速度依存性を有する力学挙動に関する実験的研究)

ザイン マクスード

ZAIN MAQSOOD

Experimental Study on Loading Rate Dependent Mechanical Behavior of Artificially Bounded Geomaterials

(人工的に固結させた地盤材料の載荷速度依存性を有する力学挙動に関する実験的研究)

By

ZAIN MAQSOOD
ザイン マクスード

A thesis submitted to
Department of Civil Engineering
of
The University of Tokyo
In partial fulfilment of the requirements for the degree of

Doctor of Philosophy

The University of Tokyo, Tokyo, Japan
August 2019

Dedicated to my father (Maqsood Ahmad) and my father-in-law (Ijaz Ahmad) for their unconditional love and support …

論文の内容の要旨
Thesis Summary

Experimental Study on Loading Rate Dependent Mechanical Behavior of Artificially Bounded Geomaterials

(人工的に固結させた地盤材料の載荷速度依存性を有する力学挙動に関する実験的研究)

ザイン マクスード

In the present era of infrastructure development, the need of "Sustainable Construction" is deemed indispensable among stakeholders and policy makers associated with construction industry. The philosophy of "Sustainable construction" is not only limited to the construction phase but also includes the efficient deconstruction of infrastructure and recycling/reuse of resources to minimize the waste materials produced during demolishing phase. In the past decades, emerging sustainability challenges have been posed by the gypsum plasterboard waste generated during the manufacturing, construction and demolishing phases of gypsum plasterboards, also known as drywall. For instance, Japan annually generates around 1.6 million tons of gypsum plasterboard waste, and the disposal of this waste often raise austere financial and environmental issues. Besides other financial and environmental issues, this waste is also prone to release toxic Hydrogen Sulfide (H_2S) gas under moist anaerobic conditions.

Inspired from the above stated principles of "Sustainable construction", a process of recycling of gypsum plasterboard waste is adopted globally for the production of recycled gypsum, chemically known as "Bassanite" or hemi hydrate calcium sulfate ($CaSO_4.1/2H_2O$). Furthermore, the application of this recycled gypsum as a potential cementing/stabilizing agent in ground improvement projects and foundation works have recently gained attention of researchers. However, the long-term performance of gypsum mixed geomaterials is still dubious as the time-dependent strength and deformation behaviour of gypsum treated geomaterials has not yet been examined thoroughly.

It is also an established fact that the strength and deformation characteristics of bounded geomaterials are susceptible to change with time, known as “Time Effects”, and are broadly classified into ageing and loading rate (viscous) effects. Moreover, the long term performance of these geomaterials are governed by these “Time Effects”, In the present study, loading rate dependent behavior of artificially produced bounded geomaterials, viz. gypsum and cement treated geomaterials; are meticulously examined at a wider range of strain rates under unconfined and confined loading conditions. The role of loading rate dependency (viscosity) of these geomaterials in rational comprehension of the behaviour under creep and cyclic loading demands detailed investigation. Additionally, a thorough study of the effects of loading rate on the strain localization is considered essential to plausibly apprehend the deformation characteristics of these bounded geomaterials.

A number of laboratory produced specimens of Gypsum Mixed Sand (GMS) and Cement Treated Sand (CTS) were prepared by mixing Silica Sand No. 6, water, bentonite, and gypsum/cement. In order to assess the reliability of the obtained test results, a criterion based on the absolute value of average difference between the local strains measured at the opposite ends of specimen was proposed. This criterion proved to be vital to scrutinize the reliable results for further analysis.

The effects of ageing were examined by conducting a series of unconfined monotonic tests on GMS and CTS specimens cured at different periods of curing, ranging from 2 days to 9 months. A reduction of about 20% in Unconfined Compressive Strength (UCS) was witnessed for GMS specimen within first month of curing, and no effects of ageing were observed up to 9 months of curing. Under similar testing conditions, GMS specimens prepared by using different batches of gypsum showed significant differences in peak strength. This variability in strength is potentially associated with the presences of different impurities and additives, such as soluble calcium sulphate anhydrite, calcium sulphate dihydrate and potassium sulphate etc. On the other hand, a continuous increase in UCS for CTS specimens was observed during first month, and the UCS values were roughly constant afterwards, up to 6 months of curing.

The loading rate dependent behavior of GMS and CTS were examined at wide range of strain rates, ranging 2.0E-05 to 5.4E+00 %/min. (5 folds). A very unique and

significant loading rate dependency of GMS was witnessed, as peak strength reduction of about 88% was reported with a decrease in strain rate by 120 times, viz. 2.4E-2 to 2.0E-4 %min. Moreover, pre-peak stiffness, failure strain and post-peak behavior of GMS was also found to be significantly governed by the loading rate. The effects of loading rate on the mechanical behaviour of GMS were divided into three distinct zones of strain rates, viz. Zones 1, 2 and 3. Substantial reduction in peak strength and pre-peak stiffness of GMS specimen with the decrease in strain rate was observed for specimens tested at strain rates lesser than 2.0E-3 %/min, viz. Zone-3. Moreover, the effects of different gypsum batches, gypsum content (G/S = 80% to 40%, where G and S stand for the weights of gypsum and sand, respectively) and curing conditions are negligible on the loading rate dependency of GMS.

On the other hand, relatively insignificant effects of loading rate on the mechanical behavior of CTS were observed. Such a prominent loading rate dependency of GMS is believed to be linked with the micromechanical peculiarities of GMS. Among these peculiarities is the inherent viscosity of the dihydrate crystals possibly due to the weak intermolecular forces. Additionally, the porous nature of interlocked needle-shape mass is also believed to induced relatively lesser frictional forces for crack propagation under slower loading rate

A series of creep and cyclic loading tests were also performed on GMS under unconfined conditions. The long-term performance of GMS under unconfined creep loading was proved to be very unpromising, and a creep load of even 32% of peak strength was able to trigger creep induced failure within 9 days. For both cyclic and creep tests on GMS, almost linear trend of axial strain accumulation with elapsed time was witnessed on full-logarithmic plot, followed by a rapid increase in axial strain values after the onset of failure. Moreover, the strain accumulation during creep was also observed to be significantly larger.

A unique relationship between the normalized failure stress and instantaneous failure strain rate of GMS specimens tested under unconfined creep and cyclic loading, and the behavior of GMS under unconfined creep and cyclic loading conditions are similar to each other and distinctively different than unconfined monotonic tests. Therefore, it is concluded that GMS is very weak against creep/cyclic loading, and long-

term in-situ performance of GMS under such loading conditions is expected to be inauspicious compared with other bounded geomaterials. Contrarily, CTS specimens were found to be significantly resistant against unconfined creep loading, as they were able to sustained high creep loads of about 75% of peak strength for more than 45 days.

In order to study the combined effects of confining stress and loading rate dependency of GMS, a series of consolidated drained triaxial tests were performed up to 800 kPa. The loading rate dependency of GMS was found to be unaffected by the effects of confining stress, and only the post-peak responses of specimens were affected by the confining stress. In addition, the deformation behavior of GMS at different isotropic drained consolidation stress levels was also studied, and the results indicate a continuous accumulation of axial strain under such loading conditions.

The strain localization characteristics of GMS were also studied using Particle Image Velocimetry (PIV) method, and it was found that the failure pattern was also dictated by the loading rate. In case of GMS specimens tested at higher loading (Zone-1), formation of shear band specimens was found to be of progressive nature, and was formed immediately after the pre-peak strain softening. The negligible amount of vertical strain accumulation in major portion of specimen indicated that limited damage of the microstructure of GMS occurred at higher strain rates. However, in spite of the fact that no visible shear bands were observed for specimen tested at strain rates lesser than 2.0E-4 %/min (Zone-3), the results of maximum shear strain distribution showed the possible existence of multiple zones of strain localization which contributed to strength reduction at lower loading rates.

ACKNOWLEDGMENT

In the Name of Allah, the All-beneficent, the All-merciful. All praise belongs to Allah (Almighty), Lord of all the worlds. Who taught by the pen. Taught man that which he knew not. Glory be to you (Almighty), we have no knowledge except what you (Almighty) have taught us. Verily, it is you (Almighty), the All-Knower, the All-Wise. May peace and blessings of Allah (Almighty) be upon Prophet Muhammad (PBUH), his honourable family and his sincere companions.

First and foremost, I would like to thank Allah (SWT) for blessing me with strength and courage to efficaciously complete my PhD.

I would like to wholeheartedly express my gratitude to my supervisor, Prof. Junichi Koseki, for his continuous technical guidance and support. His guidance and expertise proved to be vital to accomplish the goals of this research endeavour.

I am also greatly thankful to Prof. Fumio Tatsuoka (Tokyo University of Science), Prof. Reiko Kuwano (The University of Tokyo), Prof. Kimiyoshi Hayano (Yokohama National University), Associate Prof. Takashi Kiyota (The University of Tokyo), Associate Prof. Kenji Watanabe (The University of Tokyo) and Assistant Prof. Hiroyuki Kyokawa (The University of Tokyo) for their valuable technical suggestions and recommendations.

I also acknowledge the technical support provided by Mr. Takeshi Sato regarding the experimental activities of this research.

Besides, I would also like to thank my family members, friends and colleagues for their support and encouragement. Lastly, I would like to thank Ministry of Education, Supports, Science and Technology (MEXT) for providing the financial support for doctoral studies at The University of Tokyo, Japan.

August 16, 2019
The University of Tokyo
Tokyo, Japan

TABLE OF CONTENTS

APPENDIX-A

LIST OF FIGURES

LIST OF TABLES

INTRODUCTION AND LITERATURE REVIEW

1.1 PREAMBLE

The strength and deformation characteristics of bounded geomaterials, viz. natural rocks and cemented soils, are principally governed by the ageing and loading rate (viscosity), often termed as "time effects" [1]. Consequently, rational evaluation of long-term performance of geotechnical structures necessitates comprehensive cognizance of these time dependent strength and deformation characteristics. In the present study, an arduous attempt has been made to unveil the salient aspects of time dependent mechanical behavior of two different types of laboratory produced geomaterials, viz. Gypsum Mixed Sand (GMS) and Cement Treated Sand (CTS); by performing a wide range of laboratory tests including monotonic, creep and cyclic loading tests under unconfined and confined conditions. In addition, the effects of loading rate on strain localization characteristics of GMS were also studied using Particle Image Velocimetry (PIV) technique.

1.2 MOTIVATION AND SIGNIFICANCE

In the present era of infrastructure development, the need of "Sustainable Construction" is deemed indispensable among stakeholders and policy makers associated with construction industry, and is typically referred as "creating a healthy built environment using resource-efficient, ecologically-based principles" [2]. The philosophy of "Sustainable Construction" is not only limited to the construction phase but also includes the efficient deconstruction of infrastructure and recycling/reuse of resources to minimize the waste materials produced during demolishing phase [3]. These aspects are categorized in to six broad principles of "Sustainable Construction" proposed by Kibert, C.J., as shown in Table 1.

In the past decades, emerging sustainability challenges have been posed by the

Table 1.1. The principles of "Sustainable Construction" [4]

Principle No.	Principle	Remarks
1	Minimize resource consumption	Conserve
2	Maximize resource reuse	Reuse
3	Use renewable or recycle resources	Renew/Recycle
4	Protect the natural environment	Protect Nature
5	Create a healthy, non-toxic environment	Non-Toxic
6	Pursue quality in creating the built environment	Quality

gypsum plasterboard waste generated during the manufacturing, construction and demolishing phases of gypsum plasterboards also known as Drywall. Gypsum plasterboards are commonly used in the construction of interior walls and ceilings of homes and commercial buildings, as shown in Figs. 1.1 and 1.2. In United Sates, approximately 1.7 million tons of gypsum plasterboard waste was produced in 1990 during the construction phase, and was disposed to about 2000 landfills [5].

Fig. 1.1. Use of gypsum plasterboard as interior wall [6]

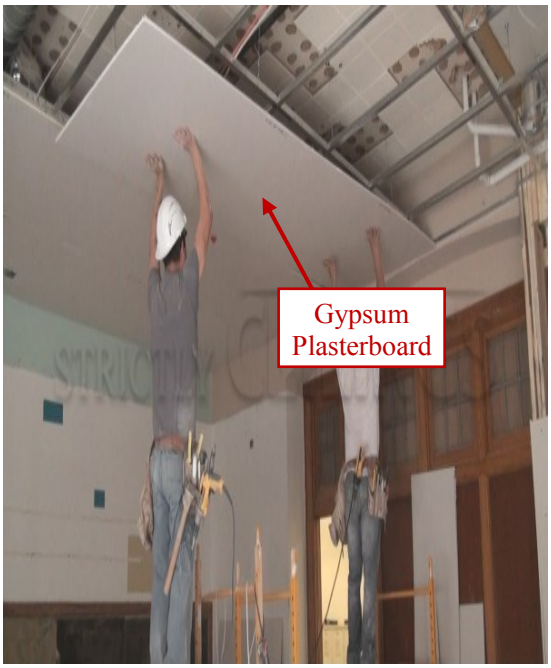

Fig. 1.2. Use of gypsum plasterboard as interior ceiling [7]

Likewise, Japan annually generates around 1.6 million tons of gypsum plasterboard waste, and the disposal of this waste often raise austere financial and environmental issues. The large quantities of gypsum waste is usually disposed to landfills, as shown in Fig. 1.3, and this process typically requires a paramount amount of financial resources due to high landfill acquisition and maintenance costs. Besides other environmental issues such as ground water and soil contamination, this waste is also prone to release toxic Hydrogen Sulfide (H_2S) gas under moist anaerobic conditions [8].

Fig. 1.3. Gypsum plasterboard waste disposal landfills [9, 10]

Inspired from the above stated principles of "Sustainable Construction", a process of recycling of gypsum plasterboard waste is adopted globally for the production of recycled gypsum, chemically known as "Bassanite" or hemi hydrate calcium sulfite ($CaSO_4.1/2H_2O$). Furthermore, the application of this recycled gypsum as a potential cementing/stabilizing agent in ground improvement projects has recently gained attention of researchers, and some fundamental chemical and mechanical characteristics of recycled gypsum stabilized soils have also studied [8]. However, the long-term performance of gypsum treated geomaterials is still dubious as the time-dependent strength and deformation behaviour of gypsum treated geomaterials has not yet been examined thoroughly.

On the other hand, cement is widely used to enhance the mechanical properties of soils, and copious lucrative attempts have already been made to study the time-dependent

mechanical behavior of cement treated soils and other bounded geomaterials [11]. Nevertheless, most of the studies are based on a relatively narrow range of loading/strain rate variations, and our understanding of the behavior of bounded geomaterials at strain rates lesser than 1.0E-4%/min. is still limited. Therefore, it is lucrative to comprehensively examine the time dependent strength and deformation characteristics of stabilized soils using gypsum and cement, at a wider range of strain rates. The ample conception of these characteristics will not only assist in cost-effective design but will also ensure unswerving risk estimation. Furthermore, scrupulous assessment of these characteristics will also believe to be prolific for the reliable of constitutive modeling.

1.3 PROBLEM STATEMENT

As highlighted earlier, the effects of loading rate on the strength and deformation behavior of typical bounded geomaterials, viz. natural rocks and cemented soils, are generally studied by adopting a relatively narrow range of loading rate variations, and the loading rate dependency of gypsum treated soils has not yet been studied scrupulously. Moreover, there may exist plentiful in-situ conditions, such as natural slopes, embankments and large-scale foundations, where the loads are induced at very slower rates than those of typically espoused in laboratory testing. In order to address these issues, it is indispensable to meticulously examine the loading rate dependent behavior of gypsum and cement treated geomaterials, at a wider range of strain rates under unconfined and triaxial loading conditions. The role of loading rate dependency (viscosity) of these geomaterials in rational comprehension of the behaviour under creep and cyclic loading demands detailed investigation. Additionally, a thorough study of the effects of loading rate on the strain localization is considered essential to plausibly apprehend the deformation characteristics of these bounded geomaterials.

1.4 LITERATURE REVIEW

It is a well-acknowledged fact that the strength and deformation characteristics of bounded geomaterials, viz. natural rocks and cemented soils, are susceptible to momentous changes with time, and these time dependent variations are often termed as “time effects”. Based on the mechanisms, these “time effects” are further classified into

ageing and loading rate (viscous) effects, as shown in Table 1.2. The effects of ageing are the changes in the intrinsic properties of geomaterials with time due to hydration/curing, cementation and weathering etc., and these effects are studied with reference to a fixed reference time. On the other hand, effects of loading rate are attributed to the viscous behavior of geomaterials, and irreversible strain rates is considered to examine these effects on the strength and deformation characteristics [12]. Therefore, it is essential to thoroughly study the effects of ageing and loading on the mechanical behavior of bounded geomaterials for the rational prediction of their long-term performance.

Table. 1.2. Details of "time effects" [12]

	Phenomenon	Mechanism or Material Property	Parameter	
Cement-mixed soil	True Ageing	*Time-dependent:* Material properties change with time, e.g., cementation, wheathering, etc.	Time (t_c)	
	Apparent Ageing Loading-rate Effect (creep, stress relaxation, etc.)	*Rate-dependent:* Responses of materials due to viscous property	Strain rate ($\dot{\varepsilon}^{ir}$)	**Air-dried sand**

The loading rate dependency (viscosity) of geomaterials are divided into four different types, as demonstrated in Fig. 1.4. Among them, Isotach and TESRA are of prime concern for the evaluation of loading rate dependent behavior of bounded geomaterials. The stress-strain response and strength values of an Isotach material are strictly governed by the instantaneous strain rate in the pre-peak regions, and pre-peak stiffness and peak strength of such materials increase with the corresponding increase in the instantaneous loading rate, and vice-versa. In case of TESRA, pre-peak stiffness and peak strengths are independent of instantaneous loading rate, and the momentary changes in the stress-strain response due to change in instantaneous strain rate vanishes with the increase in strain levels [13], as shown in Fig. 1.4.

In a recent embankment construction project in Gunma prefecture of Japan, the

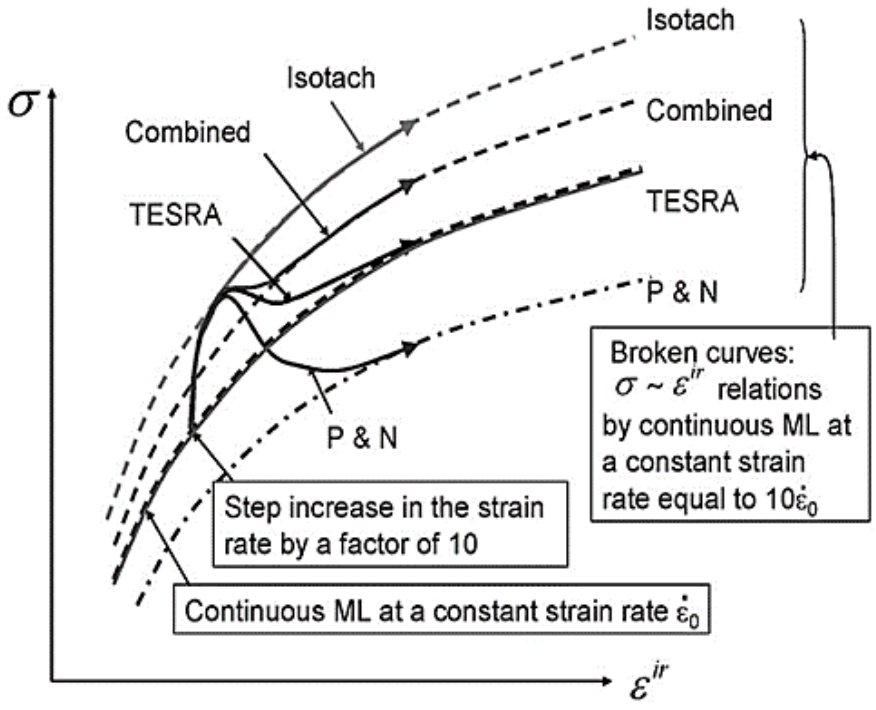

Fig. 1.4. Schematic illustration of different viscosity types [13]

potential application of recycled gypsum (Bassanite) as a stabilizing agent was studied by performing series of laboratory and field tests. The specimens for laboratory testing were prepared by mixing recycled gypsum, high plastic clays (CH) and small amount of ordinary Portland / Furnace (type B) cement. It was reported that the recycled gypsum significantly improved the unit weight and strength of the in-situ soils, as shown in Figs. 1.5 and 1.6 respectively. Additionally, it was also confirmed that the release of hazardous substances such H_2S gas and fluorine was under the allowable limits, and no adverse environmental effects were witnessed within the investigated scope of the study [8].

The Unconfined Compressive Strength (UCS) was evaluated at curing periods up to only 28 days, and loading rate was kept fixed as 1 %/min. for all these tests. In general, the UCS values of gypsum treated soils increased with the increased in ageing (curing) period, as shown in Fig. 1.6. As a result, the improvement stress ratio (untreated strength / treated strength) also reportedly increased with ageing, and the effects of ageing were significant in first 7 days, as evident in Fig. 1.6. Moreover, at a particular gypsum content, it was also observed that UCS value increase with the increase of Cement to Soil (C/S) ratio, as shown in Fig. 1.8 [8]. Promising results of recycled gypsum as a stabilizing agent have also been reported in other studies [14-16]. However, the effects of ageing (curing) on

the mechanical behavior of recycled gypsum treated geomaterials were only studied for a relatively short periods of time, and no due attention has been paid to evaluate the loading rate dependency in these studies.

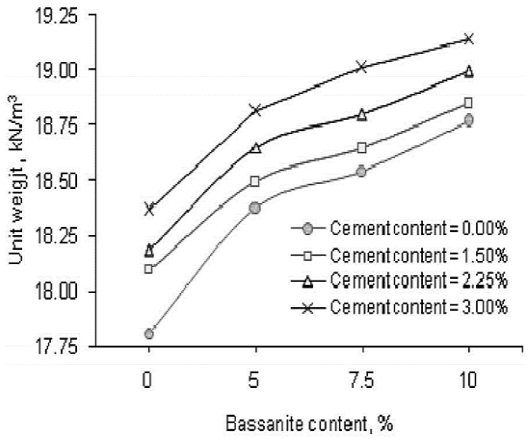

Fig. 1.5. Relationship between recycled gypsum content and unit weight [8]

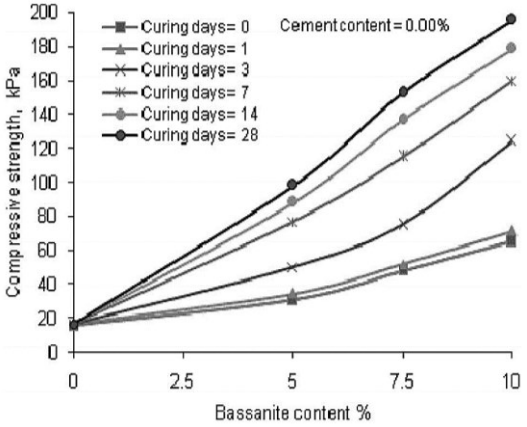

Fig. 1.6. Relationship between recycled gypsum content and UCS at different curing periods [8]

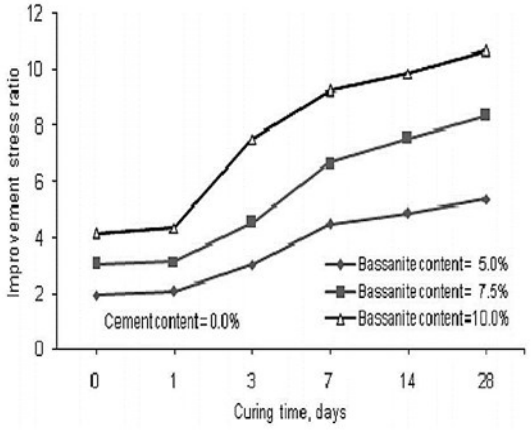

Fig. 1.7. Relationship between improvement strength ratio and curing time [8]

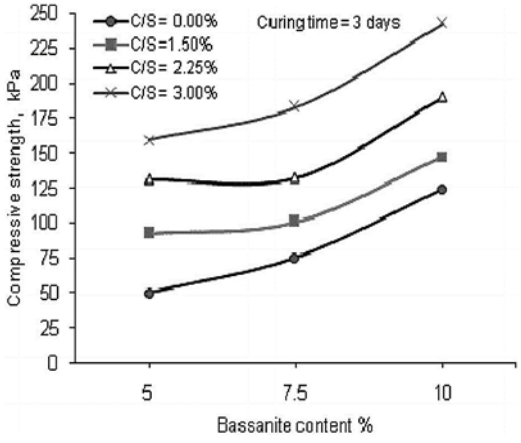

Fig. 1.8. Relationship between recycled gypsum content and UCS at different Cement/Soil ratio [8]

The effects of ageing (curing) and loading rate on the strength and deformation behavior of cement treated soils are well-documented. Contrary to gypsum treated geomaterials, the peak strength values of these cement treated soils geomaterials increase continuously for a very long duration of time, viz. up to several years, as evident in Fig. 1.9. The effects of ageing on the typical stress-strain response of cement treated soils are shown in Fig. 1.10, and relatively stiffer pre-peak responses were reported for specimens cured for longer periods [11].

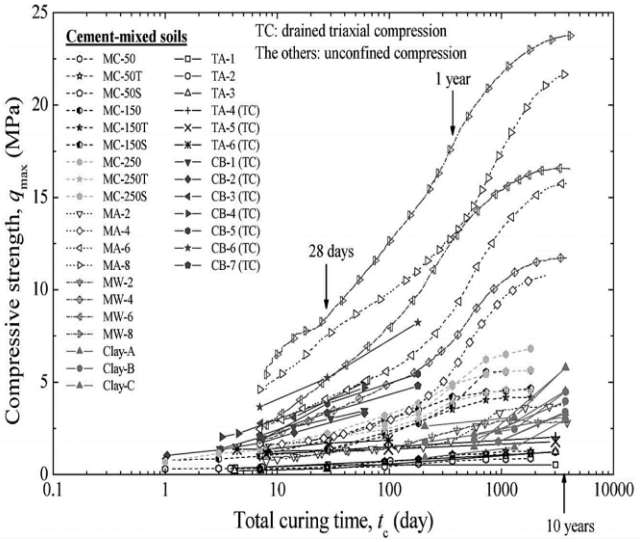

Fig. 1.9. Effects of ageing on the compressive strength of cement treated soils [11]

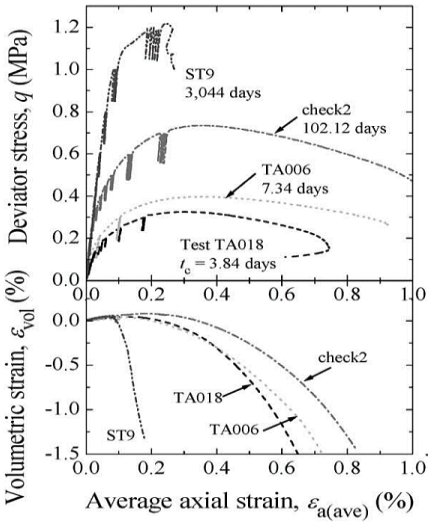

Fig. 1.10. Effects of ageing on the stress-strain response of cement treated soils [11]

In a series of consolidated drained triaxial compression monotonic tests with step changes in axial strain rate performed on cement-mixed gravels, isotach viscosity was clearly witnessed in the pre-peak regions. The strain rates were changed stepwise by the factors of 5, 25 and 125 during monotonic tests, and the obtained stress-strain responses were dictated by the instantaneous strain rate as shown in Fig. 1.11. It was also reported that the loading rate dependency of this type of cement treated geomaterials was generally the same for curing period ranging from 3 to 14 days [1].

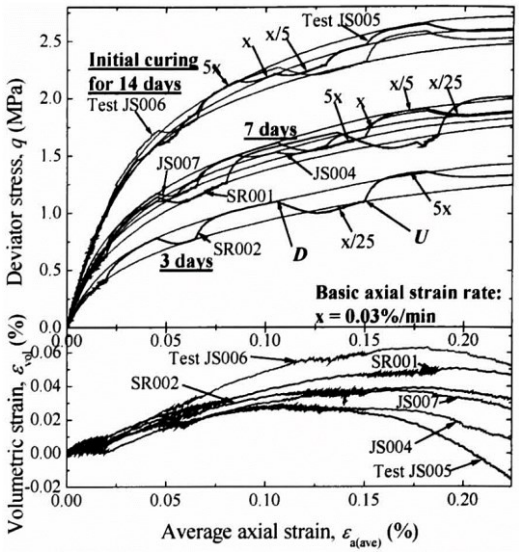

Fig. 1.11. Loading rate dependency of cement-mixed gravels [1]

Besides cement treated geomaterials, isotach viscosity in the pre-peak regions was also reported for silt-sandstone, mudstone and other sedimentary rocks (of Kazusa formation, Japan) under unconfined and consolidated drained triaxial conditions. The effects of loading rate on the stress-strain responses were studied by step-wise changing the strain rate during monotonic loading tests. In addition, drained creep loads were also applied at different stress levels to examine the effects of viscosity during creep [17, 18]. The typical stress-stress responses of these rocks are presented in Figs. 1.12 to 1.14.

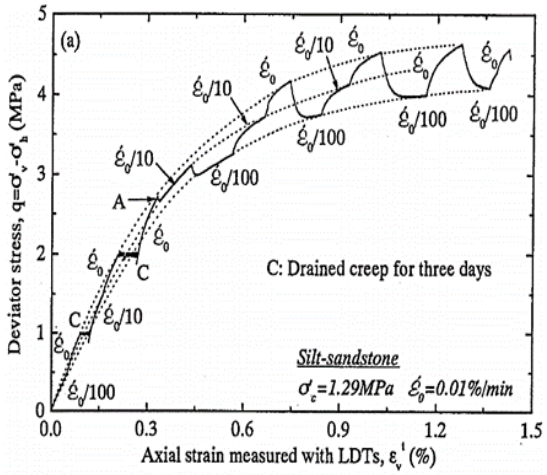

Fig. 1.12. Isotach behavior of silt-sandstone in pre-peak region [17]

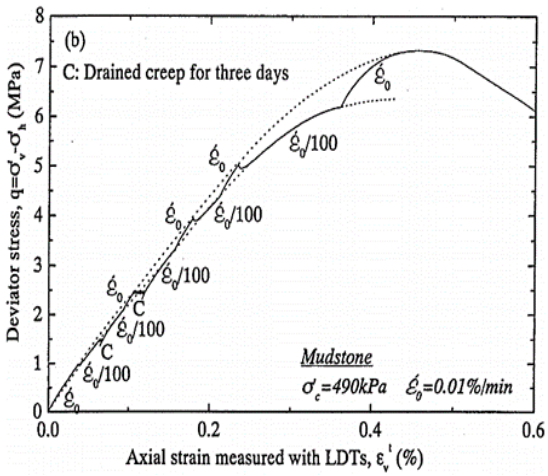

Fig. 1.13. Isotach behavior of mudstone in pre-peak region [17]

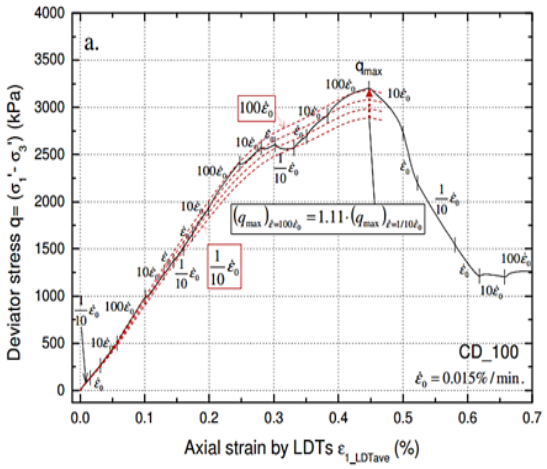

Fig. 1.14. Loading rate dependency of sedimentary rock of Kazusa formation [18]

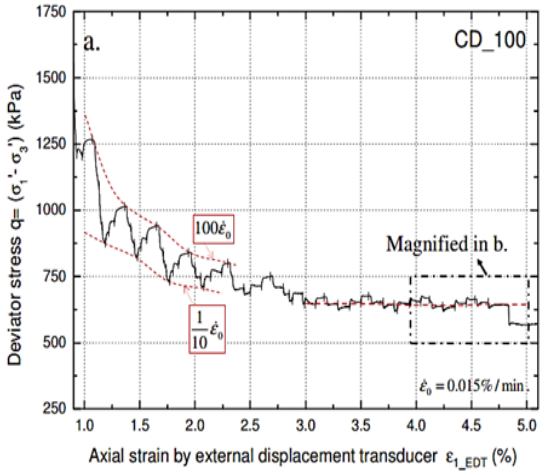

Fig. 1.15. TESRA behavior of sedimentary rock of Kazusa formation in post-peak region [18]

Similar effects of loading rates on the strength and deformation behavior of Maha Srakham Salt (of Maha Sarakham formation, Thailand) [19], limestone (of Solnhofen

Limestone formation, Germany) [20], mudstone (of Silurian formation, Australia) [21] and shale (of Kimmeridge Clay formation, England) [22] were also observed. It is noteworthy that the viscosity type of bounded geomaterials change to TESRA in the post-peak region due to loss of cementation after the formation of shear band, as shown in Fig. 1.15 [18]. In the light of these findings, it becomes certain that the strength and deformation behavior of bounded geomaterials are significantly controlled by the "time effects", viz. ageing and loading rate. However, the effects of loading rates were only studied using a limited range of strain rate variations, and no lucrative efforts were done to examine the loading rate dependency at strain rates lesser than 1.0E-4 %/min.

Rational assessment of the mechanical behavior of bounded geomaterials under creep/cyclic loading is also consider vital for the reliable prediction of their long-term performance. Besides other parameters, the tendency of residual strain accumulation due to creep/cyclic loading is particularly crucial to characterize deformation behavior. In 1995 Hyogoken-Nanbu Earthquake, only a limited amount of residual strain accumulation were observed for the sedimentary soft rocks (of Kobe formation, Japan) supporting the large foundations of Akashi Kaikyo Bridge, having a central span length of 1.99 km [23]. Conversely, traditional design approaches often envisage large amounts of residual strain accumulation under creep/cyclic loading, and result into uneconomical design solutions.

In a series of undrained triaxial cyclic loading tests performed on Mudstone and Silt-sandstone (of Kazusa Formation, Japan), almost insignificant effects of cyclic loading histories were reported on the maximum deviator stress values of these rocks, as evident in Figs. 1.16 and 1.17. Nevertheless, values of quasi-elastic undrained vertical Young's modulus of both of these rocks were slightly degraded, ranging from 10 to 20%, by undrained cyclic loading. The tendency of axial strain accumulation during cyclic loading was also witnessed to be different for mudstone and silt-sandstone. In case of mudstone only limited residual strain accumulation during cyclic loading was observed, whereas gradual accumulation of residual strain during cyclic loading was reported for silt-sand stone [24], as shown in Fig. 1.18 and 1.19 respectively.

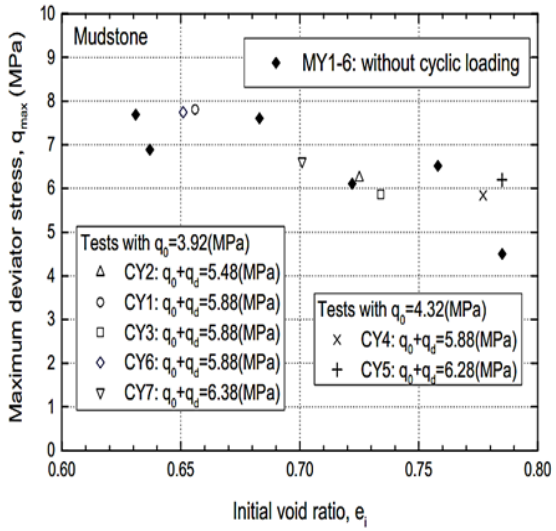

Fig. 1.16. Effects of undrained cyclic loading on maximum deviator stress of mudstone [24]

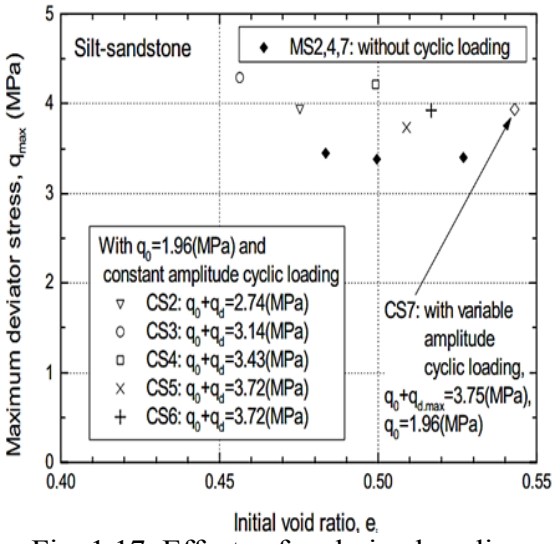

Fig. 1.17. Effects of undrained cyclic loading on maximum deviator stress of silt-sandstone [24]

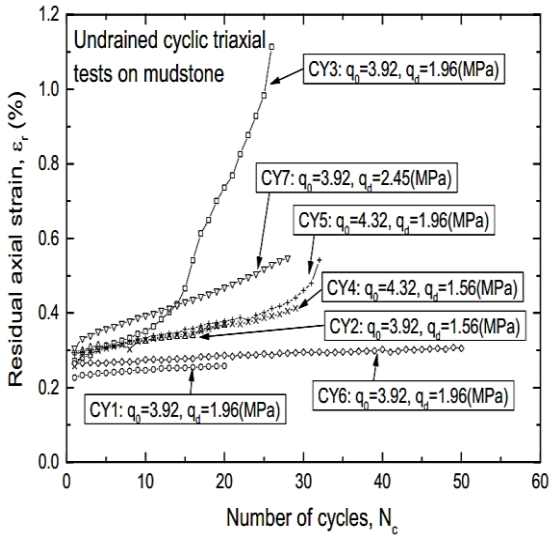

Fig. 1.18. Residual axial strain accumulation in mudstone [24]

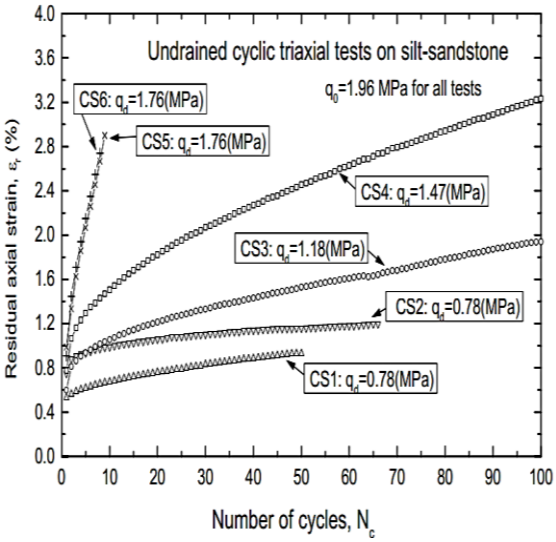

Fig. 1.19. Residual axial strain accumulation in silt-sandstone [24]

Similar effects of cyclic loading on the peak strength were also reported for laboratory produced cement treated sand under plain strain compression, and almost negligible peak strength reduction was observed due to large cyclic loading histories, as shown in Fig. 1.20. Generally, significant amount of axial strain accumulation was witnessed during the virgin loading in the first cycle, and residual strain were induced to a limited extent during cyclic loading, as evident in Fig. 1.21 [25]. However, the loading rate dependent (viscous) behavior of these bounded geomaterials were not incorporated while examining the effects of cyclic loading on the strength and deformation behavior.

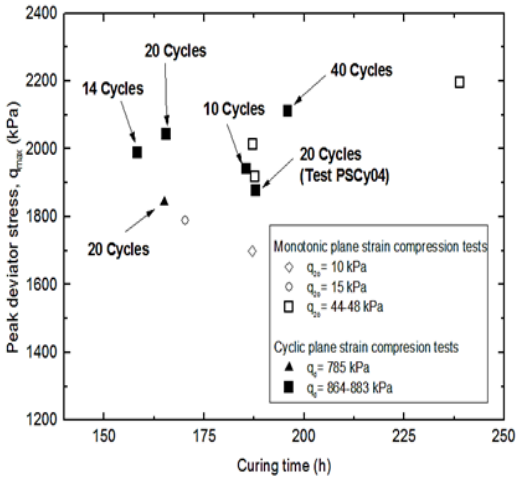

Fig. 1.20. Effects of cyclic loading on peaks strengths of cement treated sand [25]

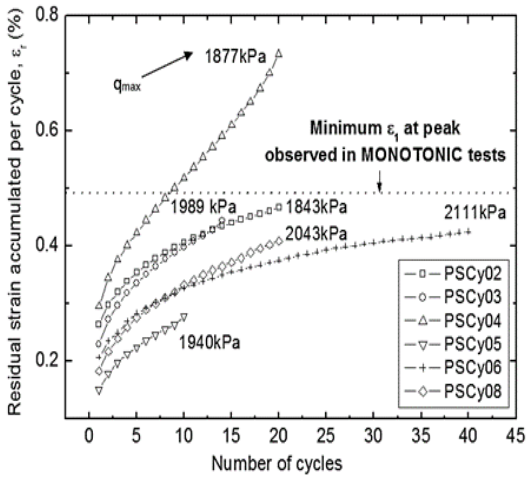

Fig. 1.21. Residual axial strain accumulation in cement treated sand [25]

It is noteworthy that the deformation characteristics under sustained/creep loading are attributed to the loading rate dependent (viscous) behavior of geomaterials. In addition to other factors, thorough understanding of creep behavior is essential to predict the long term performance of large-scale footings, natural slopes and underground tunnels etc. The results of consolidated drained triaxial tests on sedimentary rocks (of Kazusa formation, Japan) indicated a typical pattern of variation of instantaneous strain rate induced during creep loading, as shown in Fig. 1.22. The values of instantaneous strain rate induced during creep loading generally reduced to a threshold value prior to failure. Afterwards, a rapid increase in instantaneous strain rate was observed, resulting into creep failure [18].

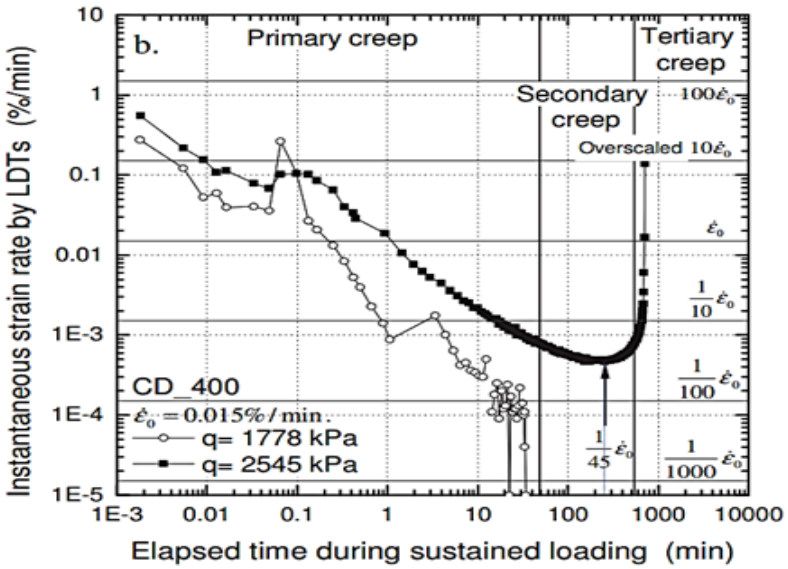

Fig. 1.22. Typical pattern of variation in strain rate during creep loading [18]

1.5 AIMS AND OBJECTIVES

The primary objective of the present study is to comprehensively examine the effects of loading rate (viscosity) on the strength and deformation characteristics of two different types of laboratory produced bounded geomaterials, viz. GMS and CTS, at a wide range of axial strain rates, ranging from about 5.0E+1 to 2.0E-5 %/min (5 folds). In order to achieve this main target, the research is divided into the following sections:

1.5.1 Specimen preparation and testing procedures

- Finalization of suitable mix proportion for the preparation of GMS and CTS specimens.
- Selection of proper testing procedures for specimens considering slow loading rate and low sustained loading (creep) tests.

1.5.2 Assessment of the reliability of test results

- Examination of the variability in tests results under similar testing conditions.
- Development of a reliability assessment criterion for the scrutiny of reliable test results.

1.5.3 Effects of ageing on the mechanical behavior of GMS and CTS

- Evaluation of the effects of ageing on the strength and deformation characteristics of GMS and CTS.
- Selection of appropriate ageing periods to examine the loading rate dependency of GMS and CTS.

1.5.4 Effects of loading rate on the mechanical behavior of GMS and CTS under monotonic loading conditions

- Study of the loading rate dependent behavior of GMS and CTS at wide range of strain rates, ranging from 5.0E+1 to 2.0E-5 %/min, under unconfined monotonic conditions.
- Effects of loading rate under triaxial monotonic loading conditions, and their comparison with the unconfined results.

- Investigation of the possible interaction between ageing and loading rate effects on the mechanical behavior of GMS.

1.5.5 Behavior of GMS and CTS under unconfined creep and cyclic loading

- Study of the strength and deformation characteristics of GMS and CTS under unconfined creep loading conditions.
- Deformation behavior of GMS under unconfined cyclic loading conditions.
- Consideration of the role of loading rate dependent (viscous) behavior of GMS and CTS during creep and cyclic loading.

1.5.6 Effects of loading rate on strain localization characteristics of GMS

- Application of PIV method to study the effects of loading rate on strain localization characteristics of GMS.

1.5.7 Summary of results and Discussion

- Comparison of test results of GMS and CTS under different loading conditions.
- Interpretation of the findings of analysis results.

1.6 SCOPE AND LIMITATIONS OF THE PRESENT STUDY

The present research is intended to address a broad spectrum of issues requisite to successfully comprehend the loading rate dependency of laboratory produced bounded geomaterials. First of all, different aspects of specimen preparation and curing techniques were studied to ensure the homogeneity of laboratory produced specimens. In order to ensure the repeatability of test results, quantitative comparison of local strain measurements were perfumed to devise a reliability assessment criterion for the scrutiny of authentic test results.

Afterwards, the effects of ageing and loading rate on the mechanical behavior of GMS and CTS were comprehensively evaluated under unconfined monotonic loading conditions. The effects of loading rate were studied at a relatively wide range of axial

strain rates, viz. 5 folds. Moreover, the effects of confining pressure on the loading rate dependent characteristics of these bounded geomaterials were also studied by conducting triaxial monotonic tests. In addition, the behavior of GMS and CTS under unconfined creep and cyclic loading was evaluated by considering the loading rate dependency (viscosity) of these material. Finally, the results obtained under different loading conditions were compared, and the effects of loading rate on the strain localization characteristics of GMS and CTS were studied.

In the present study, effects of ageing and loading were examined only on the mechanical behavior of GMS and CTS, and no effort has been made to study the chemical changes due to these effects. Consequently, the triaxial tests were performed on the unsaturated specimens, and no prior saturation was done before consolidation and shearing to avoid any chemically induced changes. Moreover, the loading rate dependency of GMS and CTS was only examined in consolidated drained condition under triaxial monotonic loading.

1.7 LOCATION AND DURATION OF RESEARCH

All the activities of the present research were performed at the Geotechnical Engineering Laboratory, The University of Tokyo located at 7-3-1 Hongo, Bunkyo-ku, Tokyo, 113-8656. The present research was conducted from October 2014 to July 2019.

1.8 UNIT SYSTEM

In the present study, “System International” (S.I. system) is adopted as a unit system. Additionally, compressive stresses/strains are considered positive, and tensile stresses/strains are labelled negative.

1.9 OVERVIEW OF DISSERTATION

Based on the scope of the present study, the thesis has been divided into nine chapters and one appendix. The overview of the thesis along with the brief details of each chapter is presented as follows:

Chapter-1 presents the introduction and scope of the present study, followed by an organized review of the relevant studies.

Chapter-2 deals with the details of apparatuses used in the present study. Additionally, the procedure for the preparation of GMS and CTS specimens is also discussed in this chapter.

Chapter-3 encapsulates a proposed procedure to assess the reliability of test results using local strain measurements.

Chapter-4 deals with the effects of ageing (curing) on the mechanical behavior of GMS and CTS. The results of unconfined monotonic tests performed at different curing periods are presented and compared with each other.

Chapter-5 summarizes the loading rate dependent behavior of GMS and CTS under unconfined monotonic loading conditions.

Chapter-6 presents the effects of confining pressure on the loading rate dependency of GMS.

Chapter-7 deals with the strength and deformation behavior of GMS and CTS under creep and cyclic loading conditions.

Chapter-8 discusses the effects of loading rate on the strain localization characteristics of GMS specimens.

Chapter-9 summarizes the findings of the present study and highlights the recommendations for the future research.

1.10 REFRENCES

1. Kongsukprasert, L., and Tatsuoka, F. (2005), "Ageing and viscous effects on the deformation and strength characteristics of cement-mixed gravelly soil in triaxial compression", *Soils and Foundations*, **45(6)**, 55-74.
2. Kibert, C. J. (1994), Final Session of *First International Conference of CIB TG 16 on Sustainable Construction*, Florida.
3. Hill, R. C., and Bowen, P. A. (1997), "Sustainable construction: principles and a framework for attainment", *Construction Management & Economics*, **15(3)**, 223-239.

4. Kibert, C. J. (1994), "Establishing principles and a model for sustainable construction", *Proceedings of the first international conference on sustainable construction*, Florida, 1994.

5. Marvin, E. (2000), "Gypsum wallboard recycling and reuse opportunities in the state of Vermont", *Vermont Agency of Natural Resources*.

6. M&M Seamless Gutters Inc., "Front view of gypsum wall, plasterboard is under construction", cited from https://getmmseamless.com/construction/front-view-of-gypsum-wall-plasterboard-is-under-construction/ dated May 11, 2019.

7. Strictly Ceilings®, "Drywall suspended ceiling grid", cited from https://www.strictlyceilings.com/virtualShowroom/drywallgrid dated May 11, 2019

8. Ahmed, A., Ugai, K., and Kamei, T. (2011), "Laboratory and field evaluations of recycled gypsum as a stabilizer agent in embankment construction", *Soils and Foundations*, **51(6)**, 975-990.

9. REGYP PTY LTD, "Plasterboard waste collection", cited from https://www.regyp.com.au/services/ dated May 11, 2019.

10. Bow Valley Waste Management Commission, "Francis Cooke site", cited from http://bvwaste.ca/wp-content/uploads/2012/11/Drywall-Cropped-for-Home-Page.jpg dated May 11, 2019.

11. Kongsukprasert, L., Tatsuoka, F., & Takahashi, H. (2007), "Effects of curing period and stress conditions on the strength and deformation characteristics of cement-mixed soil", Soils and Foundations, 47(3), 577-596.

12. Kongsukprasert, L., Kuwano, R., & Tatsuoka, F. (2002), "Ageing effects on the stress-strain behaviour of cement-mixed granular materials", *Proceedings of the Thirty-seventh Japan National Conference on Geotechnical Engineering*, 813-814.

13. Tatsuoka, F., Di Benedetto, H., Enomoto, T., Kawabe, S., and Kongkitkul, W. (2008), "Various viscosity types of geomaterials in shear and their mathematical expression", *Soils and Foundations*, **48(1)**, 41-60.

14. Kotake, N., and Sano, H. (2018), "Hardening performance of reclaimed gypsums for stabilizing agent to improve soft clayey ground", *Journal of Material Cycles and Waste Management*, 1-11.

15. Kamei, T., Ahmed, A., and Ugai, K. (2013), "Durability of soft clay soil stabilized with recycled Bassanite and furnace cement mixtures", *Soils and Foundations*, **53(1)**, 155-165.

16. Kamei, T., Ahmed, A., Horai, H., and Ugai, K. (2015), "A novel solidification technique for fluorine-contaminated bassanite using waste materials in ground improvement applications", *Journal of Material Cycles and Waste Management*, **17(2)**, 380-390.

17. Hayano, K., Matsumoto, M., Tatsuoka, F., and Koseki, J. (2001), "Evaluation of time-dependent deformation properties of sedimentary soft rock and their constitutive modeling", *Soils and Foundations*, **41(2)**, 21-38.

18. Miyashita, Y., Koseki, J., Namikawa, K., and Matsumoto, M. (2015), "Study on viscous property of sedimentary soft rock in drained triaxial and unconfined compression tests", *Deformation Characteristics of Geomaterials: Proceedings of the 6th International Symposium on Deformation Characteristics of Geomaterials*, **6**, 575-58.

19. Fuenkajorn, K., Sriapai, T., and Samsri, P. (2012), "Effects of loading rate on strength and deformability of Maha Sarakham salt", *Engineering Geology*, **135**, 10-23.

20. Rutter, E. H. (1972), "The effects of strain-rate changes on the strength and ductility of Solenhofen limestone at low temperatures and confining pressures", *International Journal of Rock Mechanics and Mining Sciences & Geomechanics Abstracts*, **9(2)**, 183-189.

21. Chiu, H. K., Johnston, I. W., and Donald, I. B. (1983), "Appropriate techniques for triaxial testing of saturated soft rock", *International Journal of Rock Mechanics and Mining Sciences and Geomechanics Abstracts*, **20(3)**, 107-120.

22. Swan, G., Cook, J., Bruce, S., and Meehan, R. (1989), "Strain rate effects in Kimmeridge Bay shale", *International Journal of Rock Mechanics and Mining Sciences & Geomechanics Abstracts*, **26(2)**, 135-149.

23. Yamagata, M., Yasuda, M., Nitta, A., and Yamamoto, S. (1996), "Effects on the Akashi Kaikyo bridge", *Soils and Foundations*, **36(Special)**, 179-187.

24. Koseki, J., Indou, H. and Hayano, K. (2003), "Cyclic triaxial tests on residual deformation and small strain properties of soft rocks", *Proceedings of Deformation Characteristics of Geomaterials*, 247-255.

25. Koseki, J., Salas-Monge, R., & Sato, T. (2003), "Plane strain compression tests on cement-treated sands," Proceedings of the First Japan-US Workshop on Testing, Modeling, and Simulation, American Society of Civil Engineers, 429-443.

EXPERIMENTAL EQUIPMENT AND LABORATORY PRODUCTION OF GMS AND CTS

2.1 PREAMBLE

In the field of geotechnical engineering, laboratory testing is undoubtedly regarded as an essential tool to estimate the engineering characteristics of geomaterials. Several advanced laboratory testing procedures have been evolved with time, and the results obtained through these laboratory tests are often served as the foundation for the reliable constitutive modeling of geomaterials [1]. For the present study, two different apparatuses, viz. unconfined compression machine and triaxial compression machine; were used to conduct laboratory testing, and their details are presented in this chapter. Additionally, the procedure for the laboratory production of GMS and CTS specimen is also discussed comprehensively.

2.2 UNCONFINED COMPRESSION MACHINE

A strain controlled unconfined compression machine capable of exerting monotonic and cyclic loading was used in the present study, shown in Fig. 2.1. To conduct unconfined monotonic tests at wide range of strain rate, different configurations of speed-reduction gear boxes attached with the AC-servo motor were used [2]. At a particular gear configuration, the axial strain rate was manually controlled by adjusting the speed of AC-servo motor. Additionally, the creep tests were performed by applying infinitely small loading/unloading cycles to overcome the technical limitation associated with the apparatus. The details of different components of this apparatus is as follows.

1. Mechanical Axial loading system comprising of electromagnetic clutches, gears and AC-servo motor [2].
2. To avoid potential damage to the loading shaft, a moveable top cap was intentionally used, and bottom pedestal was kept fixed, as shown in Fig. 2.1.

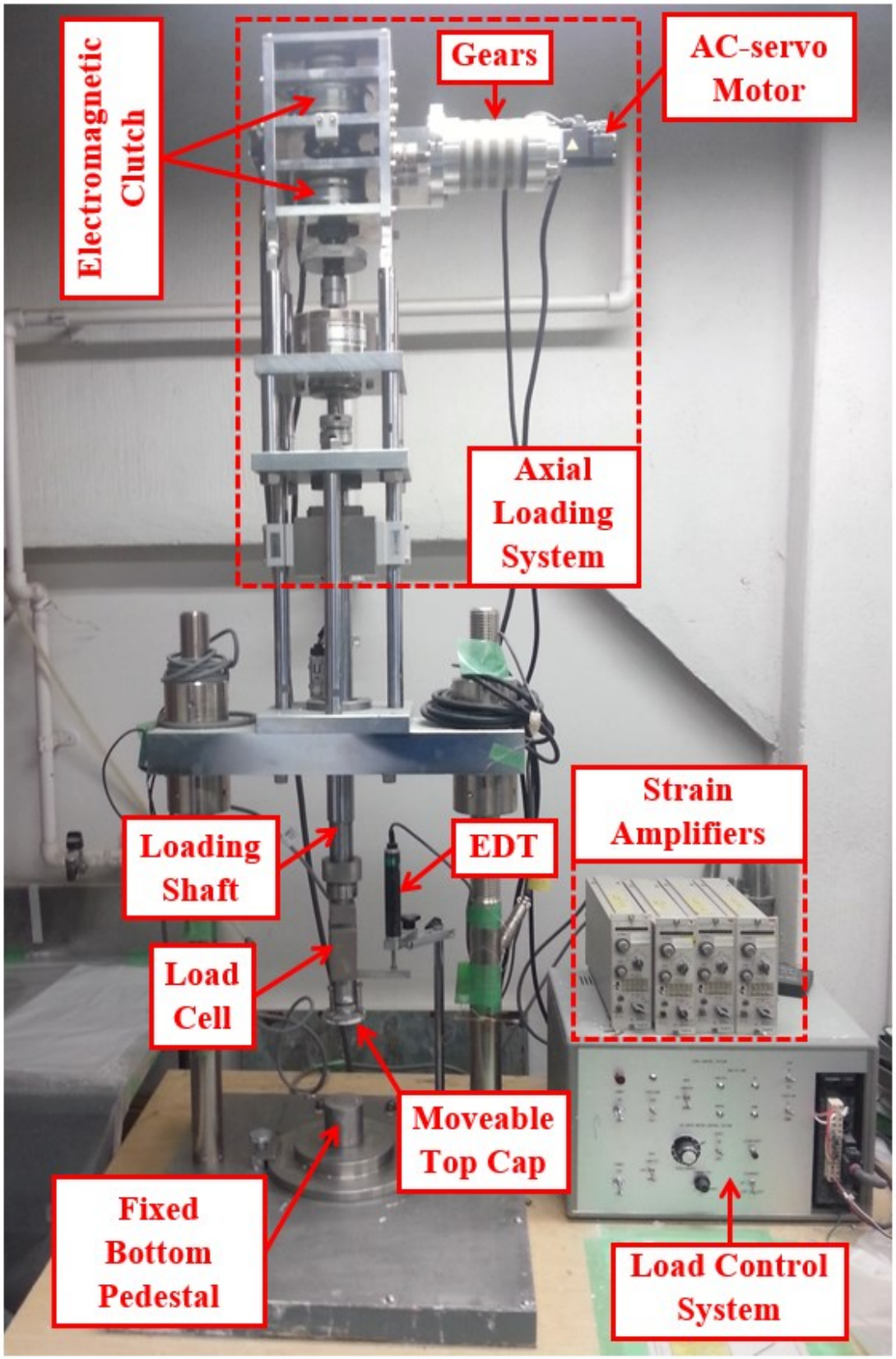

Fig. 2.1. Unconfined Compression Machine

3. A total of four transducers, viz. load cell, External Displacement Transducer (EDT) and a pair of Local Displacement Transducers (LDTs) [3], were used to record the mechanical response of specimens. The details of these transducers will be discussed in Section 2.4.
4. In order to amplify the signals obtained from the attached transducer four strain amplifiers were utilized.
5. A USB compatible type data logger (AIO-160802AY-USB) manufactured by CONTEC was used for analogue to digital conversion and vice-versa, as shown in Fig. 2.2.
6. A computer connected with the data logger was used to record the data and also to control the loading configuration during unconfined cyclic loading tests.

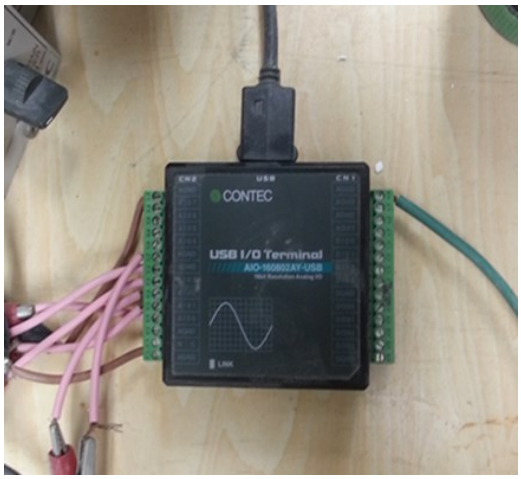

Fig. 2.2. USB compatible type data logger

2.3 TRIAXIAL COMPRESSION MACHINE

The triaxial compression machine used in this study is shown in Fig. 2.3. For monotonic loading tests, the desired strain rate can be achieved by utilizing suitable speed-reduction gear boxes configuration and by controlling the speed of AC-servo motor using the computer program. Moreover, the creep and cyclic loading tests were also performed by controlling the load control system using sets of appropriate input commands [2]. The details of numerous components of triaxial compression machine is as follows.

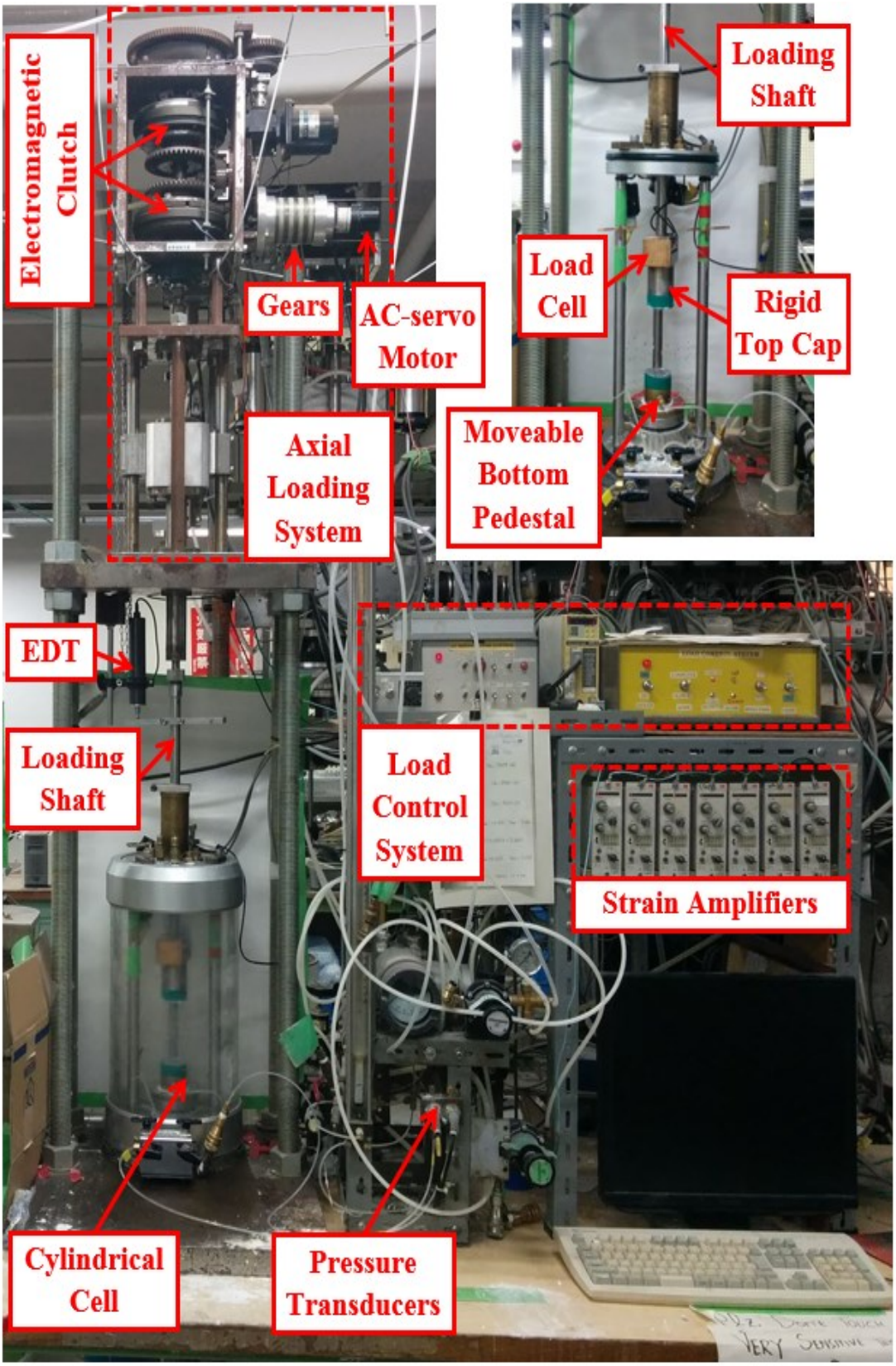

Fig. 2.3. Triaxial Compression Machine

1. Automated main mechanical axial loading system consisting of electromagnetic clutches, gears and AC-servo motor [2].
2. An auxiliary assembly of gear and additional motor was installed to manually swiftly maneuver the loading shaft prior and after testing.
3. A moveable bottom pedestal was used to avoid any damage to loading shaft during testing, along with a fixed rigid cap, as shown in Fig. 2.3.
4. In order to fully record the mechanical response of specimen during triaxial testing, a total of six transducers, viz. load cell, External Displacement Transducer (EDT), a pair of Local Displacement Transducers (LDTs) [3], pore-pressure sensor and cell pressure sensor; were attached with this machine. Further details of these transducers will be explained in Section 2.4.
5. A total of six amplifier were used to amplify the signals received for the attached transducers.
6. An assembly of analogue to digital and digital to analogue converters (manufactured by Interface® Corporation) were attached to store the recorded data on to computer, and to control the loading system automatically using computer program [2].

2.4 DETAILS OF TRANSDUCERS

As highlighted earlier, a total of four and six transducers were attached with unconfined and triaxial compression machines respectively. The details of different type of transducers are discussed together as follows:

2.4.1 Load Cells

A load cell manufactured by Tedea-Huntleigh (Model No. 619), and having a maximum capacity of 19.6 kN was attached with the loading shaft of unconfined compression machine as shown in Figs. 2.1 and 2.4. On the other hand, a custom built load cell (maximum capacity ≈ 50 kN) was installed inside the cylindrical cell of the triaxial compression machine, as shown in Figs. 2.3 and 2.5. The calibration results of these load cells are presented in Appendix-A.

2.4.2 External Displacement Transducers (EDTs)

The EDTs attached with both of these machines were manufactured by Tokyo Sokki Kenkyujo Co., Ltd. The EDT used in unconfined compression machine, viz. Model No. CDP-25; has a maximum capacity of 25mm, as shown in Figs. 2.1 and 2.6. Moreover, an EDT (Model No. CDP-50) having a maximum capacity was installed in triaxial compression machine, as shown in Fig. 2.7. The details of calibration of these EDTs are discussed in Appendix-A.

Fig. 2.4. Tedea-Huntleigh load cell (unconfined compression machine)

Fig. 2.5. Custom built load cell (triaxial compression machine)

Fig. 2.6. CDP-25 type EDT (unconfined compression machine)

Fig. 2.7. CDP-50 type EDT (triaxial compression machine)

2.4.3 Local Displacement Transducers (LDTs)

In addition to EDT, a pair of LDTs [3] were attached on the opposite sides of the specimens to measure the local strain free from the undesirable effects of bedding error [4], as shown in Fig. 2.8. These LDTs are capable of measuring strains up to 10^{-6}, and their calibration details are presented in Appendix-A.

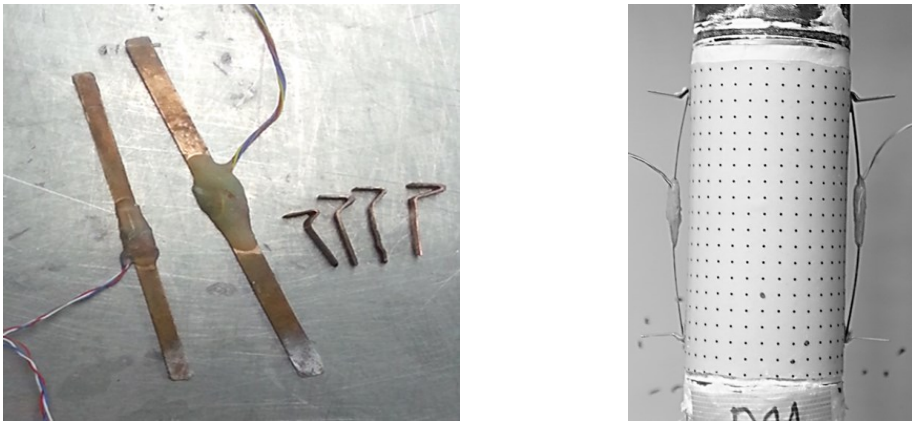

(a) LDTs and hinges (b) LDTs attached with specimen

Fig. 2.8. Local Displacement Transducers (LDTs)

2.4.4 Pressure Transducers

A pair of pressure transducers manufactured by Kyowa Electronic Instruments Co., Ltd., were installed in the triaxial compression machine to record the cell pressure and pore pressure during confined testing, as shown in Fig. 2.9. The maximum capacity of each of these pressure transducers is 1.0 MPa, and the calibration details of these transducers are discussed in Appendix-A.

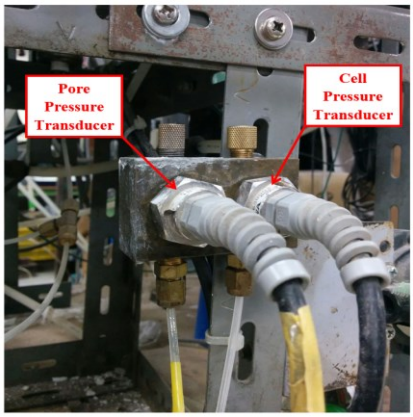

Fig. 2.9. Pressure transducers installed in triaxial compression machine

2.5 MATERIALS

GMS and CTS specimens were prepared by uniformly mixing the fixed percentages of materials as per Table 2.1. The gypsum used in the present study was manufactured by Yoshino Gypsum Co. Ltd., and 4 different batches of same type of commercially produced gypsum was used to meet the demands for this extensive study. For GMS specimens, two different mix proportions, viz. GMS(MP1) and GMS(MP2) were selected to examine the role of cementation content on the loading rate dependency.

Table 2.1. Details of mix proportion for GMS and CTS specimens

ID	Silica Sand No. 6 (S)	Water (W)	Bentonite (B)	Gypsum (G)	High Early Strength Cement (C)	Binder/Sand
	(%)	(%)	(%)	(%)	(%)	
GMS(MP1)	42.35	23.75	0.00	33.90	0.00	G/S=80%
GMS(MP2)	55.00	22.00	1.00	22.00	0.00	G/S=40%
CTS	46.60	29.80	5.00	0.00	18.60	C/S=40%

On the other, high early strength cement was used for the preparation of CTS specimens, and a small percentage of bentonite was also used to avoid excessive bleeding. The materials was kept air-tight throughout to avoid any detrimental effects of atmospheric moisture. Additionally, dental gypsum was used to cap the top and bottom ends of specimens to avoid any premature tensile cracking [5]. In order to cast specimens, air-tight plastic molds having diameter and height of 50 and 100 mm were used.

2.6 PREPARATION OF GMS AND CTS SPECIMENS

Almost similar procedure for the preparation of both GMS and CTS specimens were adopted and the step-wise preparation procedure [6, 7] is as follows.

1. The desired amount of materials were weighted carefully, and were manually mixed together to form a uniform slurry as shown in Figs 2.10(a) and 2.10(b). To cast a single specimen, approximately 400g of slurry was required.

(a) Weighted materials

(b) Preparation of slurry

(c) Initial curing in plastic molds

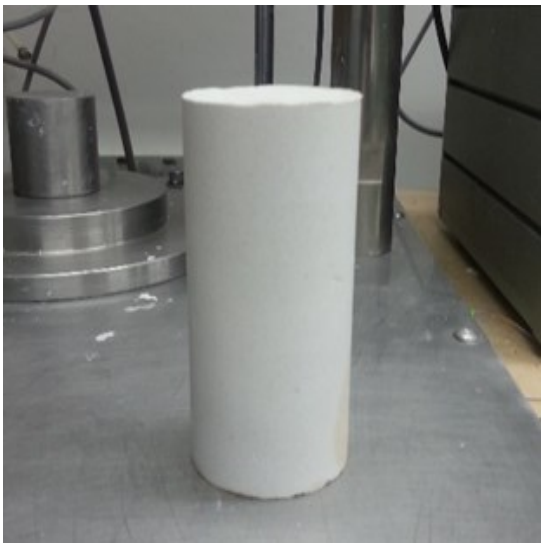

(d) Hardened GMS specimen

Fig. 2.10. Different stages of specimen preparation [6, 7]

2. Afterwards, the slurry was poured into the plastic molds in two layers, and gentle tapping on the outside of plastic molds were done using rubber hammer to remove any trapped air in the slurry.
3. By using a straight edge spatula, the extra slurry from the top of plastic molds were removed to ensure the flatness of the top edge of specimens.
4. As an initial phase of curing, these molds were than kept air-tight for the desired duration, as shown in Fig. 2.10(c).
5. On the completing of initial phase of curing, the hardened specimens were unmolded, as shown in Fig. 2.10 (d).

6. The hardened specimens were further cured using different techniques, and the details of different curing procedure are discussed in Chapter No. 4.
7. Finally, at targeted total period of curing, the specimens were tested as per the desired loading conditions.

2.7 REFRENCES

1. Fu, Q., Hashash, Y. M., Jung, S., and Ghaboussi, J. (2007), "Integration of laboratory testing and constitutive modeling of soils," *Computers and Geotechnics*, **34(5)**, 330-345.
2. Santucci de Magistris, F., Koseki, J., Amaya, M., Santucci de Magistris, F., Koseki, J., Amaya, M. (1999), "A triaxial testing system to evaluate stress-strain behavior of soils for wide range of strain and strain rate," *Geotechnical Testing Journal*, **22(1)**, 44-60.
3. Goto, S., Tatsuoka, F., Shibuya, S., Kim, Y., and Sato, T. (1991), "A simple gauge for local small strain measurements in the laboratory," *Soils and Foundations*, **31(1)**, 169-180.
4. Koseki, J., Salas-Monge, R., and Sato, T. (2003), "Plane strain compression tests on cement-treated sands," *Proceedings of the First Japan-US Workshop on Testing, Modeling, and Simulation*, American Society of Civil Engineers, 429-443.
5. Maqsood, Z. and Koseki, J. (2015), "Behavior of gypsum mixed sand under unconfined monotonic and cyclic loading conditions," *GeoKanto*, Recital group of Japanese Geotechnical Society.
6. Maqsood, Z. (2016), "Behavior of gypsum mixed sand under unconfined monotonic and cyclic loading conditions," Master Thesis, The University of Tokyo.
7. Maqsood, Z. and Koseki, J. (2019), "Time dependent strength and deformation characteristics of bounded geomaterials," *9th Asian Young Geotechnical Engineering Conference*, (submitted)

RELIABILITY ASSESSMENT CRITERION USING LOCAL STRAIN MEASUREMENTS

3.1 PREAMBLE

In the present study, significant variations in the peak strength values of GMS specimens was observed under similar testing conditions. However, repeatability of test results is deemed pivotal to evaluate the loading rate dependency of geomaterials, especially at higher loading rates where the effects of loading rates on strength values are quite marginal [1]. In order to address this issue, a criterion based on the quantitative comparison between the locally measured strains at the opposite sides of specimen is proposed. Based on this criterion, the reliability of obtained test results was assessed and representative results were scrutinized for further analysis.

3.2 DISPARITIES IN TEST RESULTS

A total of 28 unconfined monotonic test results were conducted on 3 ± 0.25 days cured GMS-MP1 (Batch-A) specimens at five different loading rates, and the results are summarized in Table 3.1 [2]. All of these tests were performed on unconfined monotonic machine equipped with a moveable top cap to avoid any potential damage to the loading shaft. The top edges of the specimens was flatten using sand paper, and the specimens were capped at top and bottom edges to avoid any premature tensile cracking [3]. Additionally, the specimens were wrapped using 0.3 mm rubber membrane, and the average strain rates were computed using LDTs [4].

The unit weights of each of these specimens were computed by dividing the weight of specimen prior to testing by its volume, and the average value was found to be about 18.4 kN/m^3. Moreover, the values of unit weight were found to be practically consistent with each other, highlighting the integrity of the mixing process, as shown in Table 3.1. Furthermore, the moisture content was computed after the completion of test.

Table 3.1 Test results of unconfined monotonic tests series (GMS-MP1(A), 3±0.25 days curing) [2]

Series ID	Test ID	Avg. Axial Strain Rate	Unit Weight Before Testing	Moisture Content After Testing	UCS	Failure Strain				Failure Time
						EDT	LDT-1	LDT-2	Avg. LDT	
		(%/min)	(kN/m^3)	(%)	(kPa)	(%)	(%)	(%)	(%)	(min)
S1	S1-UM1	1.6E-01	18.3	30.1	4799	0.293	0.305	0.313	0.309	1.8
	S1-UM2		18.4	29.8	4810	0.306	0.312	0.325	0.319	1.8
	S1-UM3		18.4	30.6	4716	0.290	0.246	0.301	0.274	1.8
S2	S2-UM1	6.0E-02	18.3	31.7	4535	0.358	0.365	0.428	0.397	5.7
	S2-UM2		18.3	32.5	4367	0.340	0.371	0.328	0.350	5.4
	S2-UM3		18.2	31.5	4312	0.395	0.381	0.271	0.326	5.3
	S2-UM4		18.3	32.1	3810	0.378	0.457	0.131	0.294	4.7
	S2-UM5		18.3	29.9	4082	0.228	0.066	0.390	0.228	4.9
	S2-UM6		18.3	30.0	4643	0.372	0.455	0.285	0.370	5.6
	S2-UM7		18.4	30.2	4739	0.366	0.448	0.275	0.361	5.8
	S2-UM8		18.4	30.0	4647	0.340	0.409	0.311	0.360	5.6
S3	S3-UM1	2.4E-02	18.6	31.8	4266	0.439	0.432	0.553	0.492	19.9
	S3-UM2		18.5	33.9	4103	0.475	0.622	0.360	0.491	20.1
	S3-UM3		18.5	33.0	3293	0.255	0.070	0.697	0.384	17.4
	S3-UM4		18.4	31.3	4174	0.440	0.514	0.567	0.541	19.9
S4	S4-UM1	8.2E-03	18.4	30.7	3324	0.821	0.991	0.299	0.645	72.2
	S4-UM2		18.3	33.7	3090	0.543	0.417	0.525	0.471	60.0
	S4-UM3		18.5	34.2	3590	0.575	0.461	0.713	0.587	67.7
	S4-UM4		18.6	33.2	3870	0.587	0.512	0.619	0.565	69.9
	S4-UM5		18.5	32.6	3637	0.535	0.402	0.704	0.553	69.2
	S4-UM6		18.5	33.3	3652	0.834	1.059	0.145	0.602	73.7
S5	S5-UM1	3.1E-03	18.4	32.3	2737	0.778	0.592	1.029	0.810	271.3
	S5-UM2		18.6	31.3	2956	0.776	0.674	1.101	0.887	273.9
	S5-UM3		18.4	30.7	2926	0.961	0.547	1.284	0.916	323.1
	S5-UM4		18.4	31.1	2911	0.812	1.019	0.697	0.858	286.8
	S5-UM5		18.5	33.7	2987	0.784	0.690	0.958	0.824	271.1
	S5-UM6		18.4	32.9	2896	0.739	0.749	0.858	0.804	253.5
	S5-UM7		18.5	33.7	2609	0.956	1.510	0.291	0.901	279.9

Fig. 3.1 shows the relationship between UCS and average strain rate, and a general trend of reduction in UCS with the decrease of loading rate was witnessed [5, 6]. The details of this loading rate dependency of GMS will be discussed comprehensively in Chapter No. 5. Additionally, significant variations in UCS values can be witnessed under similar loading rates, as evident in Fig. 3.1. For instance, the UCS values for specimens tested at average strain rate of 2.4E-02 %/min fluctuate between 4266 kPa and 3293 kPa, viz. for S3-UM1 and S3-UM3 respectively; indicating a variation of 973 kPa (approximately 23% with respect to the maximum value of UCS).

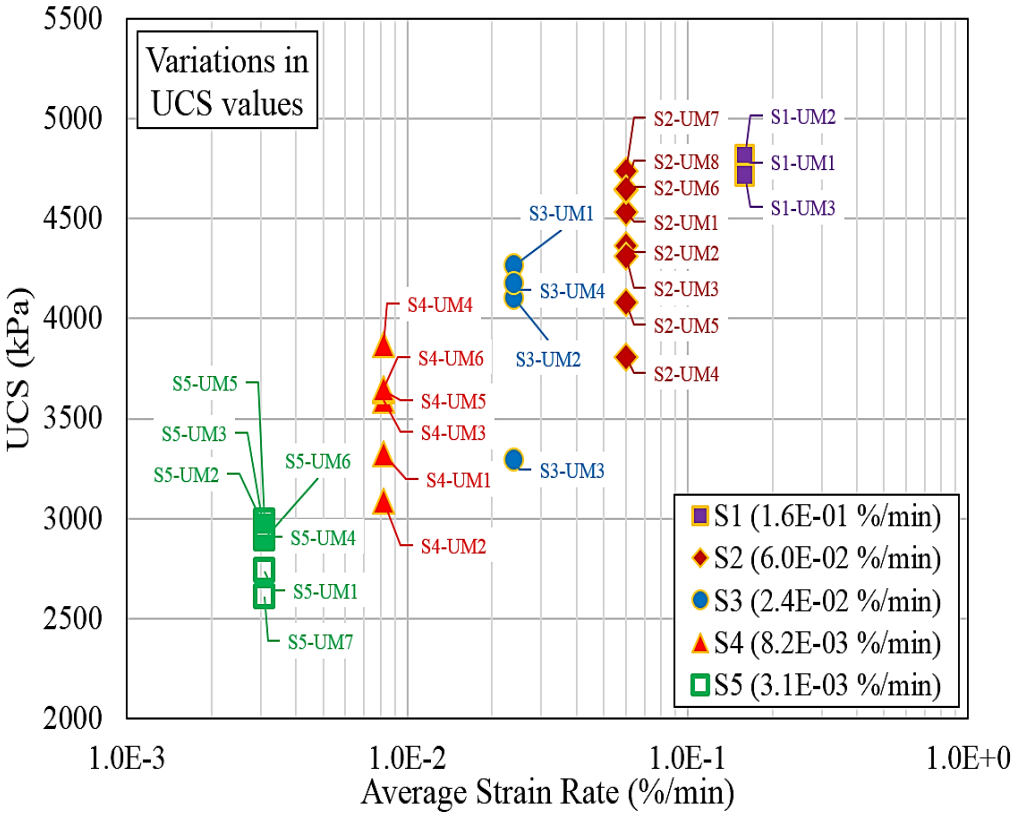

Fig. 3.1. Relationship between UCS and Average Strain Rate [2]

In order to compare the variations in results, a brief statistical analysis of UCS values obtained at different loading rates is presented in Table 3.2. Except for tests performed at 1.6E-01 %/min, substantial disparities in the results can be witnessed as indicated by the absolute variation and standard deviation. It is also noteworthy that undesirable variations in strength values pose a severe challenge to rationally examine the loading rate dependency of bounded geomaterials, especially at higher loading rates where the effects of loading rates are quite trivial [1].

Table 3.2. Statistical Analysis of UCS values [2, 5]

Series ID	Average Axial Strain Rate	No. of Tests	UCS				
			Max. Value	Min. Value	Avg. Value	Absolute Variation	Standard Deviation
	(%/min)		(kPa)	(kPa)	(kPa)	(kPa)	(kPa)
S1	1.6E-01	3	4810	4716	4775	94	51
S2	6.0E-02	8	4739	3810	4392	929	319
S3	2.4E-02	4	4266	3293	3959	973	449
S4	8.2E-03	6	3870	3090	3527	780	276
S5	3.1E-03	7	2987	2609	2860	378	136

3.3 INCONSISTENCY OF LOCALLY MEASURED AXIAL STRAINS DURING MONOTONIC TESTS

In an effort to unveil the factors responsible for the disparities in test results, the values of local strains measured at the opposite sides of specimens, using a pair of LDTs, during the monotonic loading are compared with each other. Fig. 3.2 shows the stress-strain responses of S3-UM1 and S3-UM3, and as highlighted earlier, the peak strength of S3-UM3 is about 23% lesser than S3-UM1. In case of S3-UM1, the local strains computed by both of the LDTs are of approximately similar magnitudes, indicating a uniform distribution of axial strain during monotonic loading. On the other hand, an indubitable difference in the values of estimated axial strain measured by LDT-1 and LDT-2 can be witnessed from Fig. 3.2. At a particular stress level, the value of axial strain estimated by LDT-2 is significantly larger than LDT-1, resulting into a non-uniform distribution of axial strain in specimen [2, 5].

Based on this finding, it was presumed that the discrepancies in test results can be attributed to the distribution of axial strain induced during monotonic loading. Generally, higher values of UCS were obtained for specimens having identical values of axial strains recorded by LDTs, and vice versa, as shown in Table 3.1. Moreover, it is believed that specimens having uniform axial strain distribution reflect the representative behavior under a particular loading conditions [2, 5].

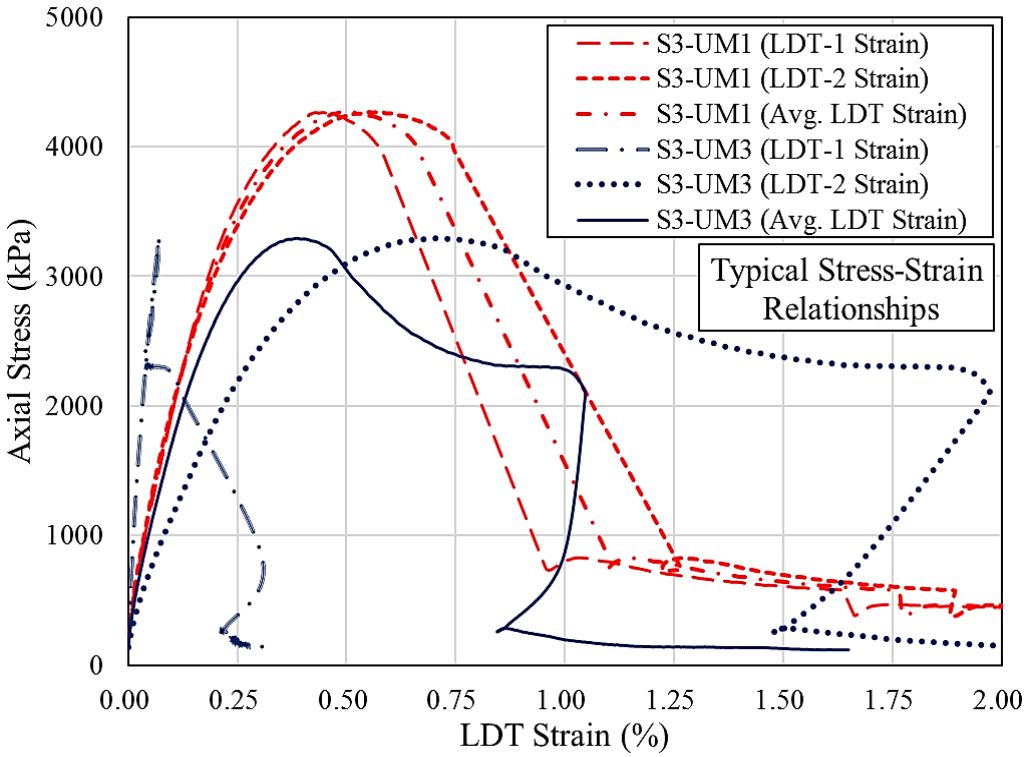

Fig. 3.2. Typical stress-strain relationships at 2.4E-2 %/min [6]

3.4 RELIABILITY ASSESMENT CRITERION BASED ON LOCAL AXIAL STRAIN MEASUREMENTS

To rationally quantify the differences between locally measured strains at the opposite sides of the specimen, Absolute Average Differences (AAD), of local strains measured using LDT-1 and LDT-2 were computed at four different strain levels, viz. 25%, 50%, 75% and 100% of EDT failure strain using Eq. (1).

$$\text{AAD} = \left|\frac{\text{Strain}_{\text{LDT}-1} - \text{Strain}_{\text{LDT}-2}}{\text{Strain}_{\text{LDT}-1} + \text{Strain}_{\text{LDT}-2}}\right| \times 100 \qquad \text{Eq. (1)}$$

The relationship between UCS and AAD at different strain levels is presented in Figures 3.3 to 3.6. In the light of these plots, it is certain that the values of UCS generally decrease with the increase in AAD at all strain levels. Moreover, this tendency is relatively lesser prominent for specimens tested at strain rates 3.1E-03 %/min (series S5). Additionally, the values of UCS are found to be relatively consistent with each other for a certain initial range of AAD. Based on this fact, test results having AAD lesser than 25% at 50% of EDT failure strain were only selected for further analysis, and the rest of the results were simply discarded [2, 5, 6].

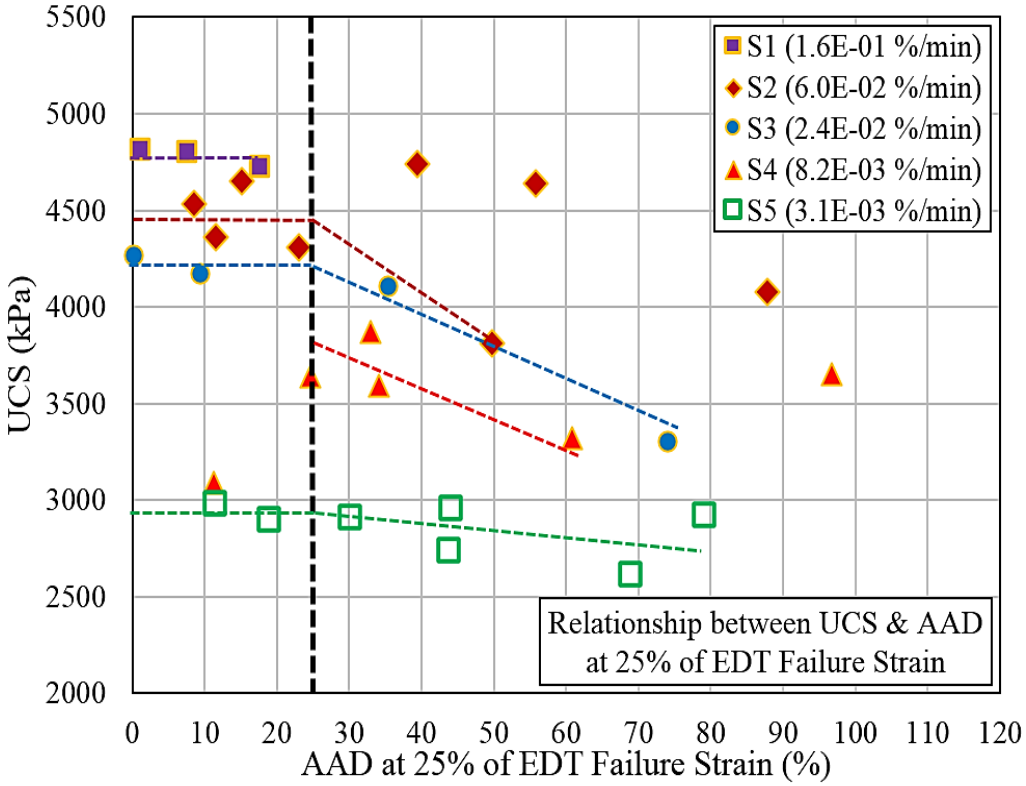

Fig. 3.3. Relationship between UCS and AAD at 25% EDT Failure Strain [2, 5]

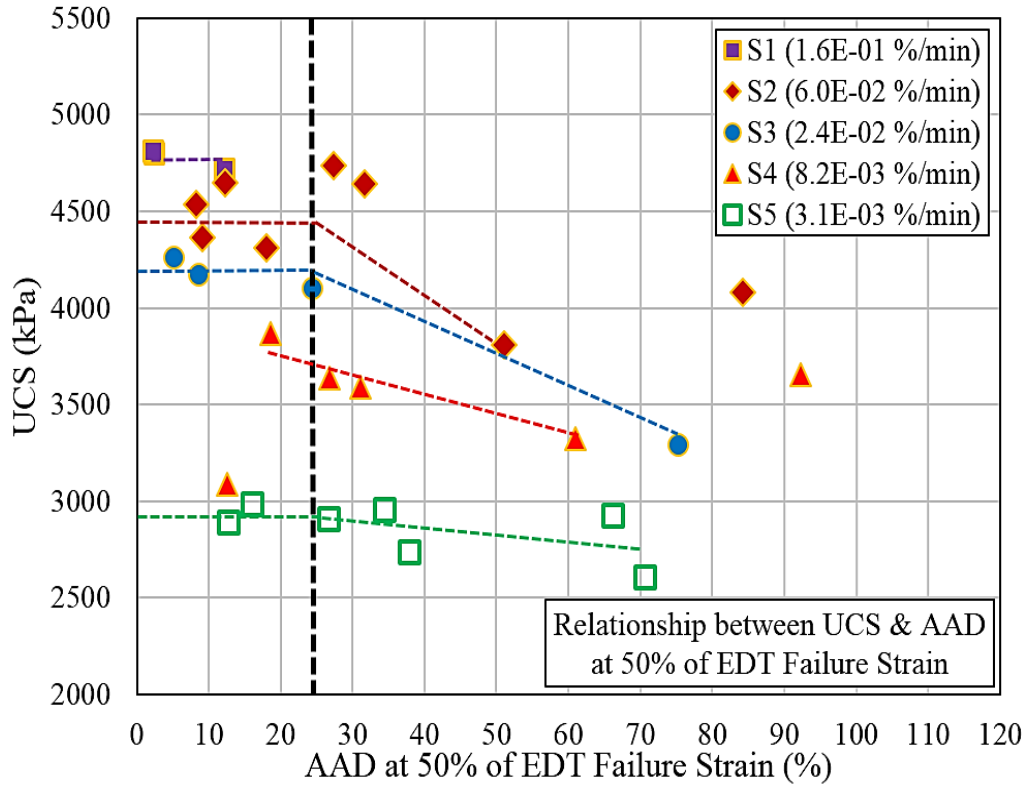

Fig. 3.4. Relationship between UCS and AAD at 50% EDT Failure Strain [2, 5, 6]

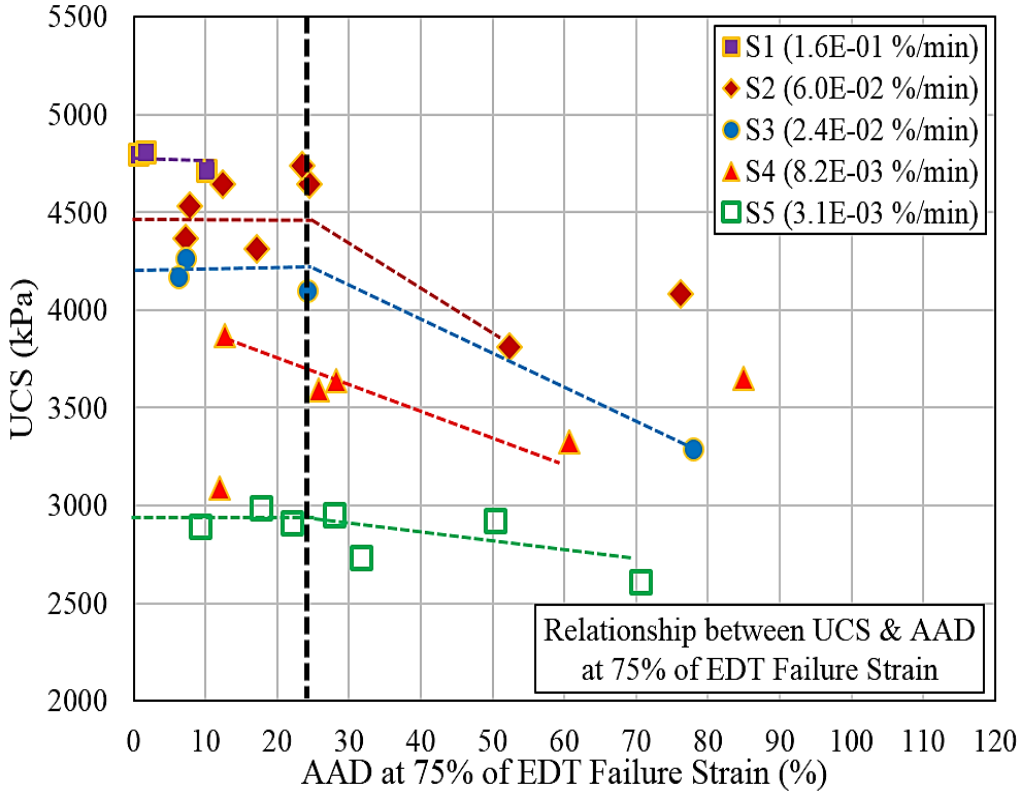

Fig. 3.5. Relationship between UCS and AAD at 50% EDT Failure Strain [2, 5]

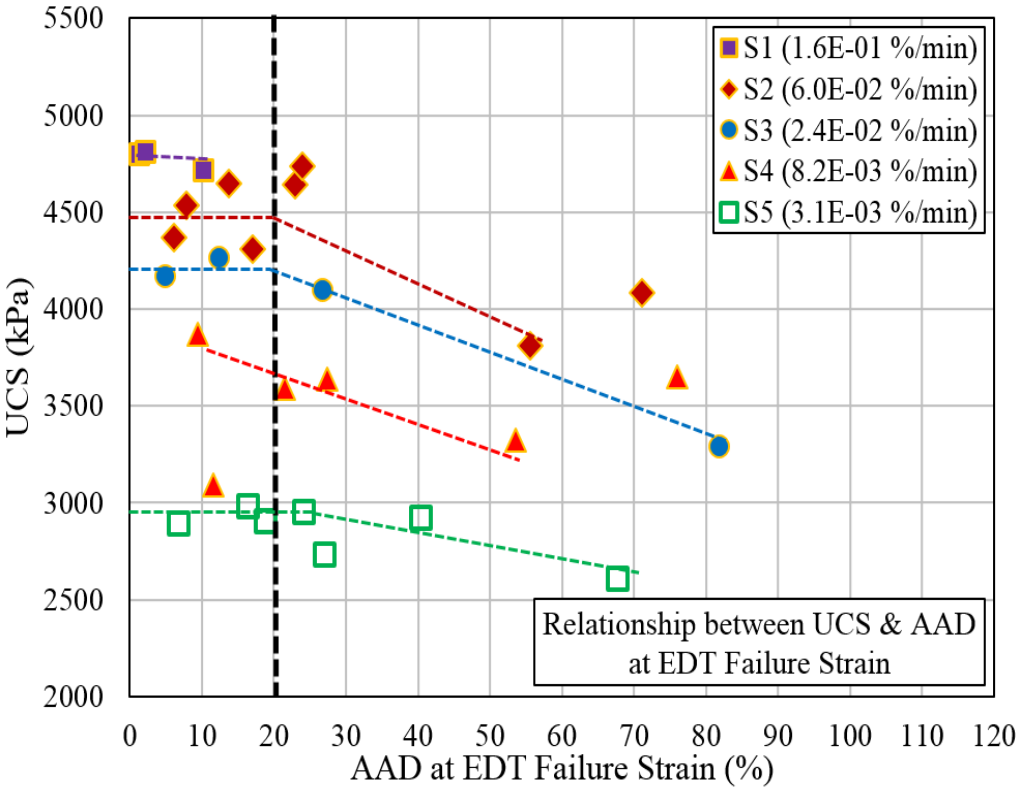

Fig. 3.6. Relationship between UCS and AAD at EDT Failure Strain [2, 5]

3.5 REPEATABILITY OF SELECTED TEST

The test results selected on the basis of reliability criterion based on local strain measurements, viz. AAD ≤ 25% at 50 EDT Failure Strain, generally showed a higher degree of repeatability as indicated by the absolute variations in UCS and standard deviations, as shown in Table 3.3. The said reliability assessment criterion is regarded to be essential to scrutinize test results, and the variations in the peak strength values are consider satisfactory for further analysis of loading rate dependency, as evident in Fig. 3.7. Moreover, the rejection rate of the test results presented in this chapter is about 54% as per this criterion [6].

Table 3.3. Statistical Analysis of Selected Test Results
(AAD ≤ 25% at 50% EDT Failure Strain)

Series ID	Average Axial Strain Rate	No. of Tests	UCS				
			Max. Value	Min. Value	Avg. Value	Absolute Variation	Standard Deviation
	(%/min)		(kPa)	(kPa)	(kPa)	(kPa)	(kPa)
S1	1.6E-01	3	4810	4716	4775	94	51
S2	6.0E-02	4	4647	4312	4392	335	154
S3	2.4E-02	2	4266	4174	3959	92	64
S4	8.2E-03	2	3870	3090	3527	780	551
S5	3.1E-03	2	2987	2896	2860	91	53

As an exception, only one selected test result of series S4, namely S4-UM2, showed significantly lower value of UCS compared with the rest of the tests performed at 8.2E-03 %/min, as shown in Fig. 3.7. Such a peculiar behavior of S4-UM2 is probably due to the indecorous preparation or any inherent non-uniformity of the specimen. Additionally, the higher values of absolute variation in UCS and standard deviation of test performed at 8.2E-03 %/min are attributed to S4-UM2. Except for S4-UM2, rest of selected test results are practically consistent with each other, signifying the effectiveness of this reliability assessment criterion based on local strain measurements [2, 6].

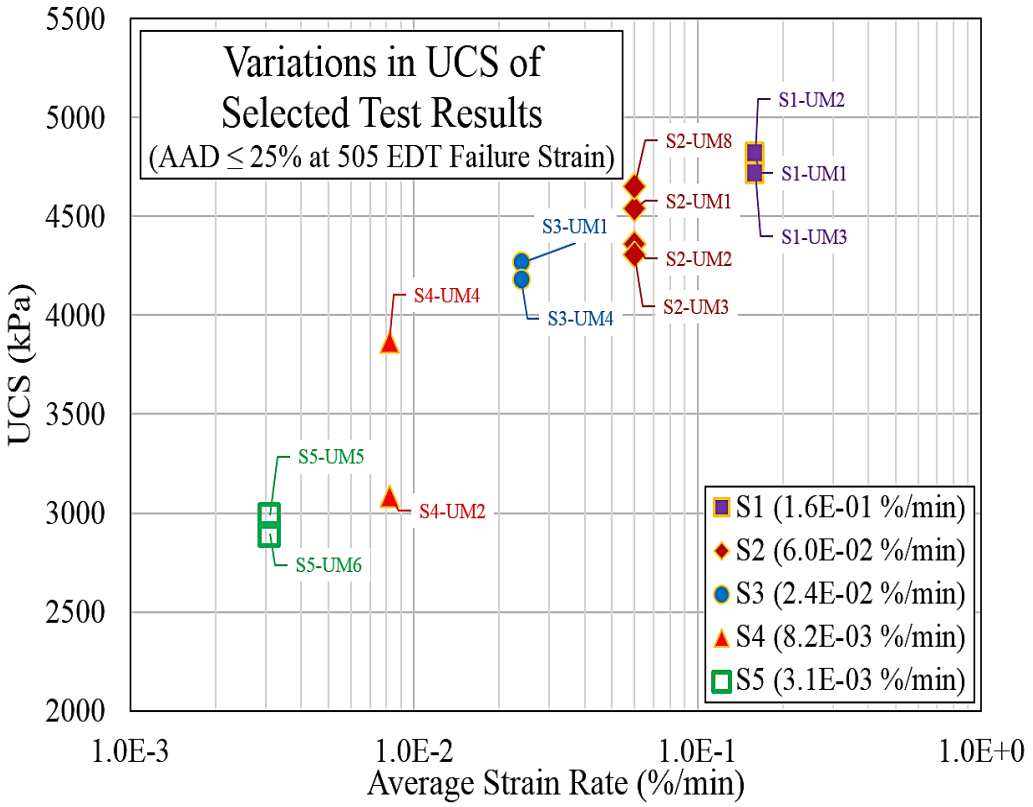

Fig. 3.7. Relationship between UCS of selected test results (AAD ≤ 25% at 50% EDT Failure Strain) and Average Strain Rate [5]

3.6 SUMMARY OF FINDINGS

- Substantial undesirable variations in UCS values of GMS specimens under similar testing conditions were observed.
- In general, higher values of UCS were reported for specimens having similar values of axial strains recorded by LDTs during monotonic loading, indicating a relatively uniform distribution of axial strain in specimen.
- The inconsistency between the locally measured axial strains by a pair of LDTs were quantitatively analyzed using Absolute Average Difference (AAD) of LDTs computed at opposite sides of the specimen.
- Based on the relationships between UCS values and AAD computed at four different strain levels, it was found that the UCS values generally decrease with the increase of AAD.
- For a certain initial range of AAD, the values of UCS were observed to be relatively consistent with each other.

- In the light of above stated findings, a reliability assessment criterion to scrutinize the test results is proposed. As per this criterion, all the test results having AAD lesser than 25% at 25% EDT Failure Strain were only selected for further analysis of loading rate dependency.
- The selected test results showed higher degree of consistency, signifying the effectiveness of the proposed reliability assessment criterion using local strain measurements.

3.7 REFRENCES

1. Chiu, H. K., Johnston, I. W., and Donald, I. B. (1983), "Appropriate techniques for triaxial testing of saturated soft rock", *International Journal of Rock Mechanics and Mining Sciences and Geomechanics Abstracts*, **20(3)**, 107-120.
2. Maqsood, Z. (2016), "Behaviour of gypsum mixed sand under unconfined monotonic and cyclic loading conditions," *Master's Thesis*, *The University of Tokyo,* Japan.
3. Maqsood, Z. and Koseki, J. (2015), "Behavior of gypsum mixed sand under unconfined monotonic and cyclic loading conditions," *GeoKanto, Japanese Geotechnical Society,* Japan.
4. Goto, S., Tatsuoka, F., Shibuya, S., Kim, Y., and Sato, T. (1991), "A simple gauge for local small strain measurements in the laboratory," *Soils and Foundations*, **31(1)**, 169-180.
5. *Maqsood*, Z. and Koseki, J. (2016). "Use of local strain measurements for rational evaluation of loading rate dependency of Gypsum Mixed Sand", *The 18th International Summer Symposium, JSCE,* Japan.
6. Maqsood, Z., Koseki, J. and Kyokawa, H. (2019), "Effects of loading rate on strength and deformation characteristics of gypsum mixed sand", *7th International Symposium on Deformation Characteristics of Geomaterials*, Glasgow. (accepted)

EEFECTS OF AGEING ON THE MECHANICAL BEHAVIOR OF GMS AND CTS

4.1 PREAMBLE

Long term mechanical behavior of bounded geomaterials are dictated by both ageing effects and loading rate (viscous) effects. Therefore, it was deemed indispensable to thoroughly study the effects of ageing (curing) period on the strength and deformation characteristics of laboratory produced GMS and CTS, prior to the evaluation of loading rate dependency. These ageing effects are typically attributed to the changes in inherent characteristics of bounded geomaterials with time due to different phenomenon, including hydration/curing, cementation and weathering etc. This chapter comprehends the ageing effects on the mechanical behavior of GMS and CTS specimens cured for different periods, ranging from 2 days to 9 months. Based on the obtained results, appropriate curing periods were proposed to reliably examine the loading rate dependency of GMS and CTS for the later part of this research endeavor.

4.2 CURING PROCEDURE OF GMS AND CTS SPECIMENS

GMS and CTS specimens were prepared in laboratory as per the procedure mentioned in Section 2.6 of Chapter No. 2. In an effort to devise a pragmatic procedure of curing, a total of four different curing procedures were initially studied, and their details are discussed elsewhere [1, 2]. Keeping in view the extensive demand and homogeneity of cured specimens, the following curing procedure was considered to be the most feasible [3]:

1. The uniformly mixed slurry was poured into the plastic molds, and kept air-tight for 48±3 hours, as shown in Fig. 4.1(a). This phase of curing is labeled as Initial Mold Curing (IMC), and was unerringly adopted for all GMS and CTS specimens.

2. After the completion of IMC, the specimens were than unmolded to obtain hardened specimens.
3. As a secondary phase of curing, these hardened specimens were wrapped using polythene plastic sheet, labeled as Polythene Sheet Curing (PSC), until testing. The specimens subjected to PSC are shown in Fig. 4.1(b).
4. The start of mixing process is regarded as the reference to calculate the total ageing/curing period.

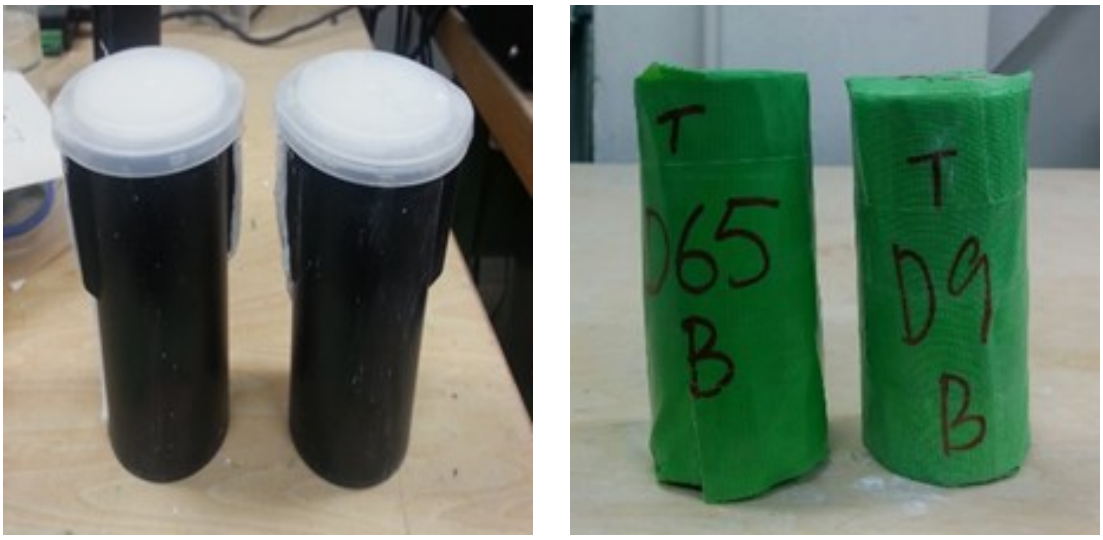

(a) Initial Mold Curing (b) Polythene Sheet Curing

Fig. 4.1. Curing procedure of GMS and CTS specimens [3]

4.3 TESTING PROCEDURE

At the targeted period of curing, GMS and CTS specimens were unwrapped and the following testing procedure was adopted for unconfined testing [1]:

1. The height of specimen was measured at three different points using Vernier caliper, and the average value of height was estimated.
2. Afterwards, the weight of specimens were recorded using weight balance.
3. The bulk unit weight of specimen was computed using the average height and weight of specimen.
4. Two sets of points were marked on the opposite sides of specimen to highlight the positions of the attachment of hinges for LDTs [4].
5. The specimen was then wrapped into 0.3 mm thick rubber membrane, and glue is applied on the surface of specimen at marked points [2].

6. Before placing the specimen in the apparatus, the centering of loading shaft, top cap and bottom pedestal was ensured.
7. In order to cap the bottom edge of specimen, slurry of dental gypsum and water was poured on the bottom pedestal, and the specimen was then placed on it [2].
8. The same slurry was then poured on the top edge of specimen, and the contact between the top cap and specimen was made by manually lowering the loading shaft [2].
9. In order to study the strain localization characteristics, a grid of black latex dots having a uniform spacing of 5 mm were pasted on the member of selected specimens. Moreover, a digital camera capable of taking photos at regular interval was also placed in front of the grid pasted on the specimen.
10. A total of four hinges were attached at the marked points using glue for the attachment of LDTs.
11. The specimen was then left for approximately 15 minutes to ensure hardening of capping material and glue.
12. Afterwards, a pair of LDTs were attached to the specimens by means of hinges, and were left for about 15 minutes to eradicate the undesirable effects of creep induced in hinges. The schematic illustration of specimen is shown in Fig. 4.2.
13. The monotonic loading at desired strain rate was than applied, and the test was stopped at desired strain level.

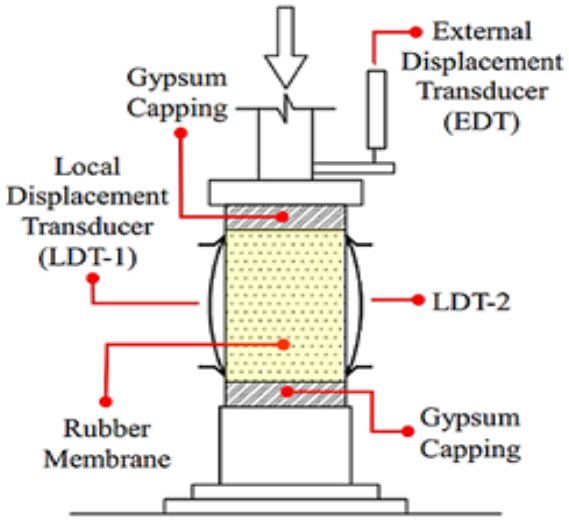

Fig. 4.2. Schematic illustration of specimen during testing [3]

14. After the completion of tests, a number of pictures of the failed specimen were taken to qualitatively study the failure pattern.
15. Generally, three small portions of failed specimen were placed into the oven for moisture content determination.

4.4 EFFECTS OF AGEING ON GMS

4.4.1 Hydration of gypsum

Commercially produced gypsum used for the preparation of GMS contains 99% β-form of calcium sulphate hemihydrate (β-$CaSO_4.1/2H_2O$, labeled as β-hemihydrate) by weight. This form of hemihydrate is manufactured by adopting dry methods (calcining etc.) from calcium sulphate dihydrate ($CaSO_4.2H_2O$, labeled as dihydrate). On mixing with water, a highly exothermic hydration reaction of hemihydrate yields the crystalized dihydrate as follows [5, 6]:

$$CaSO_4.1/2H_2O + 3/2\ H2O \rightarrow CaSO_4.2H_2O + Heat \qquad \text{(Eq-4.1)}$$

The hardened dihydrate mass produced by the hydration of β-hemihydrate is highly porous in nature comprising of fibrous and branching interlocked needles of β-dihydrate crystals, as shown in Fig. 4.3. Similarly, α-dihydrate crystals formed during the hydration of the other form of hemihydrate, viz. α-hemihydrate; also possess similar crystalline structure with relatively larger size needled-shape crystals and with higher degree of interlocking with each other [5, 7]. It is also noteworthy that expansion of slurry is also accompanied during hydration, and an overall increase of about 42% of volume of solid per unit volume of slurry was witnessed for water to gypsum ratio of 0.6 [6].

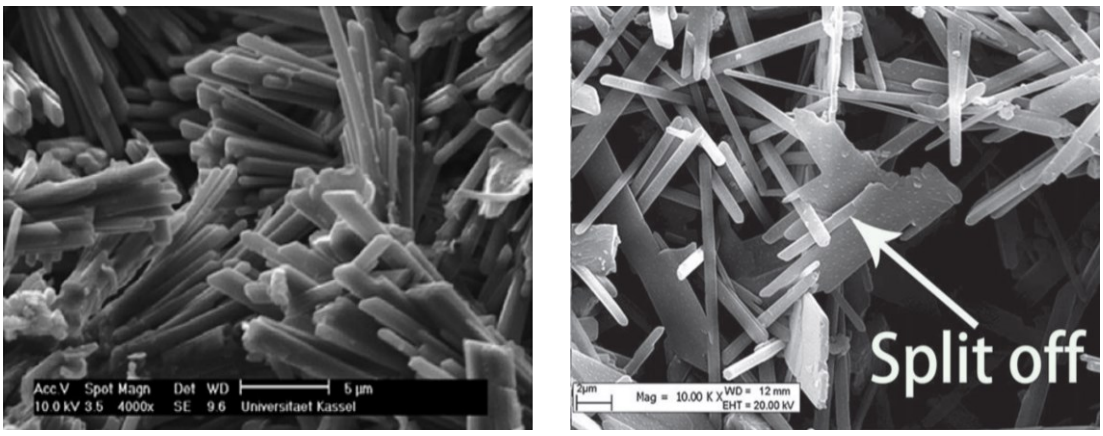

Fig. 4.3. Scanning electron micrograph of dihydrate crystals produced as a result of hydration reaction of β-hemihydrate [5, 8].

4.4.2 Test Results of GMS

A total of 18 unconfined monotonic tests were performed on GMS-MP1 specimens cured from 3 days up to 9 months, and results are presented in Table 4.1 [1]. Depending on the gypsum batch type (A, D and E) used for the preparation of GMS, the results are categorized into three series, viz. GMS-MP1(A), GMS-MP1(D) and GMS-MP1(E). Moreover, GMS-MP1(A) specimens were tested using Unconfined Compression Machine at an average strain rate of 6.9E-02 %/min, while the rest of tests were performed specimens were performed on Triaxial Compression Machine at average strain rate of about 2.3E-02 %/min., as highlighted in Table 4.1.

Table 4.1. Test Results of GMS-MP1 Curing Time Series [1]

Machine Type	Series ID	Average Axial Strain Rate	Test ID	Total Curing Time	Bulk Unit Weight Before Testing	Moisture Content After Testing	UCS	Failure Strain		Failure Time
								EDT	Avg. LDT	
		(%/min)			(kN/m^3)	(%)	(kPa)	(%)	(%)	(min)
UCM*	GMS-MP1(A)	6.9E-02	GA1-CT1	3 Days	18.3	31.7	4535	0.358	0.397	5.7
			GA1-CT2		18.3	32.5	4367	0.340	0.350	5.4
			GA1-CT3		18.2	31.5	4312	0.395	0.326	5.3
			GA1-CT4		18.4	30.0	4647	0.340	0.360	5.6
			GA1-CT5	2 Months	18.4	29.1	3687	0.754	0.536	10.9
			GA1-CT6	3 Months	18.3	28.1	3485	0.307	0.294	4.9
			GA1-CT7		18.1	29.1	3709	0.358	0.375	5.1
			GA1-CT8	4 Months	18.1	29.7	3805	0.389	0.440	5.4
			GA1-CT9		18.1	29.6	3576	0.388	0.390	5.1
			GA1-CT10		18.0	28.1	3468	0.312	0.374	4.8
			GA1-CT11	5 Months	17.9	26.9	3651	0.386	0.467	5.2
			GA1-CT12	9 Months	17.9	26.3	3587	0.373	0.436	5.0
TCM**	GMS-MP1(D)	2.4E-02	GD1-CT1	3 Days	18.5	34.3	3465	0.573	0.417	17.4
			GD1-CT2	1 Month	18.4	34.3	2688	0.680	0.429	18.7
			GD1-CT3	3 Months	18.3	33.4	2595	0.641	0.428	18.4
TCM**	GMS-MP1(E)	2.2E-02	GE1-CT1	3 Days	18.5	33.9	2899	0.635	0.432	19.8
			GE1-CT2	7 Days	18.5	33.3	2576	0.676	0.471	20.8
			GE1-CT3	14 Days	18.4	31.0	2450	0.691	0.455	22.1

* Unconfined Compression Machine, ** Triaxial Compression Machine

4.4.3 Significance of impurities and additives in gypsum

As per the manufacturer, setting time of this gypsum type is about 1 hour, and hardening of slurry achieved during 48±3 hours of IMC. The effects of ageing/curing period on the peak strength values of GMS in normal and semi-logarithmic plots are shown in Figures 4.4 and 4.5. At a particular curing period, GMS-MP1 specimens prepared using different Batches of gypsum, viz. Batch A, D and E, showed different peak strength. For instance, GMS-MP1(D) and GMS-MP(E) specimens are tested at about identical loading rates but the strength value of GMS-MP1(D) is about 20% higher than GMS-MP1(E) at a curing period of 3 days, as evident in Figures 4.4 and 4.5.

Likewise, GMS-MP1(A) showed significantly higher strength values compared to the rest of the specimens [1], and the average peak strength of GMS-MP1(A) was found to be about 50% higher than GMS-MP1(E). Although GMS-MP1(A) specimens were tested at slightly higher loading rates compared to the other specimens, but it is ostensible that such large differences in strength values at a given period of curing are majorly attributed to different batches of gypsum used for the preparation of specimens. At a curing period of 3 days, estimated test results of GMS specimens prepared using different gypsum batches are compared in Table 4.2.

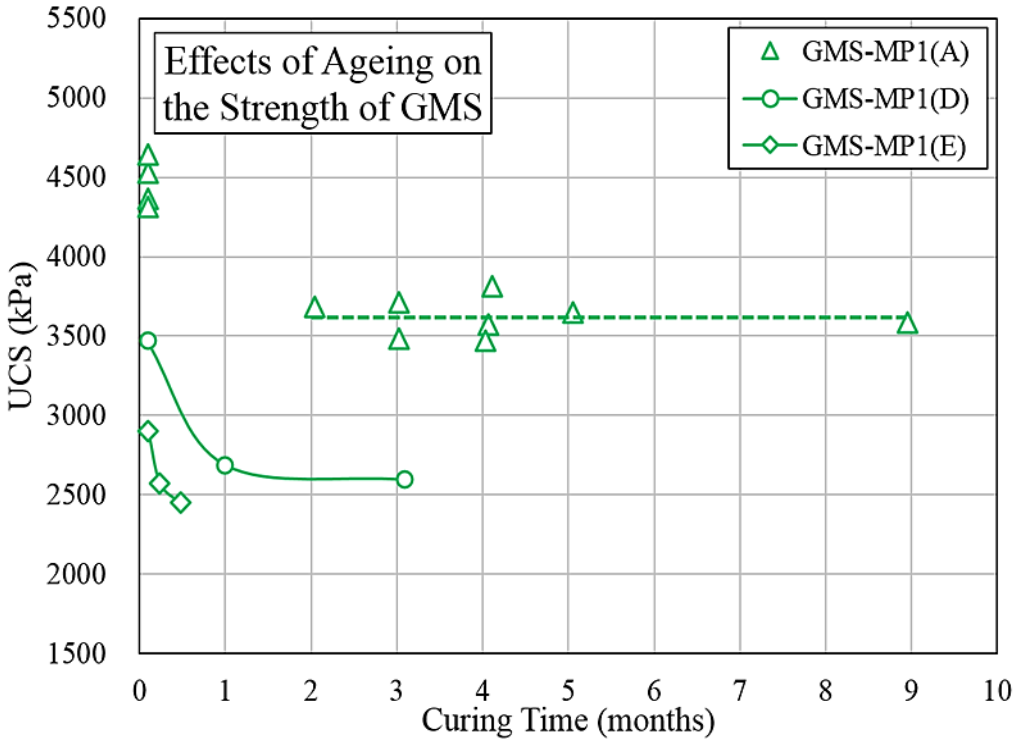

Fig. 4.4. Effects of ageing/curing on the UCS of GMS(MP1)

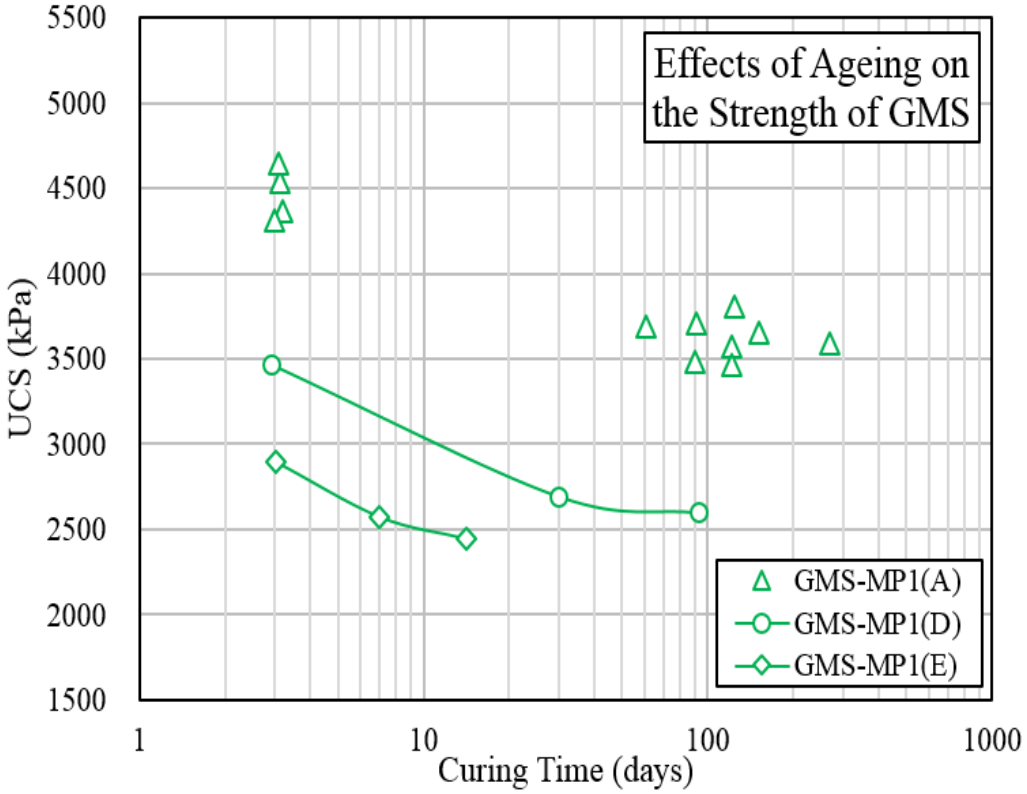

Fig. 4.5. Semi-logarithmic plot between ageing/curing and UCS of GMS(MP1)

In order to correlate the above highlighted discrepancies in the strength values of GMS-MP1, the effects of curing period on the values of bulk unit weight and moisture content are shown in Fig. 4.6 and 4.7 [1]. In general, a decreasing trend of bulk unit weight and moisture content was observed with the increase of curing period. As highlighted earlier, the time required for the completion of hydration reaction of gypsum was about 1 hour, and the amount of water, acting as one of the reactants, required for the hydration reaction is resultantly consumed within this earlier period of time. However, it is noteworthy that the average value of moisture content of GMS-MP1(A) measured after the testing at a curing period of 3 days was found to be relatively lower than GMS-MP1(D) and GMS-MP1(E), as shown in Fig 4.7 and Table 4.2.

As the total amount of water, gypsum and sand was fixed for all the specimens prepared by using different gypsum batches, lower value of moisture content of GMS-MP1(A) indicates that a relatively higher amount of total added gypsum was consumed during hydration resulting higher quantity of hardened dihydrate crystals in the set mass. Conversely, lower moisture content values indicate the presence relatively higher

amounts of additive or impurities in other gypsum batches, viz. Batch-D and E, as lower water was consumed during initial hydration. Moreover, the decrease of moisture with curing periods can possibly be consumed during delayed hydration of residual reactants, and with the release of excess pore water due to evaporation [7]. The presence of such evaporated moisture was observed at the inner surface of polythene sheets used for wrapping of specimens.

Table 4.2. Estimated Test Results of GMS-MP1 & CTS at Curing of 3 Days

Machine Type	Series ID	Average Axial Strain Rate	Bulk Unit Weight Before Testing	Moisture Content After Testing	UCS	Failure Strain		Failure Time
						EDT	Avg. LDT	
		(%/min)	(kN/m^3)	(%)	(kPa)	(%)	(%)	(min)
UCM*	GMS-MP1(A)	6.9E-02	18.3	31.4	4465	0.358	0.358	5.5
TCM**	GMS-MP1(D)	2.4E-02	18.5	34.3	3465	0.573	0.417	17.4
TCM**	GMS-MP1(E)	2.2E-02	18.5	33.9	2898	0.635	0.432	19.8
TCM**	CTS(A)	1.5E-02	18.1	32.8	1982	0.472	0.252	14.1

* Unconfined Compression Machine, ** Triaxial Compression Machine

The presences of different impurities and additives ominously control the strength characteristics of hardened gypsum, and the differences in the strength values of GMS-MP1 specimens prepared using different batches of commercially produced gypsum can be associated with the role of these constituents. Among other undesirable impurities in commercially produced gypsum, soluble calcium sulphate anhydrite ($CaSO_4$) is one of such commonly found impurity due to the over-dehydration of calcium sulphate dihydrate during the manufacturing process. The delayed hydration of calcium sulphate anhydrite results in to the disruption in the interlocking of dihydrate crystals, and ultimately leads to the reduction in peak strength [5, 9].

On the other hand, numerous additives are frequently introduced in commercially produced gypsum to control the setting time and other hardening characteristics. For instance, calcium sulphate dihydrate and potassium sulphate (K_2SO_4) are often used as nucleating agent and accelerator respectively. The presence of calcium sulphate dihydrate results into the reduction of the size of the hardened dihydrate crystals by increase in

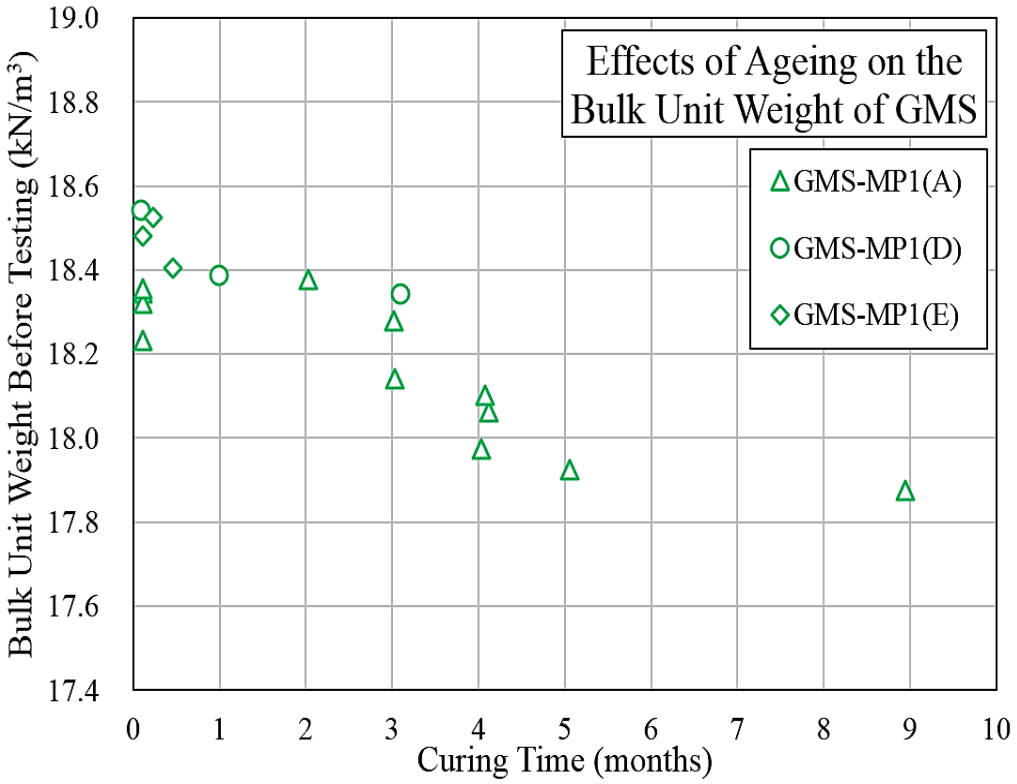

Fig. 4.6. Relationship between bulk unit weight and curing time of GMS-MP1

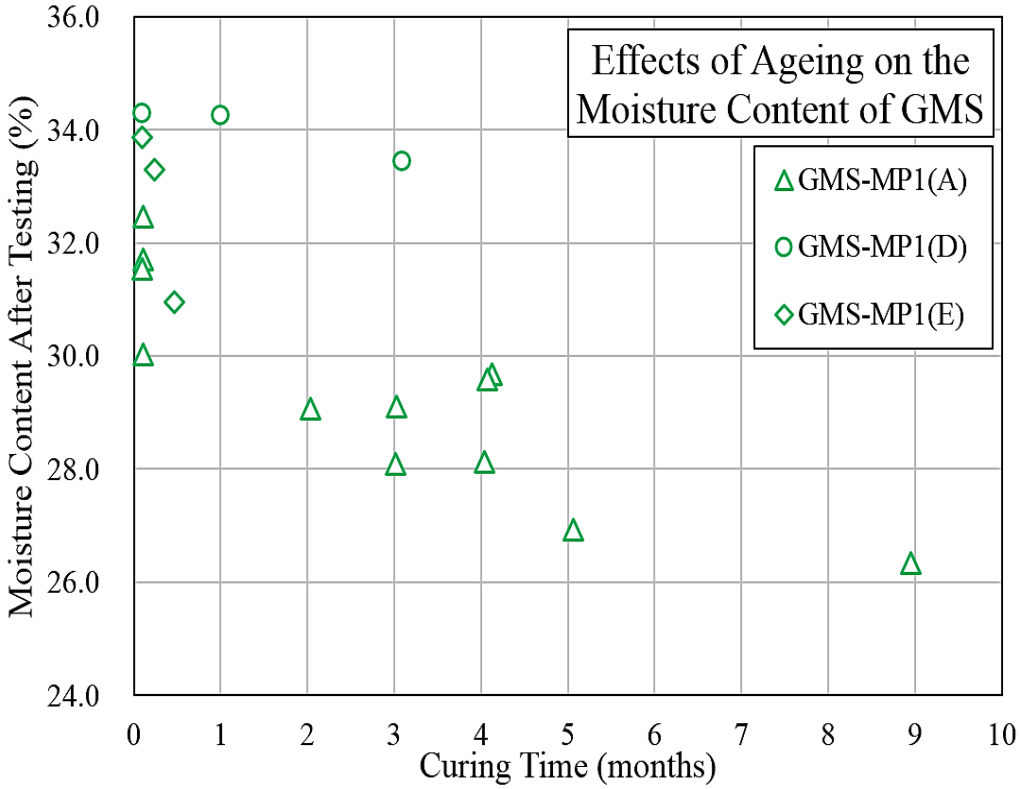

Fig. 4.7. Relationship between moisture content and curing time of GMS-MP1

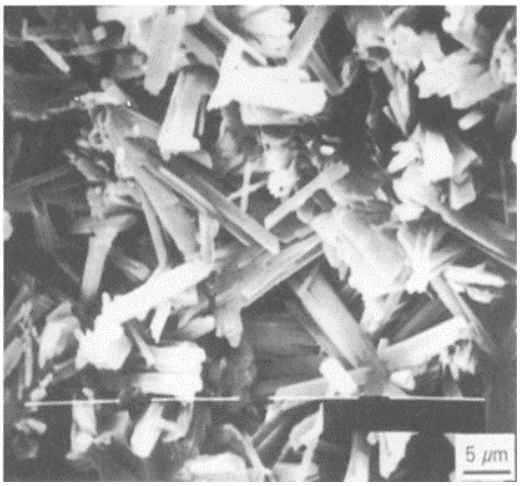

Fig. 4.8. Scanning electron micrograph of hardened gypsum [9]

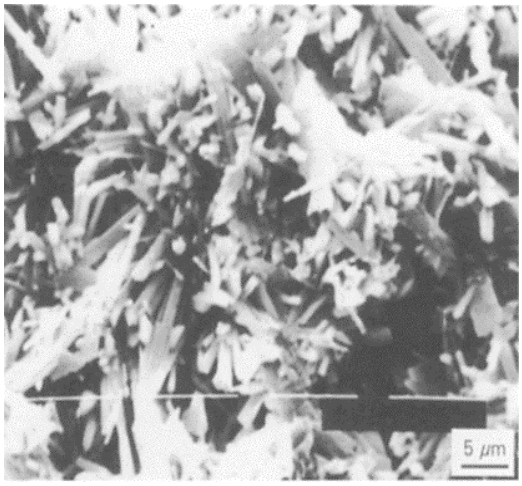

Fig. 4.9. Scanning electron micrograph of hardened gypsum with 2% dihydrate [9]

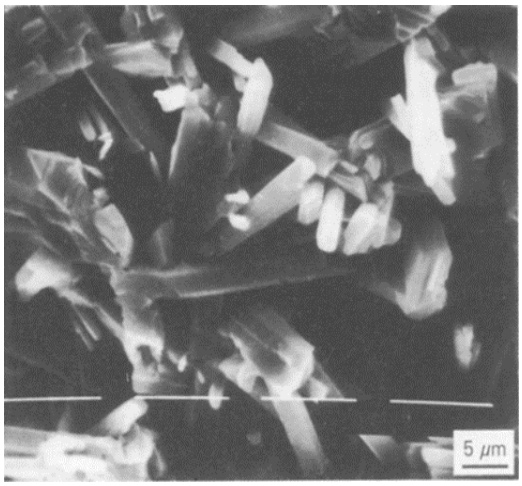

Fig. 4.10. Scanning electron micrograph of hardened gypsum with 2% potassium sulphate [9]

number of nuclei for crystal to grow, whereas potassium sulphate cause an increase in the size of hardened β-dihydrate crystals due to increase in the rate of crystal growth, as shown in Figures 4.8 to 4.10. Such changes in the crystal sizes reduce the interlocking bonding between the needled-shape crystals, and result into a decreased ultimate strength [5, 9]. Therefore, it can be postulated that different batches of commercially produced gypsum used in the present study have different amounts of additives or impurities, and their effects are noticeably reflected in obtained results, as evident in Figures 4.4 and 4.5.

4.4.4 Effects of ageing on the mechanical behavior of GMS-MP1

In addition to the effects of different gypsum batches on the strength values of GMS-MP1, the UCS values of GMS-MP1 were found to be significantly higher at a

curing period of 3 days, and a noticeable reduction in peak strength was observed during the first month of curing. For instance, the peak strength values of 3465 kPa of GMS-MP1(D) was witnessed at a curing period of 3 days, and it reduced merely to 2688 kPa during 1 month curing, as evident in Fig. 4.4 and Table 4.1. Similar trend of reduction in peak strength during the earlier periods of curing was also observed for GMS-MP1(A) and GMS-MP1(E). However, no noticeable effects of ageing on the peak strength values of GMS-MP1 were observed after this earlier 1 month of ageing/curing.

In order to compare this tendency of strength reduction in earlier periods of ageing, peak strength values at different curing periods are normalized with the UCS values of respective gypsum batches obtained at 3 days of curing, and are plotted against curing time, as shown in Figures 4.11 and 4.12. In spite of differences in the absolute peak strength values of GMS-MP1 specimen prepared by using different gypsum batches, a normalized strength reduction of about 20% occurred during the first month of ageing/curing, and no further reduction was observed afterwards, as evident in Figures 4.11 and 4.12. However, no noticeable effects of ageing on the failure strain values of GMS-MP1 were witnessed, as shown in Fig. 4.13.

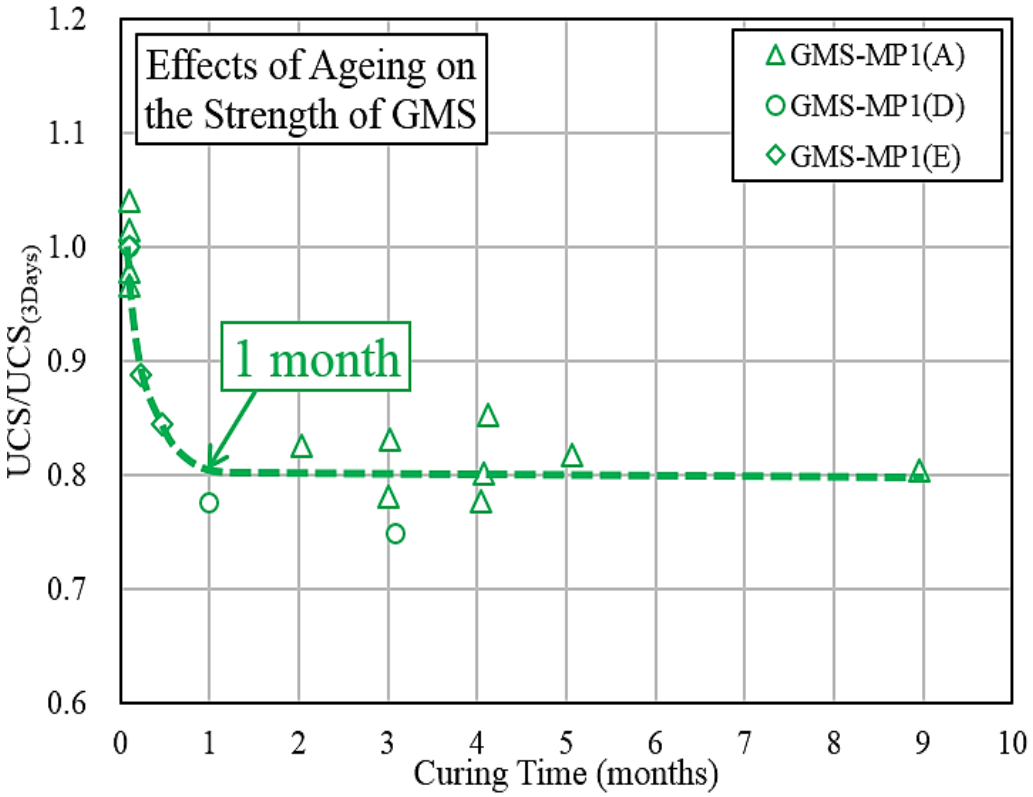

Fig. 4.11. Effects of ageing/curing on the normalized peak strength of GMS-MP1

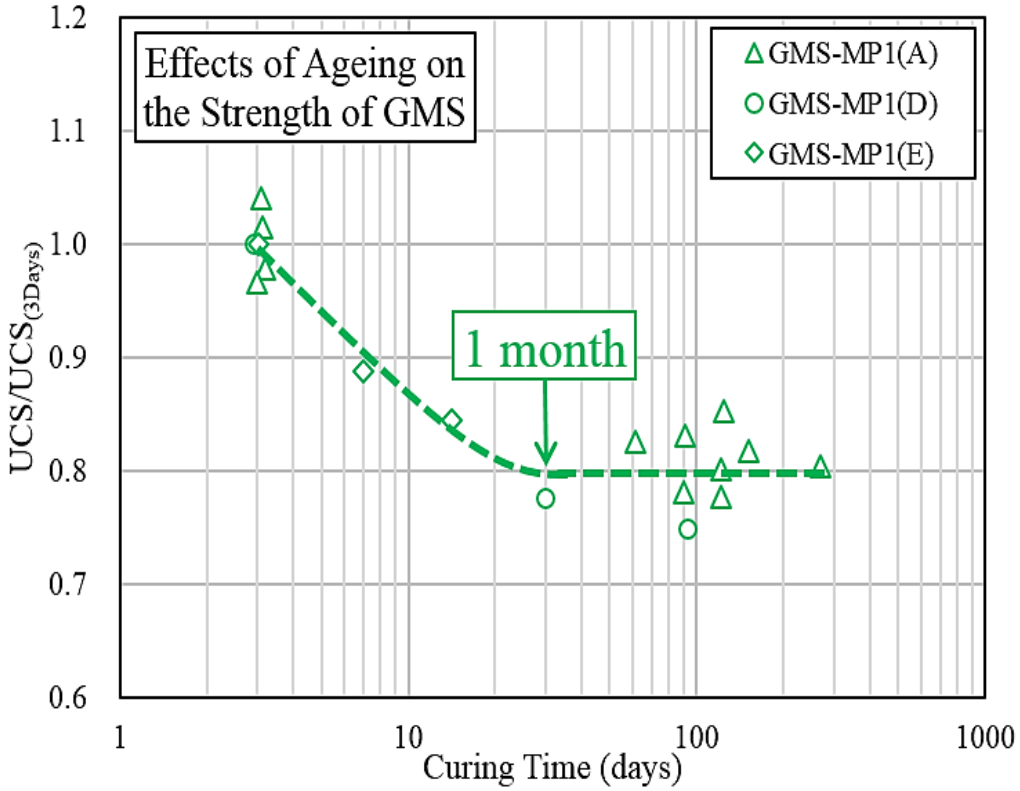

Fig. 4.12. Semi-logarithmic plot between ageing/curing and normalized peak strength of GMS-MP1

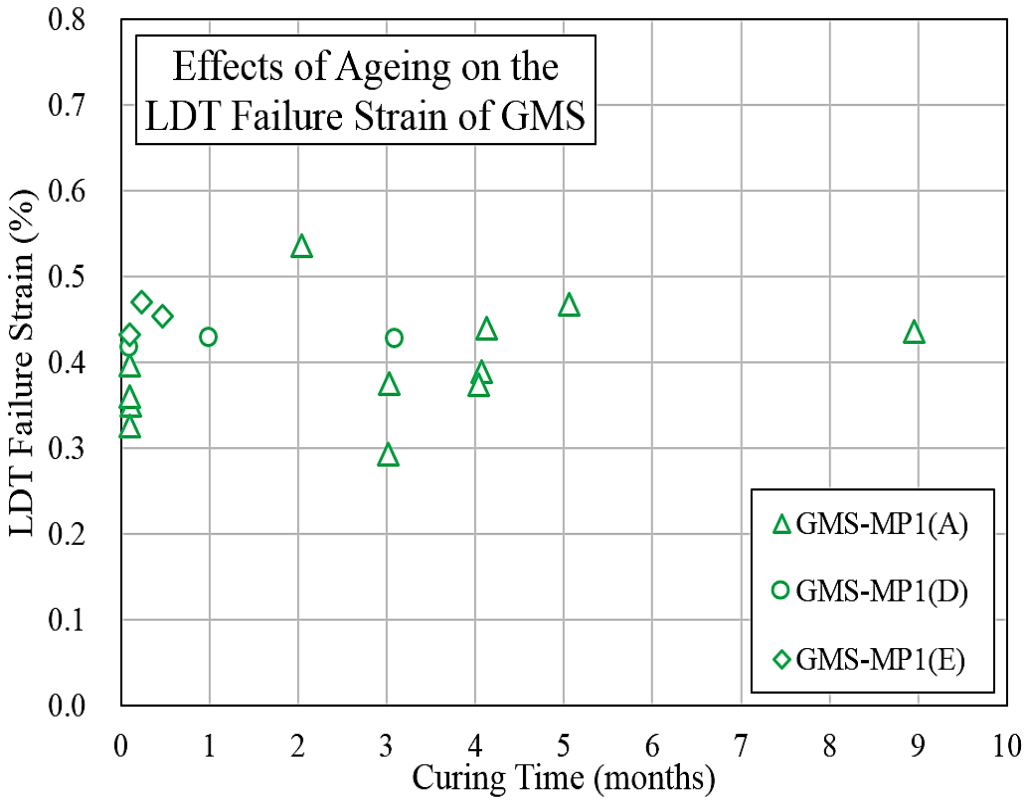

Fig. 4.13. Effects of ageing/curing on the failure strain of GMS-MP1

Similar tendency of reduction in peak strength values during the earlier periods of curing was also reported by Guan et al., as shown in Fig. 4.14, and the effects of humidity on the peak strength values and microstructure growth were examined by conducting series of unconfined compression tests along with SEM tests on gypsum (β-hemihydrate) mixed sand specimens, cured at different humidity conditions. Based on the obtained results, it was concluded that the humidity significantly affects the migration of pore water to the atmosphere, resulting changes in the rate of growth of dihydrate crystals. The amount of needled-shape crystals generally decreases with the increase of humidity at a fixed curing period [8].

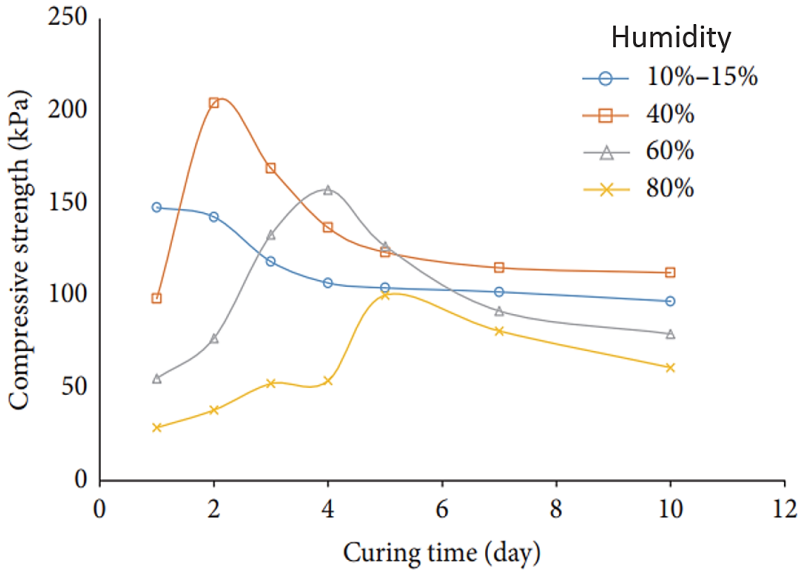

Fig. 4.14. Effects of ageing on the peak strength of gypsum (β-hemihydrate) mixed sand at different levels of humidity [8]

At higher values of humidity, the hydration reaction of gypsum is relatively prolonged and formation of new crystals continues for longer durations. Additionally, the tendency of intersection of needled-shaped crystals of dihydrate increases with curing period during at a fixed value of humidity, as shown in Fig. 4.15. At a particular value of humidity, the reduction of peak strength was attributed to the volume expansion of hardened mass and formation of additional microspores during the delayed formation of new dihydrate crystals, as evident in Fig. 4.15 [8]. Based on these findings, it can be stated that polythene sheet wrapped around GMS-MP1 specimens restricted to evaporate freely into the atmosphere, and resulted into the volume expansion of specimens due to the formation of delayed hydration products.

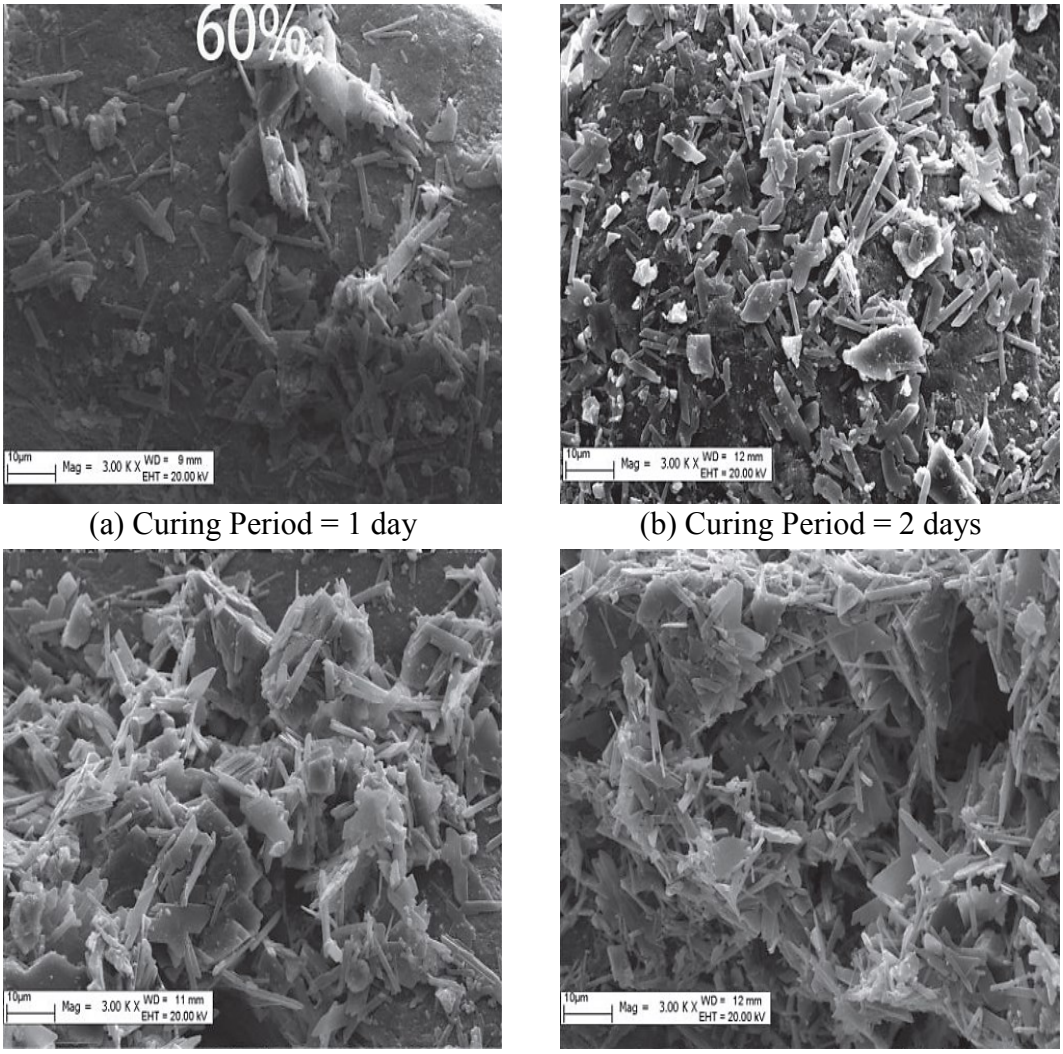

(a) Curing Period = 1 day (b) Curing Period = 2 days

(c) Curing Period = 3 days (c) Curing Period = 4 days

Fig. 4.15. Effects of ageing on the microstructure of gypsum (β-hemihydrate) mixed sand at 60% humidity [8]

In addition, reduction in the tensile strength of hardened gypsum was also witnessed in a series of three point bending tests performed on saturated specimens prepared by mixing water and gypsum (α-hemihydrate and β-hemihydrate) at a ratio of 0.6. For instance, a reduction of about 20% in the tensile strength, viz. modulus of rupture; was observed shortly after the completion of hydration reaction, and the values of modulus of rupture became stable afterwards, as shown in Fig. 4.16. It was stated that the microcracking due to the thermal gradation induced by the hydration reaction may have contributed to the reduction of strength. Furthermore, a possibility of relief of internal stresses formed due to the pushing forces exerted by different nuclei of crystals was also considered accountable for this behavior [7].

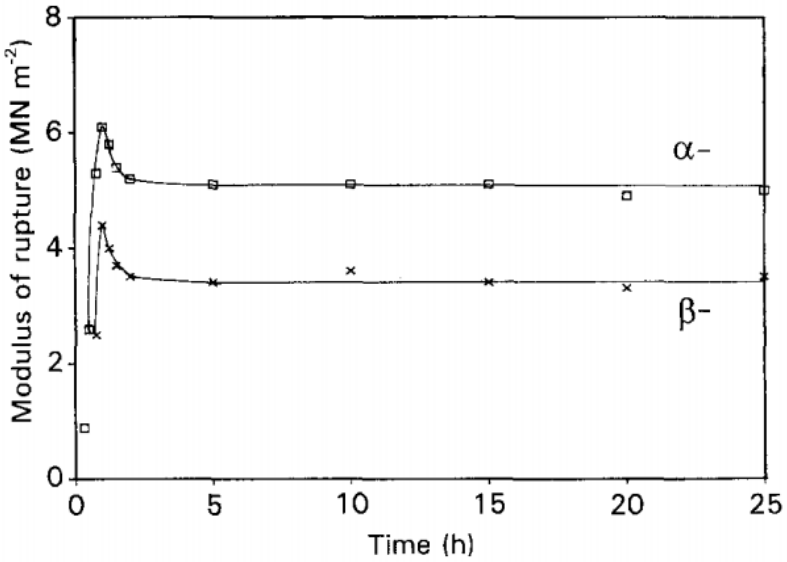

Fig. 4.16. Effects of ageing on the tensile strength of hardened gypsum [7]

The stress-strain relationships of GMS-MP1(D) are shown in Fig. 4.17. At a curing period of 3 days, a stiffer pre-peak response was witnessed, followed by a significant post-peak strain softening. For comparison purposes, normalized stress-strain responses are also plotted in Fig. 4.18 by dividing the stress and strain values with the values of UCS and failure strain estimated at 3 days of curing. In general, a reduction of post-peak stiffness was observed in earlier 1 month of curing, and no further noticeable effects of ageing on the stress-strain behavior of GMS-MP1(A) were observed during 1 to 3 months, as shown in Fig. 4.17. Additionally, the change in stress-strain behavior during the first month of curing is found to be more prominent during first 7 days, and then these effects of ageing on the mechanical behavior of GMS-MP1 start to diminish gradually, as shown in Figures 4.19 and 4.20.

The above stated findings are also supported by the stress-strain responses of GMS-MP1(D) specimens, as about identical stress-strain responses and similar reduction in pre-peak stiffness was observed during the earlier periods of curing, and no further effects of ageing were observed up to curing period of about 9 months, as shown in Figures 4.21 and 4.22. However, one of the GMS-MP1(D) specimens tested at a curing period of 2 months exhibited exceptionally ductile behavior probably due to unknown reasons, possible due to some inherent non-homogeneity in the specimen. Based on the above stated findings, it was opted to study the loading rate dependency of GMS at two different curing periods, viz. 3 days and 3 months.

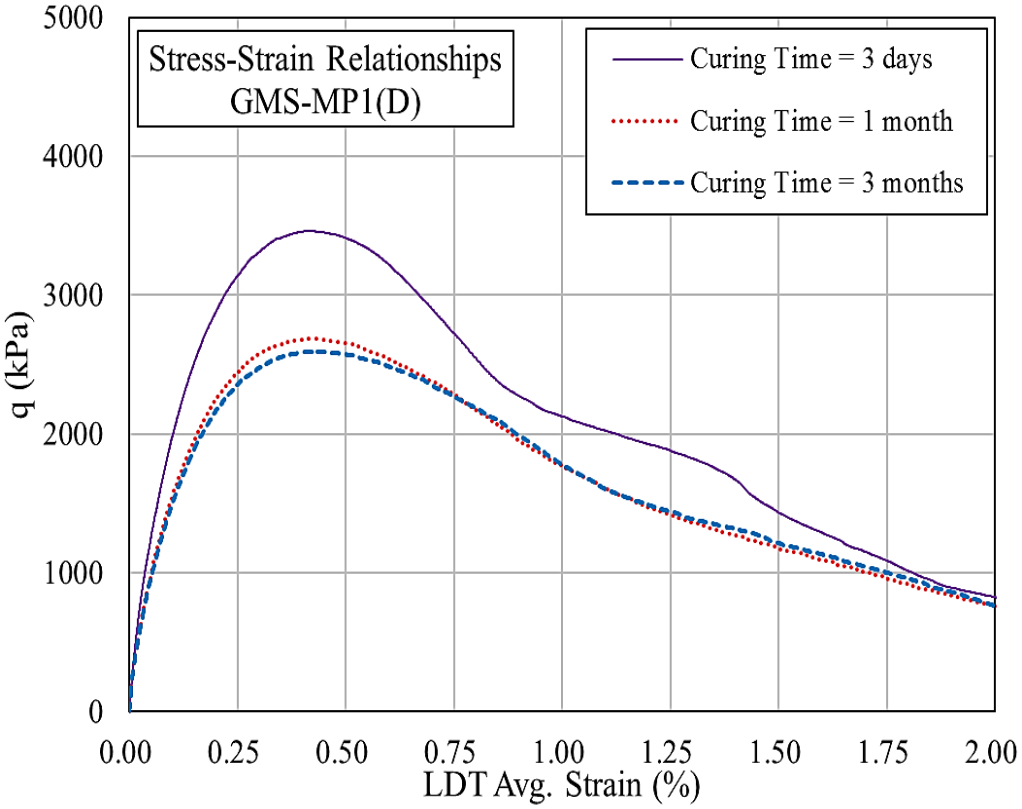

Fig. 4.17. Typical stress-strain of GMS-MP1(D)

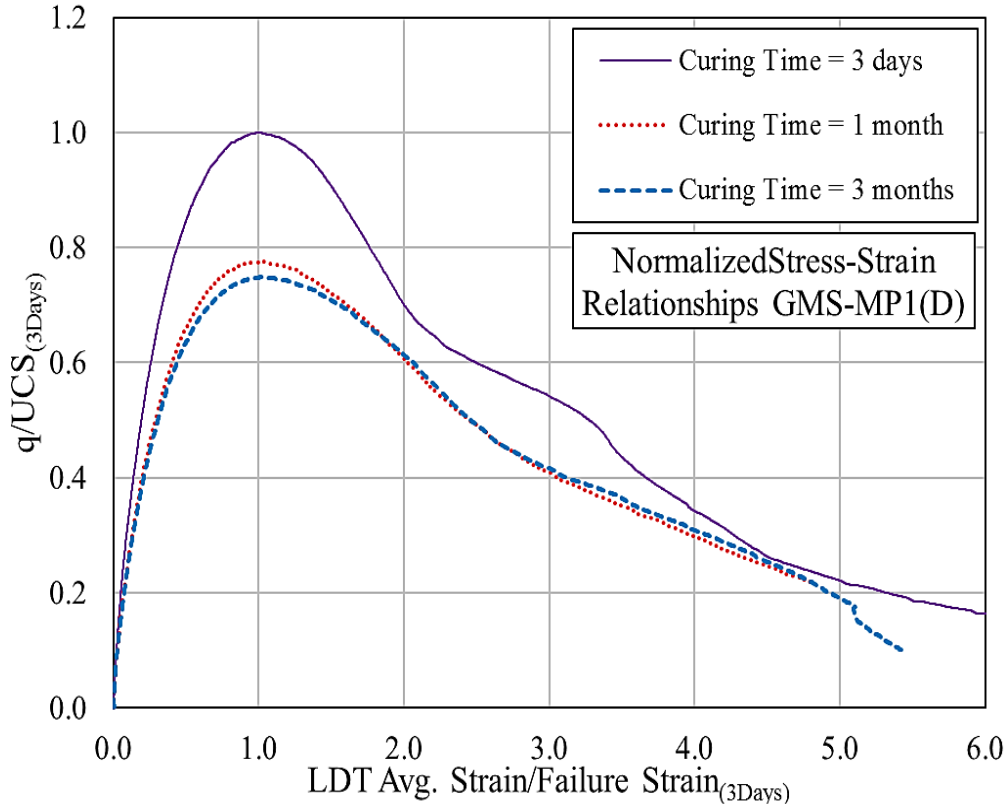

Fig. 4.18. Typical normalized stress-strain of GMS-MP1(D)

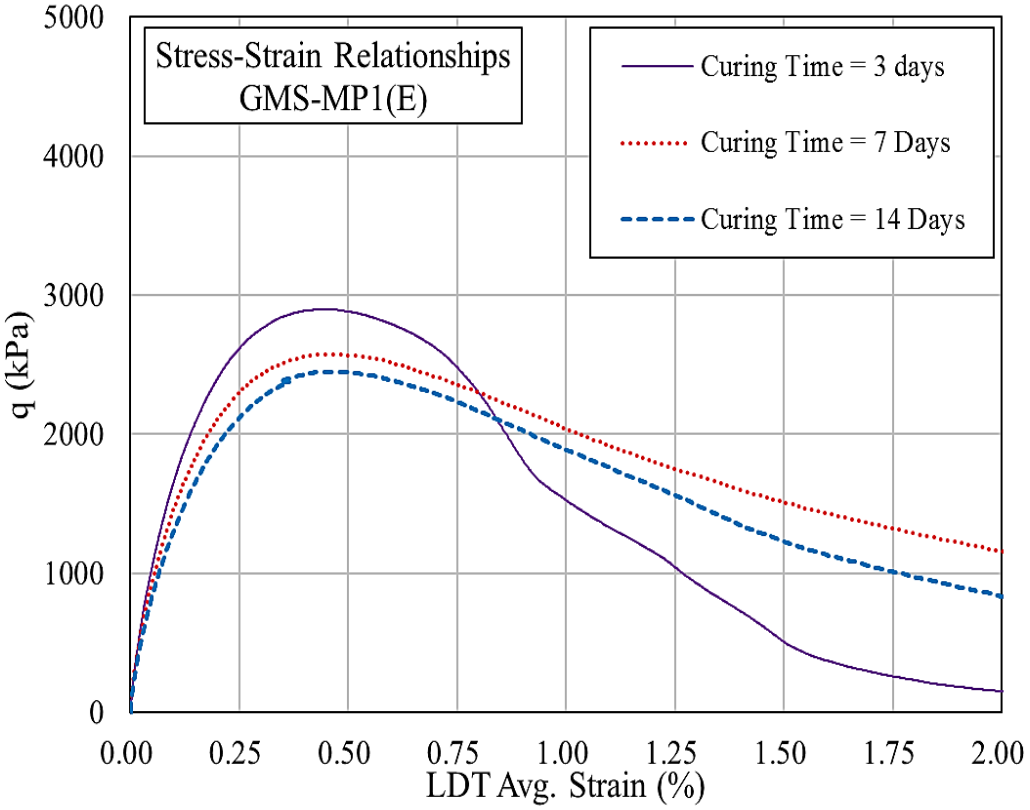

Fig. 4.19. Typical stress-strain of GMS-MP1(E)

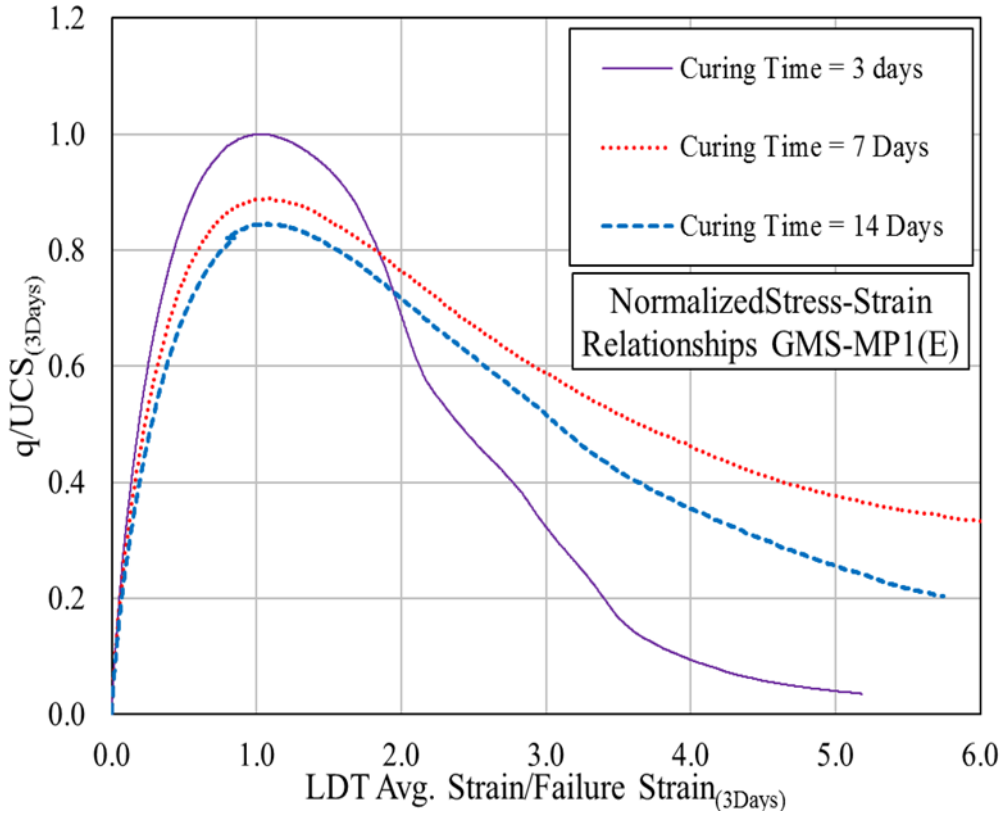

Fig. 4.20. Typical normalized stress-strain of GMS-MP1(E)

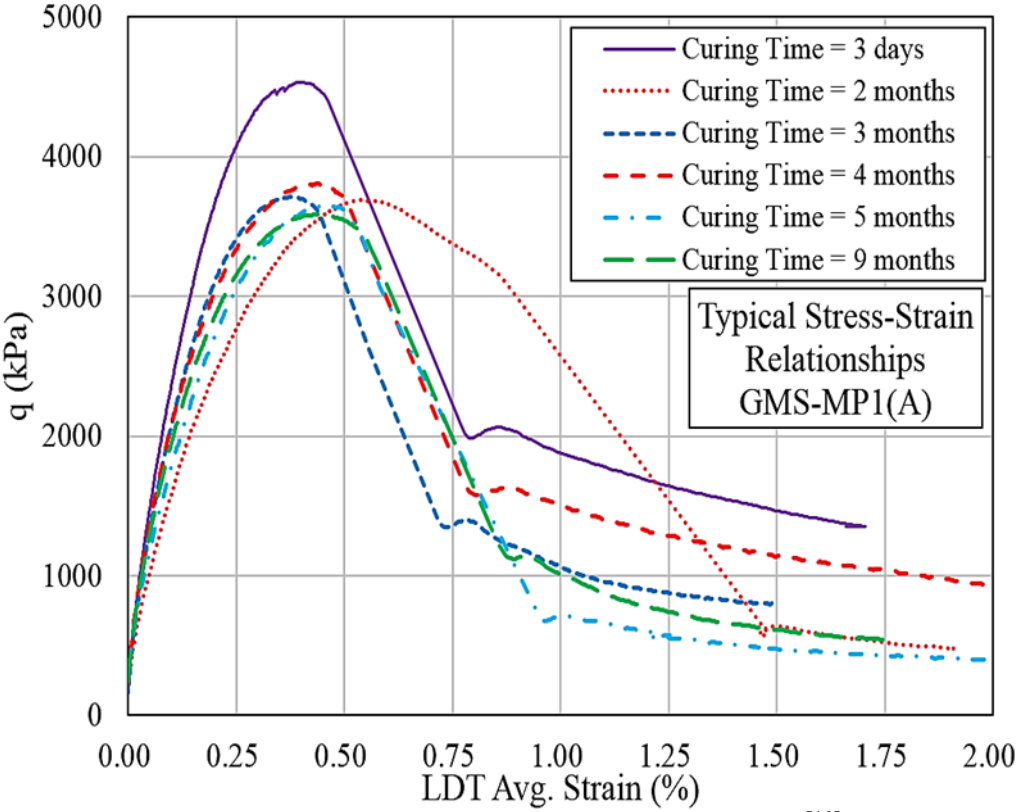

Fig. 4.21. Typical stress-strain of GMS-MP1(A) [10]

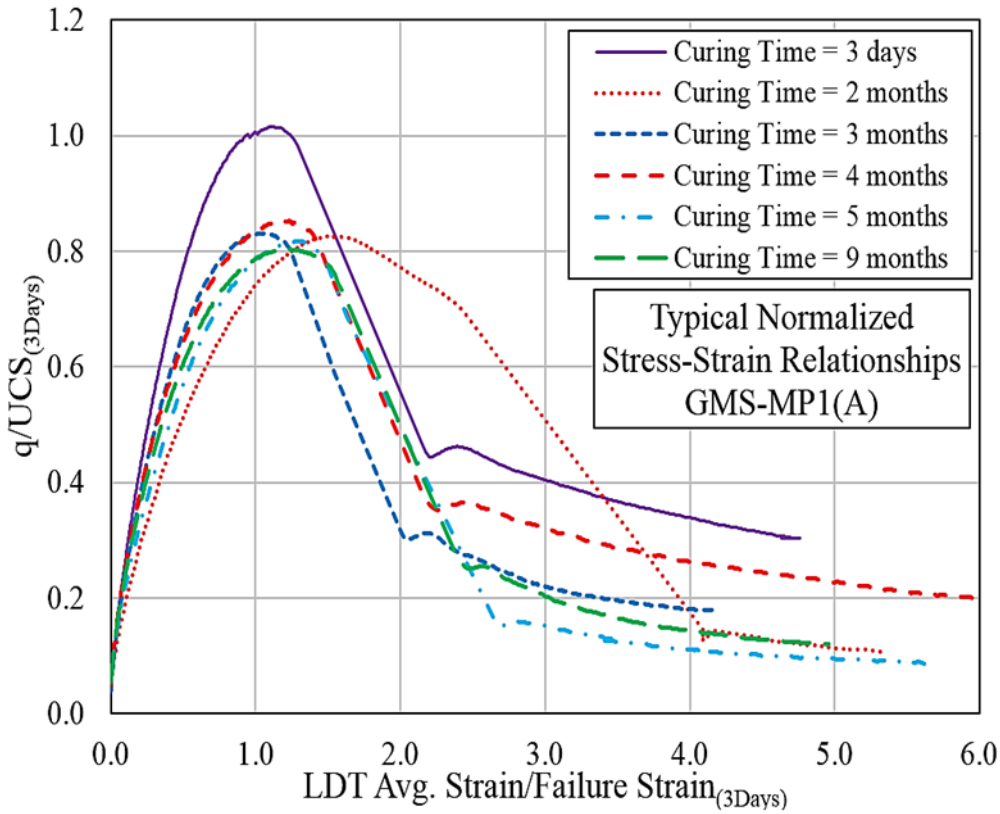

Fig. 4.22. Typical normalized stress-strain of GMS-MP1(A)

4.5 EFFECTS OF AGEING ON CTS

4.5.1 Hydration of cement

High Early Strength (HES) cement manufactured by Sumitomo Osaka Cement Co. Ltd., Japan, was used for the preparation of CTS specimens. Typically HES cement contains higher percentage of Tricalcium Silicate ($3CaO.SiO_2$, labeled as C_3S), and lower quantity of Dicalcium Silicate ($2CaO.SiO_2$, labeled as C_2S) compared with Ordinary Portland Cement (OPC) . Owing to high C_3S content and smaller particle size, hydration reaction is accelerated and higher strength is achieved at a relatively shorted periods of curing. The hydration reaction of HES cement mainly produces calcium hydroxide ($Ca(OH)_2$, labeled as CH) and calcium silicate hydrate ($3CaO.2SiO_2.3H_2O$, labeled as C-S-H gel) as per the following equations [11]:

$$2(3CaO.SiO_2) + 6H_2O \rightarrow 3CaO.2SiO_2.3H_2O + 3Ca(OH)_2 \quad \text{(Eq-4.2)}$$

$$2(2CaO.SiO_2) + 4H_2O \rightarrow 3CaO.2SiO_2.3H_2O + Ca(OH)_2 \quad \text{(Eq-4.3)}$$

In cement mixed sand, cement paste is intended to bind the sand particles, and hydration products are formed around sand particles, as shown in Figures 4.23 and 4.25. C-S-H gel is one of the principal product of hydration reaction that dictates the strength characteristics, and it is known to be a poorly crystalline sheet-like mass, as evident in Fig 4.23. The major proportion of the strength is achieved during early hydration of C_3S, and CH produced during the hydration reaction, as shown in Fig. 4.23, is responsible for long-term strength development due to its pozzolanic reactions with soils [11-14].

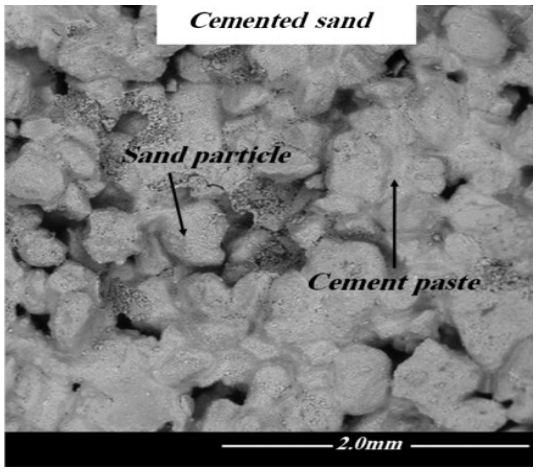

Fig. 4.23. Scanning electron micrograph of cement mixed sand [12]

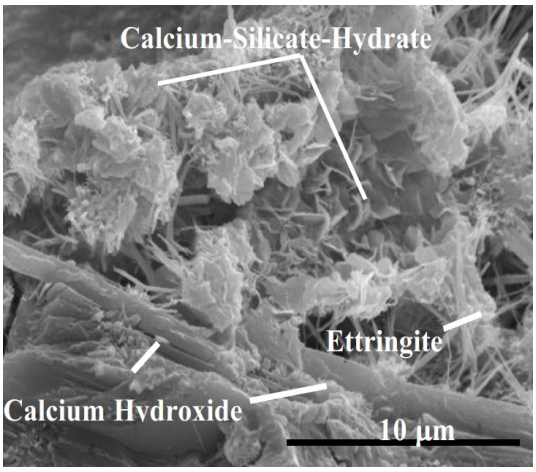

Fig. 4.24. Scanning electron micrograph showing C-S-H gel and $Ca(OH)_2$ [14]

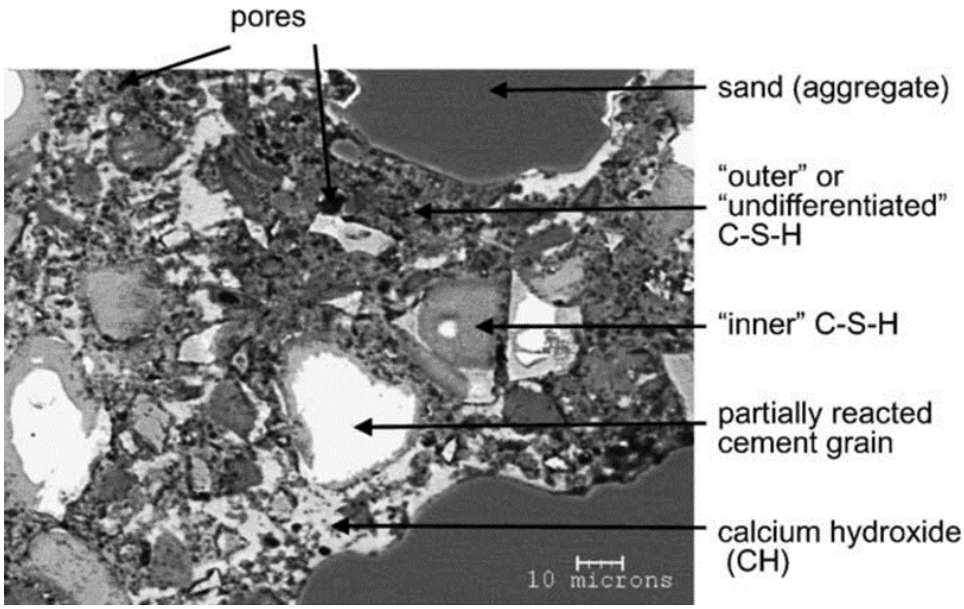

Fig. 4.25. Typical Backscatter Electron (BSE) image of cement mixed sand [13]

The schematic illustration of typical strength development of in-situ mixing of cement with soils is shown in Fig. 4.26. In case of clayey soils, the addition of dry cement results into the reduction of water content and some improvement in strength also occurs due to the cation exchange by the cement. However, the major proportion of strength enhancement in the earlier curing periods is due the formation of hydration products, such as C-S-H gel. Afterwards, pozzolanic reaction of CH with soils contribute towards a relatively slower rate of increase in long-term strength, as shown in Fig. 4.26 [15].

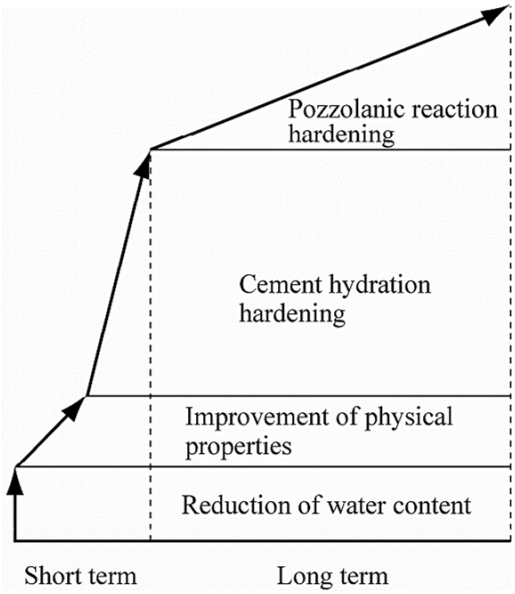

Fig. 4.26. Schematic illustration of strength development in cement mixed soils [15]

4.5.2 Test Results of CTS

The results of unconfined monotonic tests performed on CTS specimens cured from 2 days to 7 months are presented in Table 4.3. The average specimen height was measured to be about 95 mm, and top edges of specimens were flatten using sand paper. All of these tests were conducted at an average strain rate of 1.5E-02 %/min using triaxial compression machine. The tests were performed by adopting the same procedure as mentioned in Section 4.3, and the reliability of these tests were assured using the criterion stated in Chapter No. 3 [16].

Table 4.3. Test Results of CTS Curing Time Series [3]

Machine Type	Series ID	Average Axial Strain Rate	Test ID	Total Curing Time	Bulk Unit Weight Before Testing	Moisture Content After Testing	UCS	Failure Strain		Failure Time
								EDT	Avg. LDT	
		(%/min)			(kN/m^3)	(%)	(kPa)	(%)	(%)	(min)
TCM**	CTS(A)	1.5E-02	CA-CT1	2 Days	18.1	33.1	1757	0.468	0.253	13.4
			CA-CT2	5 Days	18.1	32.2	2439	0.480	0.250	15.5
			CA-CT3	7 Days	18.2	31.8	2805	0.484	0.237	15.5
			CA-CT4	10 Days	18.0	31.8	3014	0.661	0.244	17.8
			CA-CT5	14 Days	18.1	31.1	3535	0.515	0.265	18.3
			CA-CT6	21 Days	18.1	30.3	3976	0.568	0.278	17.4
			CA-CT7	1 Month	18.3	29.8	3981	0.626	0.258	20.7
			CA-CT8		18.0	30.5	3928	0.639	0.304	20.4
			CA-CT9	1.5 Months	17.9	30.7	3487	0.559	0.239	15.8
			CA-CT10	2 Months	18.0	30.8	3522	0.583	0.302	16.4
			CA-CT11	3 Months	18.0	30.3	3860	0.591	0.262	17.5
			CA-CT12	4 Months	17.8	30.9	3866	0.609	0.278	16.6
			CA-CT13	6 Months	17.9	28.9	3841	0.683	0.354	19.2
			CA-CT14	7 Months	17.7	26.8	4553	0.695	0.359	20.0

** Triaxial Compression Machine

4.5.3 Effects of ageing on the mechanical behavior of CTS

Figures 4.27 and 4.28 shows the effects of curing/ageing period on the unconfined compressive strength of CTS(A) in normal and semi-logarithmic plot respectively. As a result of hydration reaction of cement, a continuous increase in peak strength values was observed during the 21 days of curing, and no further effects of curing on the UCS values were witnessed up to 6 months, as evident in Fig. 4.23. In the first month, the consumption of water (acting as a reactant) during the hydration process is indubitably reflected in the variation of content with time, and continuous reduction in moisture content with curing time was witnessed during this period, as shown in Fig. 4.29. Afterwards, the values of moisture content are relatively constant up to 4 months, indicating the completion of hydration reaction, resulting into negligible increase in the strength of CTS, as shown in Figures 4.27 and 4.29 [3].

The values of bulk unit weight of CTS specimens are relatively scattered, but generally slight reduction with curing time was observed, as shown in Fig. 4.30. It is also noteworthy that the peak strength value of specimen cured for 7 months, viz. CA-CT14, was slighter higher than the rest of the specimens. Additionally, the values of moisture content and bulk unit weight estimated at this curing period are markedly lesser, and it is presumed that either delayed pozzolanic reaction or drying of specimen resulted into this slight increase in strength, as evident in Figure 4.29 to 4.30.Although the value of moisture content at curing period of 6 month was also relatively lesser, but the effect of this moisture reduction was not prominent on the peak strength of specimen [3].

The effects of ageing on the values of failure strains estimated using EDT and LDTs are shown in Fig. 4.31. The influence of bedding error is clearly evident as the values of failure strains measured using EDT are significantly higher than LDTs. Generally, a slight increase in failure strain with curing time was observed during the first month of curing, and the values are generally constant between the curing periods of 1 to 4 months. Furthermore, a minor increase in the failure strain values of specimens tested at curing period of 6 and 7 months was also witnessed.

Stress-strain response of CTS is also affected significantly during the first month of curing, and significant increase in pre-peak stiffness and post-peak strain softening with curing time was witnessed during this earlier phase of curing, as shown in Figures

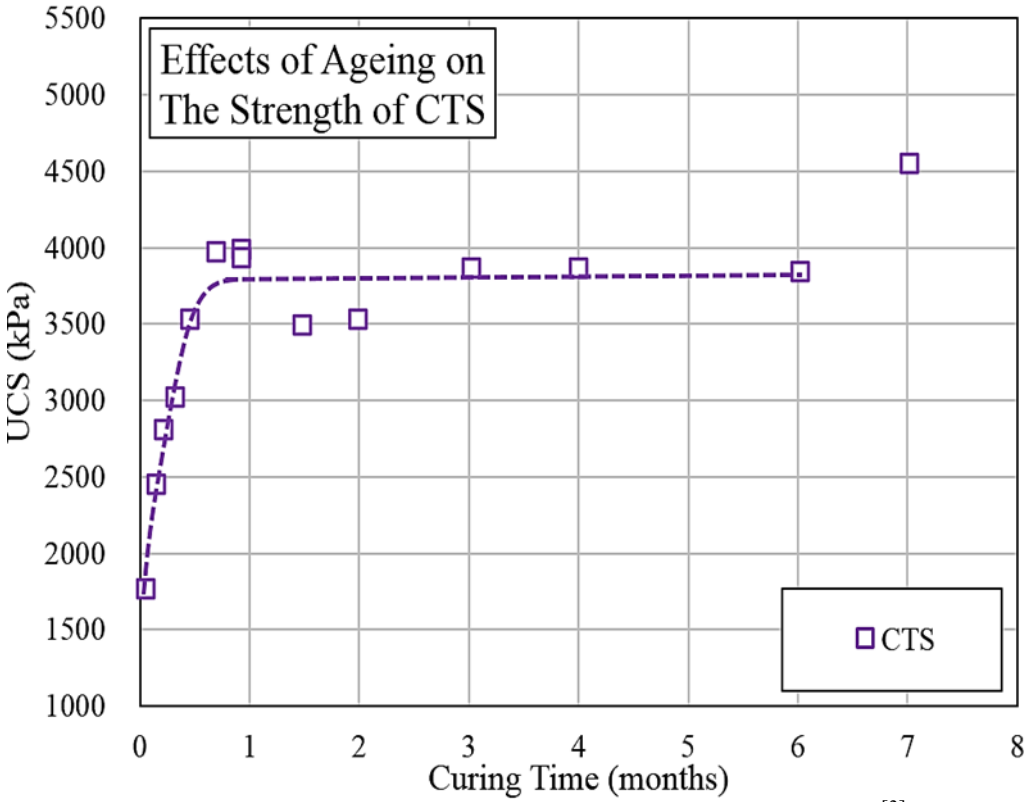

Fig. 4.27. Effects of ageing/curing on the UCS of CTS(A) [3]

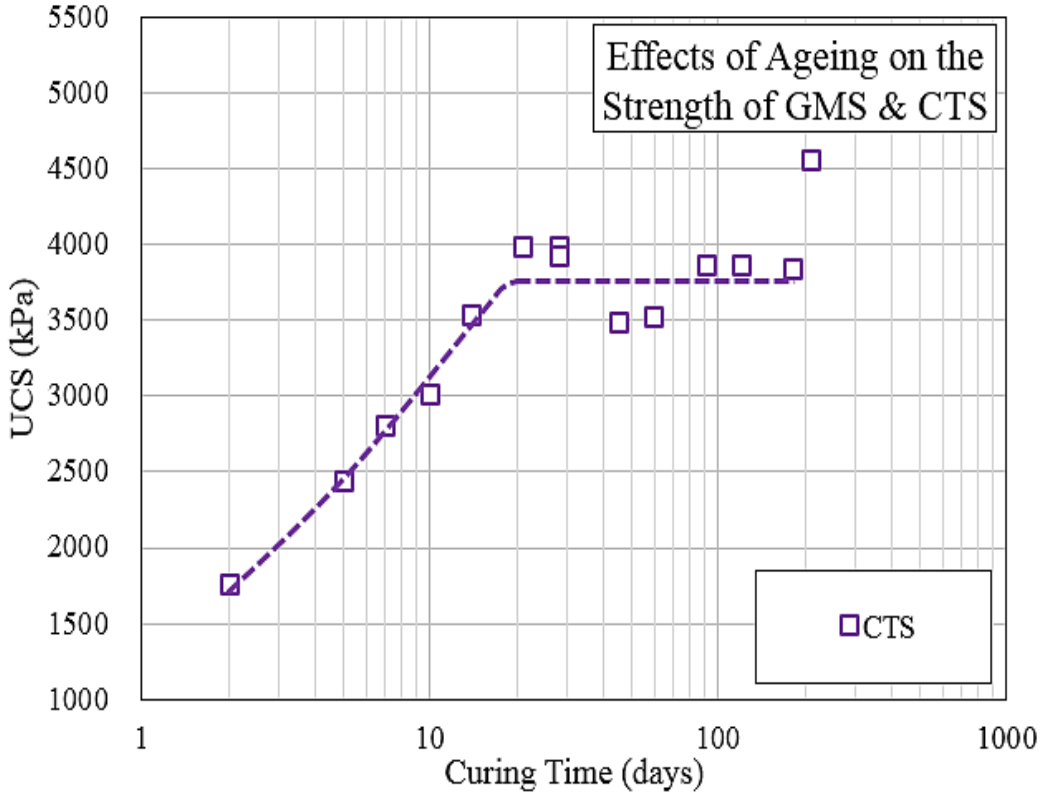

Fig. 4.28. Semi-logarithmic plot between ageing/curing and UCS of CTS(A)

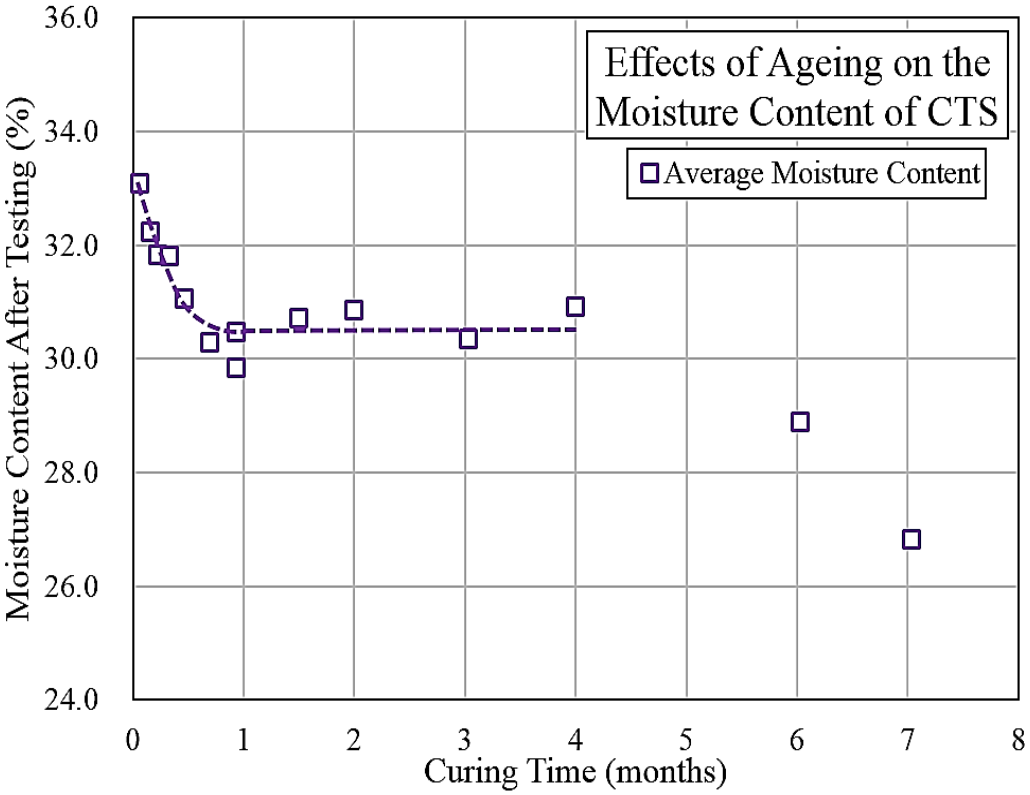

Fig. 4.29. Effects of ageing/curing on the moisture content of CTS(A)

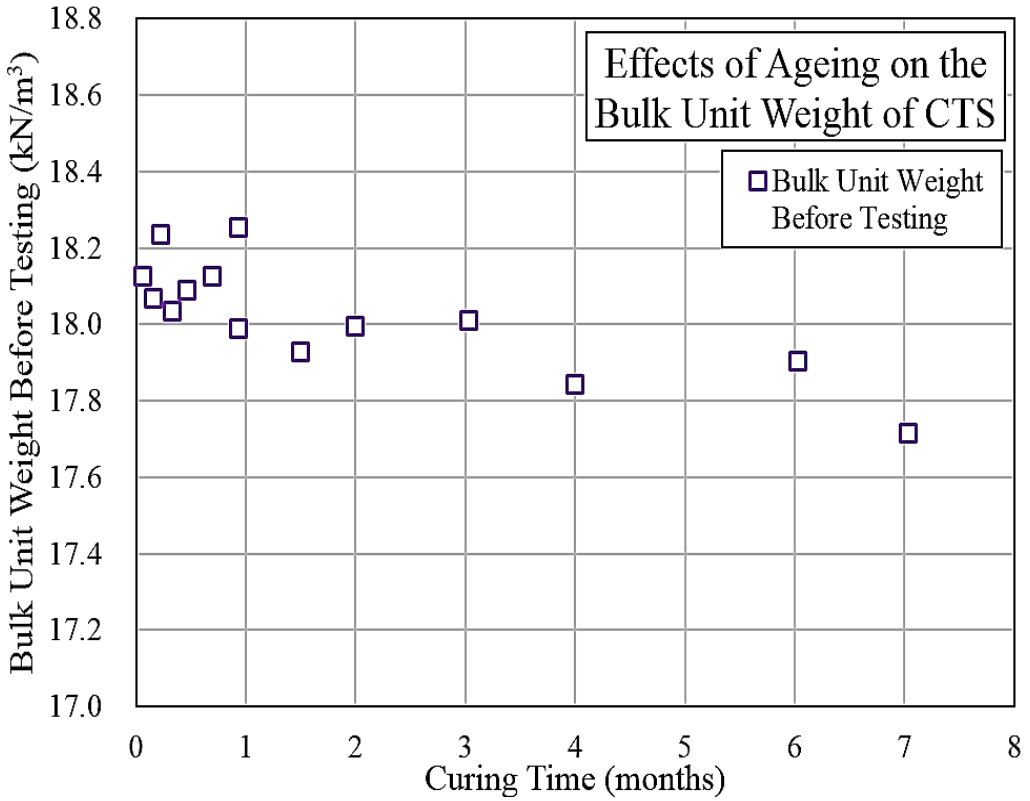

Fig. 4.30. Effects of ageing/curing on the bulk unit weight of CTS(A)

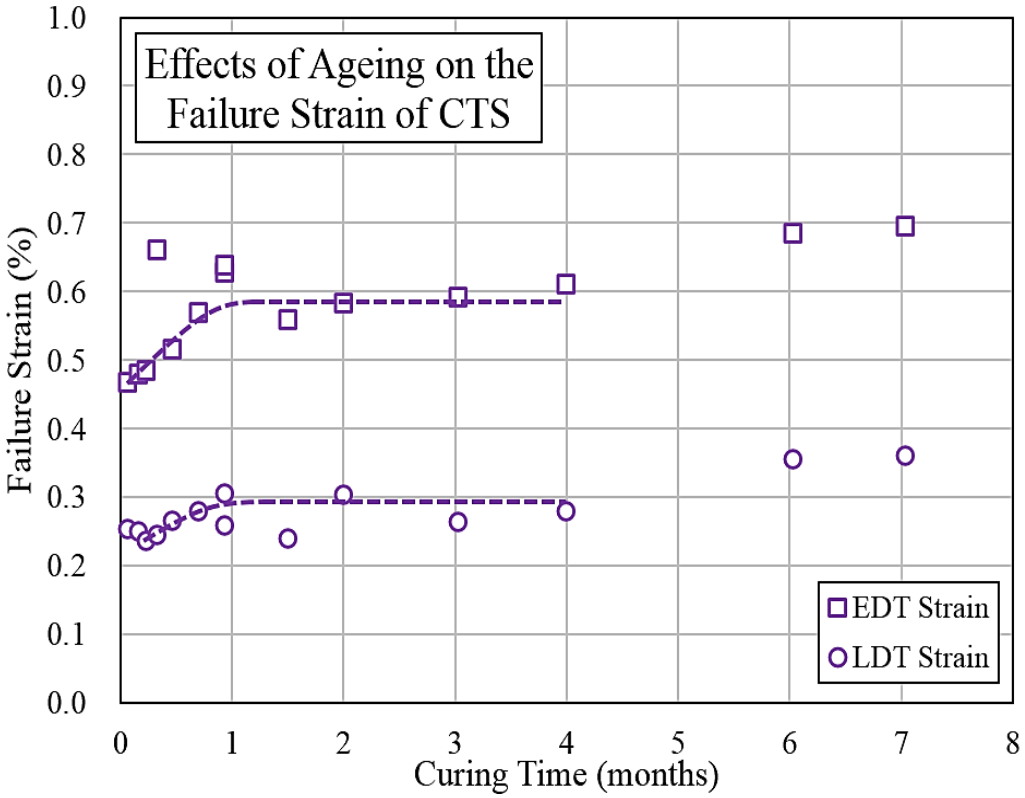

Fig. 4.31. Effects of ageing/curing on the failure strain of CTS(A)

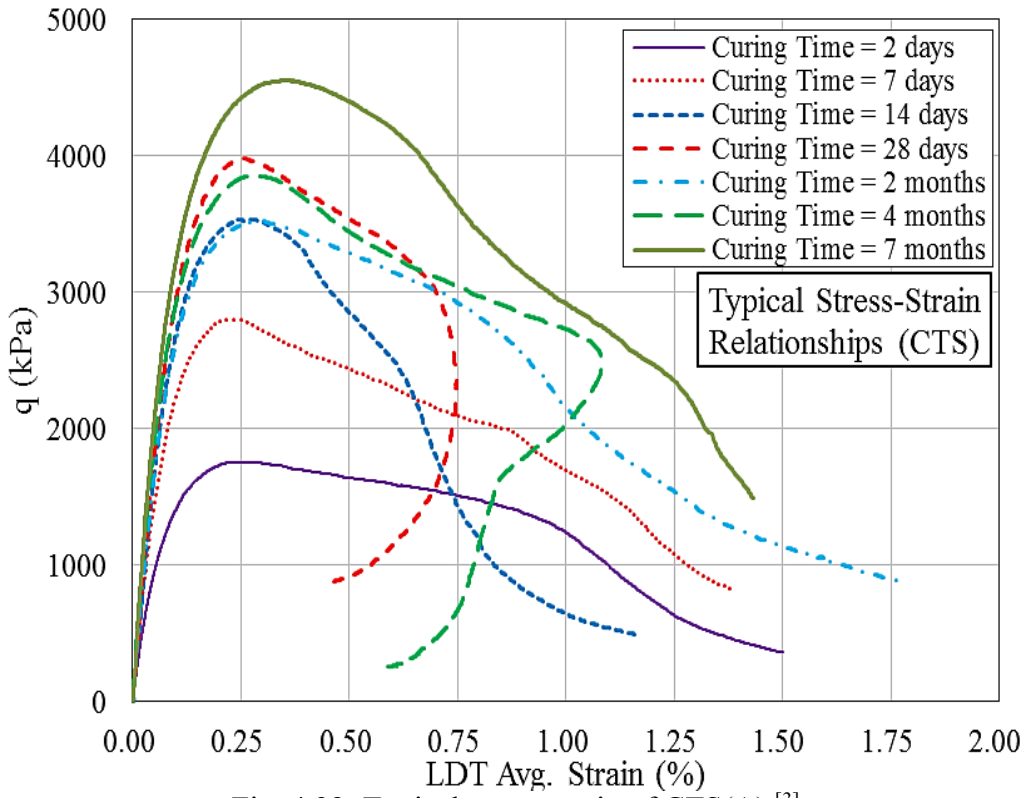

Fig. 4.32. Typical stress-strain of CTS(A) [3]

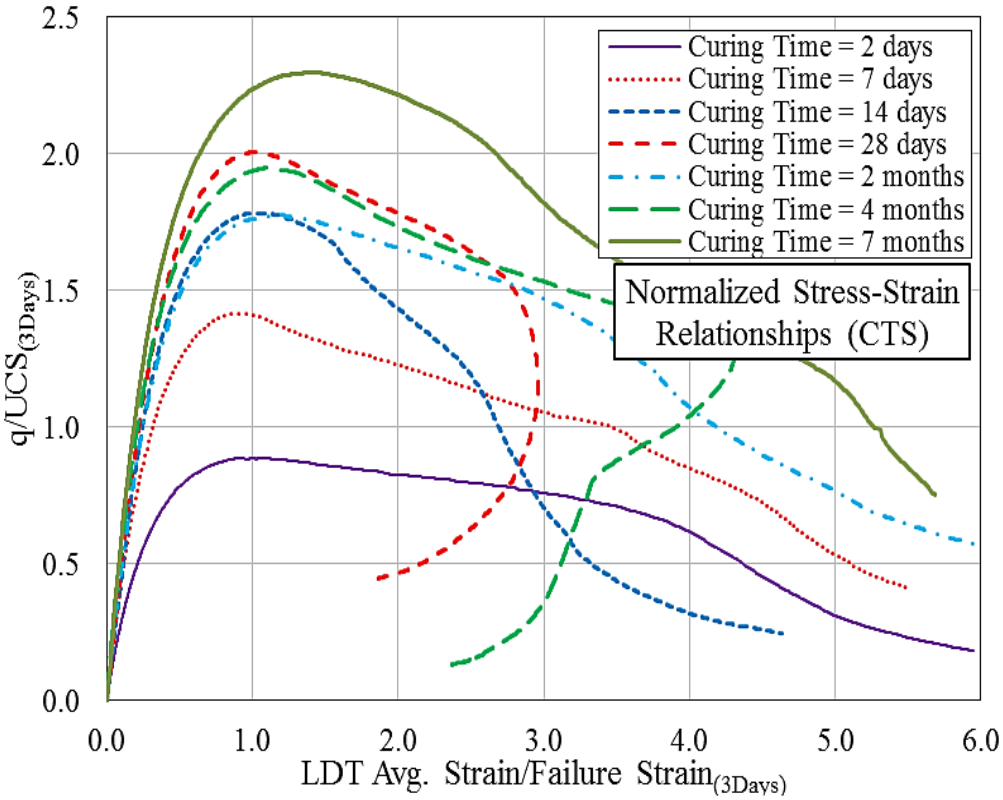

Fig. 4.33. Typical normalized stress-strain of CTS(A)

4.32 and 4.33. The value of UCS at 3 days of curing was approximated by interpolating the peak strength values between 2 and 5 days. However, the effects of ageing on stress-strain response are practically insignificant between curing periods of 1 to 6 months. Additionally, a stiffer response was observed for specimen tested at a curing period of 7 month [3]. In order to examine the loading rate dependency of CTS, two different curing periods curing periods, viz. 28 days and 6 months, were selected based on the these findings.

4.6 SUMMARY OF FINDINGS

- The hardened dihydrate mass produced by the hydration of gypsum (β-hemihydrate) is highly porous in nature comprising of fibrous and branching interlocked needles of β-dihydrate crystals.
- At a particular curing period, GMS-MP1 specimens prepared by using different batches of gypsum showed significant differences in peak strength. This variability in strength is associated with the presences of different impurities and additives, such as soluble calcium sulphate anhydrite, calcium

sulphate dihydrate and potassium sulphate etc. These impurities and additives affects the crystal sizes of dihydrate, and ultimately lead to the reduction in strength.

- A noticeable reduction in peak strength of GMS-MP1 was observed during the first month of curing. Based on the effects on humidity on the hydration, it was conceived that the polythene sheet wrapped around GMS-MP1 specimens restricted to evaporate freely into the atmosphere, and resulted into the volume expansion of specimens due to the formation of delayed hydration products.
- At a curing period of 3 days, a stiffer pre-peak response of GMS-MP1 was witnessed, followed by a significant post-peak strain softening. Reduction of pre-peak stiffness was observed in earlier 1 month of curing, and no further noticeable effects of ageing on the stress-strain behavior of GMS-MP1(A) were observed during 1 to 9 months.
- Based on the above stated findings, it was opted to study the loading rate dependency of GMS at two different curing periods, viz. 3 days and 3 months.
- The hydration reaction of cement mainly produces calcium hydroxide and C-S-H gel. C-S-H gel is one of the principal product of hydration reaction that dictates the strength characteristics, and it is known to be a poorly crystalline sheet-like mass. In case of cement mixed sand, major proportion of strength enhancement in the earlier curing periods is due the formation of hydration products, such as C-S-H gel.
- A continuous increase in the peak strength values of CTS was observed in the first month of curing, and no further effects of curing on the UCS values were witnessed up to 6 months. Besides, a slight increase in failure strain with curing time was observed during the first month of curing, and the values were generally constant between the curing periods of 1 to 4 months.
- In case of CTS, significant increase in pre-peak stiffness and post-peak strain softening with curing time was witnessed during the first month of curing. However, the effects of ageing on stress-strain response were practically insignificant between curing periods of 1 to 6 months.

- In order to examine the loading rate dependency of CTS, two different curing periods curing periods, viz. 28 days and 6 months, were selected based on the above stated findings.

4.7 REFRENCES

1. Maqsood, Z. (2016), "Behaviour of gypsum mixed sand under unconfined monotonic and cyclic loading conditions," *Masters Thesis*, *The University of Tokyo,* Japan.
2. Maqsood, Z. and Koseki, J. (2015), "Behavior of gypsum mixed sand under unconfined monotonic and cyclic loading conditions," *GeoKanto, Japanese Geotechnical Society,* Japan.
3. Maqsood, Z. and Koseki, J. (2019), "Time dependent strength and deformation characteristics of bounded geomaterials," *9th Asian Young Geotechnical Engineering Conference*, (submitted)
4. Goto, S., Tatsuoka, F., Shibuya, S., Kim, Y. and Sato, T. (1991), "A simple gauge for local small strain measurements in the laboratory," *Soils and Foundations*, **31(1)**, 169-180.
5. Singh, N. B. and Middendorf, B. (2007), "Calcium sulphate hemihydrate hydration leading to gypsum crystallization," *Progress in crystal growth and characterization of materials*, **53(1)**, 57-77.
6. Lewry, A. J. and Williamson, J. (1994), "The setting of gypsum plaster - Part I The hydration of calcium sulphate hemihydrate," *Journal of Materials Science*, **29(21)**, 5279-5284
7. Lewry, A. J. and Williamson, J. (1994), "The setting of gypsum plaster - Part II The development of microstructure and strength," *Journal of Materials Science*. **29(21)**, 5524-5528.
8. Guan, W., Zhang, D., Wen, Y. and Wang, X. (2016), "Influence of curing humidity on the compressive strength of gypsum-cemented similar materials," *Advances in Materials Science and Engineering*, vol. 2016.
9. Lewry, A. J. and Williamson, J. (1994), "The setting of gypsum plaster - Part III The Effect of Additives and Impurities," *Journal of Materials Science*, **29(23)**, 6085-6090.

10. Maqsood, Z., Koseki, J. and Kyokawa, H. (2019), "Effects of loading rate on strength and deformation characteristics of gypsum mixed sand", *7th International Symposium on Deformation Characteristics of Geomaterials*, Glasgow. (accepted)
11. Shetty, M. S. (2005), "Concrete technology – Theory and Practice," S. Chand and Company LTD., Revised Edition, 14-32.
12. Kutanaei, S. S. and Choobbasti, A. J. (2017), "Effects of nanosilica particles and randomly distributed fibers on the ultrasonic pulse velocity and mechanical properties of cemented sand," *Journal of Materials in Civil Engineering*, **29(3)**, 04016230.
13. Scrivener, K. L. (2004), "Backscattered electron imaging of cementitious microstructures: understanding and quantification," *Cement and concrete Composites*, **26(8)**, 935-945.
14. Stutzman, P. E. (2001), "Scanning electron microscopy in concrete petrography," *Materials Science of Concrete Special Volume: Calcium Hydroxide in Concrete (Workshop on the Role of Calcium Hydroxide in Concrete), Proceedings-Anna Maria Island*, Florida, 59-72.
15. Kitazume, M. (2005), "State of practice reports: Field and laboratory investigations, properties of binders and stabilized soils," *Proceedings of the International Conference on Deep Mixing Best Practice and Recent Advances*, Stockholm, Sweden, **2**, 660-684.
16. Maqsood, Z. and Koseki, J. (2016). "Use of local strain measurements for rational evaluation of loading rate dependency of Gypsum Mixed Sand", *The 18th International Summer Symposium, JSCE,* Japan.

LOADING RATE DEPENDENCY OF GMS AND CTS UNDER UNCONFINED MONOTONIC LOADING

5.1 PREAMBLE

It is a well-acknowledged fact that the mechanical behavior of bounded geomaterials, viz. natural rocks and cemented soils, are dictated by the loading rate [1]. The loading rate dependency due to the viscous behavior of geomaterials is a vital aspect to evaluate their long-term performance, and reliability of constitutive modeling momentously hinges on the rational evaluation of these loading rate dependent characteristics. This chapter elucidates loading rate dependency of GMS and CTS at a wide range of loading rates, ranging from 4.4E+0 to 1.9E-5 %/min (5 folds), under unconfined monotonic loading conditions. The effects of loading rate on the strength and deformation behavior of GMS and CTS are discussed thoroughly, and the results of GMS are classified into three different zones of strain rates. Moreover, the effects of loading rate on the mechanical behavior are correlated with the tendency of accumulated elastic and plastic strain energies at different loading rates to unveil the mechanism of loading rate dependency of bounded geomaterials.

5.2 LOADING RATE DEPENDENCY OF GMS UNDER UNCONFINED MONOTONIC LOADING

In order to evaluate the effects of loading rate on the strength and deformation behavior of GMS(MP1) specimens, a number of unconfined monotonic tests were at a wide range of strain rates, ranging from 4.4E+0 to 1.9E-5 %/min (5 folds). The specimens were cured for a period of 3 days, and the results are shown in Table 5.1 [2-6]. It is noteworthy that the testing procedure stated in Section 4.3 of Chapter No. 4 was adopted to conduct these tests, and only the results having AAD $\leq$ 25% at 50% of EDT failure strain are presented in this chapter [7].

Table 5.1. Test Results of GMS(MP1) (Curing Period = 3 Days)

Machine Type	Series ID & Batch Type	Average Axial Strain Rate	Test ID	Bulk Unit Weight Before Testing	Moisture Content After Testing	UCS	Failure Strain		Failure Time
							EDT	Avg. LDT	
		(%/min)		(kN/m^3)	(%)	(kPa)	(%)	(%)	(min)
UCM*	GMS(MP1(A)-UncMono-3D) Batch-A	1.6E-01	GA1-3D(1.6E-1)-A01	18.3	30.1	4799	0.293	0.309	1.8
			GA1-3D(1.6E-1)-A02	18.4	29.8	4810	0.306	0.319	1.8
			GA1-3D(1.6E-1)-A03	18.4	30.6	4716	0.290	0.274	1.8
		6.3E-02	GA1-3D(6.3E-2)-A04	18.3	31.7	4535	0.358	0.397	5.7
			GA1-3D(6.3E-2)-A05	18.3	32.5	4367	0.340	0.350	5.4
			GA1-3D(6.3E-2)-A06	18.2	31.5	4312	0.395	0.326	5.3
			GA1-3D(6.3E-2)-A07	18.4	30.0	4647	0.340	0.360	5.6
		2.6E-02	GA1-3D(2.6E-2)-A08	18.6	31.8	4266	0.439	0.492	19.9
			GA1-3D(2.6E-2)-A09	18.4	31.3	4174	0.440	0.541	19.9
		7.9E-03	GA1-3D(7.9E-3)-A10	18.3	33.7	3090	0.543	0.471	60.0
			GA1-3D(7.9E-3)-A11	18.6	33.2	3870	0.587	0.565	69.9
		3.2E-03	GA1-3D(3.2E-3)-A12	18.5	33.7	2987	0.784	0.824	271.1
			GA1-3D(3.2E-3)-A13	18.4	32.9	2896	0.739	0.804	253.5
TCM**	GMS(MP1(C)-UncMono-3D) Batch-C	2.1E-01	GC1-3D(2.1E-1)-C01	18.5	34.5	3512	0.581	0.306	1.4
			GC1-3D(2.1E-1)-C02	18.6	31.7	3555	0.545	0.303	1.5
		7.4E-02	GC1-3D(7.4E-2)-C03	18.6	34.1	3383	0.537	0.320	4.3
		3.8E-02	GC1-3D(3.8E-2)-C04	18.4	34.2	3151	0.528	0.343	9.0
		2.7E-02	GC1-3D(2.7E-2)-C05	18.6	34.2	3074	0.607	0.390	14.6
		2.1E-02	GC1-3D(2.1E-2)-C06	18.6	32.7	3039	0.597	0.359	16.7
			GC1-3D(2.1E-2)-C07	18.7	31.9	2986	0.563	0.368	17.4
			GC1-3D(2.1E-2)-C08	18.6	32.0	3036	0.639	0.367	18.0
		3.9E-03	GC1-3D(3.9E-3)-C09	18.6	31.0	2343	0.733	0.566	148.9
		1.7E-03	GC1-3D(1.7E-3)-C10	18.6	28.9	1667	0.863	0.759	453.7
UCM*	GMS(MP1(D)-UncMono-3D) Batch-D	4.4E+00	GD1-3D(4.4E+0)-D01	18.6	34.3	4507	0.547	0.267	0.1
			GD1-3D(4.4E+0)-D02	18.6	33.2	4388	0.557	0.259	0.1
		8.0E-01	GD1-3D(8.0E-1)-D03	18.5	33.5	3878	0.238	0.264	0.3
TCM**		1.9E-01	GD1-3D(1.9E-1)-D04	18.4	33.7	4004	0.559	0.273	1.4
		2.4E-02	GD1-3D(2.4E-2)-D05	18.5	34.3	3465	0.573	0.417	17.4
		1.6E-03	GD1-3D(1.6E-3)-D06	18.6	34.2	2241	0.940	0.760	483.2
UCM*		2.1E-04	GD1-3D(2.1E-4)-D07	18.6	21.8	644	0.417	0.513	2623.0
		1.9E-05	GD1-3D(1.9E-5)-D08	18.6	25.1	115	0.161	0.147	8520.0

* Unconfined Compression Machine, ** Triaxial Compression Machine

The specimens were prepared by using three different batches of gypsum, viz. Batch A, C and D, and the results are categorized based on Batch type, as shown in Table 5.1. A reference values of strain rate, viz. 2.0E-2 %/min, was selected to compare the effects of loading rate on GMS specimens belonging to different gypsum batches and curing periods. The estimated results of GMS and CTS at 2.0E-2% min. are presented in Table 5.2 [2-6].

Table 5.2. Estimated Test Results of GMS and CTS
at Average Strain Rate = 2.0E-02 %/min

Specimen Type	Series ID	Gypsum or Cement Batch ID	Gypsum/Sand or Cement/Sand	Total Curing Time	UCS	Failure Strain	
						EDT	Avg. LDT
			(%)		(kPa)	(%)	(%)
GMS	GMS(MP1(A)-UncMono-3D)	A	80	3 Days	4150	0.466	0.561
	GMS(MP1(A)-UncMono-90D)	A	80	90 Days	3245	0.469	0.521
	GMS(MP1(C)-UncMono-3D)	C	80	3 Days	3035	0.639	0.367
	GMS(MP1(D)-UncMono-3D)	D	80	3 Days	3425	0.576	0.431
	GMS(MP1(D)-UncMono-90D)	D	80	90 Days	2495	0.651	0.440
	GMS(MP2(D)-UncMono-3D)	D	40	3 Days	875	0.433	0.329
CTS	CTS(MP1(A)-UncMono-28D)	A	40	28 Days	3930	0.639	0.289
	CTS(MP1(A)-UncMono-180D)	A	40	180 Days	3870	0.681	0.351

5.2.1 Effects of loading rate on unconfined compressive strength of GMS

Typical stress-strain and normalized stress-strain relationships of GMS(MP1) specimens prepared by Batch-D, viz. series GMS(MP1(A)-UncMono-3D), are presented in Figures 5.1 and 5.2. The stress and strain values were normalized by using peak strength and failure strain values estimated at an average strain rate of 2.0E-2 %/min. Significant effects of loading rate on UCS and stress-strain responses are evident from these relationships. Generally, higher values of UCS were witnessed for specimens tested at higher strain rates, and a significant reduction in UCS can be witnessed with the decrease of strain rate. For instance, specimen GD1-3D(4.4E+0)-D01 tested at an average

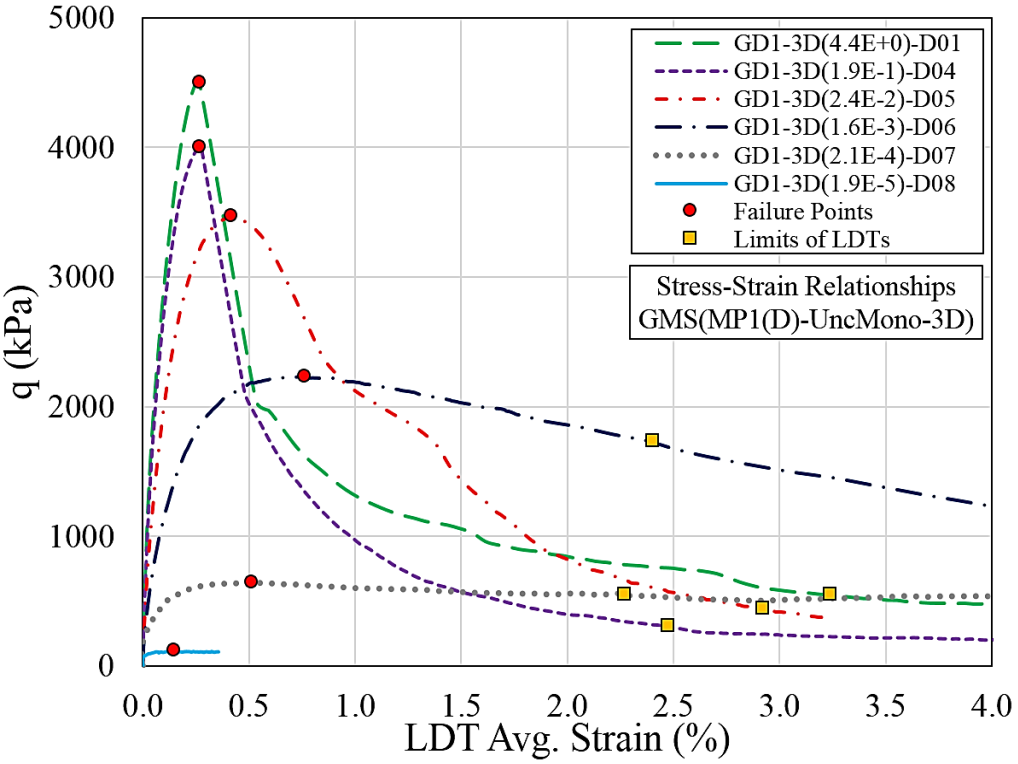

Fig. 5.1. Typical stress-strain relationships
GMS(MP1(D)-UncMono-3D), modified after [5]

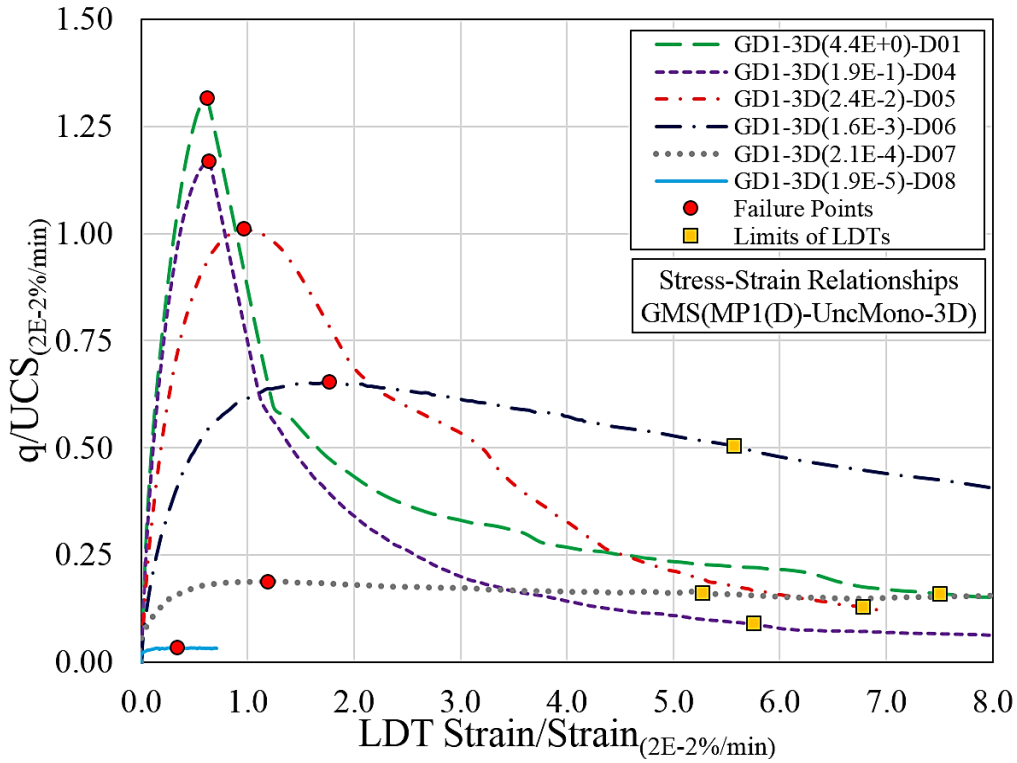

Fig. 5.2. Typical normalized stress-strain relationships
GMS(MP1(D)-UncMono-3D)

strain rate of 4.4E+0 %/min showed a UCS value of 4507 kPa, and it immensely reduced to merely 115 kPa at 19.E-5 %/min., viz. GD1-3D(1.9E-5)-D08, as shown in Fig. 5.1. At lower ranges of strain rates, the effects of strain rates on the mechanical behavior of GMS are quite substantial, as a normalized peak strength reduction of about 80% was witnessed for a decrease in strain rate by of approximately 115 times, viz. 2.4E-2 to 2.1E-4 %/min, as evident in Fig. 5.2 [5].

In an effort to find possible correlations, the effects of loading rate are expressed in terms of full-logarithmic plots between UCS (or normalized peak strength) and corresponding instantaneous strain rate at failure, as shown in Figures 5.3 and 5.4. The instantaneous strain rates at failure were typically estimated by computing strain rates between 98% of failure strain and failure strain. Considering the technical limitations of sampling devices especially at higher strain rates, the instantaneous strain rates in some cases were approximated between around 85% of failure strain and failure strain due to the non-availability of recorded data [2].

Based on these relationships, the effects of loading rate on the peak strength can be divided into three distinct zones of strain rates, labelled as Zone-1, 2 and 3 in Fig. 5.4. The effects of loading rate on normalized peak strength of GMS(MP1) are relatively trivial for specimens having instantaneous failure strain rates higher than approximately 5.0E-1 %/min, viz. Zone-1, as evident in Fig. 5.4. On the other hand, substantial reduction in normalized peak strength with the decrease in strain rate was observed at for specimens tested at instantaneous strain rates lesser than 2.0E-2 %/min, viz. Zone-3. The effects of loading rate on the normalized peak strength of specimens belonging to Zone-2 are also evident but are relatively lesser than Zone-3, as shown in Fig. 5.4 [2-6].

5.2.2 Effects of loading rate on deformation characteristics of GMS

The values of failure strains of GMS(MP1) specimens were also influenced by the loading rate, and variations of failure strains (and normalized failure strain) with instantaneous loading rate at failure in full-logarithmic plot are presented in Fig. 5.5 and 5.6. Normalized failure strain values can also be categorized into the three zones of strain rates, as in case of normalized peak strength. The values of normalized failure strain are witnessed to be independent of loading rate for specimens belonging to Zone-1, as shown

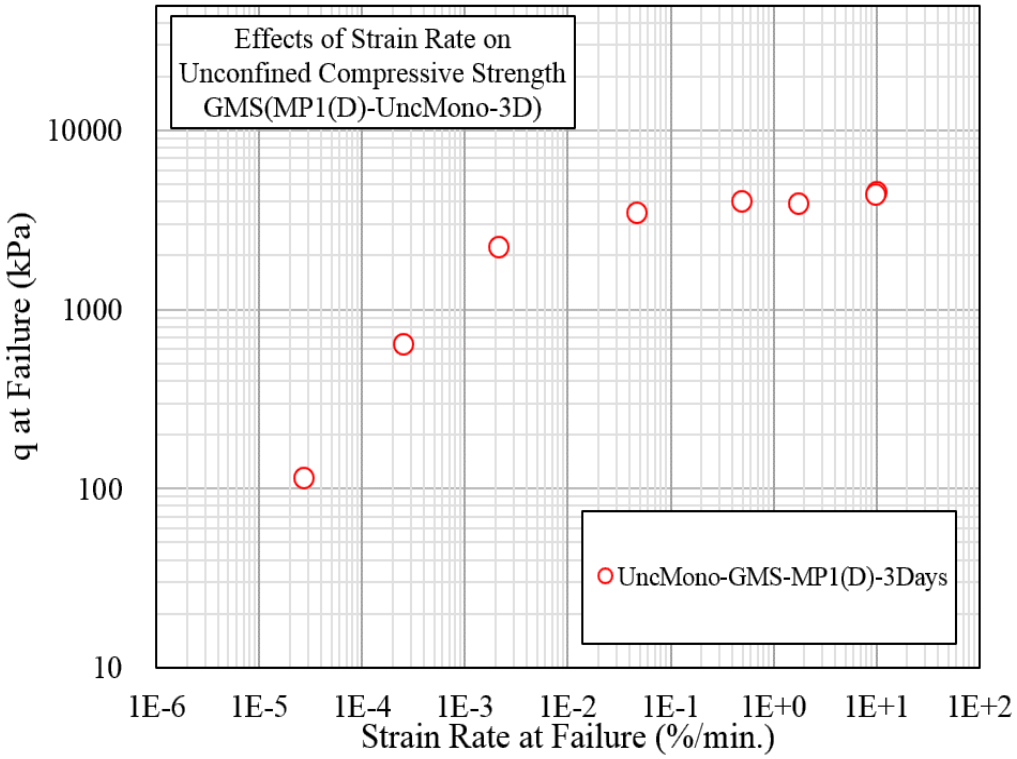

Fig. 5.3. Relationship between UCS and instantaneous strain rate at failure GMS(MP1(D)-UncMono-3D)

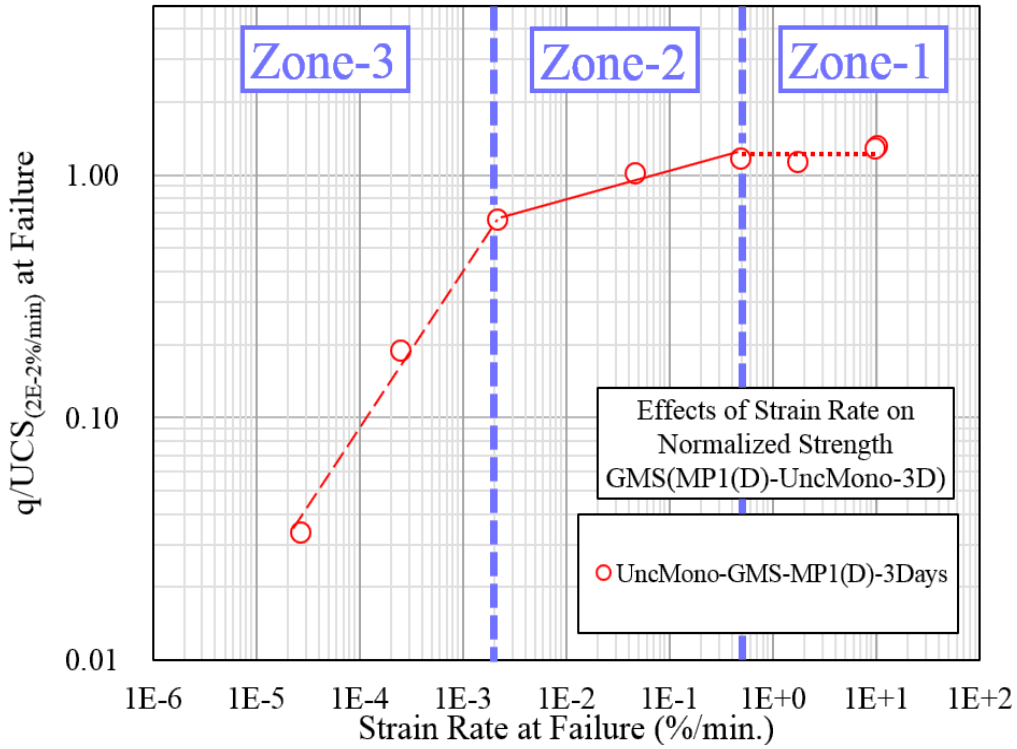

Fig. 5.4. Relationship between normalized peak strength and instantaneous strain rate at failure GMS(MP1(D)-UncMono-3D), modified after [5]

in Fig. 5.6. However, an increasing trend of normalized failure strain was observed with the decrease in loading rate for specimens of Zone-2, and the maximum value of normalized failure strain was observed at 2.0E-2 %/min, as shown in Fig. 5.6. The effects of loading rate on normalized failure strain in Zone-3 was found to be opposite of Zone-2, as a trend of reduction in normalized failure strain with the decrease in loading rate was captured, as evident in Fig. 5.6 [4, 2].

The effects of loading rate on the pre-peak stiffness of GMS(MP1) are also very prominent, as relatively stiffer pre-peak responses of GMS(MP1) were observed at higher strain rates, and pre-peak stiffness decreases with the decrease in strain rate, as evident in Fig. 5.1. Owing to the limited working range of LDTs, the stress-strain relationships in the post-peak regions were further extended by utilizing the adjusted EDT values of axial strains. The post-peak strain softening is also very pronounced at higher strain rates, and this tendency also vanishes in specimens tested at loading rate lesser than about 2.0E-4 %/min, as shown in Figures 5.1 and 5.2 [4, 2].

The failure pattern of GMS(MP1) specimens are also influenced by the loading rate, and visible formation of shear bands were witnessed for specimens tested at average strain rates higher than 2.0E-3 %/min, viz. Zones 1 and 2. Generally, clear and distinct shear bands were observed at higher loading rates, as shown in Figures 5.7(a) to 5.7(b), and relatively diffused and multiple shear bands were observed with the decrease in loading rate, as evident in Fig. 5.7(c). On the other hand, only budging was observed for specimens tested at strain rates lesser than 2.0E-3 %/min, viz. Zone-3, and no visible cracks or shear bands were observed with the inspection of naked eye, as shown in Fig. 5.7(d) [4, 2].

5.2.3 Effects of different gypsum batches on loading rate dependency of GMS

As highlighted earlier in section No. 4.4.3 of Chapter No. 4, the peak strength values of specimens prepared by different gypsum batches are ominously different possible due to the presences of different impurities and additives. In order to examine the influence of different batches of gypsum on the loading rate dependency of GMS, the stress-strain and normalized stress-strain relationships of GMS(MP1) specimens prepared using Batch-A and Batch-C gypsum are also presented in Figures 5.8 to 5.11. Irrespective

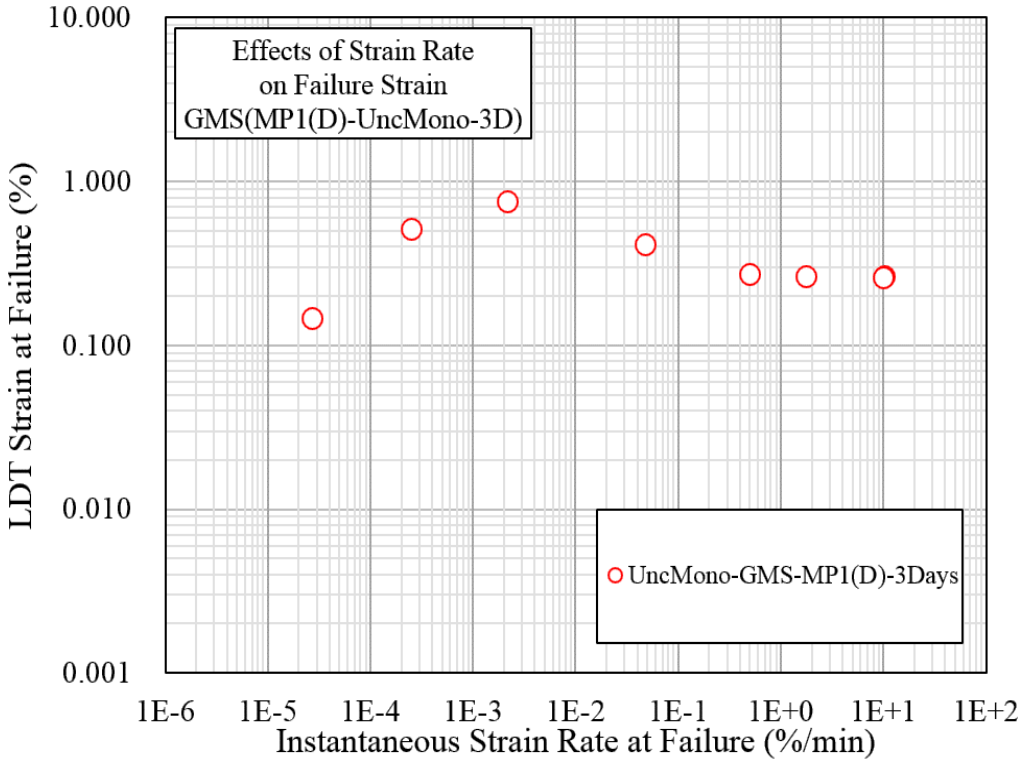

Fig. 5.5. Relationship between failure strain and instantaneous strain rate at failure GMS(MP1(D)-UncMono-3D), modified after [5]

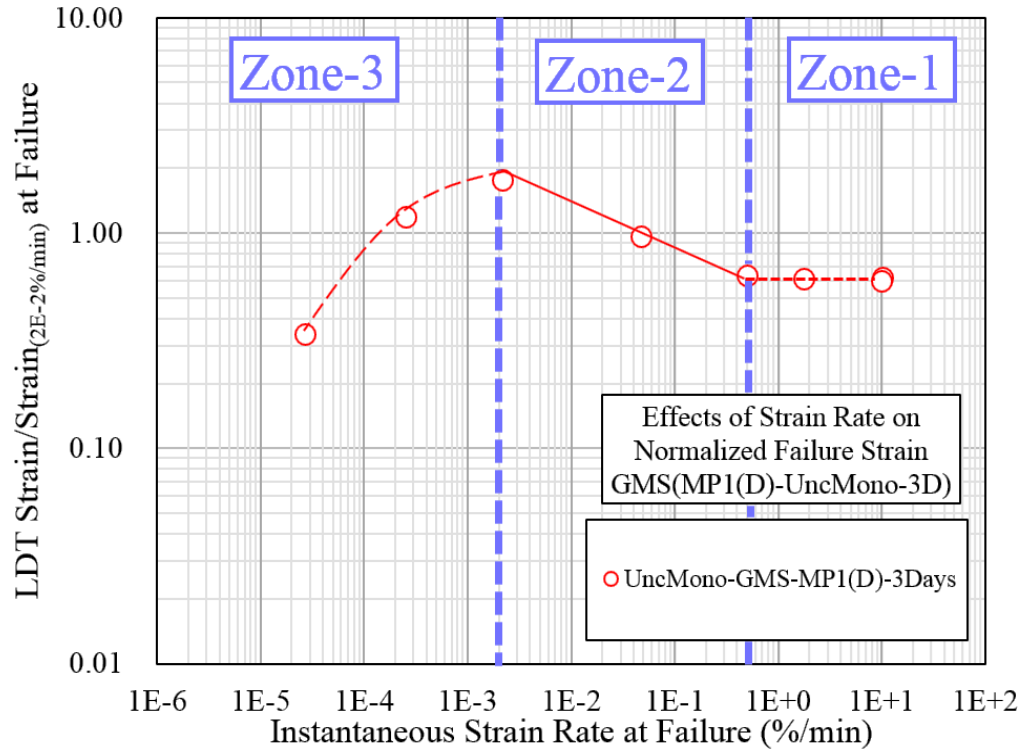

Fig. 5.6. Relationship between normalized failure strain and instantaneous strain rate at failure GMS(MP1(D)-UncMono-3D), modified after [2]

(a) GD1-3D(4.4E+0)-D01

(b) GD1-3D(2.4E-2)-D05

(c) GD1-3D(1.6E-3)-D06

(d) GD1-3D(2.1E-4)-D07

Fig. 5.7. Failure pattern of GMS(MP1(D)-UncMono-3D) specimens

of the differences in absolute strength values and stress-strain responses of GMS specimens belonging to different batches, the effects of loading rate on the normalized peak strength and normalized stress-strain responses of all the specimens are fairy identical, as evident from Figure 5.2, 5.8 and 5.11 [2, 3, 5 and 6].

Although the specimens prepared by Batch-A and Batch-C were tested for a relatively narrow range of strain rates, but the relationships between UCS (and normalized peak strength) and instantaneous strain rate at failure are typically the same as of Batch-D specimens, as evident from Figures 5.12 and 5.13. Moreover, the effects of loading rates on the failure strain (and normalized failure strains) are generally same for all the specimens, as shown in Figures 5.14 and 5.15 [2, 3, 5 and 6]. Based on these results, it can be conceived that the loading rate dependency of GMS is not affected by the presence of impurities and additive, and the viscous behavior of GMS is majorly governed by the β-hemihydrate content.

5.2.4 Effects of gypsum content on loading rate dependency of GMS

In order to quantify the effects of gypsum content on loading rate dependent behavior of GMS, another series of unconfined compressive tests were performed on 3 days cured specimens having gypsum to sand ratio of 40%, viz. series GMS(MP2(D)-UncMono-3D), and the results are presented in Table 5.3. The stress-strain and normalized stress-strain relationships of GMS(MP2(D)-UncMono-3D) are shown in Figures 5.16 and 5.17, and the UCS values of specimen having lesser gypsum content are fairly lesser. For instance, At a reference strain rate of 2.0E-2 %/min and a curing period of 3 days, the UCS of series GMS(MP2(D)-UncMono-3D) is about 75% lesser than GMS(MP1(D)-UncMono-3D), as evident in Table 5.2.

In spite of the differences in the stress-strain responses, absolute values of UCS between specimens having different gypsum content, as shown in Figures 5.16 and 5.18, the effects of loading rate on the normalized stress-strain relationships and normalized peak strength are quite identical, as shown in figures 5.17 and 5.19. Additionally, the values of failure strains and normalized failure strains are generally comparable for specimens prepared by different gypsum content, as evident in Figures 5.20 and 5.21. However, the value of failure strain of specimen test at an strain rate of 2.6E-5%, viz.

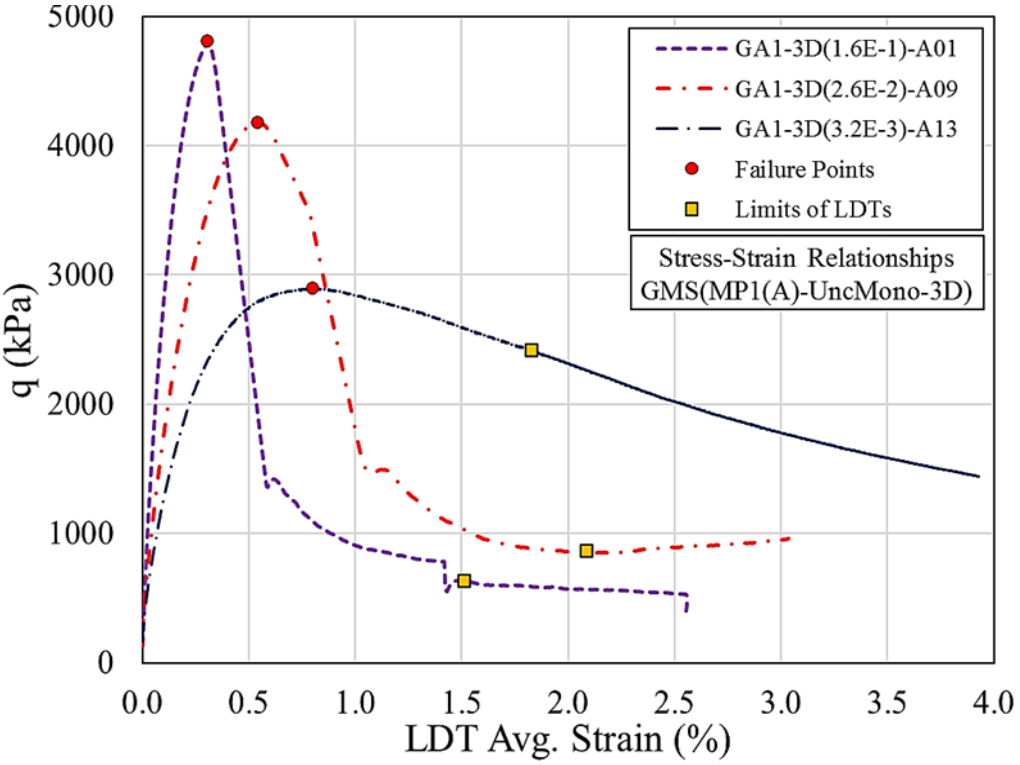

Fig. 5.8. Typical stress-strain relationships
GMS(MP1(A)-UncMono-3D), modified after [3]

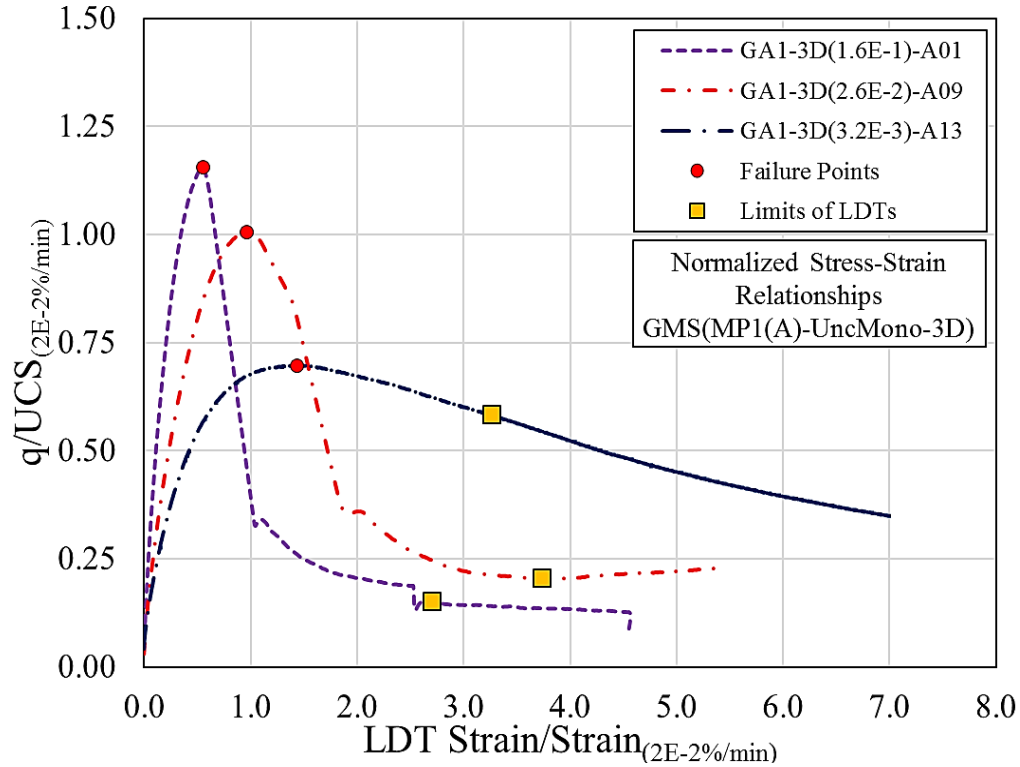

Fig. 5.9. Typical normalized stress-strain relationships
GMS(MP1(A)-UncMono-3D)

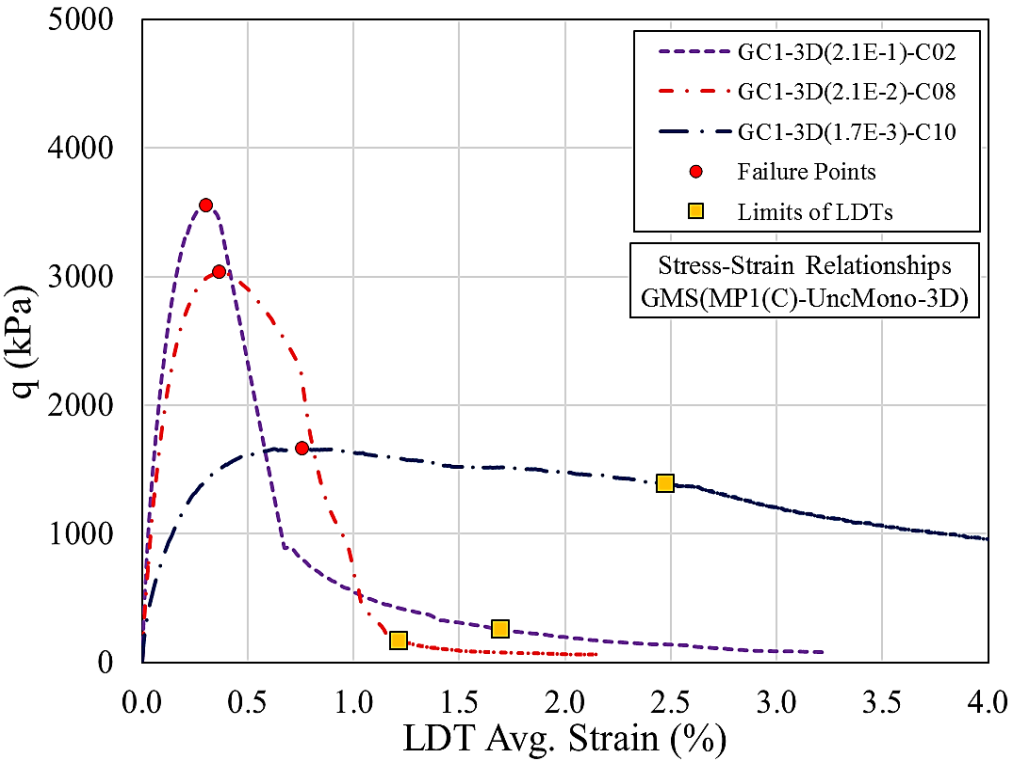

Fig. 5.10. Typical stress-strain relationships
GMS(MP1(C)-UncMono-3D), modified after [3]

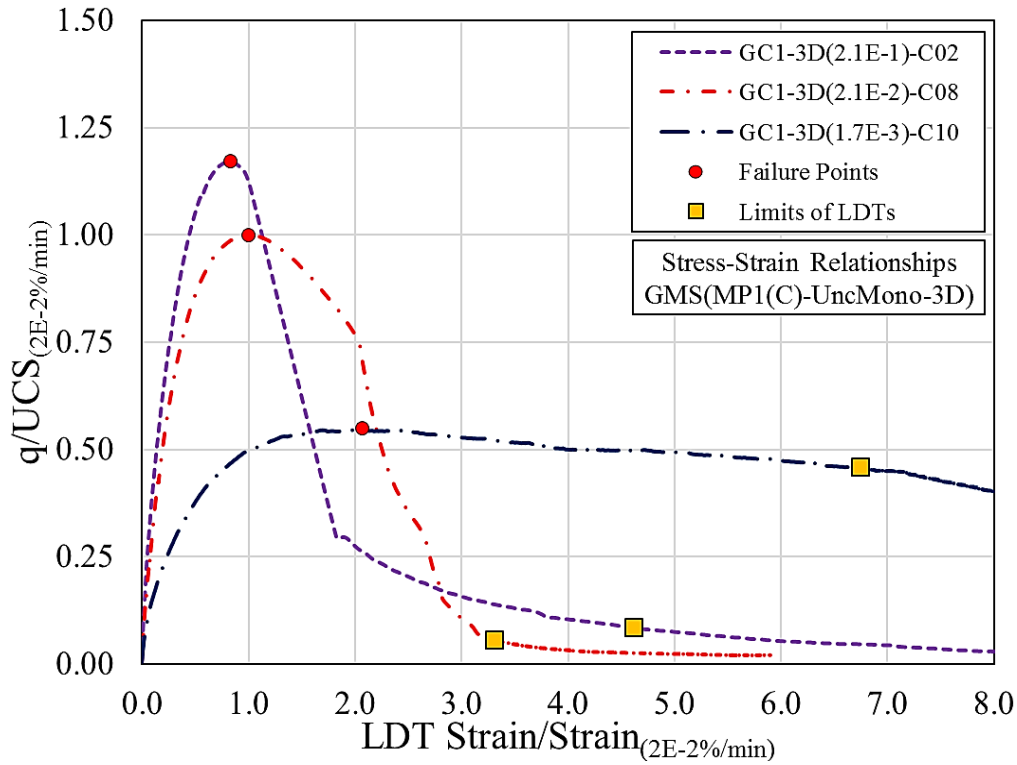

Fig. 5.11. Typical normalized stress-strain relationships
GMS(MP1(C)-UncMono-3D)

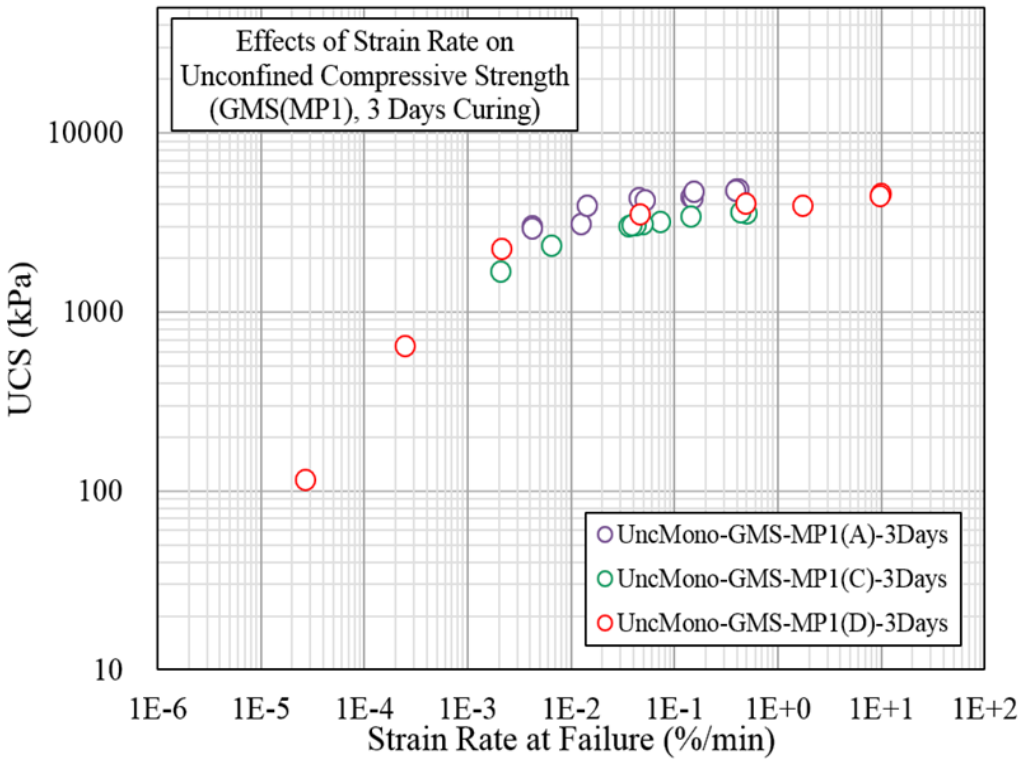

Fig. 5.12. Relationship between UCS and instantaneous failure strain rate of GMS(MP1) prepared by different gypsum batches, modified after [3, 5]

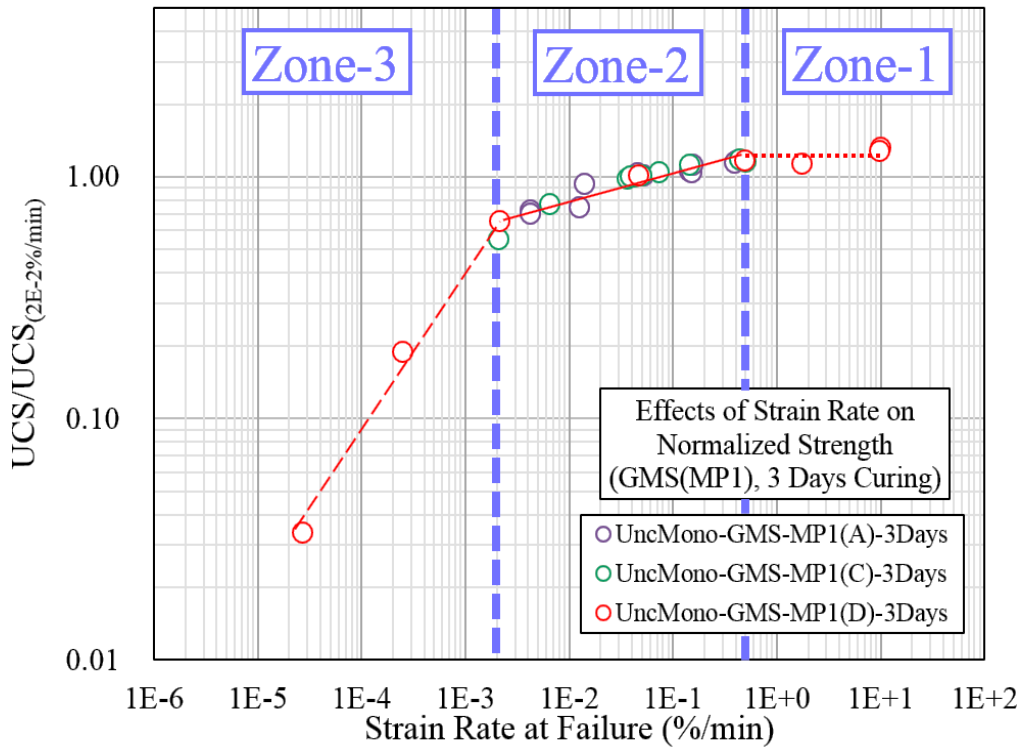

Fig. 5.13. Relationship between normalized peak strength & instantaneous failure strain rate of GMS(MP1) of different gypsum batches, modified after [6]

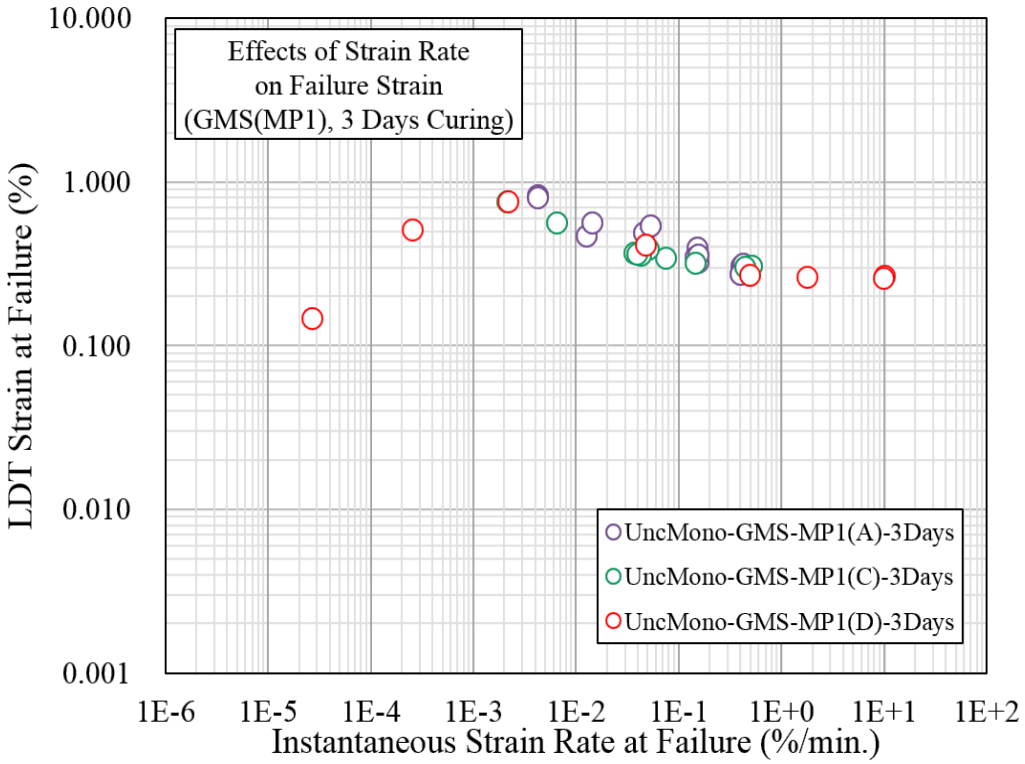

Fig. 5.14. Relationship between failure strain and instantaneous failure strain rate of GMS(MP1) prepared by different gypsum batches, modified after [3, 5]

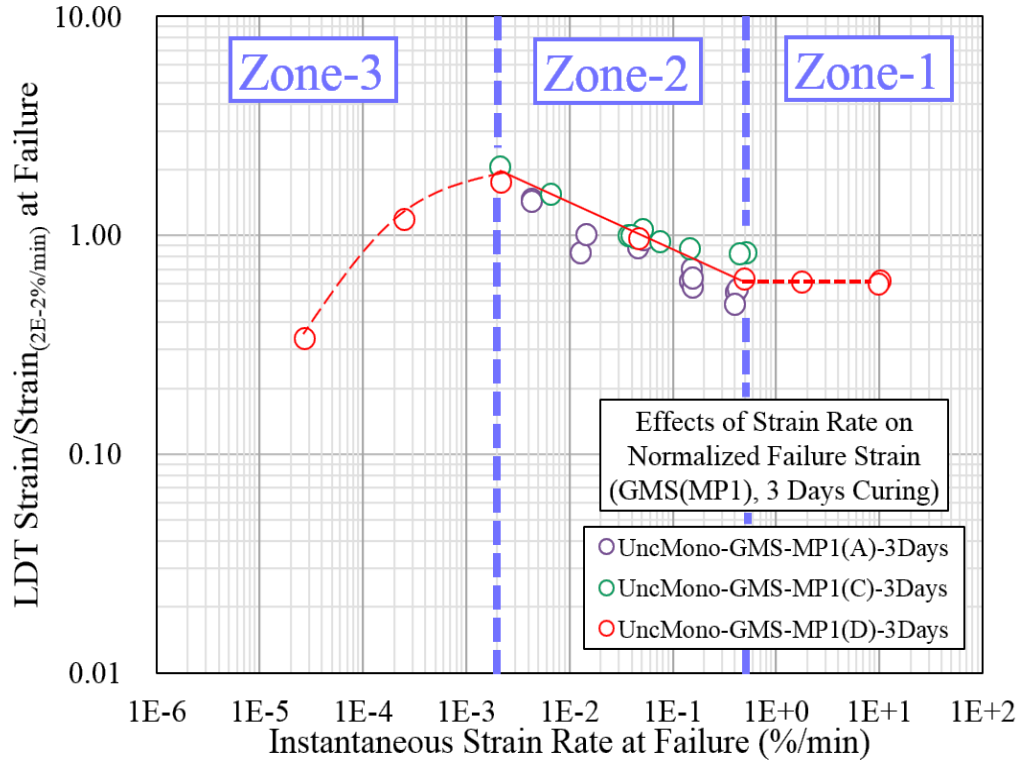

Fig. 5.15. Relationship between normalized failure strain & instantaneous failure strain rate of GMS(MP1) of different gypsum batches, modified after [3, 5 and 6]

GD2-3D(2.6E-5)-A05, is relatively lesser than the counterpart specimen having higher gypsum content, viz. GD1-3D(1.9E-5)-D08. Based on these results, it becomes certain that the variation of gypsum content (Gypsum/Sand between 80% and 40%) has no significant effects on the loading rate dependency of GMS under unconfined conditions.

Table 5.3. Test Results of GMS-MP2 (Curing Period = 3 Days)

Machine Type	Series ID & Batch Type	Average Axial Strain Rate	Test ID	Bulk Unit Weight Before Testing	Moisture Content After Testing	UCS	Failure Strain		Failure Time
							EDT	Avg. LDT	
		(%/min)		(kN/m^3)	(%)	(kPa)	(%)	(%)	(min)
UCM*	GMS(MP2(D)-UncMono-3D) Batch-D	1.4E-01	GD2-3D(1.4E-1)-D01	18.8	28.3	946	0.494	0.219	1.6
		2.8E-02	GD2-3D(2.8E-2)-D02	18.9	27.9	918	0.398	0.291	10.4
		2.4E-03	GD2-3D(2.4E-3)-D03	19.0	29.1	646	0.732	0.707	306.7
		2.1E-04	GD2-3D(2.1E-4)-D04	18.9	21.1	151	0.537	0.538	2642.3
		1.8E-05	GD2-3D(1.8E-5)-D05	18.8	24.6	19	0.006	0.006	400.2

* Unconfined Compression Machine

5.2.5 Interaction between effects of ageing and loading on the mechanical behavior of GMS

The effects of ageing and loading rate are also susceptible to interact with each other, and the mechanical behavior of bounded materials are noticeably affected by this complex interaction [1]. In order to examine the influence of this interaction on the mechanical behavior of GMS, a number of unconfined compression tests are performed on batch-D specimen cured for 90 day, viz. series GMS(MP1(A)-UncMono-180D) and GMS(MP1(D)-UncMono-180D), and the results are shown in Table 5.4. The stress-strain and normalized stress-strain relationships of GMS(MP1(A)-UncMono-180D) and GMS(MP1(D)-UncMono-180D) are presented in Figures 5.22 and 5.25. As discussed in Chapter No. 4, a reduction in UCS was observed during the first month of curing due to volume expansion caused be the delayed formation of dihydrate. The absolute UCS values of GMS(MP1(D)- UncMono-180D) specimens are lower than the counterpart specimens cured for 3 days, viz. GMS(MP1(D)- UncMono-3D) as shown in Figures 5.1 and 5.22. For instance, specimens cured for 180 days is about 20% lesser than specimens curried for 3 days at a reference loading rate of 2.0E-2 %/min, as shown in Table 5.2 [2-6].

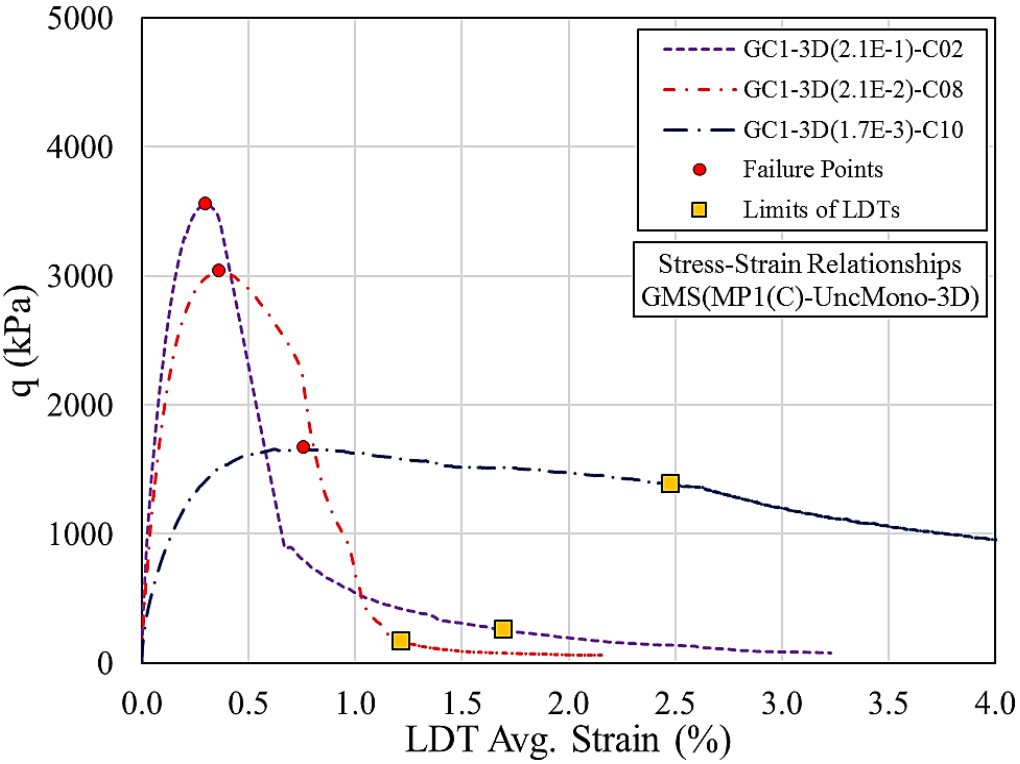

Fig. 5.16. Typical stress-strain relationships
GMS(MP2(D)-UncMono-3D)

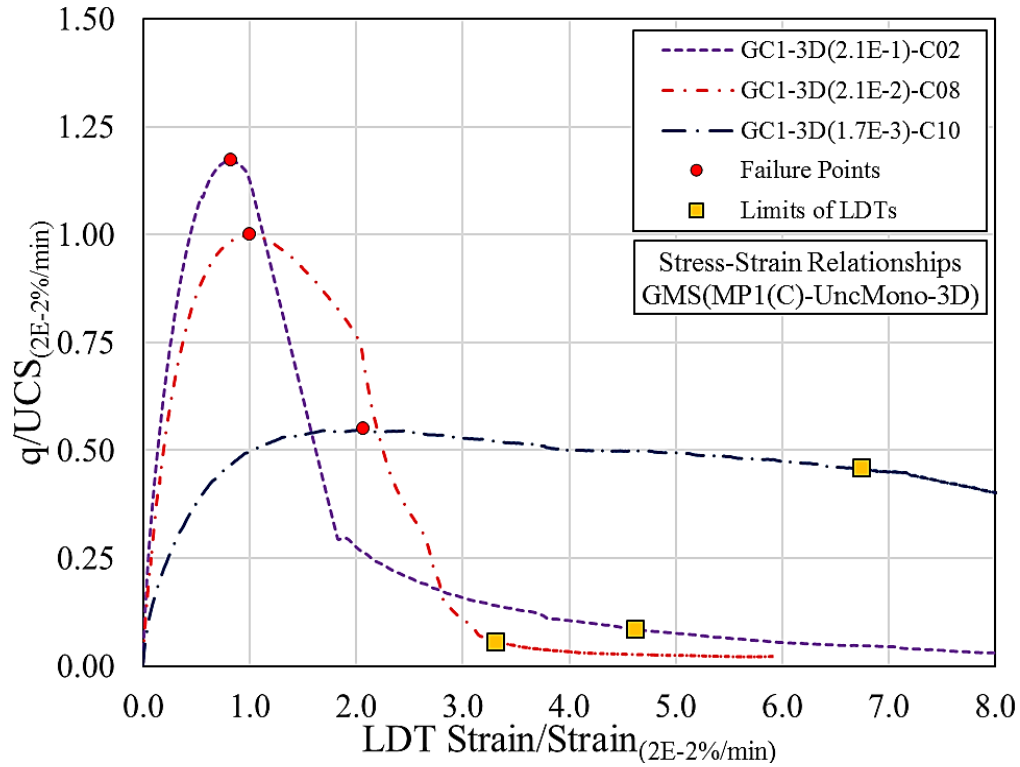

Fig. 5.17. Typical normalized stress-strain relationships
GMS(MP2(D)-UncMono-3D)

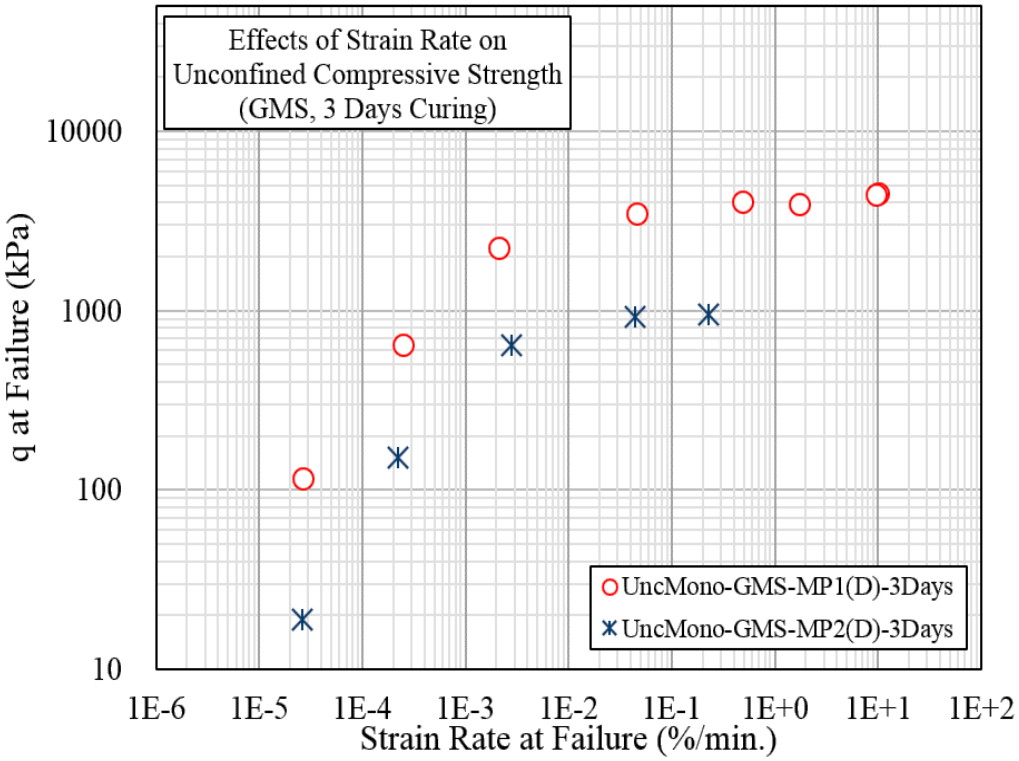

Fig. 5.18. Relationship between UCS and instantaneous strain rate at failure of GMS specimens having gypsum/sand = 80% and 40%

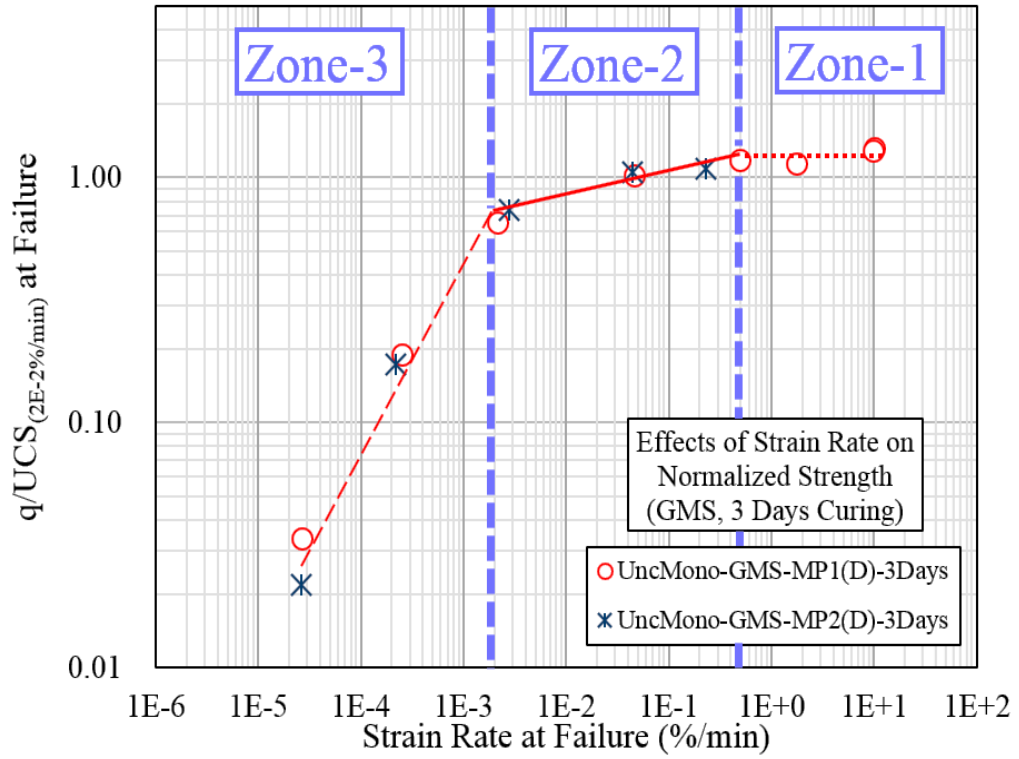

Fig. 5.19. Relationship between normalized peak strength and instantaneous strain rate at failure of GMS having gypsum/sand = 80% and 40%

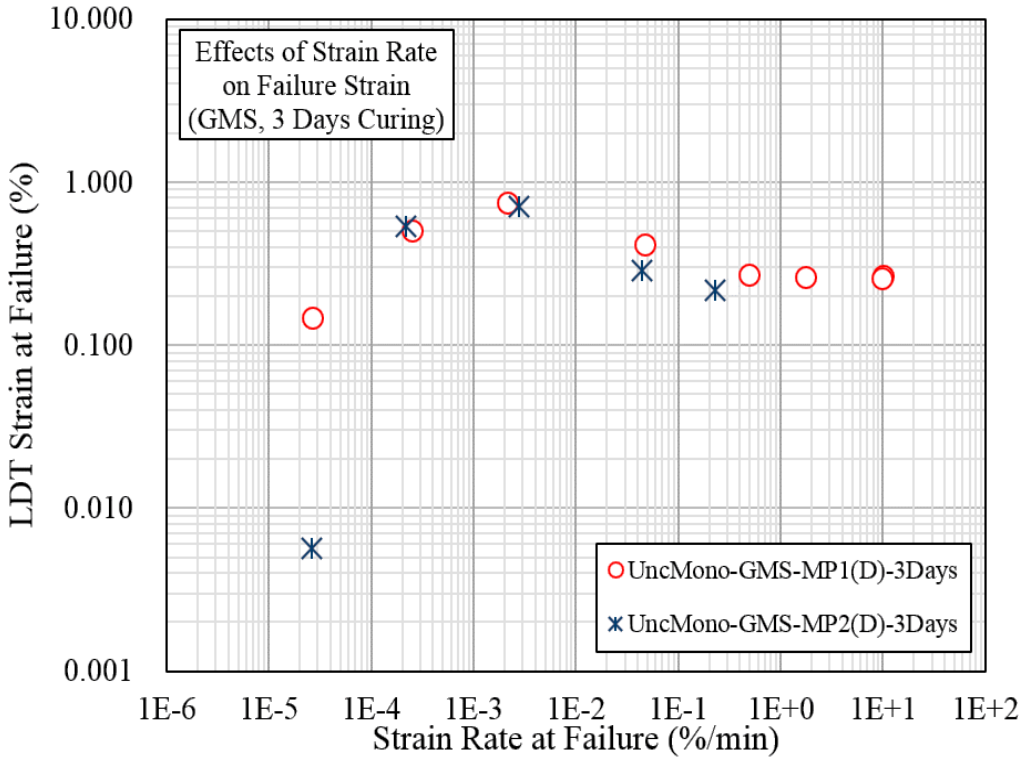

Fig. 5.20. Relationship between failure strain and instantaneous strain rate at failure of GMS specimens having gypsum/sand = 80% and 40%

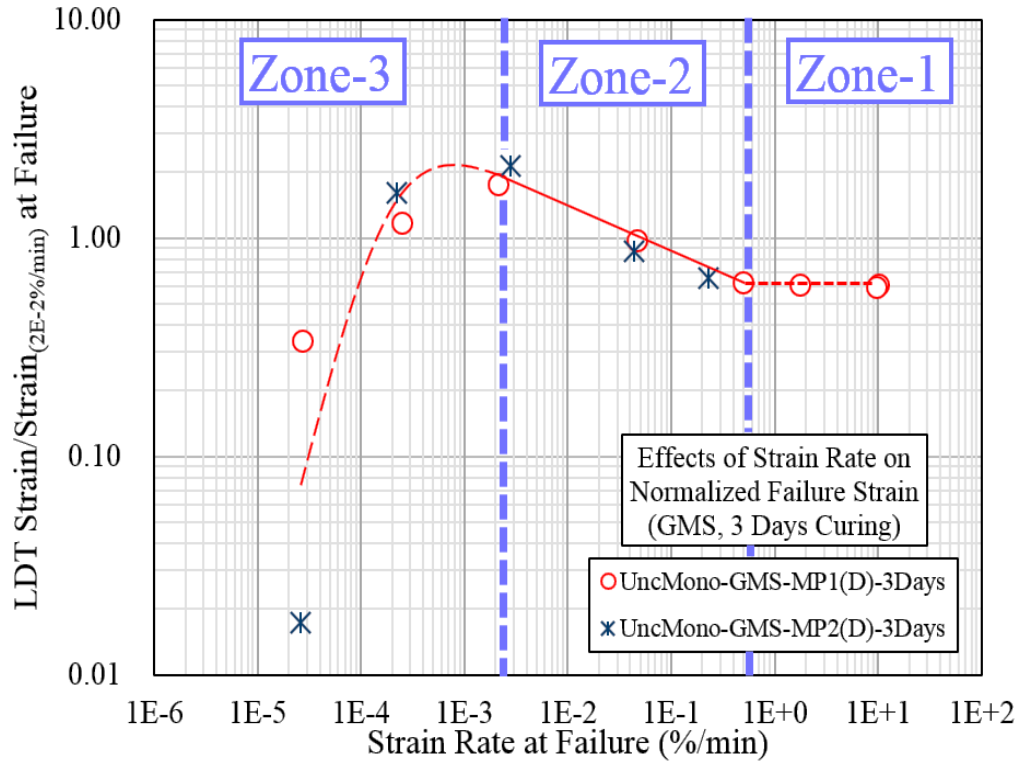

Fig. 5.21. Relationship between normalized failure strain and instantaneous strain rate at failure of GMS having gypsum/sand = 80% and 40%

The variation of peak strength and normalized peak strength with instantaneous loading rate is shown in Figures 5.26 and 5.27, and the results suggests that the effects of loading rate on the normalized stress-strain responses and normalized peak strength are similar at different periods of curing. Moreover, the curing period has not affected the trend of variation of failure strains and normalized failure strain, as evident in Figures 5.28 and 5.29. These results confidently repudiates the existence of any possible interaction between the effects of ageing and loading rate on the mechanical behavior of GMS under the studied range of curing period [2-6].

Table 5.4. Test Results of GMS-MP1 (Curing Period = 90 Days)

Machine Type	Series ID & Batch Type	Average Axial Strain Rate	Test ID	Bulk Unit Weight Before Testing	Moisture Content After Testing	UCS	Failure Strain		Failure Time
							EDT	Avg. LDT	
		(%/min)		(kN/m^3)	(%)	(kPa)	(%)	(%)	(min)
UCM*	GMS(MP1(A)-UncMono-90D) Batch-A	1.4E-01	GA1-90D(1.4E-1)-A01	18.3	28.1	3485	0.307	0.294	4.9
			GA1-90D(1.4E-1)-A02	18.1	29.1	3709	0.358	0.375	5.1
		1.6E-02	GA1-90D(1.6E-2)-A03	18.3	28.6	3028	0.540	0.618	60.6
		4.1E-03	GA1-90D(4.1E-3)-A04	18.2	29.7	2485	0.644	0.700	212.4
UCM*	GMS(MP1(D) -UncMono-90D) Batch-D	5.3E+00	GD1-90D(5.3E+0)-D01	18.4	33.2	3227	0.550	0.276	5.3
TCM**		2.5E-01	GD1-90D(2.5E-1)-D02	18.3	32.6	3099	0.617	0.357	0.3
		2.4E-02	GD1-90D(2.4E-2)-D03	18.3	33.4	2595	0.641	0.428	0.0
		1.7E-03	GD1-90D(1.7E-3)-D04	18.3	31.2	1416	0.835	0.656	0.0
UCM*		2.0E-04	GD1-90D(2.0E-4)-D05	18.4	32.9	390	0.526	0.501	0.0
		2.1E-05	GD1-90D(2.1E-5)-D06	18.5	30.3	121	0.304	0.284	0.0

* Unconfined Compression Machine, ** Triaxial Compression Machine

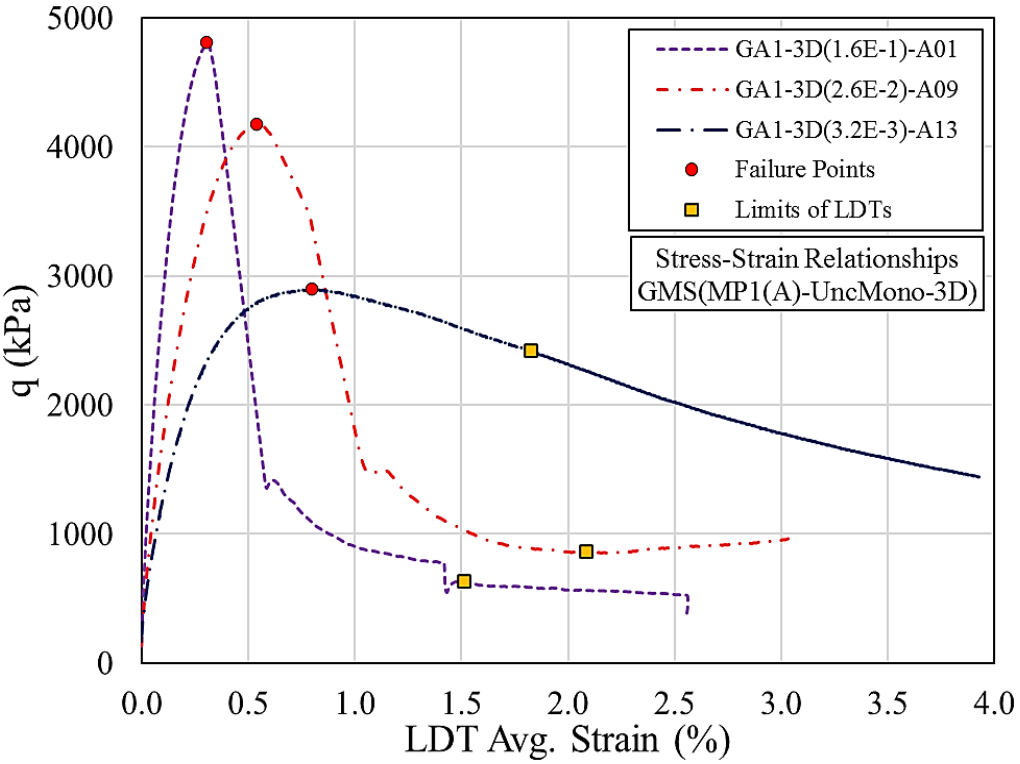

Fig. 5.22. Typical stress-strain relationships GMS(MP1(A)-UncMono-90D), modified after [2]

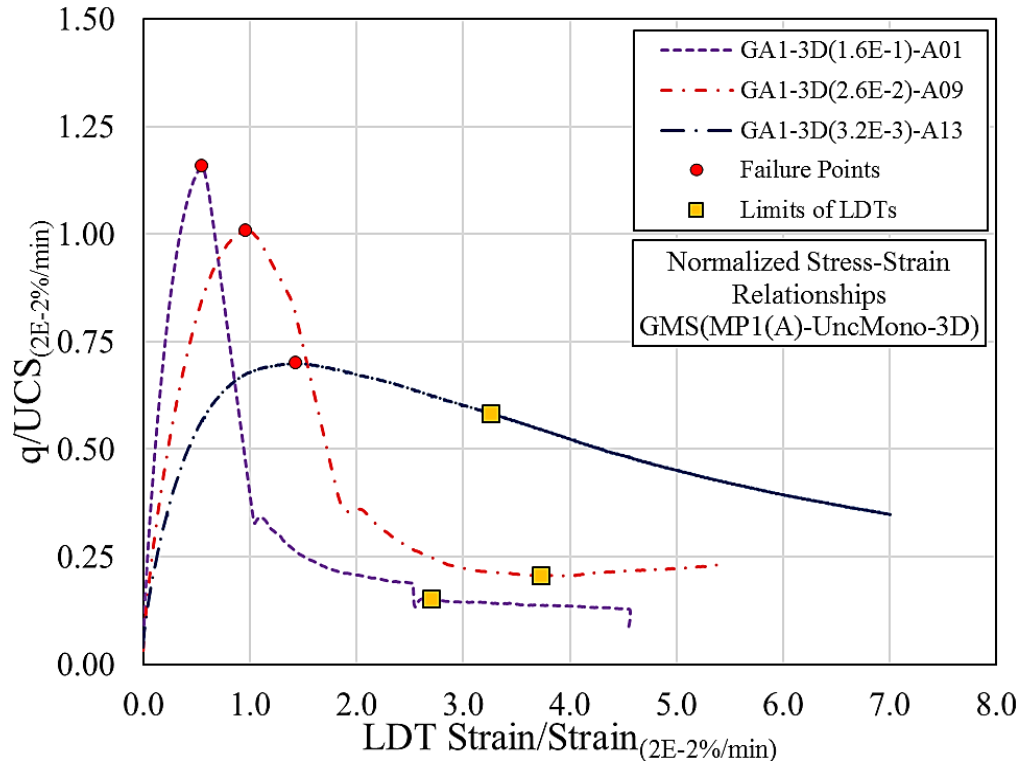

Fig. 5.23. Typical normalized stress-strain relationships GMS(MP1(A)-UncMono-90D)

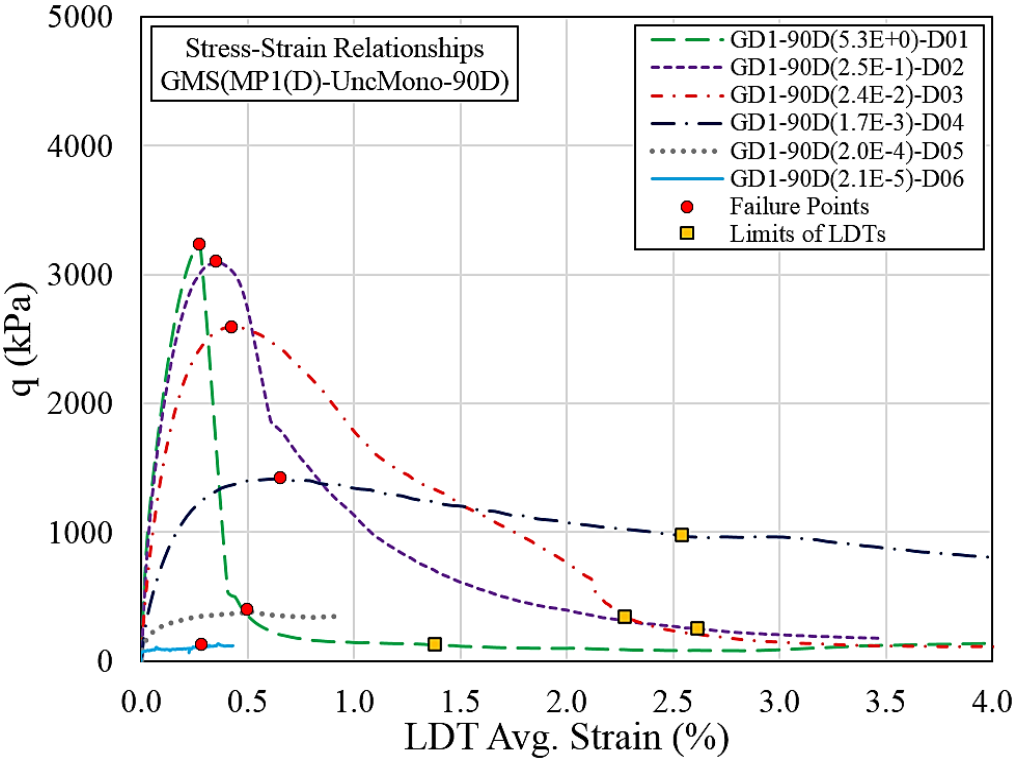

Fig. 5.24. Typical stress-strain relationships GMS(MP1(D)-UncMono-90D), modified after [2, 4]

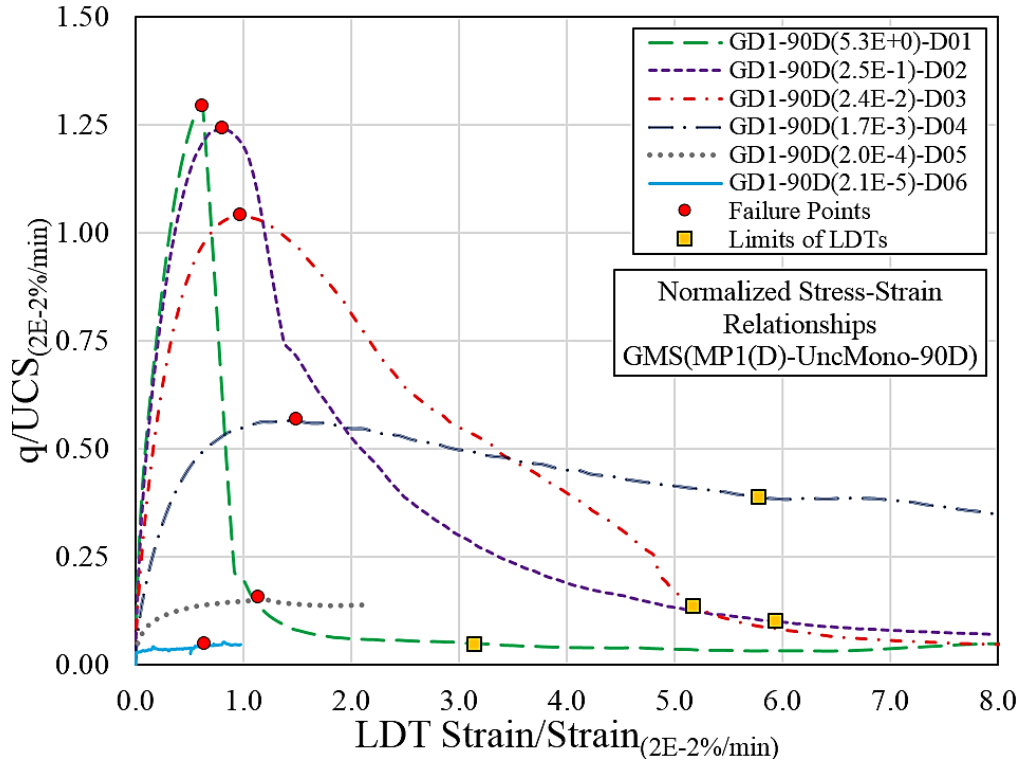

Fig. 5.25. Typical normalized stress-strain relationships GMS(MP1(D)-UncMono-90D)

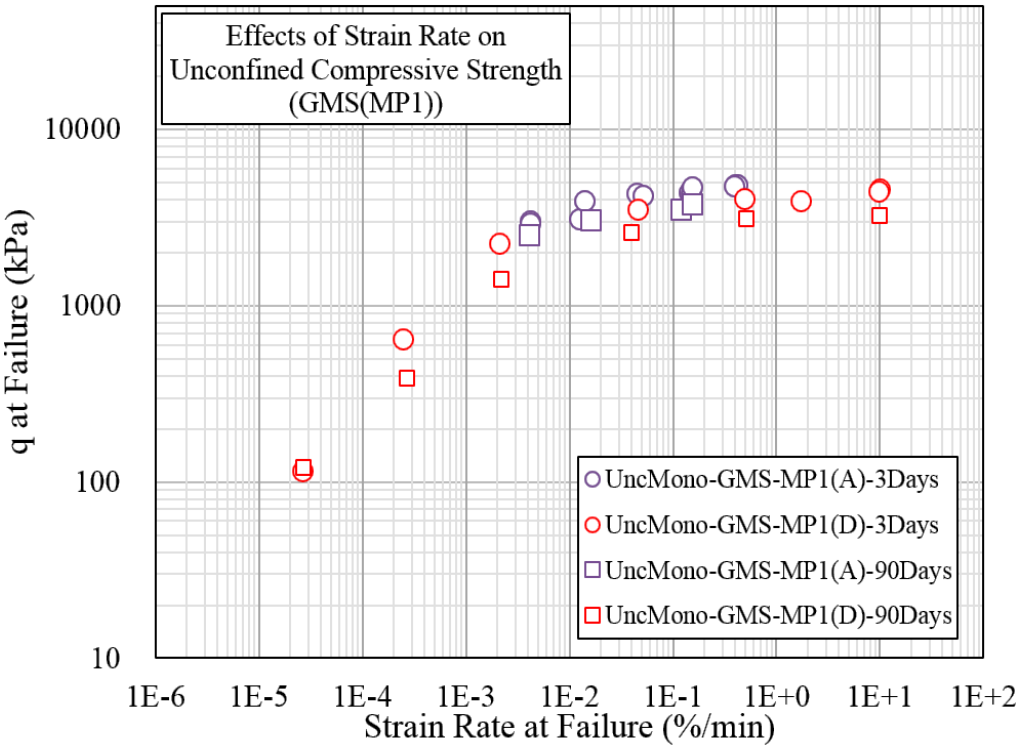

Fig. 5.26. Relationship between UCS and instantaneous failure strain rate of GMS having curing periods = 3 & 90 Days, modified after [3]

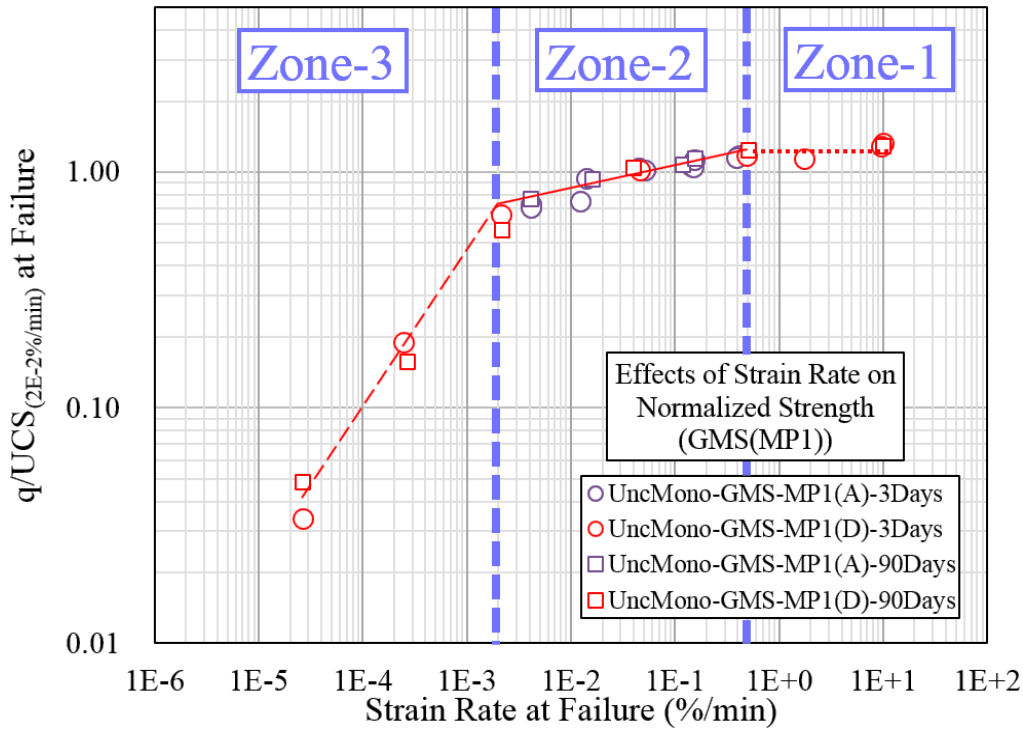

Fig. 5.27. Relationship between normalized peak strength and instantaneous failure strain rate of GMS having curing periods=3 & 90 Days, modified after [2-6]

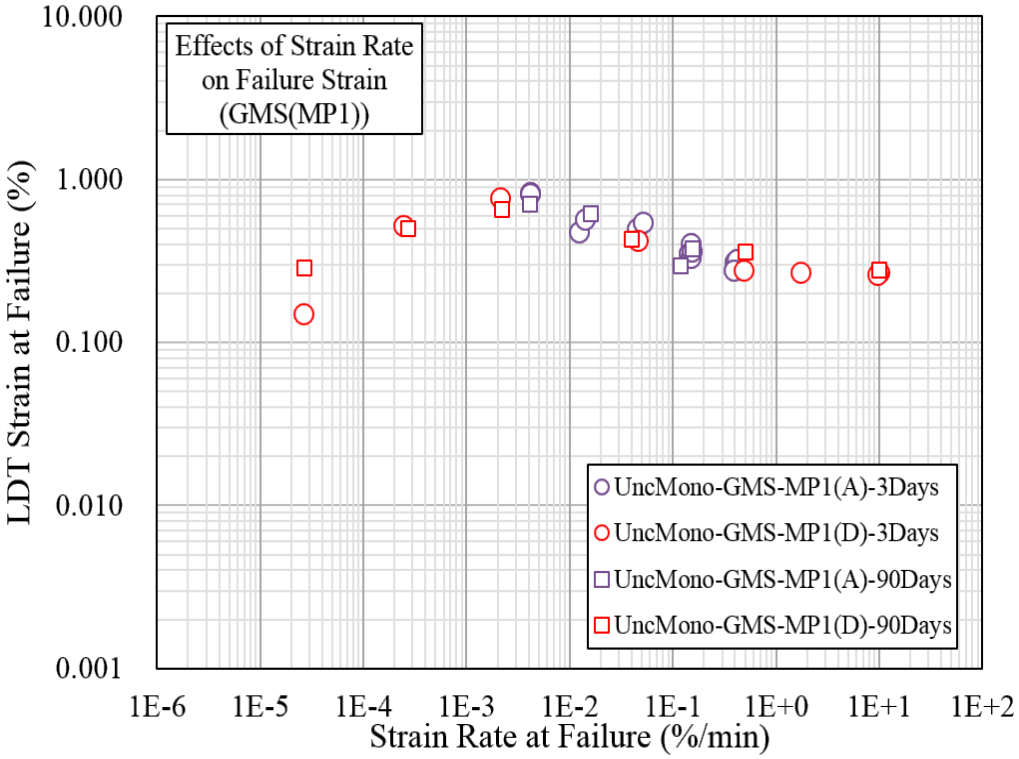

Fig. 5.28. Relationship between failure strain and instantaneous failure strain rate of GMS having curing periods = 3 & 90 Days, modified after [3]

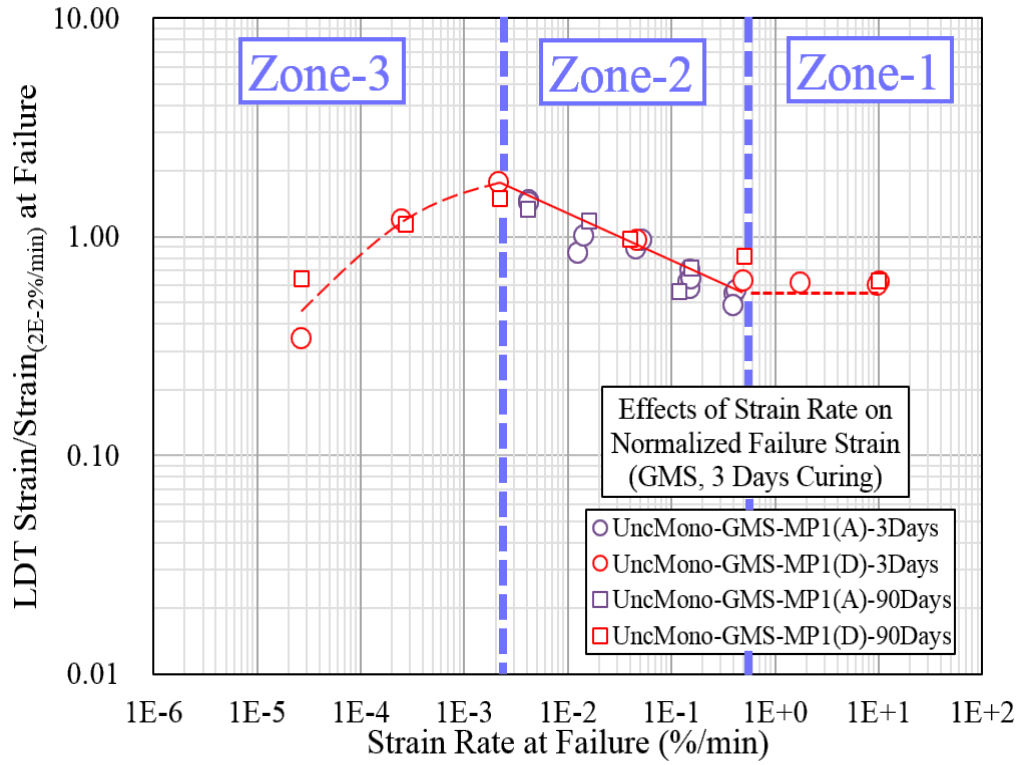

Fig. 5.29. Relationship between normalized failure strain and instantaneous failure strain rate of GMS having curing periods = 3 & 90 Days, modified after [2-6]

5.3 STRAIN ENERGY CHARACTERISTICS OF GMS AT DIFFERENT LOADING RATES

The loading rate dependency (viscous behavior) of bounded materials, such as natural rocks, is chiefly linked with intermolecular forces before the onset of microcracking, and forces induced by the friction during crack propagation. During compression, the total strain induced within a specimen can broadly classified into two components, viz. recoverable (elastic) strains and irrecoverable strains. Among these two, elastic strains are time-independent, and increment of elastic strains occur spontaneously with the corresponding increment of load. In case of bounded geomaterials, the irrecoverable strains are mainly credited to the damage of microstructure due to microcracking and other forms of plastic deformations, and these irrecoverable strains are time-dependent in nature. Therefore, the loading rate dependency is primarily governed by the micromechanical particularities of bounded geomaterials, i.e. tendency of elastic and irrecoverable strain accumulation at different loading rates [8-10].

In the light of above stated findings, the effects of loading rate (viscosity) of be expounded by considering the characteristics of strain energy stored in specimen during different loading rates. The total strain energy per unit volume (U) absorbed by the specimen can be expressed by the following expression [9]:

$$\mathrm{U} = \int_0^{\varepsilon_1} \sigma_1 d\varepsilon_1 + \int_0^{\varepsilon_2} \sigma_2 d\varepsilon_2 + \int_0^{\varepsilon_3} \sigma_3 d\varepsilon_3 \tag{5.1}$$

Where:

σ_1, σ_2 and σ_3 are the principal stresses

ε_1, ε_2 and $\varepsilon_3$are the principal strains

Additionally, this total strain energy per unit volume (U) comprises of elastic strain energy per unit volume (Ue) and dissipated strain energy per unit volume (Ud), as shown in Eq. (5.2). Elastic strain energy is released upon failure or unloading, and dissipated strain energy is the energy consumed for the formation of microcracking and permanent deformation within the specimen. The schematic illustration of elastic and dissipated strain energies is shown in Fig. 5.30 [9].

$$\mathrm{U} = \mathrm{Ue} + \mathrm{Ud} \tag{5.2}$$

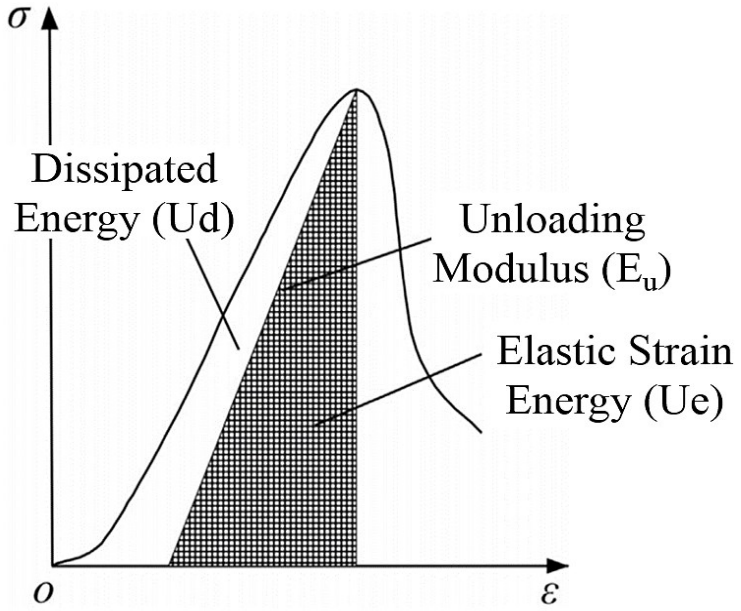

Fig. 5.30. Illustration of elastic and dissipated strain energy components, modified after [9]

In case of unconfined monotonic tests, the elastic strain energy can be approximated by the following expression [9]:

$$\text{Ue} = \frac{1}{2E_u}\sigma_1^2 \tag{5.3}$$

Where:

E_u is the unloading tangential modulus

The findings of unconfined compression tests on granite (of Jinzhou, Chine) showed that the values of unloading tangential modulus (E_u) are approximately same as of tangential modulus during loading phase (E_o), as shown in Fig. 5.31. This finding greatly simplifies the estimation of elastic strain energy, as computation of unloading tangential modulus (E_u) demands laborious superfluous testing. Therefore, the values of elastic strain energy were approximated in the present study by assuming the values of unloading tangential modulus (E_u) equal to tangential modulus at loading phase (E_o). After incorporating this assumption, the modified expression to estimate elastic strain energy per unit volume is shown in Eq. (5.4) [9].

$$\text{Ue} = \frac{1}{2E_o}\sigma_1^2 \tag{5.4}$$

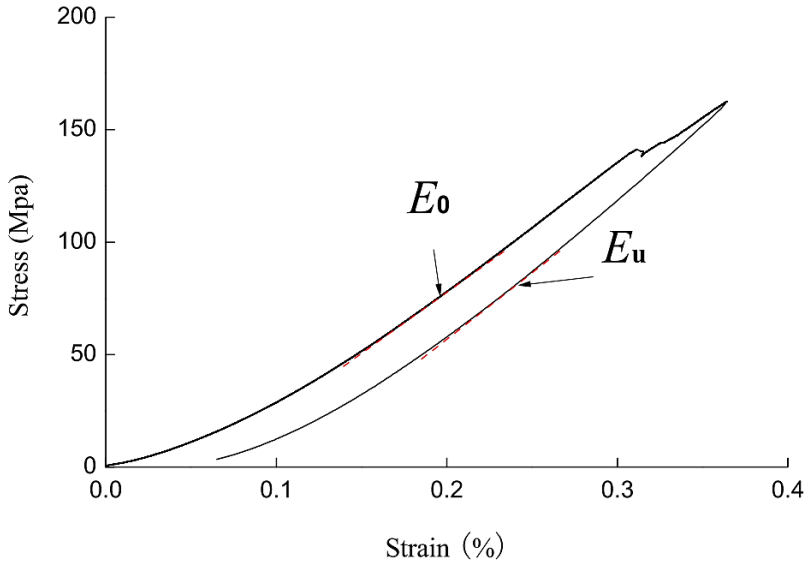

Fig. 5.31. Loading and unloading response of granite (of Jinzhou, Chine) [9]

In order to study the effects of loading rate on the characteristics of strain energy of GMS during compression, different components of strain energies were computed for GMS(MP1(D)-UncMono-90D) specimens, and the results are presented in Table 5.5. Variations of total, elastic and dissipated strain energies with loading rate is plotted in Fig. 5.33. In addition, variation of normalized elastic (Ue/U) and dissipated (Ud/U) energies with respect to total absorbed strain energy per unit volume is also shown in Fig. 5.44. Based on the trends of variations, these plots can also be classified in to same zones of strain rates as proposed earlier for GMS(MP1(D)-UncMono-3D) in Fig. 5.4 and 5.6.

Table 5.5. Estimated Strain Energies of GMS-MP1 specimens (Curing Period = 3 Days)

Series ID	Average Axial Strain Rate	Test ID	E_o	Total Energy Absorption (U)	Elastic Energy (Ue)	Dissipated Energy (Ud)	Ue/U	Ud/U	Ud/Ue
	(%/min)		(MPa)	(kJ/m^3)	(kJ/m^3)	(kJ/m^3)			
GMS(MP1(D)-UncMono-3D) Batch-D	4.4E+00	GD1-3D(4.4E+0)-D01	2138	8.32	4.75	3.57	0.57	0.43	0.75
		GD1-3D(4.4E+0)-D02	1923	7.84	5.01	2.83	0.64	0.36	0.57
	8.0E-01	GD1-3D(8.0E-1)-D03	1824	7.00	4.12	2.87	0.59	0.41	0.70
	1.9E-01	GD1-3D(1.9E-1)-D04	2059	7.81	3.89	3.92	0.50	0.50	1.01
	2.4E-02	GD1-3D(2.4E-2)-D05	1367	10.79	4.39	6.40	0.41	0.59	1.46
	1.6E-03	GD1-3D(1.6E-3)-D06	644	13.65	3.90	9.75	0.29	0.71	2.50
	2.1E-04	GD1-3D(2.1E-4)-D07	289	2.87	0.72	2.15	0.25	0.75	3.00
	1.9E-05	GD1-3D(1.9E-5)-D08	229	0.15	0.03	0.12	0.19	0.81	4.13

As stated earlier, the damage of microstructure during compression is attributed to the development of micro cracks and permanent deformations within bounded materials, resulting into the accumulation of irrecoverable strains. At lower strain rates, time between the successive increments of load is sufficient enough for ample development of irrecoverable strains. Therefore, major portion of total absorbed energy at slower loading rates comprises primarily of dissipated strain energy which is consumed in the formation of microcracking and permanent deformations of grains/particles [8-10]. This aspect is effusively binding for GMS specimens belonging to Zone-3, as evident in Figures 5.32 and 5.33. For instance, about 80% of total energy absorption consists of dissipated strain energy for specimen tested at 1.9E-5 %/min (GD1-3D(1.9E-5)-D08) and is around 4.13 times higher than elastic strain energy, as shown in Table 5.3 and Fig. 5.33.

At higher strain rates, there exist a lag between the formation of micro cracks (or permanent deformations of grains) and rapid increments of loads, resulting into reduction in proportions of dissipated strain energy. In other words, irrecoverable strains induced at higher rates of loading are comparatively lesser than elastic strains [8-10]. In case of GMS specimens belong to Zone-1, dissipated strain energy reduced to 40% of total absorbed energy and the rest 60% of absorbed energy is elastic strain energy, and dissipated energy is around 0.57 to 0.75 times of elastic energy, as shown in Table 5.3 and Fig. 5.33.

Owing to this fact that the major fraction of total strain energy is not consumed for microcracking and permanent deformation of particles, considerable strain energy is temporarily stored within the specimen in the form of elastic strain energy, and results into pseudo-confinement of specimen which ultimately enhances the peak strength [8-10]. Therefore, GMS specimens tested at higher loading rates showed relatively higher values of UCS, and it can be stated that with the increase of elastic strain energy the strength of specimen will be relatively higher, as shown in Fig. 5.33.

The relationship between normalized peak strength and instantaneous strain rate at failure of GMS(MP1(D)-UncMono-3D), shown in Fig. 5.4, can be correlated with the variations of total strain energies, normalized elastic and dissipated strains energies presented in Figures 5.22 and 5.33. In Zone-3, normalized dissipated strain energy is significantly higher than normalized elastic strain energy, and with increase of strain rate an increase in total strain energy and normalized elastic strain energy can be witnessed

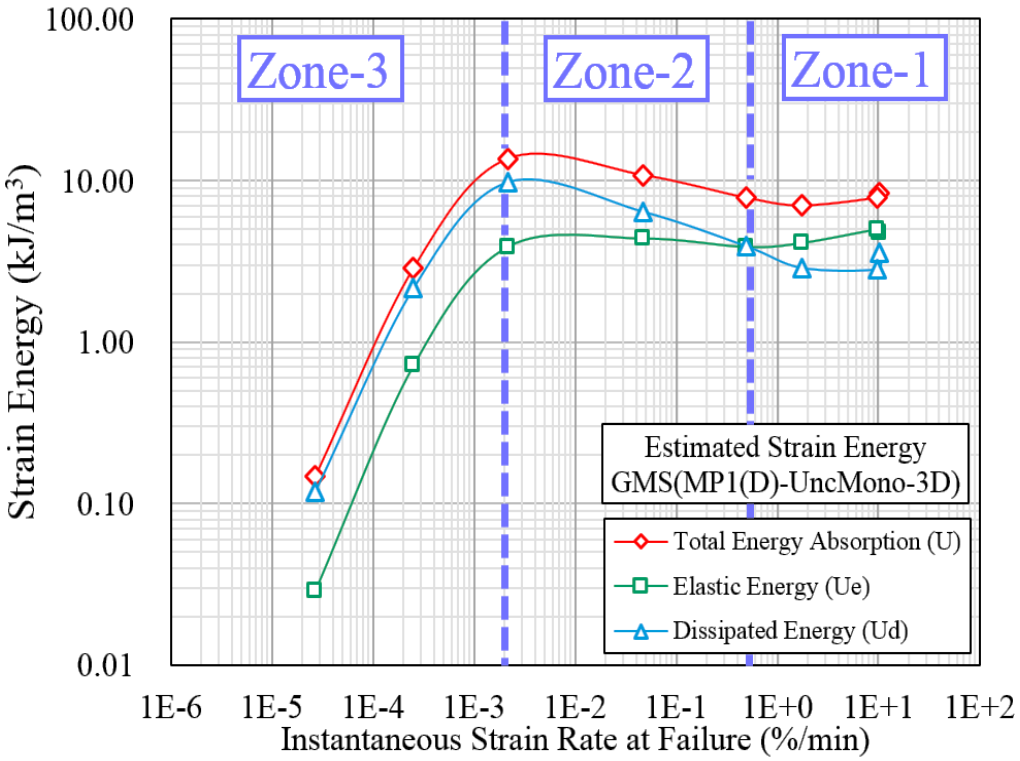

Fig. 5.32. Variation of total, elastic and dissipated strain energies with strain rate

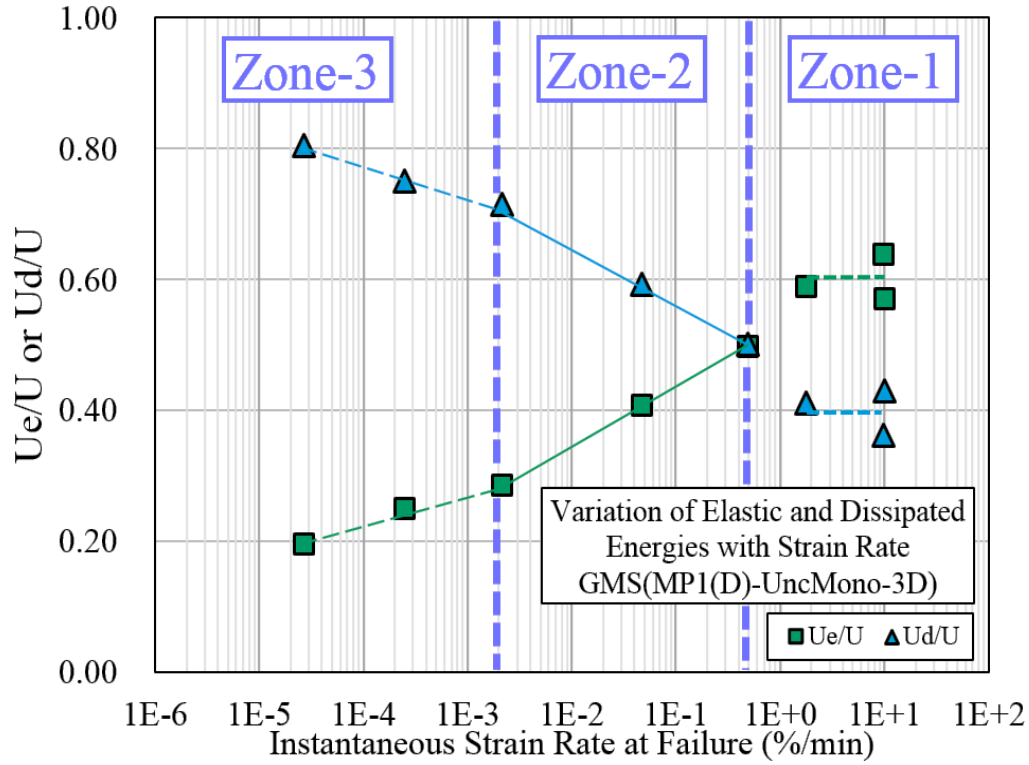

Fig. 5.33. Variation of normalized elastic and dissipated strain energies with strain rate of GMS(MP1(A)-UncMono-90D)

in Figures 5.32 and 5.33, resulting into an increase in peak strength with loading rate. It is noteworthy that the major fraction of total strain energy in Zone-3 is dissipated strain energy, and increase in normalized elastic strain energy and total strain energy in this zone results a significant increase in peak strength of GMS, as evident in Figures 5.4 and 5.33.

The normalized elastic strain energy increases rapidly with the increase of strain rate in Zone-2, and finally becomes equivalent to normalized dissipated strain energy, as shown in Fig. 5.33. Due to the relatively lower values of normalized dissipated strain energy in Zone-2 compared with Zone-3, the enhancement of peak strength with the increase in normalized elastic strain energy is relatively lesser in this zone. Finally, the values of normalized elastic energy are higher than normalized dissipated energy in Zone-1, and these values are almost insensitive to loading rates, as evident in Fig. 5.33. Consequently, the strength values of GMS specimens belonging to this zone of strain rates are higher than the rest of the specimens, and are not largely influenced by the loading rate, as shown in Fig. 5.4. Therefore, it can be inferred from these results that hardened mass comprised of dihydrate needle-shaped crystals is very sensitive to loading rate, and it is momentously susceptible to prodigious damage due to the ample formation of micro cracks at slower loading rates.

5.4 LOADING RATE DEPENDENCY OF CTS UNDER UNCONFINED MONOTONIC LOADING

The loading rate dependency of CTC specimens, cured for 28 days, was evaluated by performing unconfined compression tests at 7 different loading rates, ranging from 4.1E+00 to 3.2E-05 %/min, and the results are presented in Table 5.6.The procedure adopted to performed these test is similar to that of GMS specimens, and these specimens were also covered with 0.3 mm thick rubber membrane to minimize the variations of moisture content during testing. The stress-strain and normalized stress relationship of CTS specimens are presented in Figures 5.34 and 5.35 respectively. Except for specimen tested at 3.2E-5 %/min., viz. CA1-28D(3.2E-5)-A08, the effects of loading rate on the peak strength values and stress-strain response of CTS are relatively limited compared with GMS, as shown in Figures 5.34 and 5.35. In comparison with GMS, the post-peak strain softening in CTS specimens is also not greatly affected by the loading rates [4].

Table 5.6. Test Results of CTS (Curing Periods = 28 Days)

Machine Type	Series ID	Average Axial Strain Rate	Test ID	Bulk Unit Weight Before Testing	Moisture Content After Testing	UCS	Failure Strain		Failure Time
							EDT	Avg. LDT	
		(%/min)		(kN/m^3)	(%)	(kPa)	(%)	(%)	(min)
TCM**	CTS(MP1(A)-UncMono-28D)	4.1E+00	CA1-28D(4.1E+0)-A01	17.7	32.8	4018	0.592	0.259	0.1
		1.2E-01	CA1-28D(1.2E-1)-A02	18.2	30.8	4185	0.663	0.224	1.7
		2.1E-02	CA1-28D(2.1E-2)-A03	18.0	30.9	3930	0.640	0.288	12.8
		1.3E-02	CA1-28D(1.3E-2)-A04	18.3	29.8	3981	0.626	0.258	20.7
			CA1-28D(1.3E-2)-A05	18.0	30.5	3928	0.639	0.304	20.4
		1.8E-03	CA1-28D(1.8E-3)-A06	17.9	30.9	3571	0.556	0.296	158.5
UCM*		1.8E-04	CA1-28D(1.8E-4)-A07	18.0	26.5	3446	0.531	0.442	2347.0
		3.2E-05	CA1-28D(3.2E-5)-A08	17.9	8.8	4605	2.313	1.931	65022.5

* Unconfined Compression Machine, ** Triaxial Compression Machine

The effects of loading rate on the peak strength and normalized peak strength of CTS are plotted in Figures 5.36 and 5.37 respectively. The peak strength of GMS was relatively lesser influenced by the loading rate, and a mere reduction of about 12% was witnessed for a corresponding decrease of strain rate by 120 times, viz. 2.1E-2 to 1.8E-4 %/min, as evident in Figures 5.35 and 5.37. The peak strain (normalized peak strain) values and failure pattern of CTS specimens are also generally insensitive to loading rate for specimens tested at strain rates higher than 1.8E-04 %/min. and afterwards, an increasing trend of failure strains was observed with the decrease in loading rate, as shown in Figures 5.40(a) to 5.40(c) [4].

It is notable that the values of UCS and failure strains of specimen tested at 3.2E-5 %/min, viz. CA1-28D(3.2E-5)-A08, are portentously higher than the rest of the specimens, and the peak strength was achieved after 45 days from the start of loading. The lower value of moisture content estimated at the end of test was ominously lower, i.e. 8.8 %, indicates the drying hardening of specimen during exceptionally long periods of loading. Moreover, only bulging along with some localized visible cracking was observed at this slowest loading rate as shown in Fig. 5.40(d) [4].

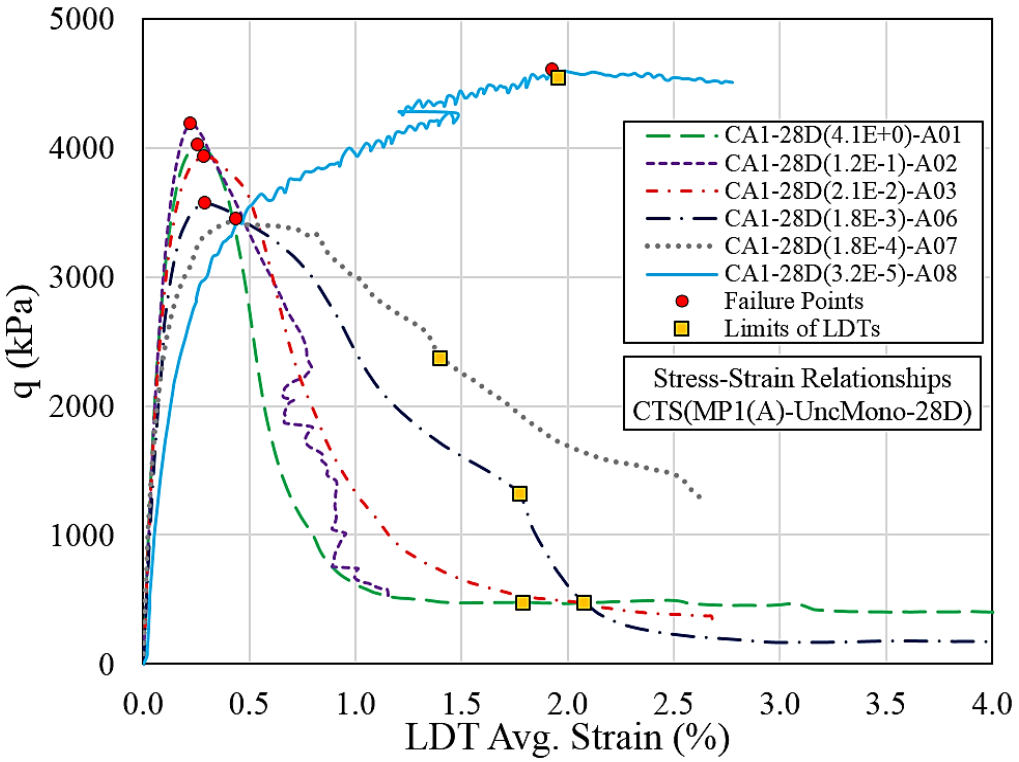

Fig. 5.34. Typical stress-strain relationships
CTS(MP1(A)-UncMono-28D)

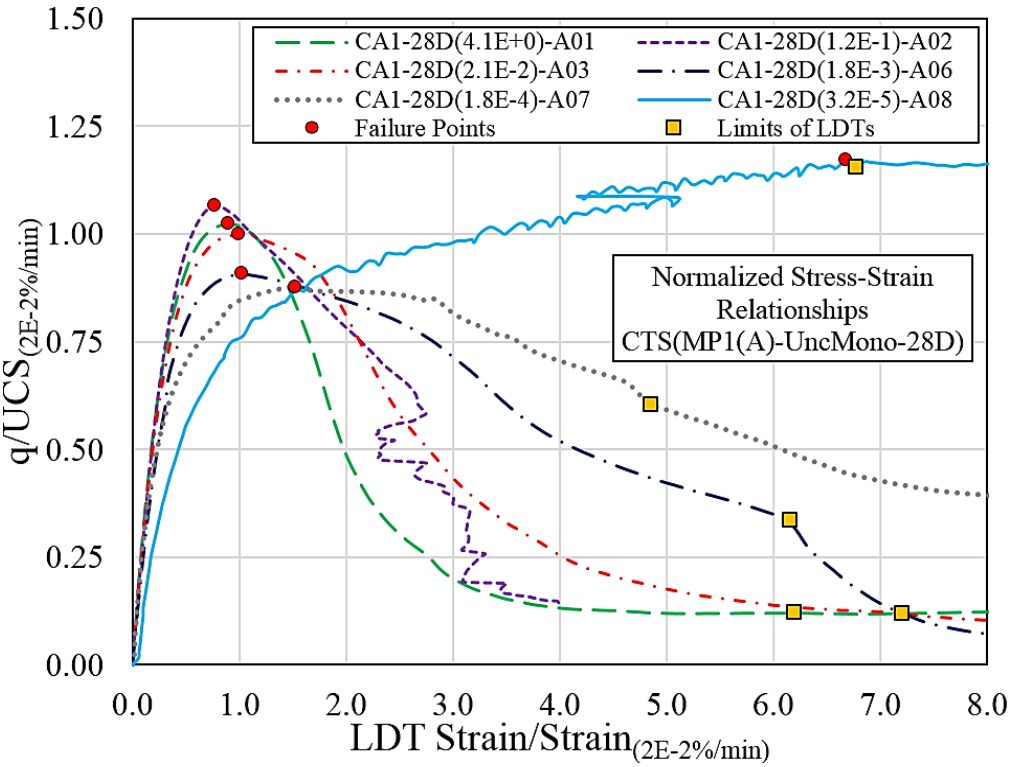

Fig. 5.35. Typical normalized stress-strain relationships
CTS(MP1(A)-UncMono-28D), modified after [4]

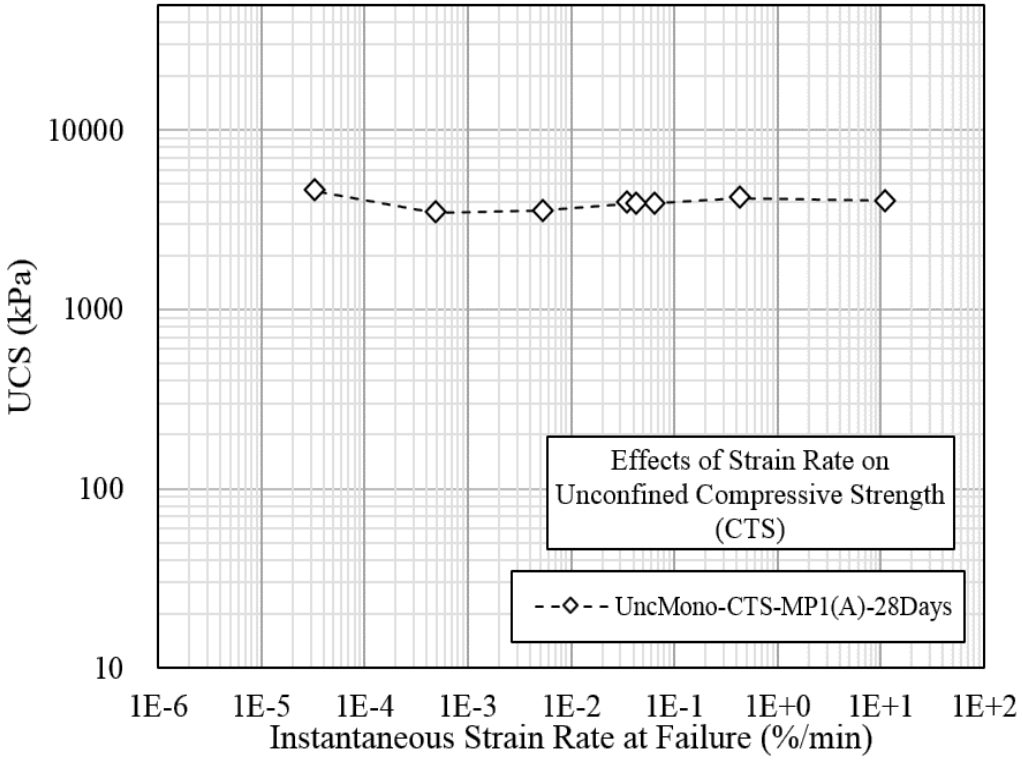

Fig. 5.36. Relationship between UCS and instantaneous strain rate at failure of CTS(MP1(A)-UncMono-28D)

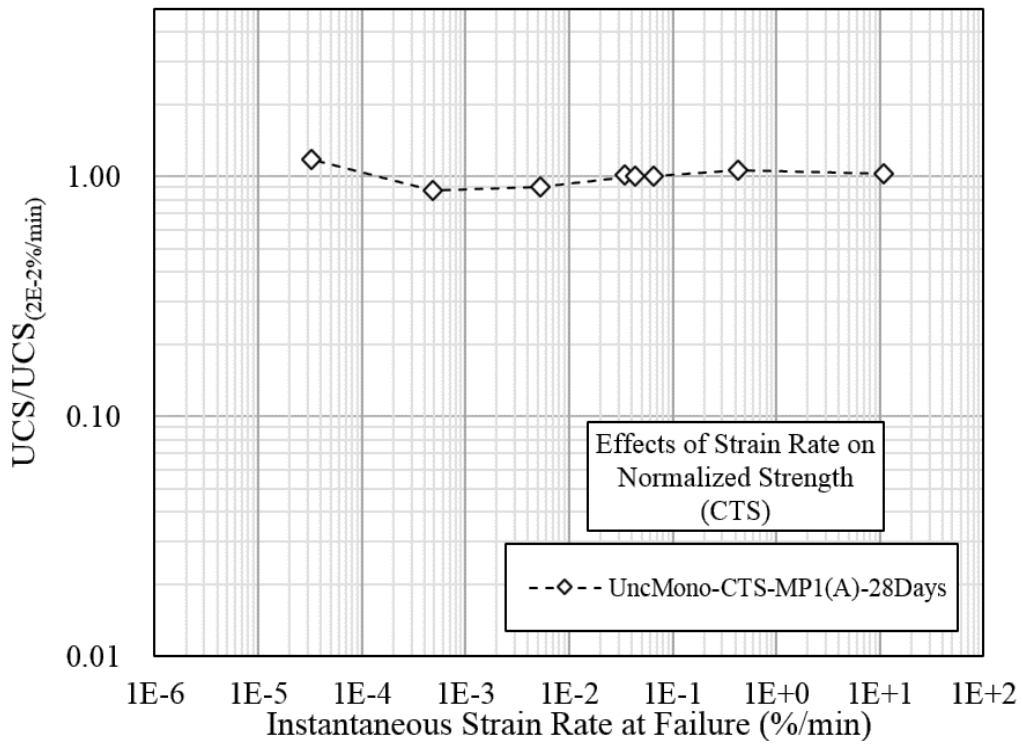

Fig. 5.37. Relationship between normalized peak strength and instantaneous strain rate at failure of CTS(MP1(A)-UncMono-28D), modified after [4]

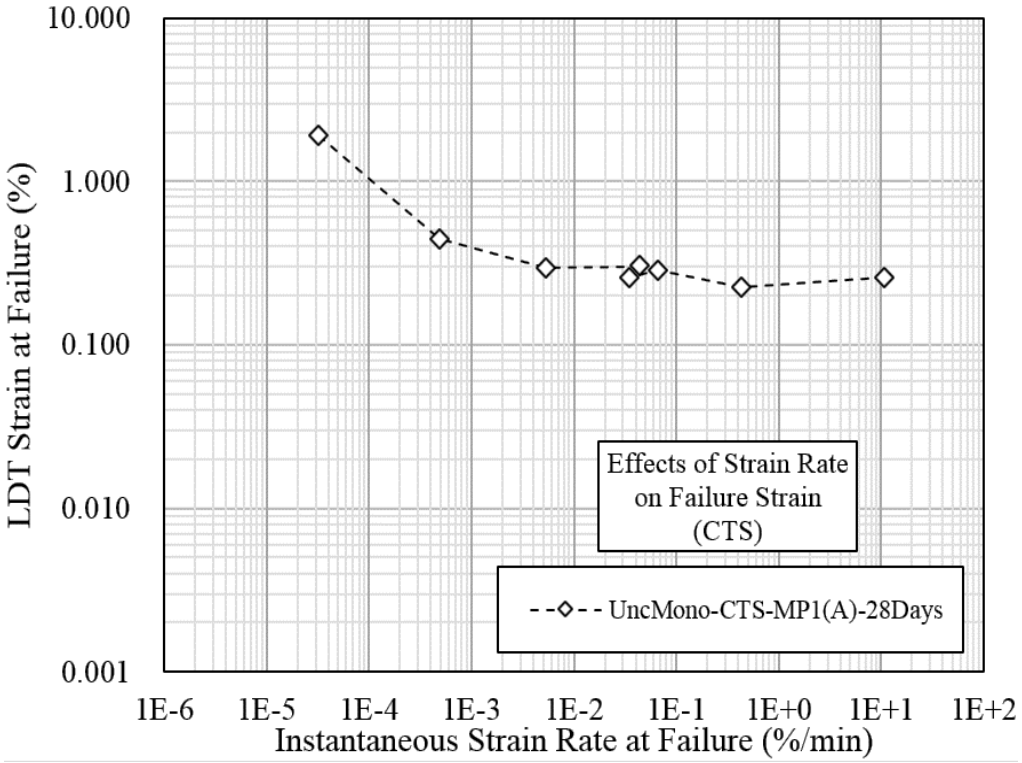

Fig. 5.38. Relationship between failure strain and instantaneous strain rate at failure of CTS(MP1(A)-UncMono-28D)

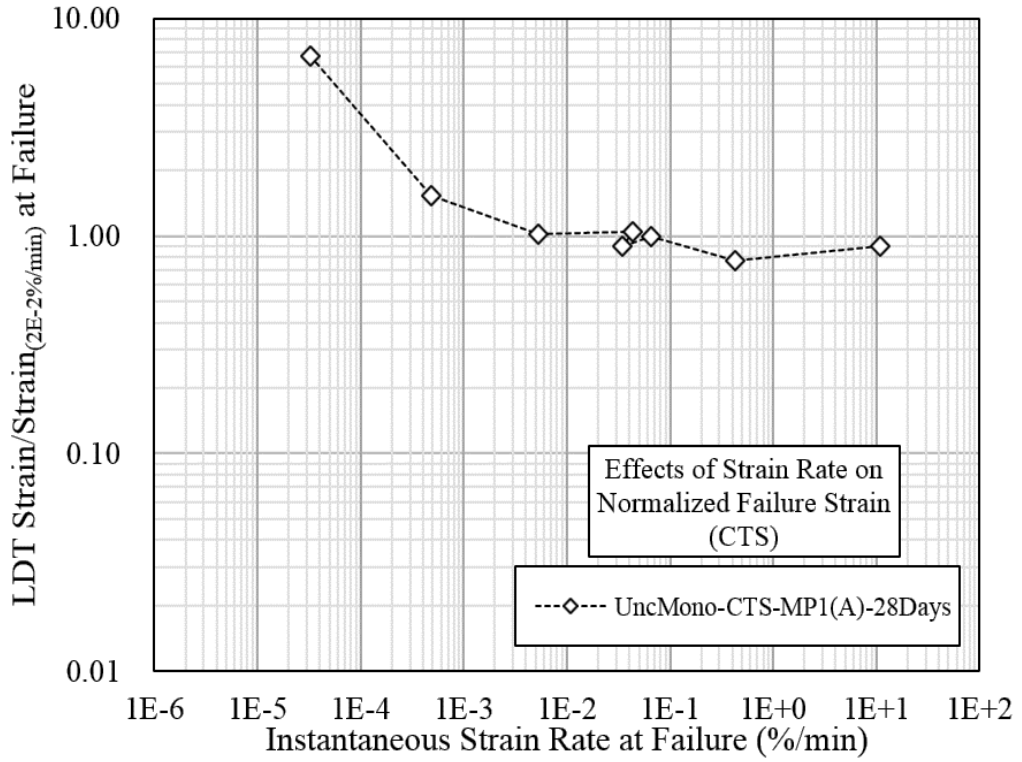

Fig. 5.39. Relationship between normalized failure strain and instantaneous strain rate at failure of CTS(MP1(A)-UncMono-28D), modified after [4]

(a) CA1-28D(4.1E+0)-A01

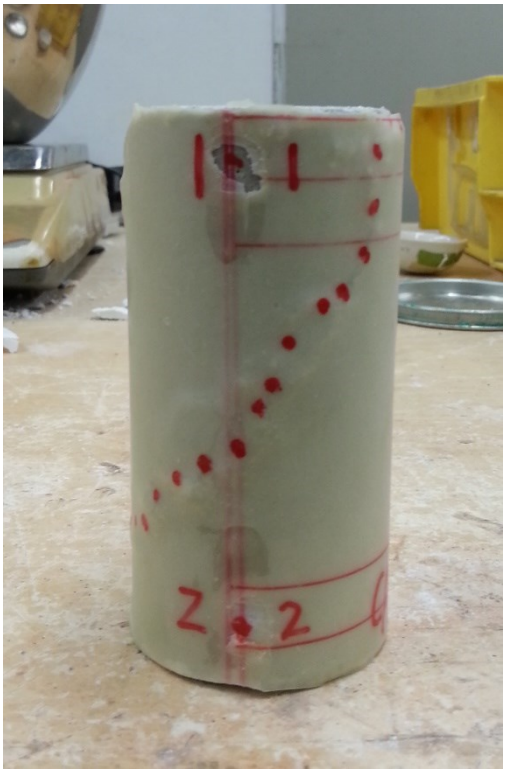

(b) CA1-28D(2.1E-2)-A03

(c) CA1-28D(1.8E-3)-A06

(d) CA1-28D(3.2E-5)-A08

Fig. 5.40. Failure pattern of CTS(MP1(A)-UncMono-28D) specimens [4]

5.5 STRAIN ENERGY CHARACTERISTICS OF CTS AT DIFFERENT LOADING RATES

Adopting the same procedure discussed earlier in Section 5.3, total, elastic and dissipated strain energies per unit volume of CTS specimens during compression at different loading rates were estimated, and the results are summarized and potted in Table 5.7 and Fig. 5.41 respectively. Except for specimen tested at 3.2E-05 %/min, viz. CA1-28D(3.2E-5)-A08, the effects of loading rate on the total strain energy per unit volume of CTS specimens are relatively trivial compared with GMS. Moreover, the normalized elastic and dissipated strain energies are also not significantly affected by the loading rates, as shown in Fig. 5.42. As a result, the peak strength of CTS was consequently not greatly affected by the loading rate, as shown in Fig. 5.36

Table 5.7. Estimated strain energies of CTS(MP1(A)-UncMono-28D) specimens

Series ID	Average Axial Strain Rate	Test ID	E_o	Total Energy Absorption (U)	Elastic Energy (Ue)	Dissipated Energy (Ud)	Ue/U	Ud/U	Ud/Ue
	(%/min)		(MPa)	(kJ/m^3)	(kJ/m^3)	(kJ/m^3)			
CTS(MP1(A)-UncMono-28D)	4.1E+00	CA1-28D(4.1E+0)-A01	2911	7.70	2.77	4.92	0.36	0.64	1.78
	1.2E-01	CA1-28D(1.2E-1)-A02	2896	6.53	3.02	3.50	0.46	0.54	1.16
	2.1E-02	CA1-28D(2.1E-2)-A03	2585	8.60	2.99	5.61	0.35	0.65	1.88
	1.3E-02	CA1-28D(1.3E-2)-A04	2780	7.50	2.85	4.65	0.38	0.62	1.63
		CA1-28D(1.3E-2)-A05	2425	8.96	3.18	5.78	0.36	0.64	1.82
	1.8E-03	CA1-28D(1.8E-3)-A06	2223	7.97	2.87	5.10	0.36	0.64	1.78
	1.8E-04	CA1-28D(1.8E-4)-A07	1917	12.29	3.10	9.19	0.25	0.75	2.97
	3.2E-05	CA1-28D(3.2E-5)-A08	699	71.45	15.18	56.28	0.21	0.79	3.71

The effects of drying hardening of CA1-28D(3.2E-5)-A08 is clearly evident from Fig. 5.41, as significantly higher amount of total strain energy was absorbed by the specimen even at slowest loading rate. Compared with dihydrate crystals, these results indicate that the deterioration in hydration products of cement, such as C-S-H gel, due to microcracking is not largely affected by the loading rate, as the fraction of normalized dissipated strain energy is relatively insensitive to loading rate.

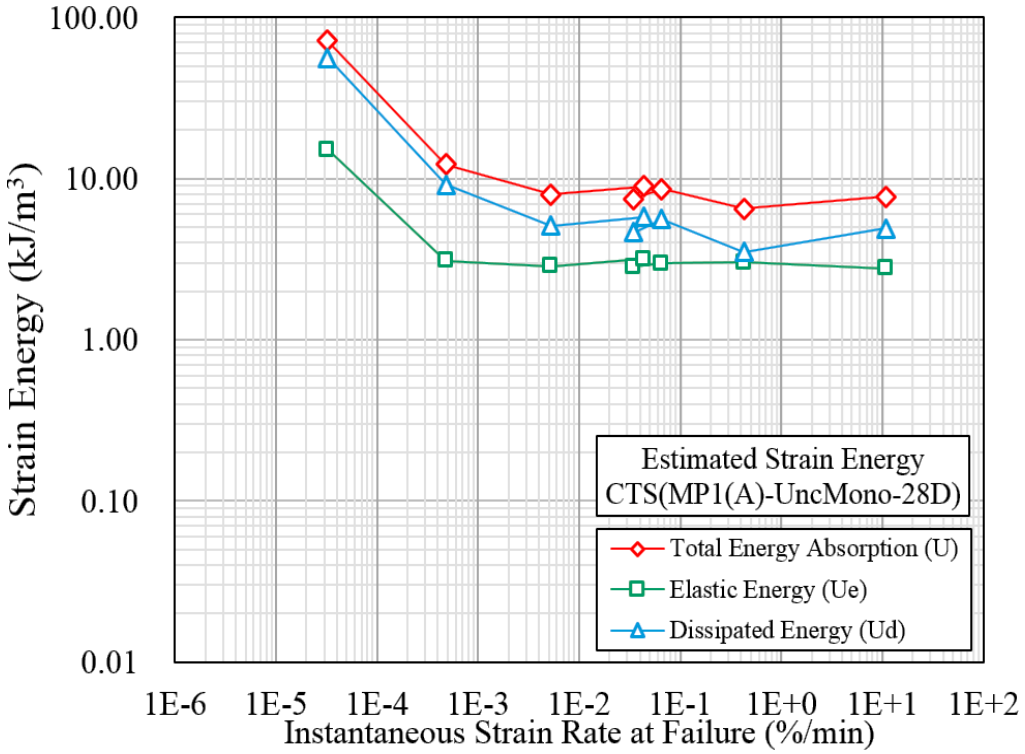

Fig. 5.41. Variation of total, elastic and plastic strain energies with strain rate of CTS(MP1(A)-UncMono-28D)

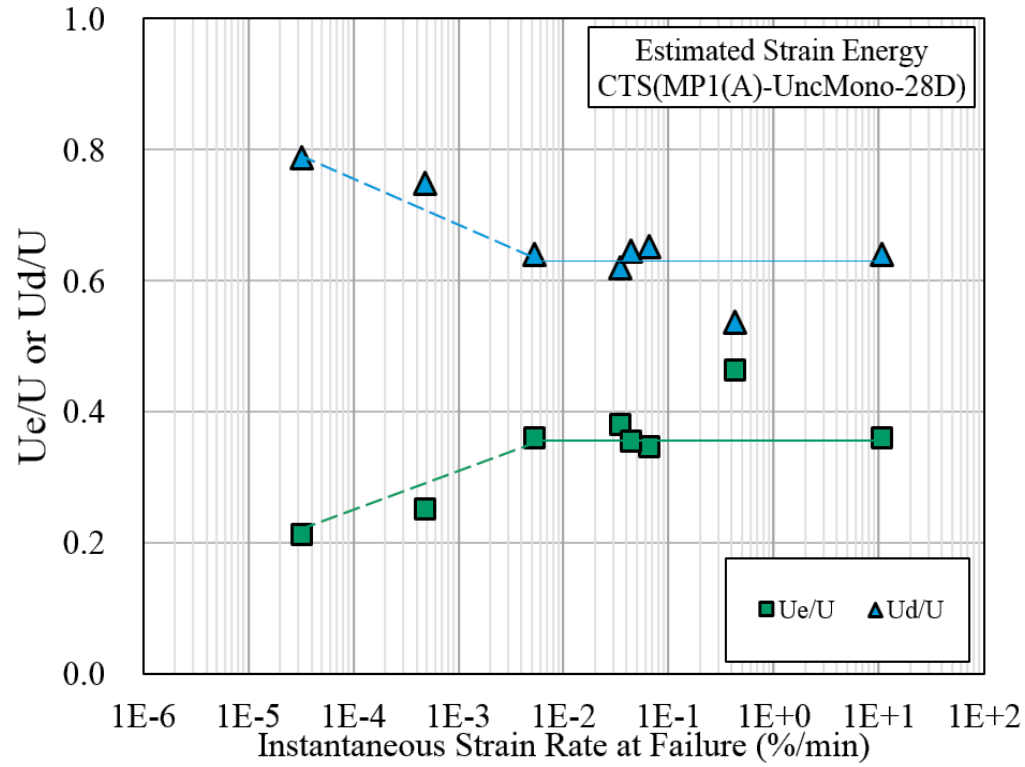

Fig. 5.42. Variation of normalized elastic and dissipated strain energies with strain rate of CTS(MP1(A)-UncMono-28D)

5.6 SUMMARY OF FINDINGS

- Significant effects of loading rate on UCS and stress-strain responses of GMS were witnessed for GMS. An increasing trend of UCS and pre-peak stiffness was observed with the increase in loading rate, and the effects of loading rate on the mechanical behaviour of GMS were divided into three distinct zones of strain rates, viz. Zones 1, 2 and 3.
- The effects of loading rate on strength and defamation characteristics of GMS were found to be relatively trivial for specimens having instantaneous failure strain rates higher than approximately 5.0E-1 %/min, viz. Zone-1. Additionally, the values of failure strain were also witnessed to be almost independent of loading rate for specimens belonging to Zone-1
- Substantial reduction in peak strength and pre-peak stiffness of GMS specimen with the decrease in strain rate was observed for specimens tested at strain rates lesser than 2.0E-3 %/min, viz. Zone-3. Besides, a trend of reduction failure strain with the decrease in loading rate was captured in this zone of strain rates.
- The effects of loading rate on the UCS and stress-strain responses belonging to Zone-2 are also evident, but were relatively lesser than Zone-3. An increasing trend of failure strain was observed with the decrease in loading rate for specimens of Zone-2, and the maximum value of normalized failure strain was observed at 2.0E-2 %/min.
- Visible formation of shear bands was witnessed for GMS specimens tested at strain rates higher than 2.0E-3 %/min, viz. Zones 1 and 2. Contrarily, only budging was observed for specimens tested at strain rates lesser than 2.0E-3 %/min, viz. Zone-3, and no visible cracks or shear bands were observed with the inspection of naked eye.
- Irrespective of the differences in absolute strength values and stress-strain responses of GMS specimens belonging to different gypsum batches, the effects of loading rate on the normalized peak strength and normalized stress-strain responses of all the specimens are fairy identical. Based on these results, it was conceived that the loading rate dependency of GMS is not affected by

the presence of impurities and additive, and the viscous behavior of GMS is majorly governed by the β-hemihydrate content.

- The amount of gypsum used for the preparation of GMS considerably controls the strength characteristics. However, the variation of gypsum content (Gypsum/Sand between 80% and 40%) has no notable effects on the loading rate dependency of GMS under unconfined conditions.
- Loading rate dependent characteristics of GMS at different curing periods confidently repudiates the existence of any possible interaction between the effects of ageing and loading rate.
- The estimation of different strain energies of GMS specimens indicated that major portion of total absorbed energy at slower loading rates comprises primarily of dissipated strain energy which was consumed in the formation of micro-cracking and permanent deformations of grains/particles, and this aspect is effusively binding for specimens belonging to Zone-3.
- In case of GMS specimens belong to Zone-1, dissipated strain energy reduced to 40% of total absorbed energy and the rest 60% of absorbed energy is elastic strain energy, and dissipated energy is around 0.57 to 0.75 times of elastic energy. Additionally, GMS specimens tested at higher loading rates showed relatively higher values of UCS, and it can be stated that with the increase of elastic strain energy the strength of specimen will be relatively higher. Finally, the values of normalized elastic energy are higher than normalized dissipated energy in Zone-1, and these values are almost insensitive to loading rates
- The normalized elastic strain energy increases rapidly with the increase of strain rate in Zone-2, and finally becomes equivalent to normalized dissipated strain energy. Due to the relatively lower values of normalized dissipated strain energy in Zone-2 compared with Zone-3, the enhancement of peak strength with the increase in normalized elastic strain energy is relatively lesser in this zone.
- The effects of loading rate on the peak strength values and stress-strain response of CTS are relatively limited compared with GMS. In comparison

with GMS, the post-peak strain softening in CTS specimens is also not greatly affected by the loading rates.

- The peak strain values and failure pattern of CTS specimens are also generally insensitive to loading rate for specimens tested at strain rates higher than 1.8E-04 %/min. and afterwards, an increasing trend of failure strains was observed with the decrease in loading rate.
- The effects of loading rate on the total strain energy per unit volume of CTS specimens are relatively trivial compared with GMS. Moreover, the normalized elastic and dissipated strain energies are also not significantly affected by the loading rates, and the peak strength of CTS was consequently not greatly affected by the loading rate.

5.7 REFRENCES

1. Kongsukprasert, L., and Tatsuoka, F. (2005), "Ageing and viscous effects on the deformation and strength characteristics of cement-mixed gravelly soil in triaxial compression", *Soils and Foundations*, **45(6)**, 55-74.

2. Maqsood, Z., Koseki, J. and Kyokawa, H. (2019), "Effects of loading rate on strength and deformation characteristics of gypsum mixed sand", *7th International Symposium on Deformation Characteristics of Geomaterials*, Glasgow.

3. Maqsood, Z. (2016), "Behaviour of gypsum mixed sand under unconfined monotonic and cyclic loading conditions," *Masters Thesis*, *The University of Tokyo,* Japan.

4. Maqsood, Z. and Koseki, J. (2019), "Time dependent strength and deformation characteristics of bounded geomaterials," *9th Asian Young Geotechnical Engineering Conference*, (submitted)

5. Maqsood, Z. and Koseki, J. (2018), "Strength and deformation characteristics of gypsum mixed sand under wide range of axial strain rate", *The 20th International Summer Symposium, JSCE*, Japan.

6. Maqsood, Z. and Koseki J. (2019), "Strength and deformation characteristics of bounded geomaterials under creep and cyclic loading considering loading rate

effects", *15th International Conference on Geotechnical Engineering*, Pakistan. (submitted)

7. Maqsood, Z. and Koseki, J. (2016). "Use of local strain measurements for rational evaluation of loading rate dependency of Gypsum Mixed Sand", *The 18th International Summer Symposium, JSCE,* Japan.
8. Mahanta, B., Singh, T. N., Ranjith, P. G. and Vishal, V. (2018), "Experimental investigation of the influence of strain rate on strength; failure attributes and mechanism of Jhiri shale," *Journal of Natural Gas Science and Engineering*, **58**, 178-188.
9. Liang, C., Wu, S., Li, X. and Xin, P. (2015), "Effects of strain rate on fracture characteristics and mesoscopic failure mechanisms of granite," *International Journal of Rock Mechanics and Mining Sciences*, **76**, 146-154.
10. Liang, W. G., Zhao, Y. S., Xu, S. G. and Dusseault, M. B. (2011), "Effect of strain rate on the mechanical properties of salt rock," *International Journal of Rock Mechanics and Mining Sciences*, **1(48)**, 161-167.

BEHAVIOR OF GMS AND CTS UNDER UNCONFINED CREEP AND CYCLIC LOADING

6.1 PREAMBLE

The long-term performance of natural slopes and large-scale foundations located in seismically active areas demands rational evaluation of strength and deformation characteristics of bounded geomaterials under creep and cyclic loading conditions. By and large, the results of tests performed on bounded geomaterials, including sedimentary rocks and cement treated sands, showed no significant effects of cyclic loading histories on the peak strength deterioration [1, 2]. Besides other important factors including small strain stiffness and failure strength, the representative strain accumulation characteristics of bounded geomaterials induced during creep and cyclic, viz. residual strains, loading play pivotal role in the reliable constitutive modeling. In the present chapter, an approach of examining the role of instantaneous strain rates induced during cyclic and creep loading is discussed to systematically highlight the effects of cyclic and creep loads on the strength and characteristics of GMS. Additionally, the results of unconfined creep tests performed on CTS are also summarized, and effects of creep loading on the mechanical behavior of GMS and CTS are compared meticulously.

6.2 TESTING PROCEDURE

The testing procedure summarized in Section 4.3 of Chapter No. 4 was adopted for unconfined cyclic and creep tests on GMS and CTS specimens. In case of creep tests, monotonic loading was first applied at a fixed nominal loading rate to achieve the targeted creep load, and the creep load was than maintained by applying infinitely small loading and unloading cycles to cope with the technical constrains of unconfined compression machine. The schematic illustration of typical stress-strain relationship of unconfined cyclic loading test is presented in Fig. 1, and definitions of numerous parameters are

highlighted. The desired maximum cyclic stress (q_{max}) was attained by first applying monotonic loading at an externally measured average strain rate of 5.6E-2 %/min, and cyclic loading of selected cyclic amplitude (q_{max}-q_{min}) was than applied uninterruptedly at the same externally controlled loading rate until failure was observed [3].

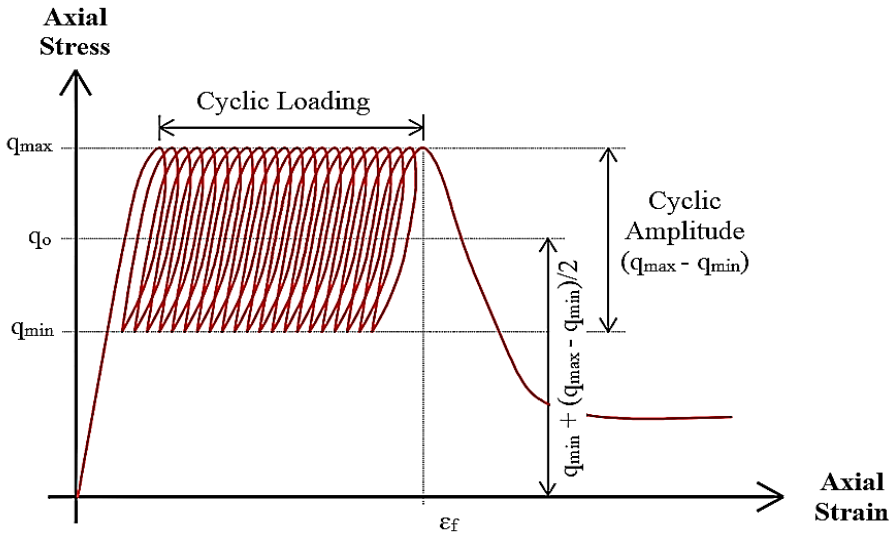

Fig. 6.1. Schematic illustration of typical stress-strain response of typical unconfined cyclic loading test [3]

As highlighted earlier in Section 5.2.1 of Chapter No. 5, two different types of strain rates, viz. Average Strain Rate (ASR) and Instantaneous Strain Rate (ISR) were considered in the present study. For all the loading conditions, ASR was calculated by dividing the total accumulated strain with the elapsed time of monotonic, creep or cyclic loading, as shown in Eq. (5.1). However, the ISR at any instant was estimated by utilizing a fixed interval of time, i.e. time required for the increment of axial strain from 98% of failure strain to failure strain, as per Eq. (2). Owing to the limitation of sampling devices, ISR in some cases were approximated between about 85% of failure strain and failure strain [3].

$$\text{Average Strain Rate (t)} = \frac{\varepsilon_{(t)} - \varepsilon_{(t_o)}}{t - t_0} \tag{6.1}$$

$$\text{Instantaneous Strain Rate (t)} = \frac{\varepsilon_{(t)} - \varepsilon_{(t-\Delta t)}}{\Delta t} \tag{6.2}$$

Where:

t = time at any instant

t_o = starting time of monotonic/cyclic/creep loading

Δt = time required for the increment of axial strain from 98% of failure strain to failure strain

$\varepsilon_{(t)}$ = axial strain computed at time "t"

$\varepsilon_{(t_o)}$ = initial value of axial stain at the start of monotonic/cyclic/creep loading

$\varepsilon_{(t-\Delta t)}$ = axial strain computed at time "$t - \Delta t$"

6.3 BEHAVIOR OF GMS UNDER UNCONFINED CREEP AND CYCLIC LAODING

6.3.1 Stress-strain response of GMS under unconfined creep loading

A series of unconfined creep tests at different axial stress levels were performed on GMS(MP1) specimens, and the results are shown in Table 6.1. All the specimens were cured for 90 days, except UncCREEP-4(GA1-310D) which was tested at a curing period of about 10 months (310 days). As discussed earlier in Chapter No. 4, the effects of ageing on the mechanical behavior of GMS(MP1) are only prominent in the initial month of curing, and it was consequently anticipated that the mechanical behavior of UncCREEP-4(GA1-310D) is similar to the rest of specimens of this series. Before the onset of creep loading, an average externally measured strain rate of 5.6E-2 %/min was opted to achieve the target creep loads [3].

Table 6.1. Test Results of GMS(MP1(A)-UncCREEP), modified after [4]

Machine Type	Series ID & Batch Type	Test ID	Bulk Unit Weight Before Testing	Moisture Content After Testing	Avg. Creep Load	q at Failure	Normalized Creep Load at Failure ($q/UCS_{(2E\text{-}2\%/min)}$)	LDT Failure Strain (ε_f)	Failure Time
			(kN/m^3)	(%)	(kPa)	(kPa)		(%)	(min)
TCM**	GMS(MP1(A)-UncCREEP) Batch-A	UncCREEP-1 (GA1-90D)	18.2	28.2	2735	2735	0.84	1.320	103
UCM*		UncCREEP-2 (GA1-90D)	18.1	28.3	2365	2367	0.73	1.619	217
TCM**		UncCREEP-3 (GA1-90D)	18.3	27.0	1875	1867	0.58	3.433	1197
UCM*		UncCREEP-4 (GA1-310D)	17.8	24.3	1035	1022	0.32	9.157	12849

* Unconfined Compression Machine, ** Triaxial Compression Machine

The stress-strain and normalized stress-strain responses of GMS(MP1(A)-UncCREEP) are presented in Figures 6.2 and 6.3. For comparison purposes, the stress-strain and normalized stress-strain responses of a typical unconfined monotonic test, viz. GA1-90D(7.2E-2)-A02, of counterpart GMS(MP1(A)-UncMono-90D) monotonic series are also plotted in Figures 6.2 and 6.3. The average strain rate of GA1-90D(7.2E-2)-A02 is comparable with the initial monotonic loading of creep tests, and stress-strain and normalized stress-strain responses of monotonic and creep tests are similar prior to the start of creep loading, as evident in Figures 6.2 and 6.3 [3].

Based on these results, it is obvious that the behavior of GMS(MP1) under unconfined creep loading is very unpromising, as a small normalized creep load of mere 32% is sufficient enough to cause a creep failure within a relatively shorter duration of time, viz. about 9 days, as shown in Table 6.1. Additionally, an increasing trend of axial strain accumulation with the decrease of creep load can also be witnessed from Figures 6.2 and 6.3. For instance, axial strain accumulation of only 1.320% was observed at normalized creep load of 84%, and this value ominously increased to 9.157% for specimen tested at normalized creep load of 32%, as mentioned in Table 6.1 [3]. The details of these aspects will be further discussed in the upcoming sections.

6.3.2 Stress-strain response of GMS under unconfined cyclic loading

The results of unconfined cyclic loading tests performed on GMS specimens cured for 90 days are shown in Table 6.2. In all of these tests, the magnitude of maximum cyclic stress was intentionally kept approximately identical, viz. qmax ≈ 84% of UCS(2.0E-2 %/min), and the value of cyclic amplitude was varied systemically in different tests to unveil the effects of cyclic amplitude on the mechanical behavior of GMS. The stress-strain and normalized stress strain responses of GMS under different cyclic loading conditions are plotted in Figures 6.4 to 6.11.In general, the number of cycles required to trigger failure increase significantly with the decrease of cyclic amplitude, as evident in Table 6.2. In spite of approximately similar value of maximum cyclic stress, specimen UncCYC-1 (GA1-90D) tested at a cyclic amplitude of 2250 kPa failed merely after 27 cycles, whereas a total of 167 cycles having amplitude of 425 kPa were sustained by UncCYC-4 (GA1-90D) before failure [3], as evident in Table 6.2.

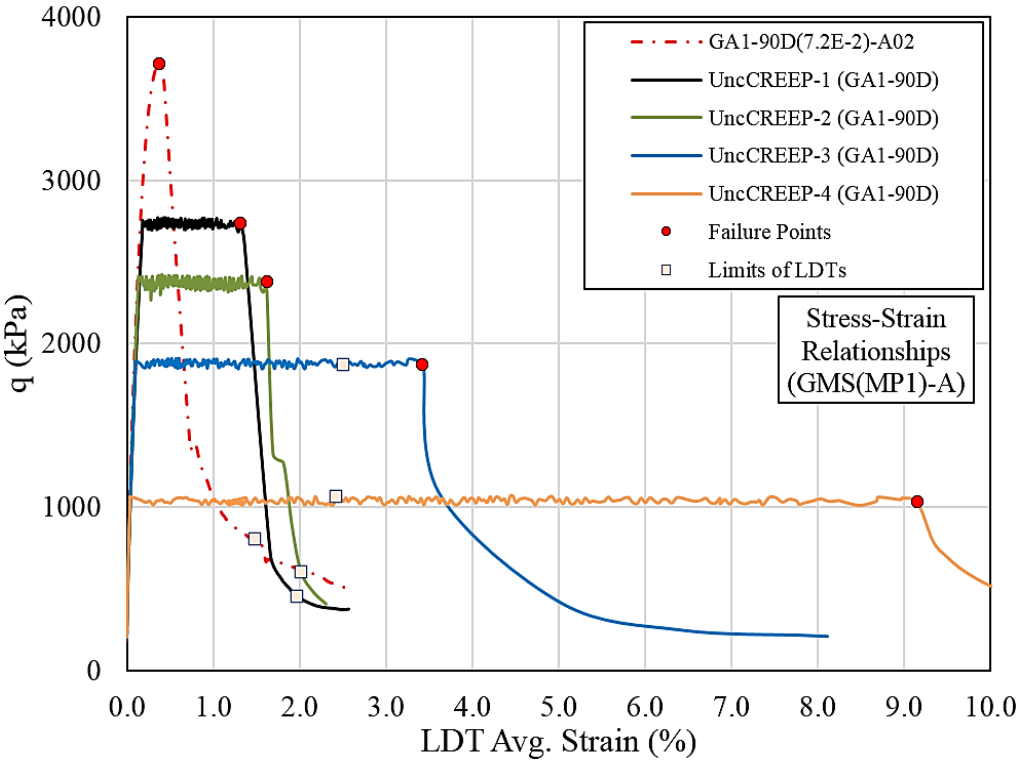

Fig. 6.2. Stress-strain relationships GMS(MP1(A)-UncCREEP), modified after [5]

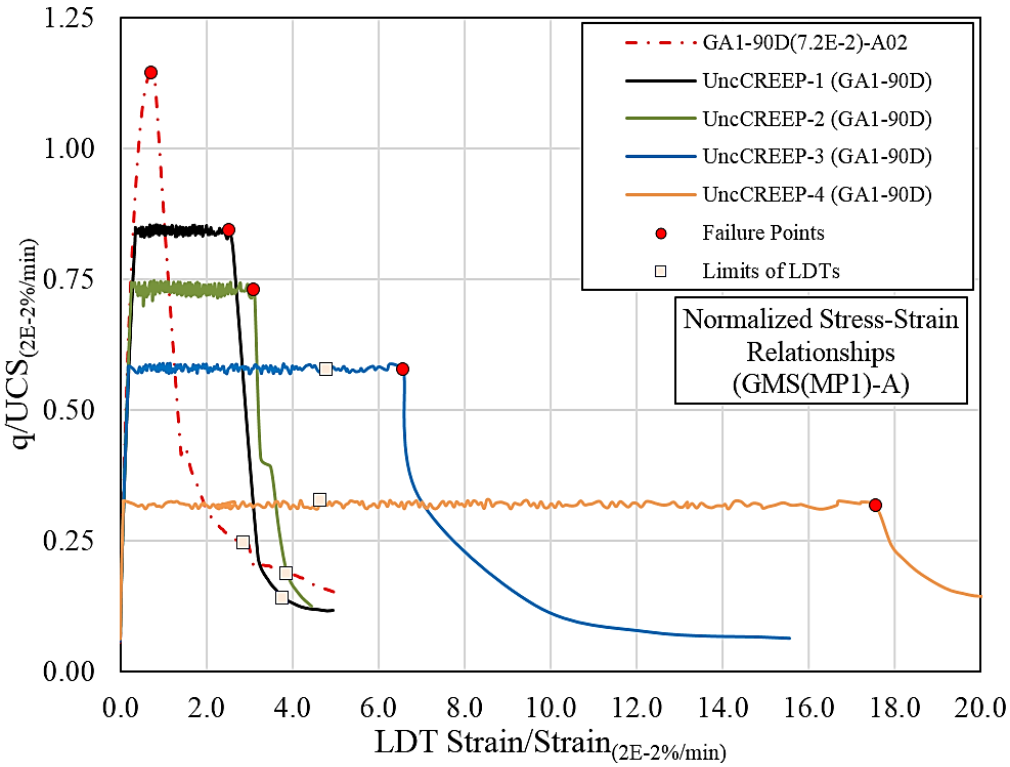

Fig. 6.3. Normalized stress-strain relationships GMS(MP1(A)-UncCREEP), modified after [3]

Irrespective of the number of cycles required to trigger failure, the effects of cyclic amplitude on axial strain accumulation during cyclic loading are also quite marginal, as the values of failure strains are approximately similar in different tests, except for UncCYC-1 (GA1-90D) which failed at slightly lesser failure strain, as shown in Table 6.2. In general, the failure strain of specimens failed under cyclic loading, except for UncCYC-1 (GA1-90D), showed failure strain of roughly 2.2~2.4 times of their counterpart unconfined monotonic tests [3], as evident in Figures 6.7, 6.9 and 6.11.

Table 6.2. Test Results of GMS(MP1(A)-UncCYC-90D), modified after [3]

Machine Type	Series ID & Batch Type	Test ID	Bulk Unit Weight Before Testing	Moisture Content After Testing	Loading Conditions				No. of Cycles	q at Failure	LDT Failure Strain (ε_f)	Failure Time
					q_{max}	q_{min}	q_o	q_{max}-q_{min}				
			(kN/m^3)	(%)	(kPa)	(kPa)	(kPa)	(kPa)		(kPa)	(%)	(min)
UCM*	GMS(MP1(A)-UncCYC-90D) Batch-A	UncCYC-1 (GA1-90D)	18.1	28.6	2790	240	1515	2550	27	2699	0.949	146
		UncCYC-2 (GA1-90D)	18.2	28.0	2850	1150	2000	1700	51	2800	1.132	167
		UncCYC-3 (GA1-90D)	18.1	28.3	2765	1915	2340	850	107	2611	1.281	165
		UncCYC-4 (GA1-90D)	18.0	28.3	2750	2325	2538	425	167	2622	1.154	126

* Unconfined Compression Machine

It is noteworthy that these values of normalized failure strains of cyclic loading tests are also comparable to the normalized failure strain of unconfined creep test performed at creep load equal to maximum cyclic stress, viz. UncCREEP-1(GA1-90D), as shown in Figures 6.3, 6.7, 6.9 and 6.11. Based on this finding, it is palpable that the values of failure strain in cyclic and creep tests are principally governed by the maximum compressive stress induced during cyclic and creep loading respectively [3]. The axial strain accumulation pattern of GMS under cyclic loading will be further elaborated in the upcoming sections.

6.3.3 Axial strain accumulation in GMS during unconfined creep and cyclic loading

Rational assessment of residual strain accumulation during creep and cyclic loading is of prime significance for the reliable prediction of long-term performance of

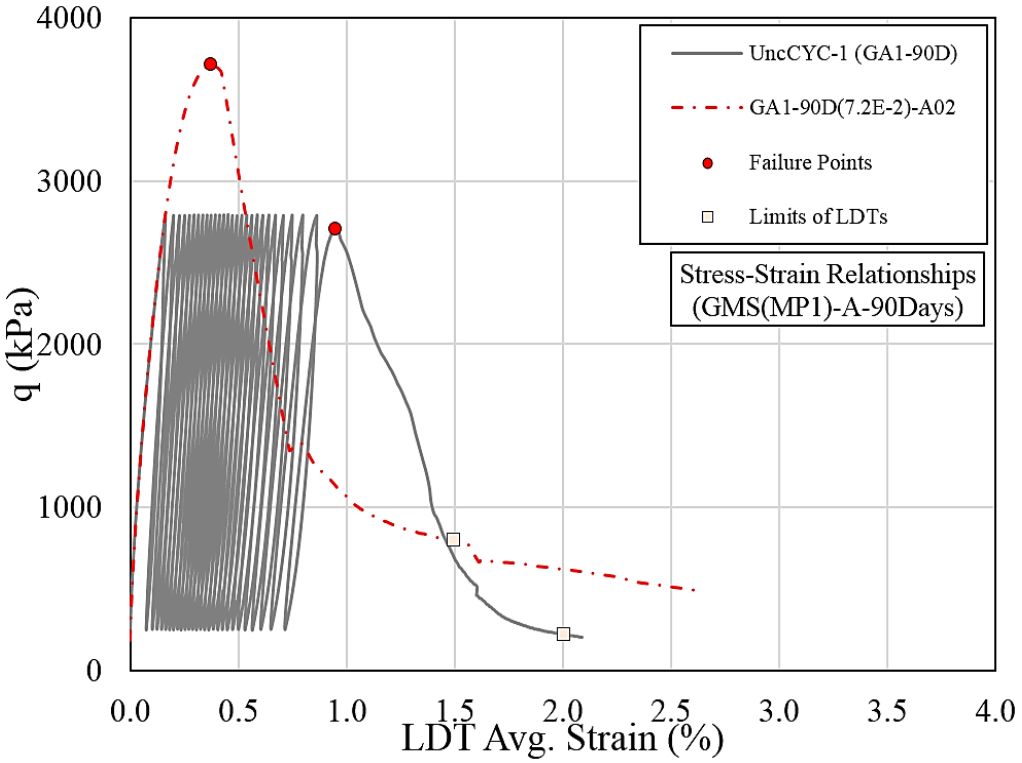

Fig. 6.4. Stress-strain relationships
UncCYC-1(GA1-90D), modified after [4]

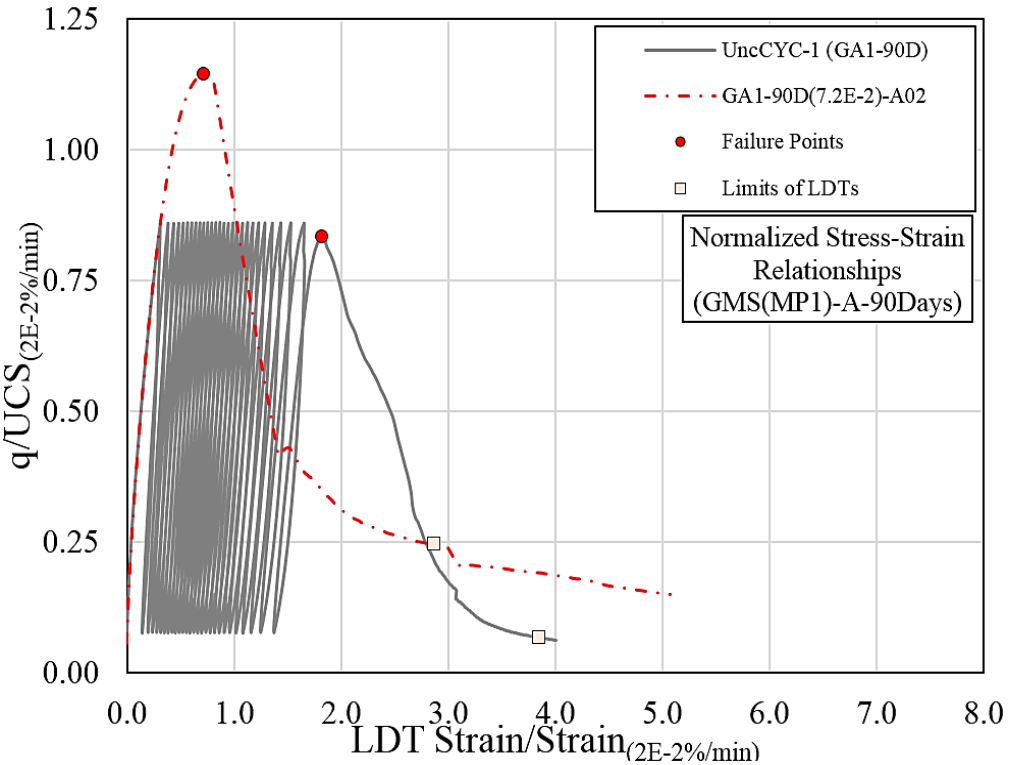

Fig. 6.5. Normalized stress-strain relationships
UncCYC-1(GA1-90D)

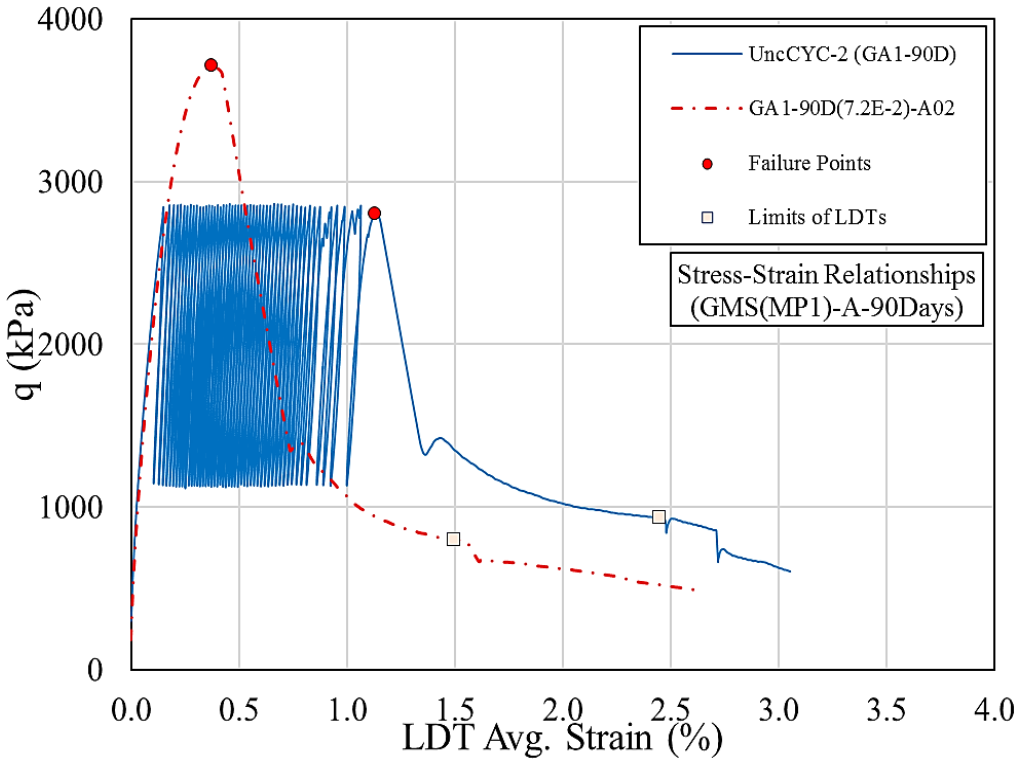

Fig. 6.6. Stress-strain relationships
UncCYC-2(GA1-90D), modified after [4]

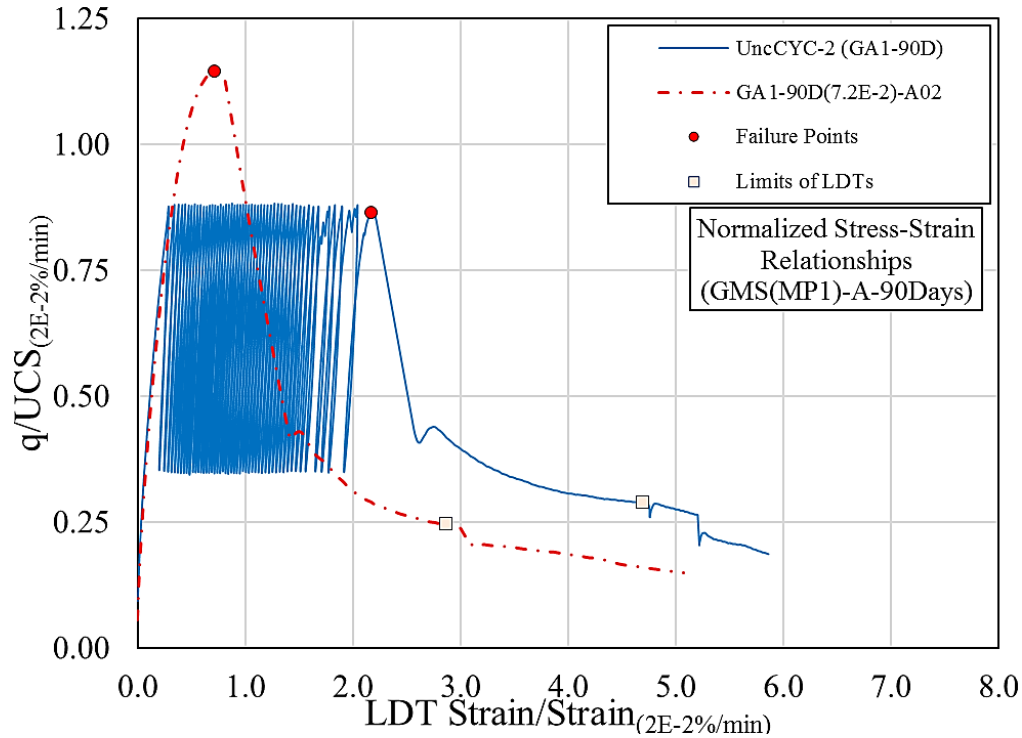

Fig. 6.7. Normalized stress-strain relationships
UncCYC-2(GA1-90D)

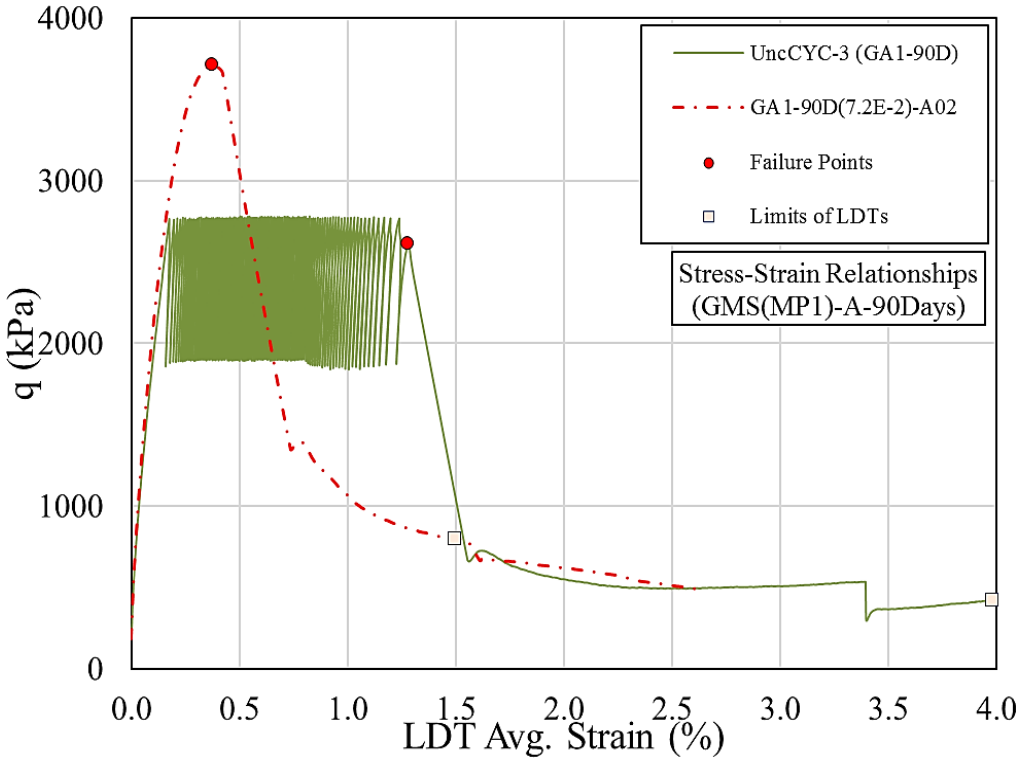

Fig. 6.8. Stress-strain relationships
UncCYC-3(GA1-90D), modified after [4]

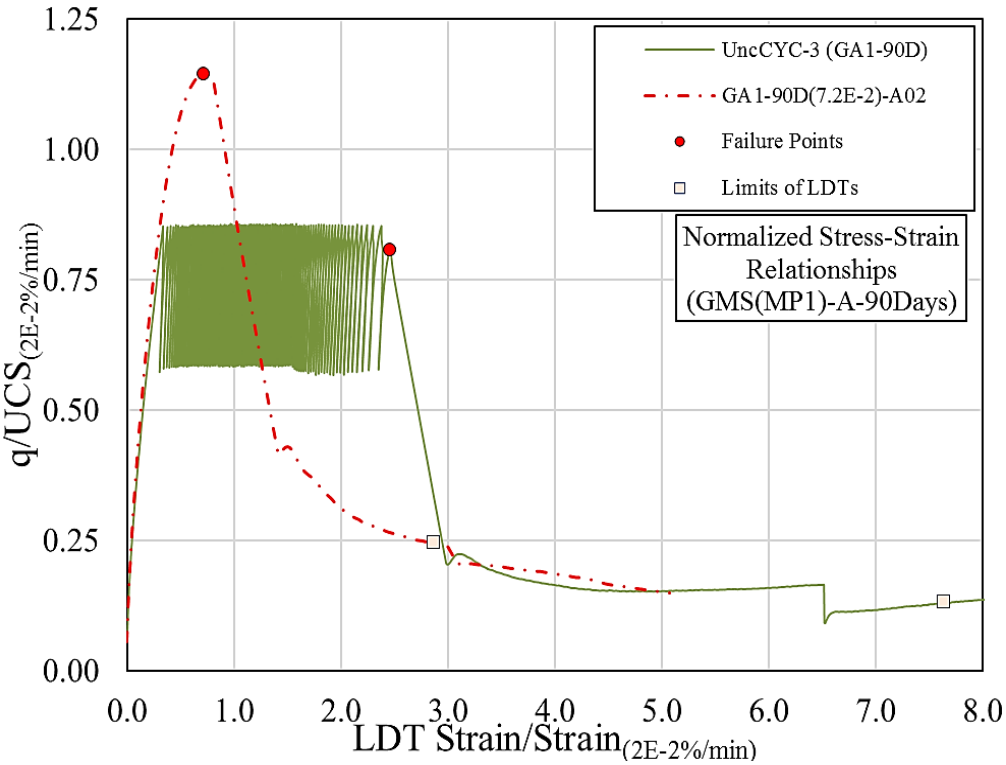

Fig. 6.9. Normalized stress-strain relationships
UncCYC-3(GA1-90D)

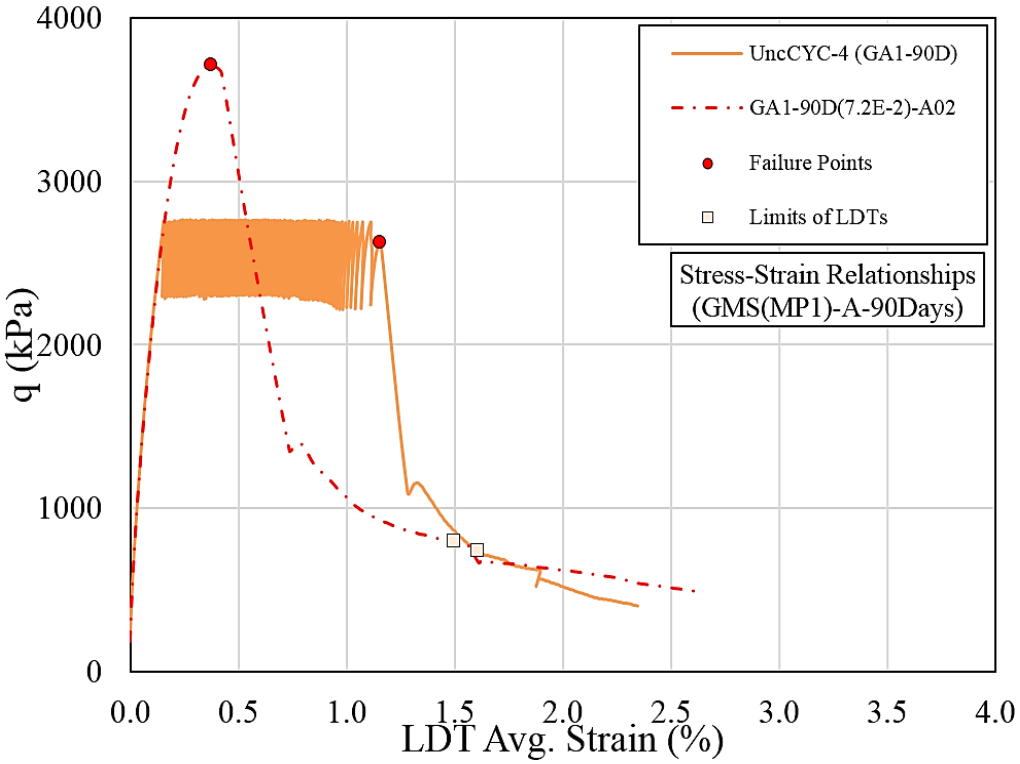

Fig. 6.10. Stress-strain relationships
UncCYC-4(GA1-90D), modified after [4]

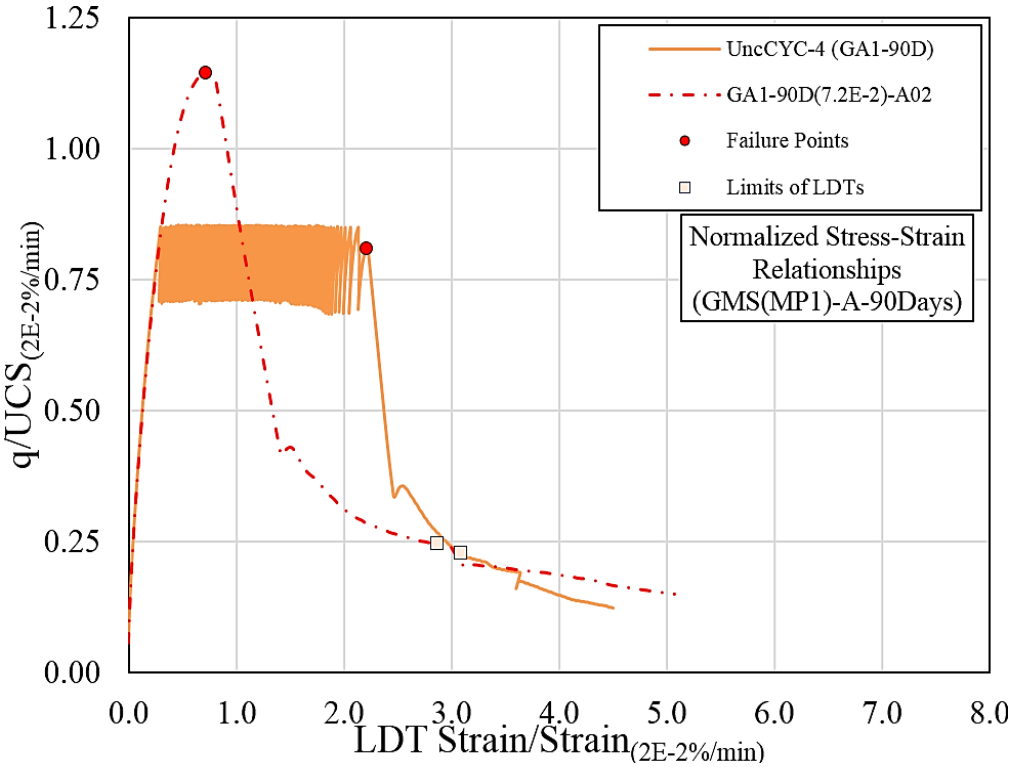

Fig. 6.11. Normalized stress-strain relationships
UncCYC-4(GA1-90D)

large-scale foundations. In general, the traditional conservative methodologies adopted by the practitioners often envisages whimsically large values of residual strain accumulation during seismic and creep loading, and ultimately results into uneconomical design of large-scale foundations. On the other hand, the residual deformations induced in sedimentary rocks supporting the large-scale foundations during seismic events were reported to be of limited extend. Therefore, comprehensive understanding of the tendency of axial strain accumulation during creep and cyclic loading is essential not only for cost-effective design solutions but also to comprehend the associated risk assessment [6, 7].

In an effort to examine the pattern of strain accumulation during creep and cyclic loading, the time histories of axial strain induced during cyclic and creep tests are plotted in Fig. 6.12. The values of axial strains corresponding to the maximum cyclic stress during cyclic loading were selected for analyzing the trends of axial strain accumulation. For both cyclic and creep tests, almost linear trend of axial strain accumulation with elapsed time was witnessed on full-logarithmic plot, followed by a rapid increase in axial strain values after the onset of failure [3], as evident in Fig. 6.12. Such a gradual trend of axial strain accumulation in silt-sandstone (of Kazusa Formation, Japan) was also observed under undrained cyclic loading [1].

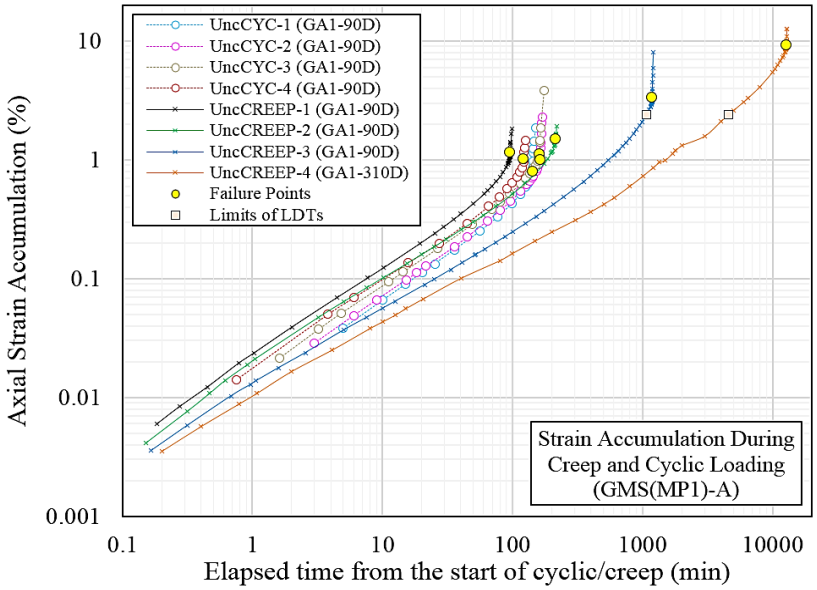

Fig. 6.12. Axial strain accumulation in GMS(MP1) during creep and cyclic loading, modified after [3]

As highlighted earlier in Section 6.3.2, the absolute value of total axial strain accumulation during cyclic loading is not greatly affected by the cyclic amplitude, and is

approximately comparable with the unconfined creep test performed at creep load equal to maximum cyclic stress, viz. UncCREEP-1(GA1-90D), as evident in Fig. 6.2. To rationally compare the trends of axial strain accumulation, normalized axial strain accumulation in GMS during cyclic and creep loading are plotted in Fig. 6.13 against the normalized elapsed time of cyclic and creep loading respectively. The plot clearly ascertain that the trends of axial strain accumulation during creep and cyclic loading are practically identical to each other, and the relationship between normalized axial strain and normalized elapsed time in the pre-failure zone can be approximated by the Eq. (6.3).

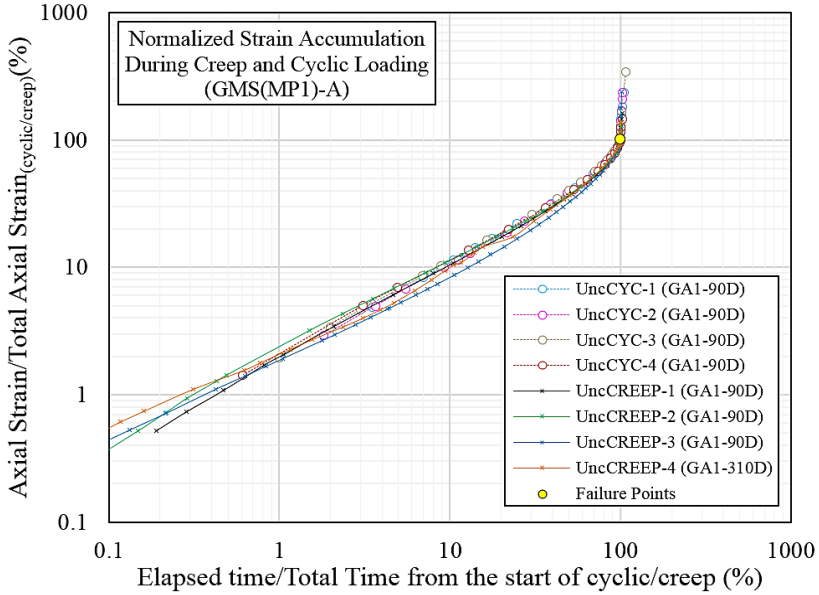

Fig. 6.13. Normalized strain accumulation in GMS(MP1) during creep and cyclic loading, modified after [3]

$$\varepsilon(t) = \alpha\, \varepsilon_f \left[\frac{t}{t_f}\right]^{\beta} \tag{6.3}$$

Where:

t = time at any instant

t_f = total time elapsed time at failure during creep/cyclic loading

$\varepsilon(t)$ = axial strain computed at time "t" (%)

ε_f = axial strain increment from the start of creep/cyclic loading till failure

α = 2.020 (constant)

β = 0.787 (constant)

The anticipated justification for the identical strain accumulation characteristics of GMS can be attributed to the intrinsic natures of different types of loading and viscous

behavior of GMS. In case of creep tests, the load is sustained at a particular axial stress level, and relatively ample time is available for the formation of micro cracks under this fixed value of axial stress. The time required for microcracking is also sufficient during cyclic loading as loading and unloading cycles applied during cyclic loading are restricted to a certain desired value of maximum cyclic stress, and no additional virgin loading is applied in a routine cyclic loading tests. Therefore, the axial strain accumulation pattern of GMS under creep and cyclic loading conditions are almost identical [3].

6.4 VARIATION OF INSTANTANEOUS STRAIN RATE IN GMS DURING CREEP AND CYCLIC LOADING

With an aim to systematically apprehend the effects of cyclic and creep loads on the strength and deformation characteristics of GMS, an approach of examining the role of ISR induced during cyclic and creep loading is envisaged. As a typical case, the pattern of variation of ISR induced during the last seven cycles of UncCYC-1(GA1-90D) are presented in Fig. 6.14., and the variation of axial stress is also plotted on the left vertical axis of this plot. It is evident from Fig. 6.14 that the ISR values fluctuate accordingly with the increase or decrease of axial stress during cyclic loading, and the maximum positive values of ISR are correspondent to the maximum cyclic stress applied during cyclic loading. Moreover, a rapid temporal increase of ISR was witnessed after the onset of failure [3], as shown in Fig. 6.14.

In the pre-failure zone, the trend of variation of maximum positive values of ISR during the cyclic loading is indicated by the red arrows in Fig. 6.14, and a gradual increase in the maximum positive ISR can be observed effusively prior to failure. The complete time histories of maximum positive values of ISR for all the cyclic loading tests are plotted on full-logarithmic scale, as shown in Fig. 6.15. In the beginning of cyclic loading, relatively higher values of maximum positive ISR were witnessed, followed by decreasing trend until a minimum threshold value. Afterwards, a relatively pronounced trend of increase in the maximum positive ISR was observed prior to the onset of failure. Such a pattern of variation of maximum values of ISR were observed for all the cyclic loading tests performed on GMS, and can be used as a tool to predict any anticipated failure of bounded geomaterials under cyclic loading. Additionally, relatively smaller values of maximum positive ISR were witnessed for specimens tested at smaller cyclic amplitudes [3], as evident in Fig. 6.15.

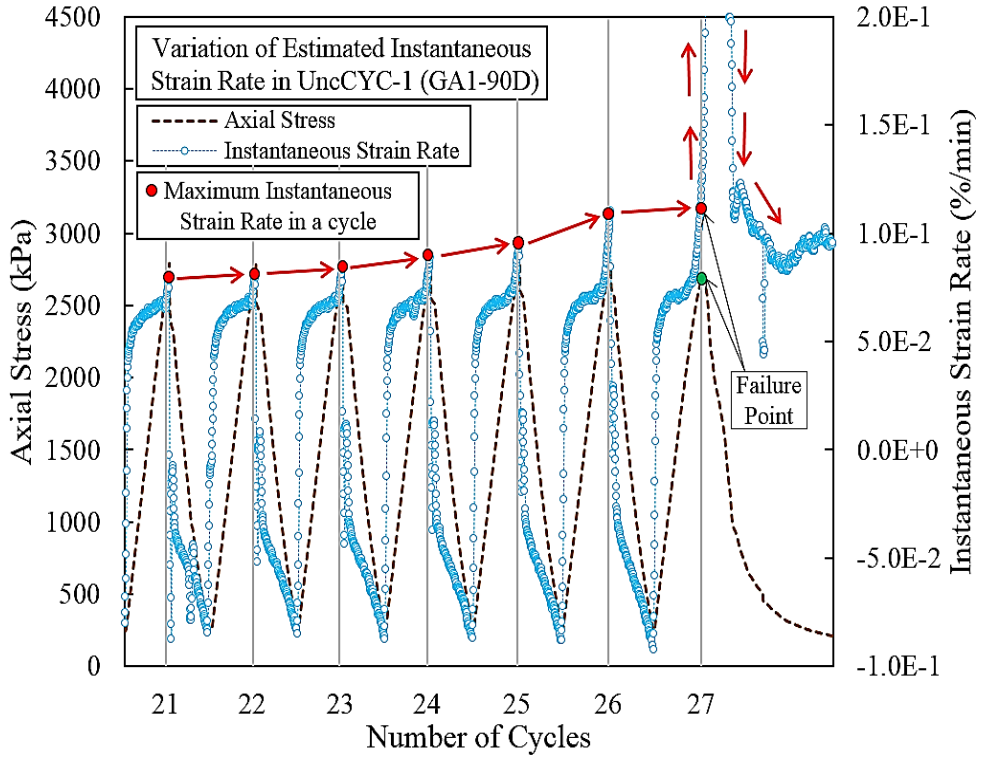

Fig. 6.14. Typical variation of Instantaneous Strain Rate (ISR) during cyclic loading, modified after [3]

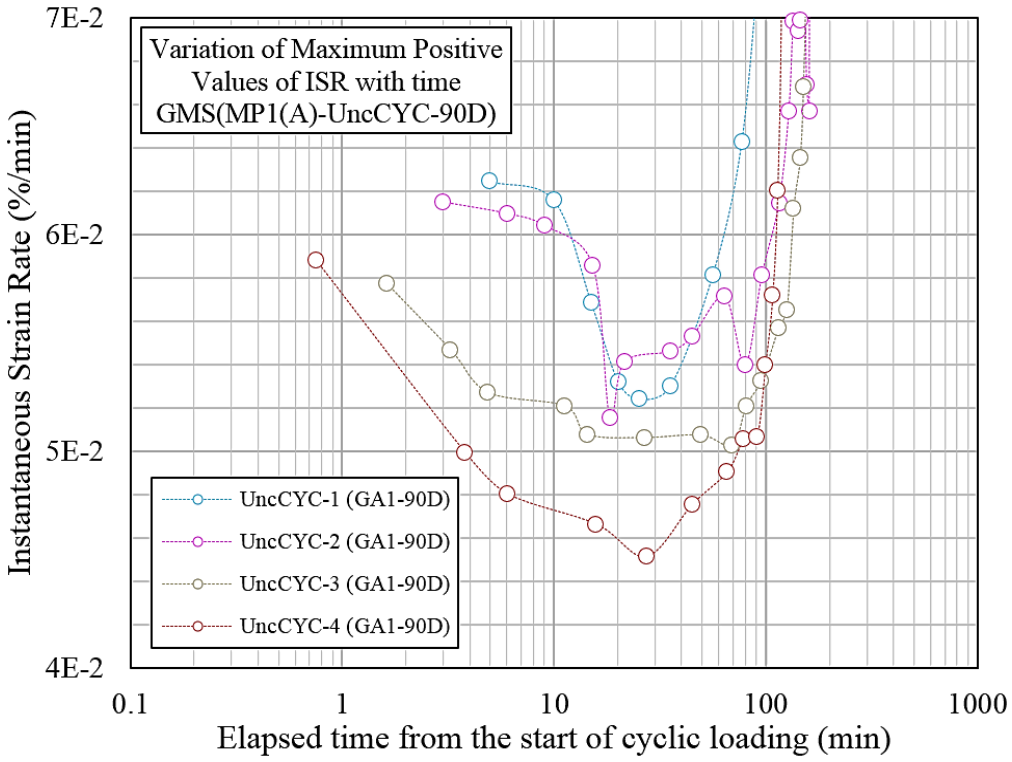

Fig. 6.15. Variation of maximum positive values of ISR for each cycle with elapsed time of cyclic loading, modified after [3]

The values of ISR induced during creep loading were estimated by adopting the similar approach, and their time histories are plotted in Fig. 6.16. The values of maximum positive ISR of cyclic loading tests are also superimposed in Fig. 6.16 for a comprehensible comparison. Although the maximum positive values of ISR induced during cyclic loading are relatively higher than their counterpart creep test performed at creep load approximately equal to maximum cyclic stress, viz. UncCREEP-1(GA1-90D); but the patterns of variation of ISR are almost identical [3]. Similar pattern of variation of ISR during consolidated drained creep conditions for sedimentary rocks [8]. Based on this plot it can be stated that the general patterns of variation of ISR of GMS during creep and cyclic loading are virtually similar. Nevertheless, during the earlier stages of creep loading, the magnitude of reduction in ISR values with time is relatively more perceptible for specimen tested at lower creep loads [3].

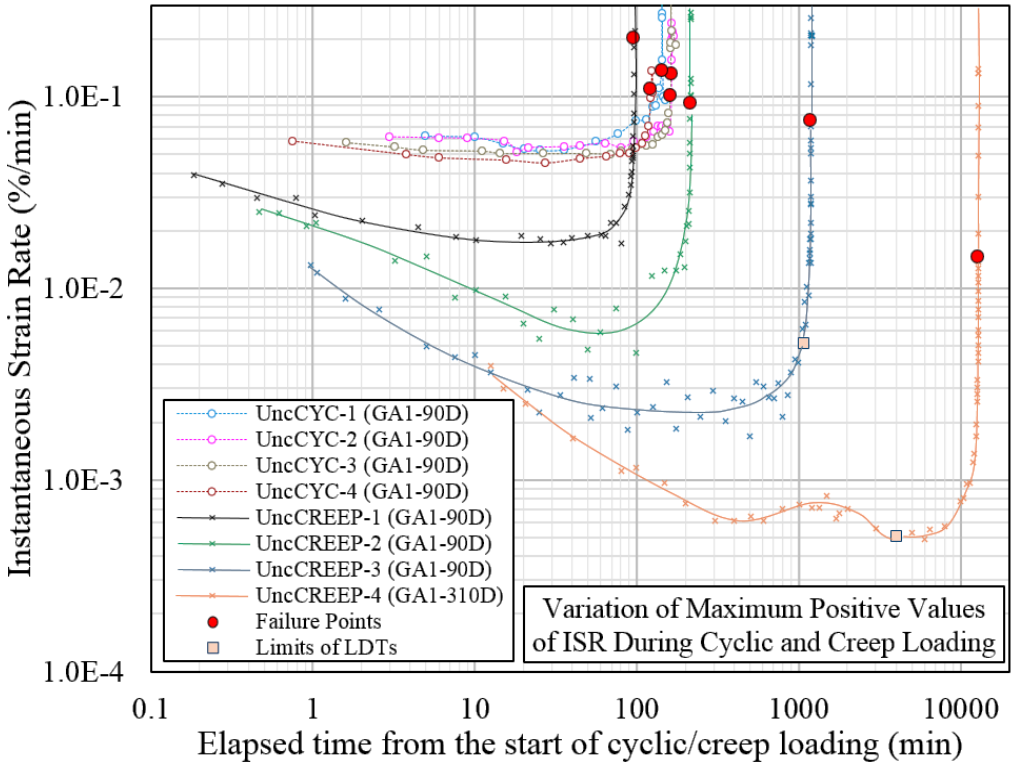

Fig. 6.16. Variation of maximum positive ISR during creep and cyclic loading with elapsed time, modified after [3]

It is also noteworthy the values of instantaneous strain rate at failure of all the cyclic loading tests are fairly comparable with each other, and no effects of cyclic amplitude are apparent on failure strain rates, as shown in Fig. 6.16. Conversely, the values of instantaneous strain rate at failure of specimens subjected to creep loading

decrease with the decrease of creep load, as evident in Fig. 6.16. The dependency of failure stress on the failure strain rates are summarized by plotting the relationships between normalized failure stress and instantaneous strain rate at failure of specimens tested under unconfined creep and cyclic loading. Additionally, the results of unconfined monotonic tests performed on specimens cured for 90 days are also presented in this plot for comparison purposes [3].

A unique relationship between the normalized failure stress and instantaneous failure strain rate of GMS specimens tested under unconfined creep and cyclic loading is clearly evident from Fig. 6.16, and reduction in normalized strength with the decrease of instantaneous strain rate is relatively larger in magnitude compared with the unconfined tests belonging to the corresponding zone of strain rate, viz. Zone-2. The results signify that the behavior of GMS under unconfined creep and cyclic loading conditions are similar to each other and distinctively different than unconfined monotonic tests [3].

The dependency of normalized failure strain on instantaneous loading rate for GMS tested under different loading conditions is presented in Fig. 6.17. The values of failure strain of specimen tested under creep and cyclic loading are consistent with each other, and are significantly higher than the unconfined monotonic tests belonging to Zone-2. In general, clear shear bands were observed for all the GMS specimens tested under unconfined cyclic and creep loading, as shown in Figures 6.19 and 6.20 respectively [3]. However, visible bulging was also observed for UncCREEP-4(GA1-310D) prior to the formation of shear band, as shown in Fig. 6.20(c).

This distinctive behavior of GMS under unconfined creep and cyclic loading conditions can be linked with the micromechanical particularities [9-11] (viscous characteristics) of GMS under different loading conditions, highlighted earlier in Section 5.3 of Chapter No. 5. These results presented in Fig. 6.17 suggest that the process of microcracking within GMS specimens under creep and cyclic loading is relatively enhanced possibly due to the highly viscosity of GMS linked with the porous hardened mass comprising of dihydrate needled-shaped crystals [12-14]. During creep and cyclic loading, the maximum stress applied to the GMS specimen is restricted to a fixed value, and no additional virgin load was further applied on GMS specimen. Therefore, the axial strains accumulate significantly due to the as ample time was available for the formation of micro cracks prior to any additional increment of axial loading. As a result the

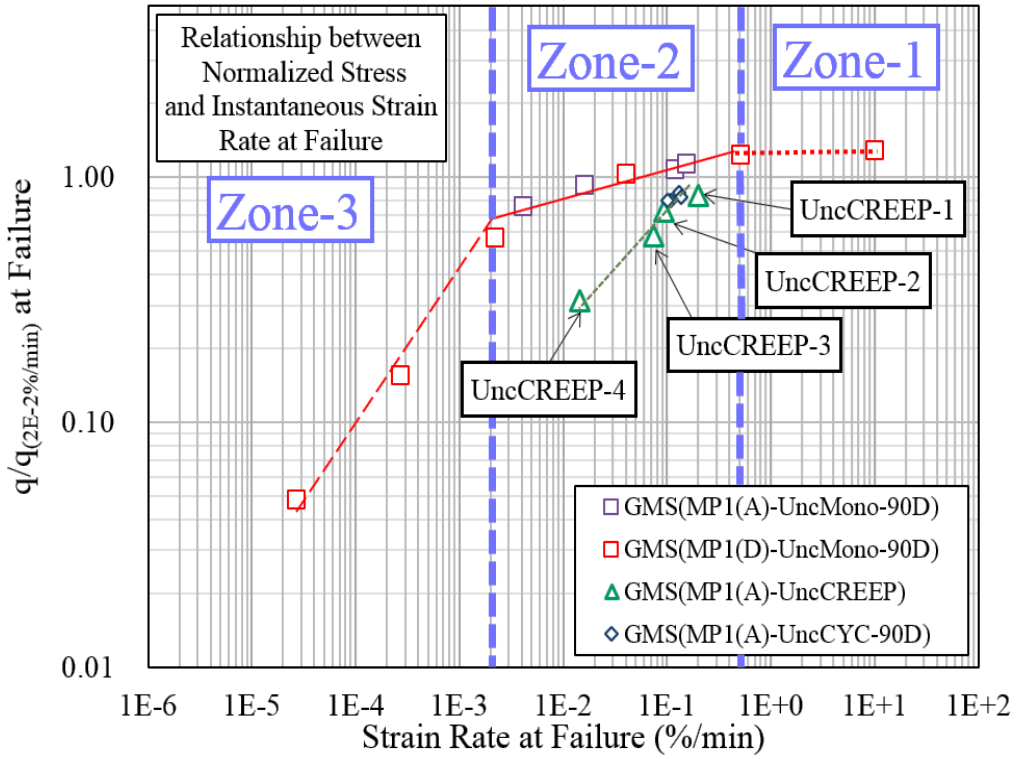

Fig. 6.17. Relationship between normalized failure stress and instantaneous failure strain rate of GMS under creep, cyclic and monotonic loading, modified after [2]

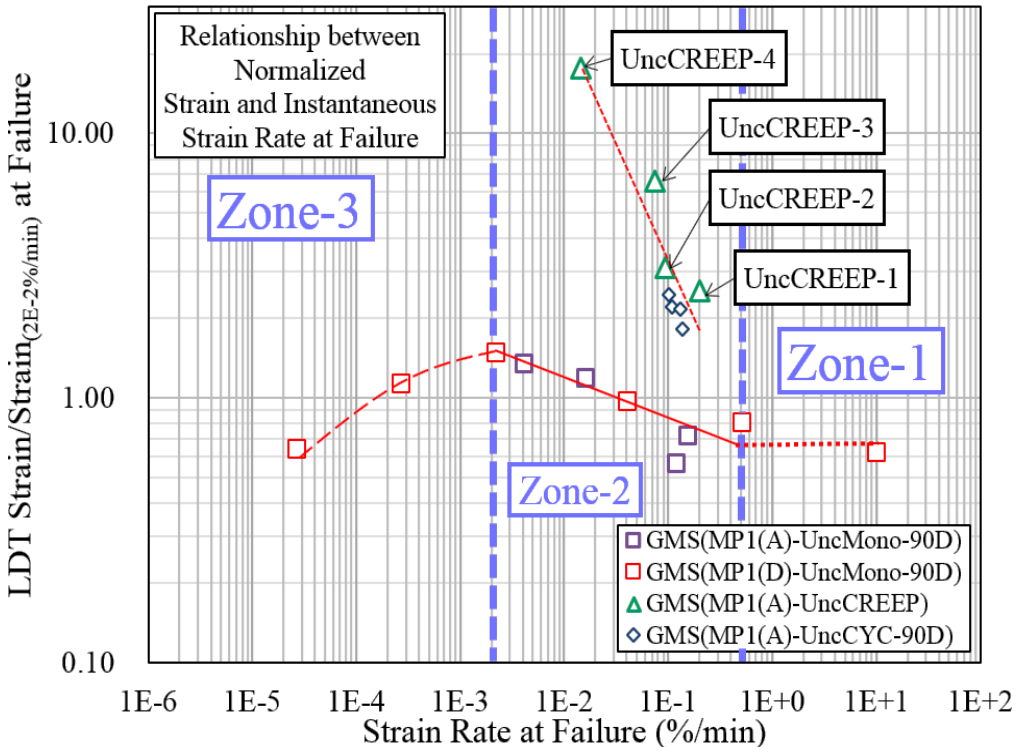

Fig. 6.18. Relationship between normalized failure strain and instantaneous failure strain rate of GMS under creep, cyclic and monotonic loading, modified after [2]

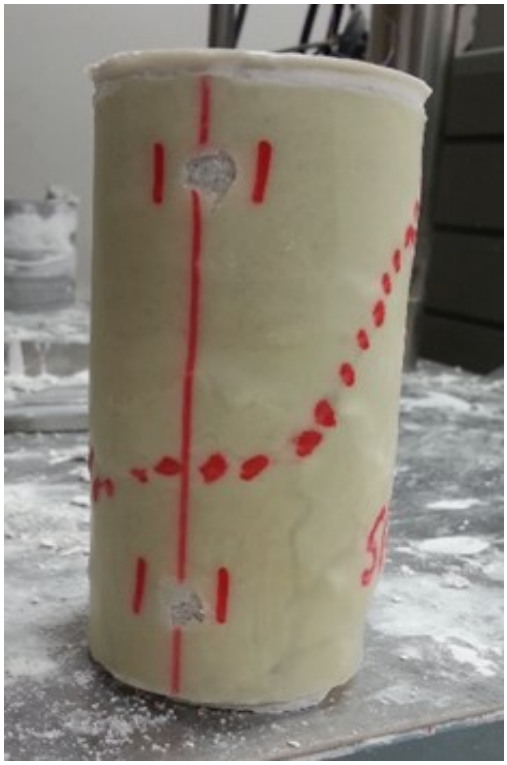

(a) UncCYC-1(GA1-90D)

(b) UncCYC-2(GA1-90D)

(c) UncCYC-3 (GA1-90D)

(d) UncCYC-4 (GA1-90D)

Fig. 6.19. Failure pattern of GMS(MP1(A)-UncCYC-90D) specimens [4]

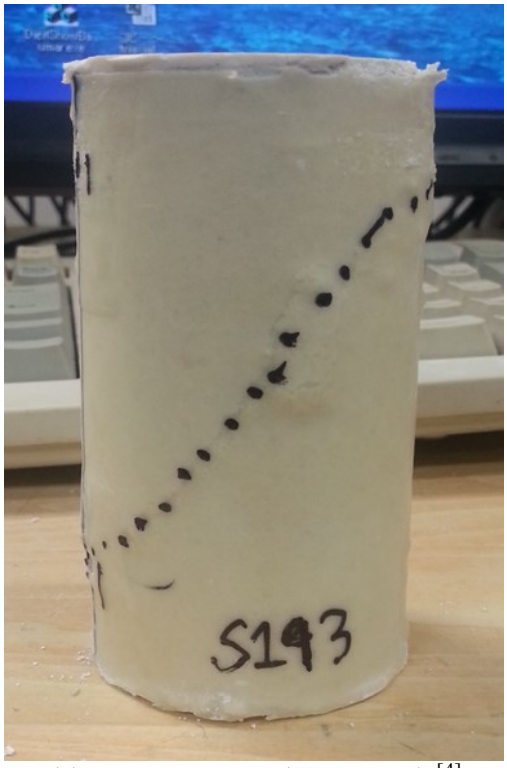

(a) UncCREEP-1 (GA1-90D) [4]

(b) UncCREEP-2 (GA1-90D) [4]

(c) UncCREEP-4 (GA1-310D)

Fig. 6.20. Failure pattern of GMS(MP1(A)-UncCREEP) specimens

hysteresis between microcracking and increment of loading [9-11] is relatively lesser during creep and cyclic loading compared with monotonic loading, as a results specimen failed under relatively lesser normalized stress due to the larger damage to the microstructure of GMS.

Owing to the intrinsic nature of monotonic loading, the successive increments of axial stress applied to the GMS specimens belonging to Zone-2 are relatively rapid compared with the specimens tested under creep and cyclic loading. At higher rate of incremental loading, the hysteresis between the formation of micro cracks in GMS and corresponding incremental loads increases, and relatively larger proportion of total strain energy absorbed by the specimen is stored as elastic strain energy. This results into strengthening of specimen, and energy dissipated in the formation of micro cracks is relatively lesser [9-11]. Therefore, normalized strength values at a particular instantaneous failure strain of unconfined monotonic tests are relatively higher than creep and cyclic loading tests.

6.5 BEHAVIOR OF CTS UNDER UNCONFINED CREEP

A total of three unconfined creep tests were conducted on CTS specimens cured for 28 days, and the specimens were loaded monotonically at an average strain rate of 1.5E-2 %/min to achieve the targeted creep load. The results of these unconfined creep tests are shown in Table 6.3, and stress-strain and normalized stress-strain relationships of these specimens are presented in Figures 6.21 and 6.22 respectively.

Table 6.3. Test Results of CTS(MP1(A)-UncCREEP-28D)

Machine Type	Series ID	Test ID	Bulk Unit Weight Before Testing	Moisture Content After Testing	Avg. Creep Load	q at Failure	Normalized Creep Load at Failure ($q/UCS_{(2E\text{-}2\%/min)}$)	LDT Failure Strain	Failure Time
			(kN/m^3)	(%)	(kPa)	(kPa)		(%)	(min)
TCM**	CTS(MP1(A)-UncCREEP-28D)	UncCREEP-1 (CA1-28D)	18.1	30.6	3730	3720	0.95	0.458	23
		UncCREEP-2 (CA1-28D)	17.9	31.3	3530	3527	0.90	0.514	58
		UncCREEP-3 (CA1-28D)	17.9	20.7	2950	No failure was observed under creep load sustained for 45 days			

** Triaxial Compression Machine

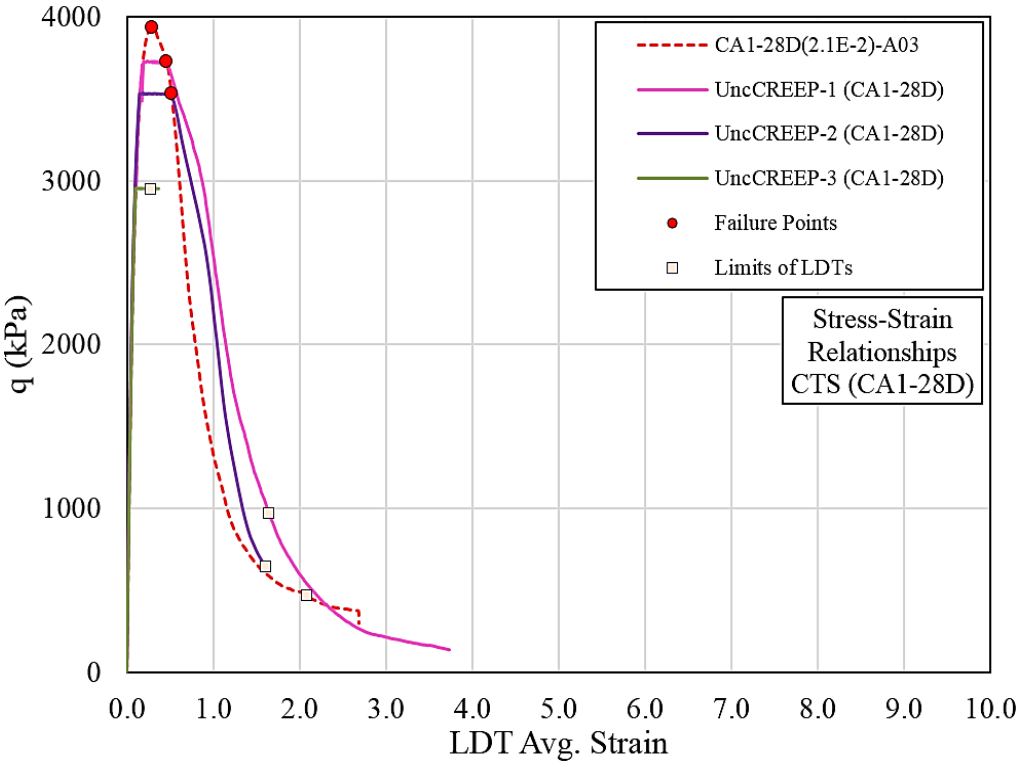

Fig. 6.21. Stress-strain relationships CTS(MP1(A)-UncCREEP-28D)

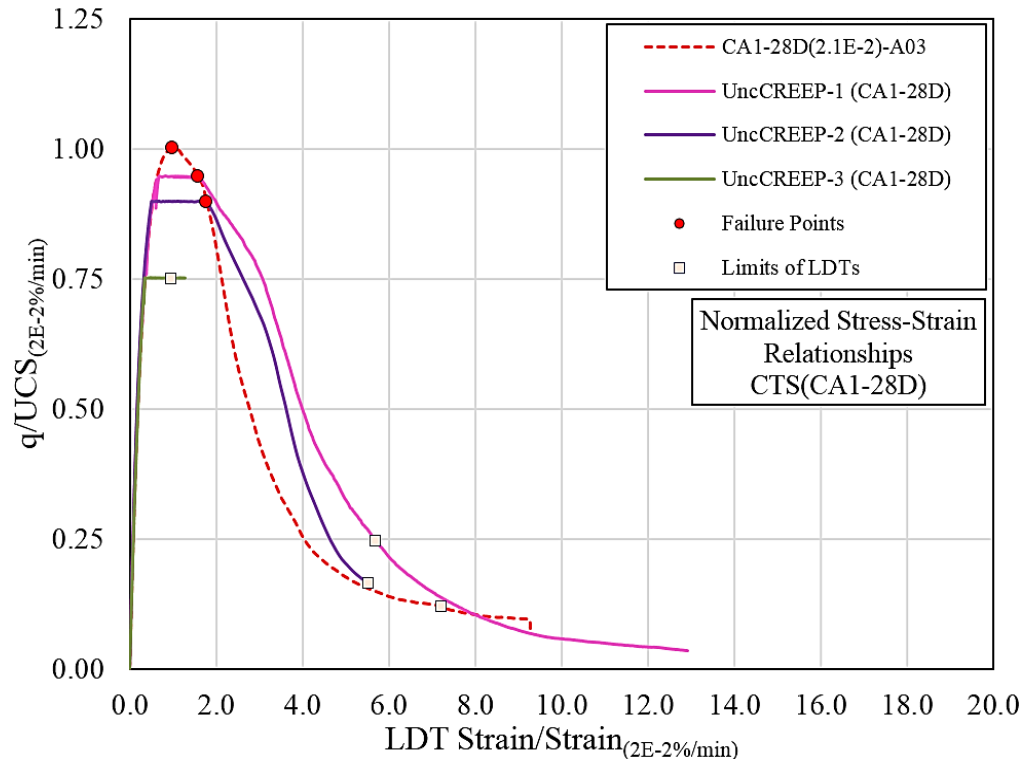

Fig. 6.22. Normalized stress-strain relationships CTS(MP1(A)-UncCREEP-28D)

Based on these results, it can be stated that the performance of CTS under unconfined creep loading conditions is considerably superior to GMS. For instance, UncCREEP-2(GA1-90D) failed under a normalized creep load of 73% within 4 hours (217 minutes), as shown in Table 6.1, whereas no creep induced failure was observed in UncCREEP-3(CA1-28D) up till 45 days under about equivalent normalized creep load, as mentioned in Table 6.3. Keeping in view the stipulated research duration, it deemed practically non-viable to further conduct creep tests on CTS at normalized creep load lesser than 75% due to the large amount of time required to witness creep induced failure.

The time histories of axial strain accumulation and instantaneous axial strain rates of CTS and GMS specimens under unconfined creep loading are compared in Figures 6.23 and 6.24. Owing to extremely slower rate of axial strain accumulation in UncCREEP-3(CA1-28D) at later stages of creep, viz. strain rates lesser than 1.0E-5 %/min, undesirable fluctuations in axial strain measurements were conquered, and the axial strain data of UncCREEP-3(CA1-28D) was filtered using adjacent-average filter [15] prior to the estimation of instantaneous strain rates. It is also worth highlighting that the creep induced axial strains are relatively lesser in CTS compared with GMS, as evident in Fig. 6.23. This aspect can be linked with the differences in the loading rate dependency (viscous behavior) of these artificially bounded geomaterials. As discussed earlier in Chapter No. 5, the loading rate dependency of CTS is fairly lesser than that of GMS, as a result the viscous deformations during sustained loading in CTS are also relatively smaller.

In spite of the fact that the instantaneous strain rates induced during creep in CTS specimens are noticeably lesser than GMS specimens subjected to equivalent normalized loads, but the trends of variation of instantaneous strain rate in both CTS and GMS are quite identical, as evident in Fig. 6.24. In case of UncCREEP-3(CA1-28D), the instantaneous strain rate markedly reduced to about 2.0E-6 %/min. during the initial 15 days, and remained approximately unchanged for further 30 days under sustained loading. Contrarily, GMS specimen tested under equivalent normalized creep load, viz. UncCREEP-3(GA1-90D) failed at quite higher value of instantaneous strain rate of about 1.0E-2 %/min, as shown in Fig. 6.24.

The effects of loading rate on the normalized failure strength and axial strain of CTS and GMS under unconfined creep loading are compared in Figures 6.25 and 6.26.

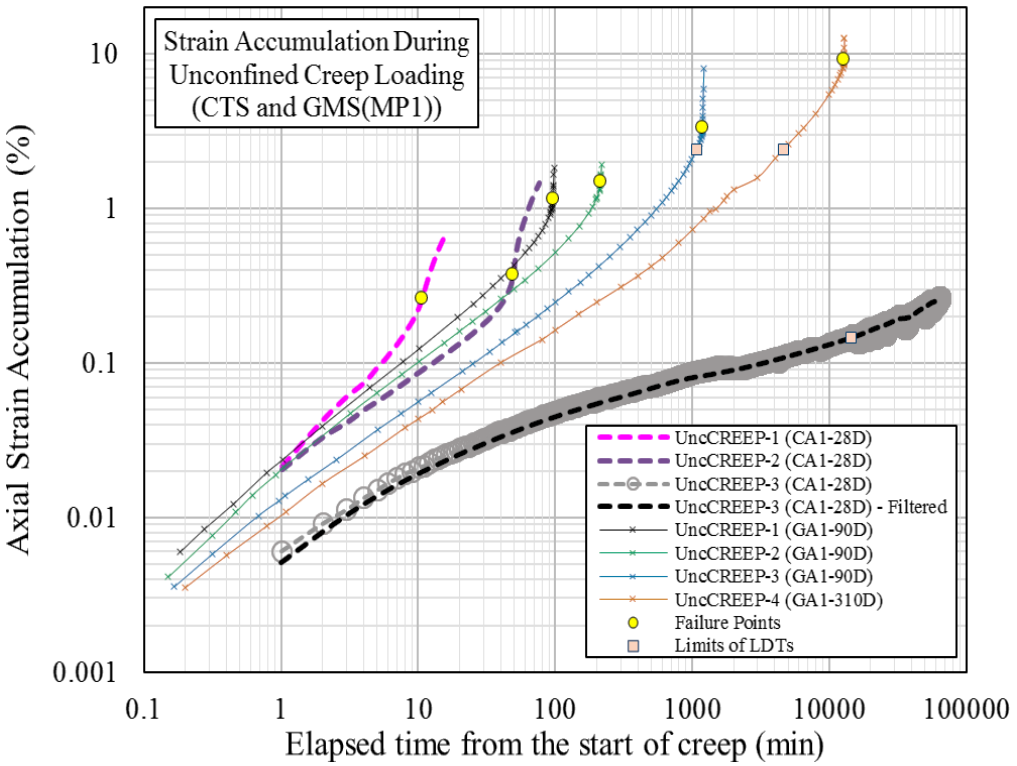

Fig. 6.23. Axial strain accumulation in GMS and CTS during unconfined creep and cyclic loading

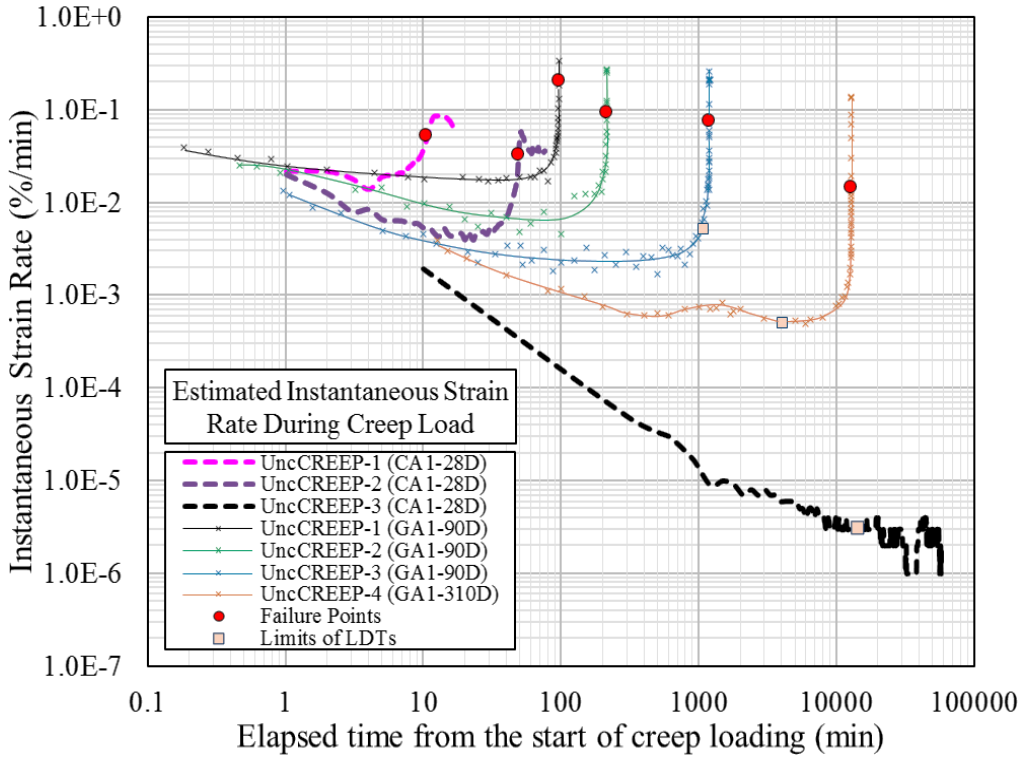

Fig. 6.24. Variation of instantaneous strain rate during unconfined creep loading with elapsed time

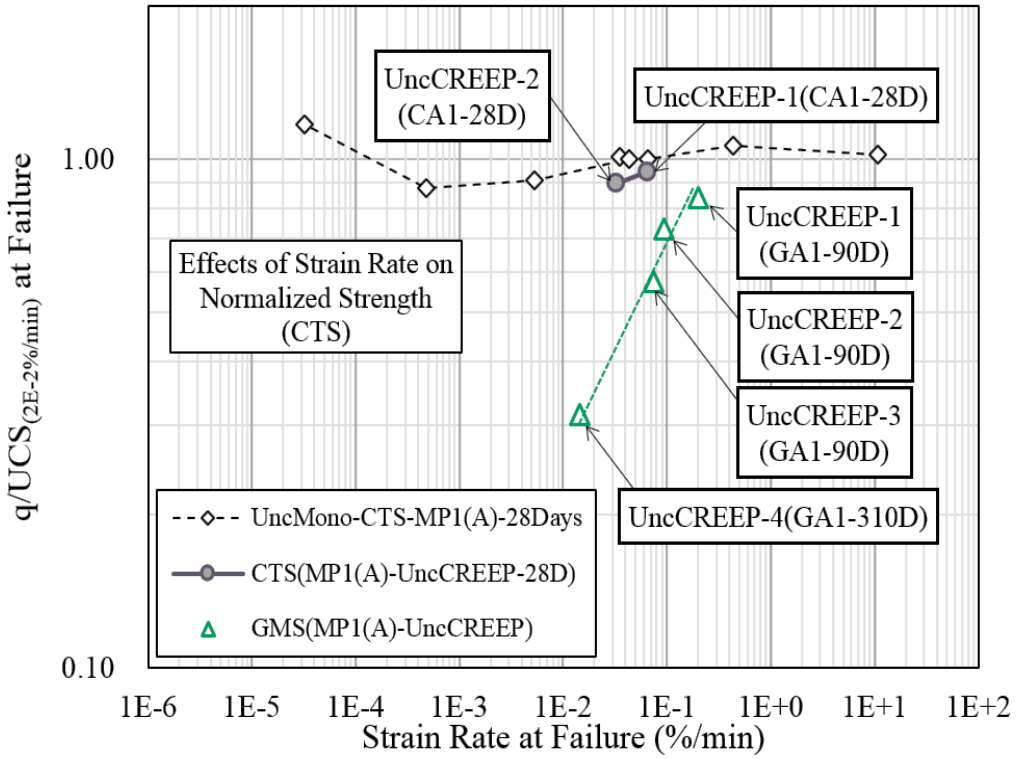

Fig. 6.25. Relationship between normalized failure stress and instantaneous failure strain rate of GMS and CTS under unconfined creep loading

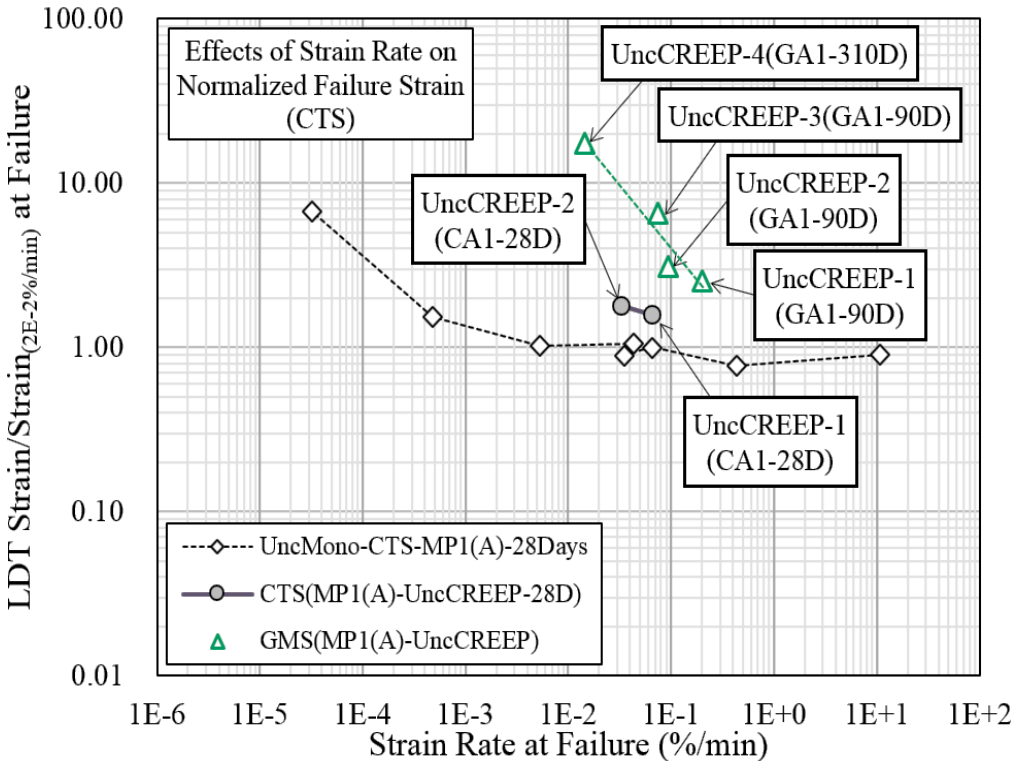

Fig. 6.26. Relationship between normalized failure strain and instantaneous failure strain rate of GMS and CTS under unconfined creep loading

Although the results of unconfined creep tests of CTS are limited, but the effects of loading rate on the normalized strength of CTS under creep loading are very inferior compared to that of GMS, as evident in Fig. 6.26. Similar conclusion can also be drawn for normalized axial failure strains, as effects of loading rate on these values are also relatively limited, as shown in Fig. 6.26. Moreover, clear and distinct shear band were witnessed for CTS specimens tested at normalized creep load higher than 90%, as shown in Fig. 6.27, and no visible shear band or cracks band were observed for UncCREEP-3(CA1-28D) on visual inspection.

(a) UncCREEP-1(CA1-28D) (b) UncCREEP-2(CA1-28D)

Fig. 6.27. Failure pattern of CTS(MP1(A)-UncCREEP-28D) specimens

6.6 SUMMARY OF FINDINGS

- The Behavior of GMS(MP1) under unconfined creep loading is very unpromising, as a small normalized creep load of mere 32% is sufficient enough to cause a creep failure within a relatively shorter duration of time, viz. about 9 days.
- An increasing trend of axial strain accumulation with the decrease of creep load was witnessed, and an axial strain accumulation of 9.157% was observed for GMS specimen tested at normalized creep load of 32%.

- In case of GMS(MP1), the number of cycles required to trigger failure under unconfined cyclic loading conditions increase significantly with the decrease of cyclic amplitude. Irrespective of the number of cycles required to trigger failure, the effects of cyclic amplitude on axial strain accumulation during cyclic loading are also quite marginal, as the values of failure strains are generally approximately similar in different tests. In general, the failure strain of specimens failed under cyclic loading showed failure strain of roughly 2.2~2.4 times of their counterpart unconfined monotonic tests.
- The results of unconfined creep and cyclic loading tests indicated that the values of failure strain in cyclic and creep tests are principally governed by the maximum compressive stress induced during cyclic and creep loading respectively.
- For both cyclic and creep tests, almost linear trend of axial strain accumulation with elapsed time was witnessed on full-logarithmic plot, followed by a rapid increase in axial strain values after the onset of failure. Moreover, the trends of axial strain accumulation during creep and cyclic loading are practically identical to each other. The anticipated justification for the identical strain accumulation characteristics of GMS was attributed to the intrinsic natures of different types of loading and viscous behavior of GMS.
- In case of cyclic loading tests on GMS, The values of instantaneous strain rate fluctuate accordingly with the increase or decrease of axial stress during cyclic loading, and the maximum positive values of ISR are correspondent to the maximum cyclic stress applied during cyclic loading.
- In the beginning of cyclic loading, relatively higher values of maximum positive ISR were witnessed, followed by decreasing trend until a minimum threshold value. Afterwards, a relatively pronounced trend of increase in the maximum positive instantaneous strain rate was observed prior to the onset of failure. The values of instantaneous strain rate at failure of all the cyclic loading tests are fairly comparable with each other, and no effects of cyclic amplitude are apparent on failure strain rates Moreover, the general patterns

of variation of instantaneous strain rate of GMS during creep and cyclic loading were virtually similar.

- A unique relationship between the normalized failure stress and instantaneous failure strain rate of GMS specimens tested under unconfined creep and cyclic loading, and the behavior of GMS under unconfined creep and cyclic loading conditions are similar to each other and distinctively different than unconfined monotonic tests.
- The values of failure strain of specimen tested under creep and cyclic loading were consistent with each other, and were significantly higher than the unconfined monotonic tests belonging to Zone-2. This distinctive behavior of GMS under unconfined creep and cyclic loading conditions was potentially linked with the micromechanical particularities (viscous characteristics) of GMS under different loading conditions.
- The performance of CTS under unconfined creep loading conditions was found to be considerably superior to GMS, as no creep induced failure was observed in CTS specimen up till 45 days under about normalized creep load of 75%.
- The creep induced axial strain accumulation was relatively lesser in CTS compared with GMS. Moreover, instantaneous strain rates induced during creep in CTS specimens were noticeably lesser than the GMS specimens subjected to equivalent normalized loads, but the trends of variation of instantaneous strain rate in both CTS and GMS were quite identical.
- Based on the results of CTS specimens tested under unconfined creep tests, effects of loading rate on the normalized strength and normalized axial strain accumulation in CTS specimens under creep loading are very inferior compared to that of GMS.

6.7 REFRENCES

1. Koseki, J., Indou, H. and Hayano, K. (2003), “Cyclic triaxial tests on residual deformation and small strain properties of soft rocks”, *Proceedings of Deformation Characteristics of Geomaterials*, 247-255.

2. Koseki, J., Salas-Monge, R., & Sato, T. (2003), "Plane strain compression tests on cement-treated sands," Proceedings of the First Japan-US Workshop on Testing, Modeling, and Simulation, American Society of Civil Engineers, 429-443.

3. Maqsood, Z. and Koseki J. (2019), "Strength and deformation characteristics of bounded geomaterials under creep and cyclic loading considering loading rate effects", *15th International Conference on Geotechnical Engineering*, Pakistan. (submitted)

4. Maqsood, Z. (2016), "Behaviour of gypsum mixed sand under unconfined monotonic and cyclic loading conditions," *Masters Thesis*, *The University of Tokyo,* Japan.

5. Maqsood, Z. and Koseki, J. (2017), "Effects of loading rate on the behaviour of Gypsum Mixed Sand", *The 19th International Summer Symposium, JSCE*, Japan.

6. Yamagata, M., Yasuda, M., Nitta, A., and Yamamoto, S. (1996), "Effects on the Akashi Kaikyo bridge," *Soils and Foundations*, **36**(Special), 179-187.

7. Namikawa, K., Terashima, Y., Inoue, T., Koseki, J., Miyashita, Y., and Matsumoto, M. (2016), "Construction of Expressway Branch Junction Structure Using Non-Cut-and-Cover Enlargement Method to Combine Two Shield Tunnels in Sedimentary Soft Rock," *Proceedings of the World Tunnel Conference 2016*, 558-568.

8. Miyashita, Y., Koseki, J., Namikawa, K., and Matsumoto, M. (2015), "Study on viscous property of sedimentary soft rock in drained triaxial and unconfined compression tests," *Deformation Characteristics of Geomaterials: Proceedings of the 6th International Symposium on Deformation Characteristics of Geomaterials*, **6**, 575-58.

9. Mahanta, B., Singh, T. N., Ranjith, P. G. and Vishal, V. (2018), "Experimental investigation of the influence of strain rate on strength; failure attributes and mechanism of Jhiri shale," *Journal of Natural Gas Science and Engineering*, **58**, 178-188.

10. Liang, C., Wu, S., Li, X. and Xin, P. (2015), "Effects of strain rate on fracture characteristics and mesoscopic failure mechanisms of granite," *International Journal of Rock Mechanics and Mining Sciences*, **76**, 146-154.

11. Liang, W. G., Zhao, Y. S., Xu, S. G. and Dusseault, M. B. (2011), "Effect of strain rate on the mechanical properties of salt rock," *International Journal of Rock Mechanics and Mining Sciences*, **1(48)**, 161-167.

12. Singh, N. B. and Middendorf, B. (2007), "Calcium sulphate hemihydrate hydration leading to gypsum crystallization," *Progress in crystal growth and characterization of materials*, **53(1)**, 57-77.

13. Lewry, A. J. and Williamson, J. (1994), "The setting of gypsum plaster - Part I The hydration of calcium sulphate hemihydrate," *Journal of Materials Science*, **29(21)**, 5279-5284

14. Lewry, A. J. and Williamson, J. (1994), "The setting of gypsum plaster - Part II The development of microstructure and strength," *Journal of Materials Science*. **29(21)**, 5524-5528.

15. Origin Lab® (2019), The adjacent-averaging method, https://www.originlab.com/doc/Origin-Help/Smooth-Algorithm cited at July 9, 2019.

LOADING RATE DEPENDENCY OF GMS UNDER TRIAXIAL MONOTONIC LOADING

7.1 PREAMBLE

The results of unconfined monotonic tests undoubtedly underlined the significant dependency of strength and deformation behavior of GMS on loading rate. However, the in-situ stress conditions are typically well-apprehended in triaxial loading testing [1], and it is lucrative to examine the combined effects of loading rate and confining stress on the mechanical behavior of GMS. In the present chapter, the loading rate dependency of GMS was evaluated at different confining stress levels, and the results are compared with monotonic loading tests. The effects of duration of drained isotropic consolidation on the behavior of GMS are highlighted. Additionally, the shear strength parameters [2], viz. cohesion (c) and angle of internal friction (ϕ), of GMS were evaluated, and their dependency on loading rate is discussed. Finally, the relationships between normalized strength and normalized confining stress at different strain rates are proposed to unswervingly quantify the combined effects of loading rate and confining stress on GMS.

7.2 TESTING PROCEDURE

In general, the procedure stated in Section 4.3 of Chapter No, 4 was followed, along with some additional steps to conduct triaxial monotonic tests. Owing to the fact that capping was applied to the top and bottom edges of specimens, anticipated drainage was ensured by attaching a grid-shaped filter paper on the surface of specimen, as shown in Fig. 7.1. Moreover, the filter paper was connected to the sides of top cap and bottom pedestal of triaxial compression machine, and the drainage lines were saturated prior to the start of test [3], as shown in Fig. 7.1. The membrane used to cover specimens was sealed from top and bottom using vacuum grease to eradicate possible leakage. In order

to avoid any likely chemical changes, no saturation of GMS specimens were done prior to the testing, and the specimens were tested at their natural water content.

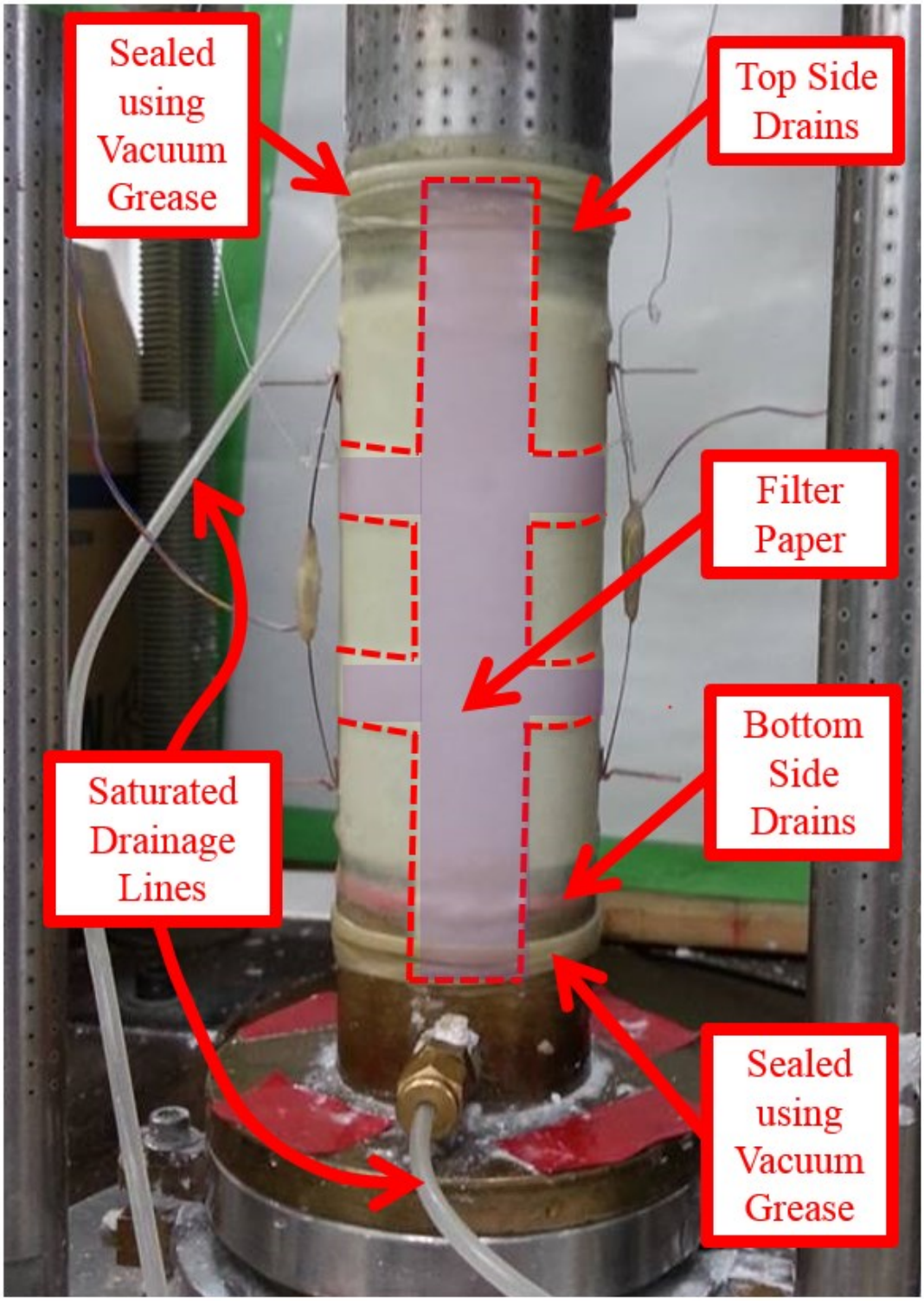

Fig. 7.1. Illustration of GMS specimen subjected to triaxial monotonic testing

In the present study, the loading conditions during a typical consolidated drained triaxial monotonic test can be divided into three stages, as illustrated in Fig. 7.2. The drainage valves were kept open throughout all these three stages to dissipate any pore-pressure induced within the specimen. During the first stage, the confining stress was increased isotopically to the targeted confining stress at a rate of about 5 kPa/min. Afterwards, the specimen was isotopically consolidated for a desired amount of time, labelled as Stage-2 in Fig. 7.2. Finally, drained monotonic loading was applied at a targeted strain rate, and the confining stress was kept constant throughout this stage. As a precautionary measure to avoid any possible breakage of bonding between the specimen and capping [4] during automated prompt shaft movement to adjust the axial load, a small deviator stress of 10 kPa was applied on the specimen during the first two stages.

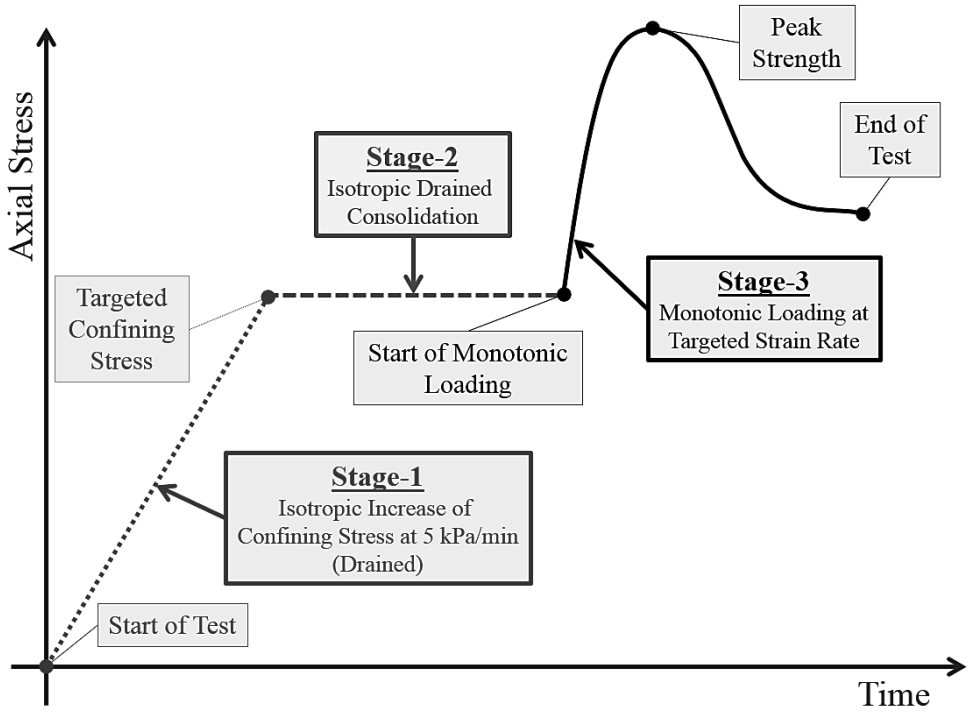

Fig. 7.2. Schematic Illustration of different loading conditions during a typical consolidated drained triaxial monotonic test on GMS

7.3 EFFECTS OF ISOTROPIC CONSOLIDATION DURATION ON THE MECHANICAL BEHAVIOR OF GMS

In an effort to select an appropriate duration of isotropic consolidation (Stage-2) for the evaluation of loading rate dependency of GMS at different confining stress, it was deemed necessary to study the effects of isotropic consolidation duration on the strength

and deformation behavior of GMS. A series of consolidated drained triaxial tests having different durations of isotropic consolidation were performed on GMS, and the results are presented in Table 7.1. The targeted confining stress of all of these tests was kept as 800 kPa, and an average strain rate of about 2.2E-02 %/min was opted for the drained monotonic loading.

Table 7.1. Test results of GMS(MP1(D)-800CDMono-3D)

Series & Batch ID	Test ID	Bulk Unit Weight Before Testing	Moisture Content After Testing	Average Strain Rate During Monotonic Loading	Confining Stress (σ_3)	Duration of Isotropic Consolidation	q at Failure (σ_1-σ_3)	Pore Pressure at Failure	Failure Strain		Failure Time
									EDT	Avg. LDT	
		(kN/m^3)	(%)	(%/min)	(kPa)		(kPa)	(kPa)	(%)	(%)	(min)
GMS(MP1(D)-800CDMono-3D) Batch-D	800GD1-3D (2.2E-2)-1Hr	18.5	28.1	2.2E-02	800	1 Hour	3868	-1.4	0.654	0.427	19.7
	800GD1-3D (2.2E-2)-12Hr	18.6	33.5	2.2E-02		12 Hours	3786	-1.8	0.664	0.438	19.6
	800GD1-3D (3.2E-2)-21.7Days	18.5	25.4	3.2E-02*		21.7 Days	4960	-2.1	0.812	-	25

*Externally measured strain rate

The variation of peak strength and failure strain of GMS(MP1(D)-800CDMono-3D) with the change in duration of consolidation time are plotted in Figures 7.3 and 7.4. The failure strains values shown in Table 7.1 and Fig. 7.4 were computed with reference to the start of monotonic loading. The values of peak strength and failure strains are approximately comparable for specimens consolidated for 1 and 12 hours, viz. 800GD1-3D (2.2E-2)-1Hr and 800GD1-3D (2.2E-2)-12Hr, suggesting no noticeable effects of duration of consolidation, as evident in Figures 7.3 and 7.4. However, significant increase in peak strength was witnessed for specimen consolidated for longer duration of 21.7 days, viz. 800GD1-3D (3.2E-2)-21.7Days, as shown in Fig. 7.3. The failure strain of 800GD1-3D (3.2E-2)-21.7Days was also observed to be somewhat higher than the rest of the specimens.

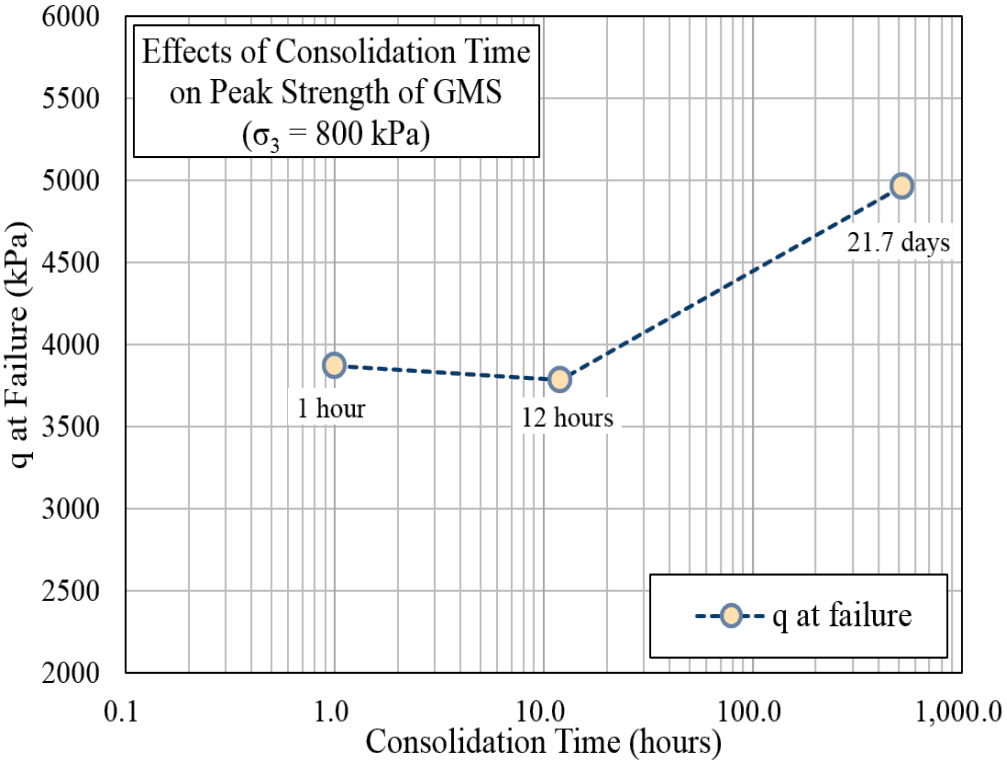

Fig. 7.3. Effects of consolidation duration on peak strength of GMS(MP1(D)-800CDMono-3D)

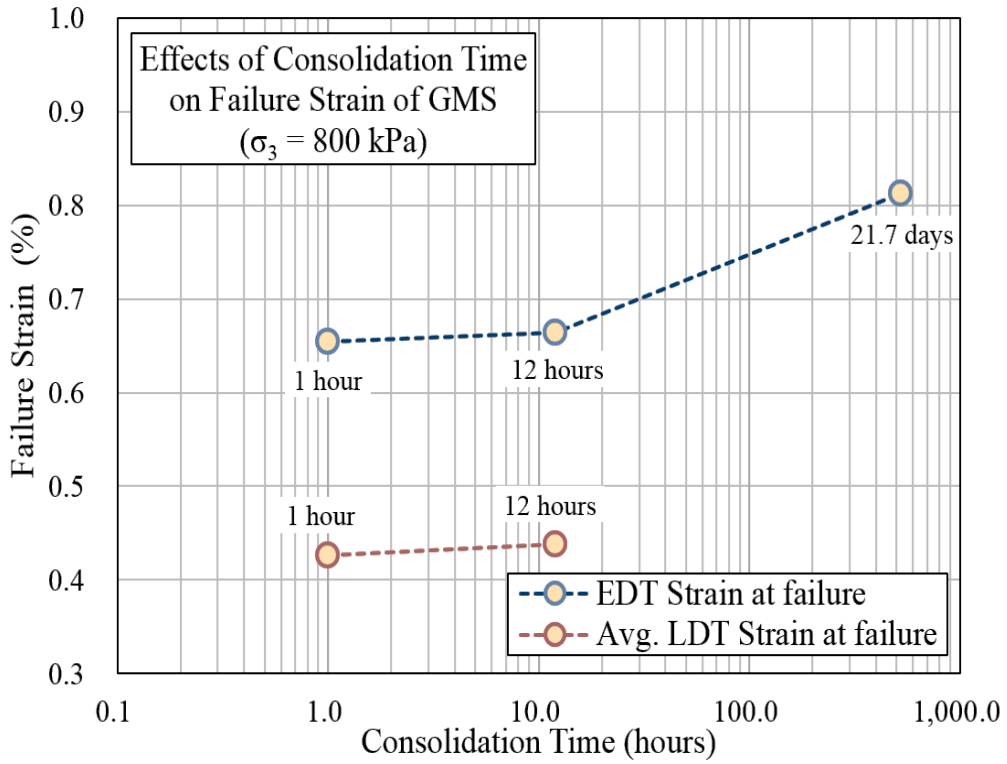

Fig. 7.4. Effects of consolidation duration on failure strain of GMS(MP1(D)-800CDMono-3D)

The stress-strain relationships of all of these specimens are shown in Figures 7.5 and 7.8, and two different references were selected to compute the axial strains. The axial strains calculated from the start of the tests were used to plot stress-strain relationships presented in Figures 7.5 and 7.6, whereas the axial strains in case of Figures 7.7 and 7.8 were computed with reference to the start of monotonic loading. It is evident from Figures 7.5 and 7.6 that GMS specimens exhibit an increasing trend of axial strain accumulation with the increase of consolidation duration. For instance, the EDT axial strain accumulation of merely 0.13% was witnessed at the end of consolidation for specimen consolidated for 1 hour, viz. 800GD1-3D (2.2E-2)-1Hr, as evident in Fig. 7.5.

On the other hand, approximately 3.0% of externally measured axial strain was witnessed for specimen consolidated for 21.7 days, viz. 800GD1-3D (3.2E-2)-21.7Days, at the end of consolidation, as shown in Fig. 7.5. The working limits of LDTs [5] were also reached during consolidation stage of 800GD1-3D (3.2E-2)-21.7Days, and the stress-strain relationships of this test using LDT are consequently not plotted in Figures 7.6 and 7.8. The time histories of pore pressure induced within GMS specimens are plotted in semi-logarithmic plot, as shown in Fig. 7.9. In general, the values of pore pressures are very limited (varies between 0 to -3 kPa) and remain almost constant throughout the test.

The results suggest that curing at higher confining stress level enhances the strength characteristics of GMS, and it is also likely that a relatively denser and stronger microstructure was rather achieved during consolidation at higher confining stresses. These findings can also be supported by the fact that the mechanical behavior of artificially bounded geomaterials improved significantly if cured at higher value of shear stress [6]. However, the stress-strain response of specimens consolidated for 1 and 12 hours are almost identical to each other, and no prominent effects of consolidation were observed within this duration period of consolidation, as shown in Fig. 5.8. Based on these findings, consolidation period of 1 hour was considered appropriate to examine the loading rate dependency at different confining stress levels.

7.4 LOADING RATE DEPENDENCY OF GMS UNDER CONSOLIDATED DRAINED MONOTONIC LOADING

Besides unconfined conditions, the loading rate dependency of GMS was examined at two different confining stress levels, viz. 400 and 800 kPa, and the specimens

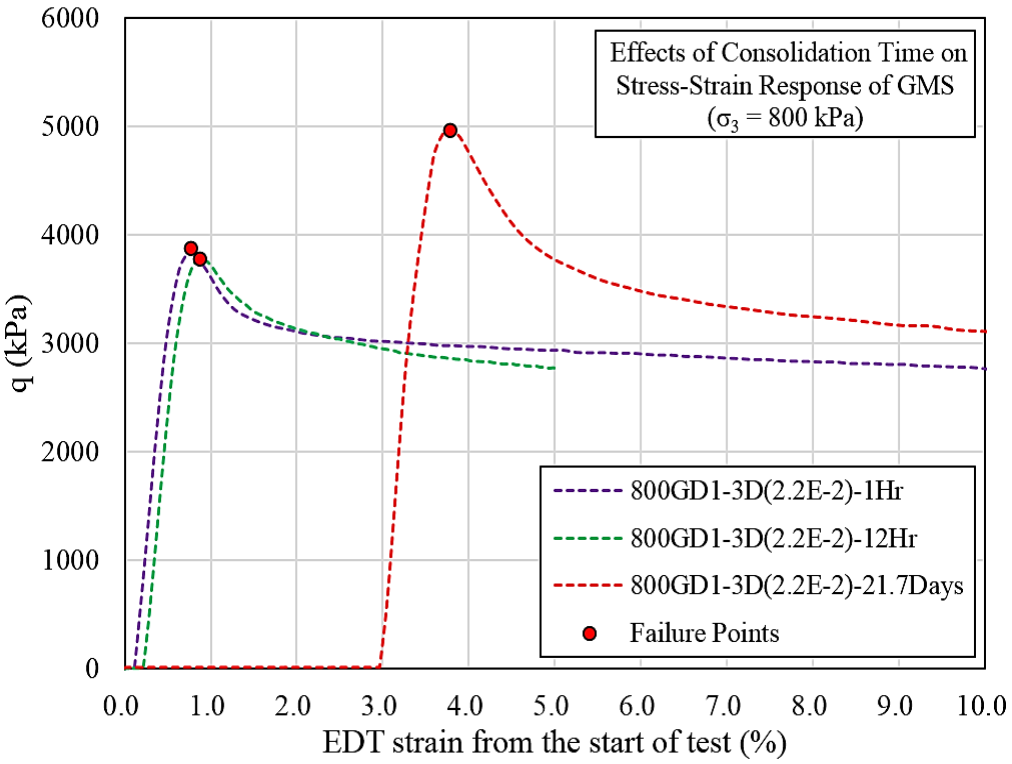

Fig. 7.5. Stress-strain relationships of GMS(MP1(D)-800CDMono-3D), (EDT strain from the start of test)

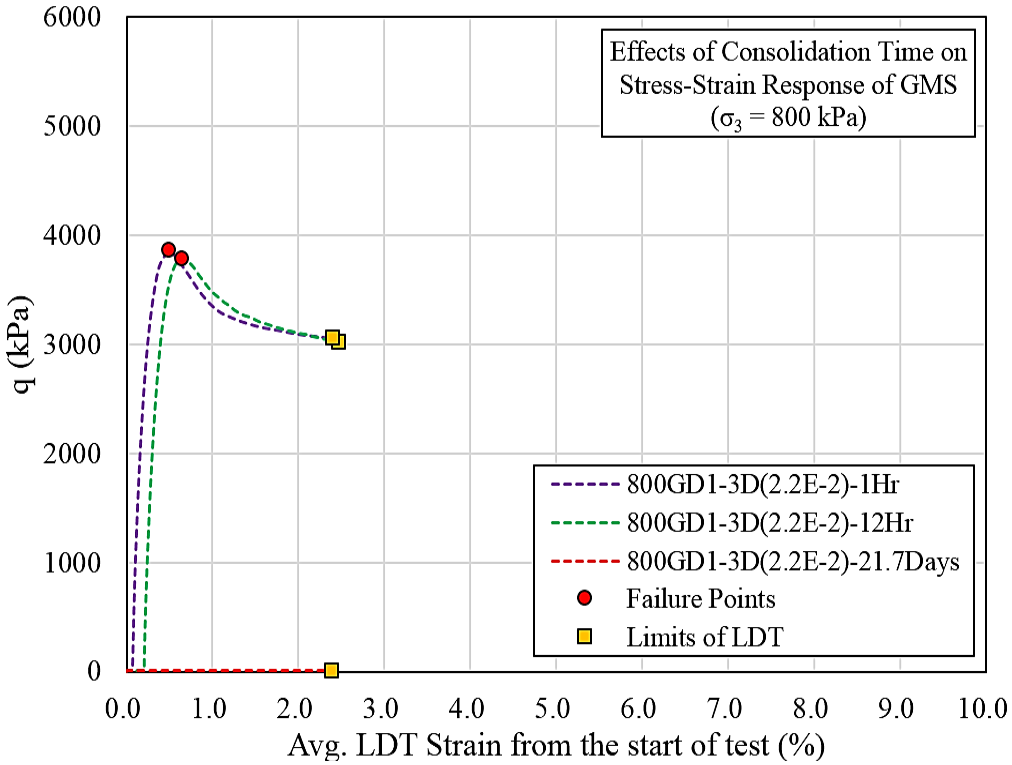

Fig. 7.6. Stress-strain relationships of GMS(MP1(D)-800CDMono-3D), (LDT strain from the start of test)

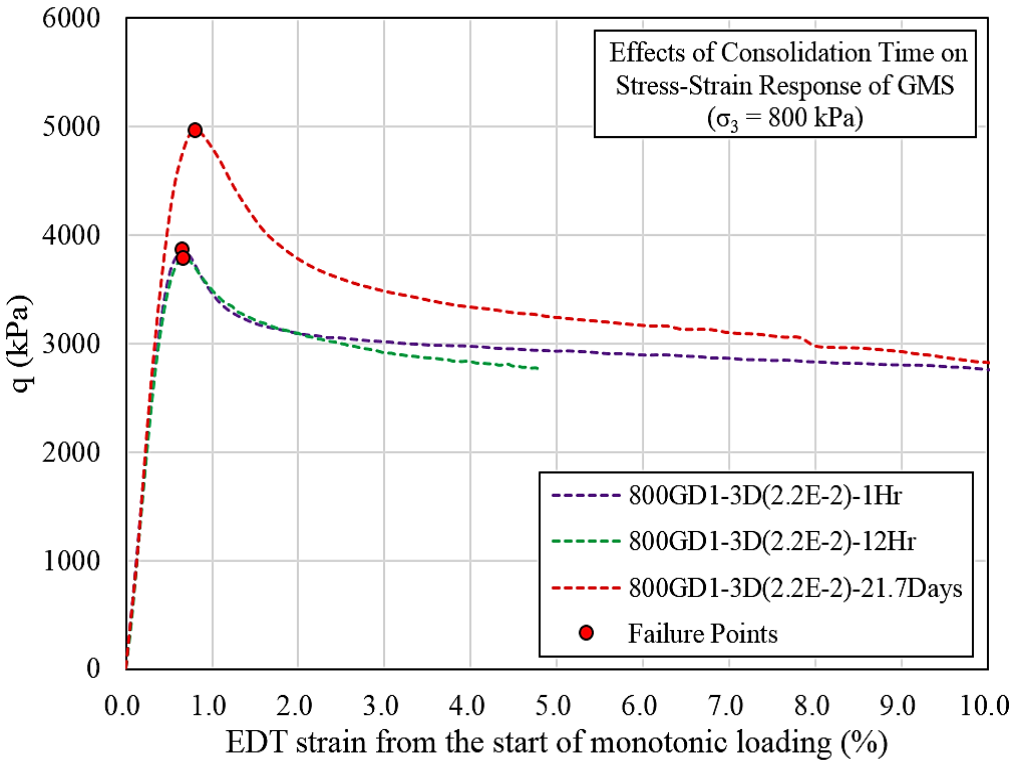

Fig. 7.7. Stress-strain relationships of GMS(MP1(D)-800CDMono-3D), (EDT strain from the monotonic loading)

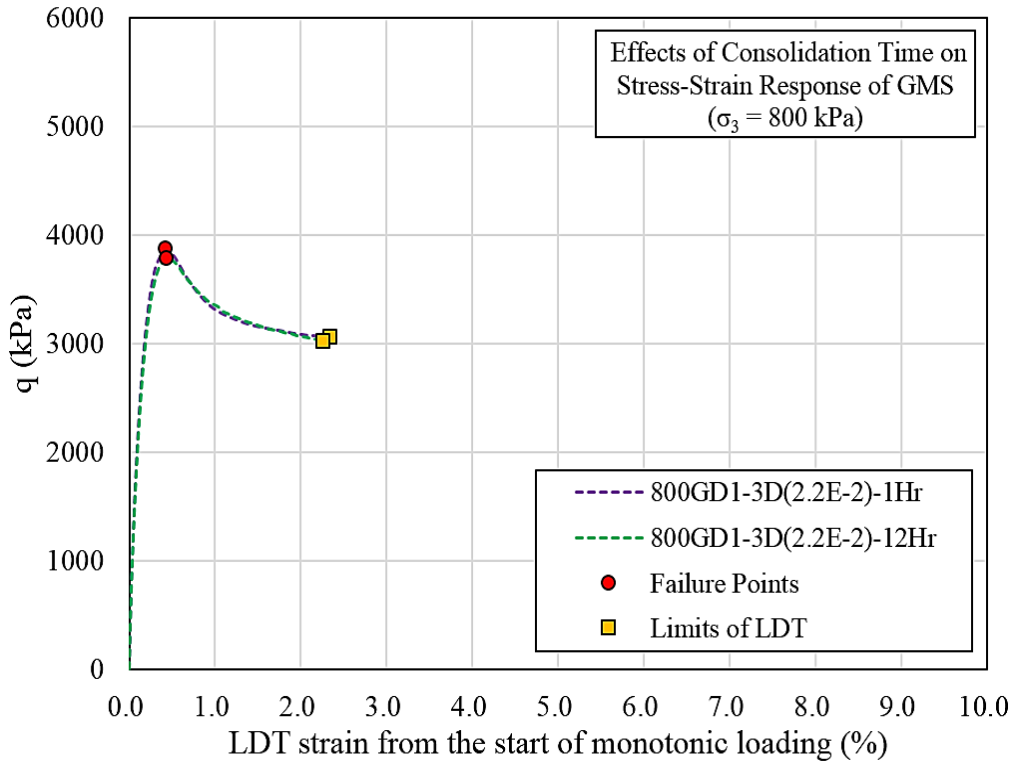

Fig. 7.8. Stress-strain relationships of GMS(MP1(D)-800CDMono-3D), (LDT strain from the monotonic loading)

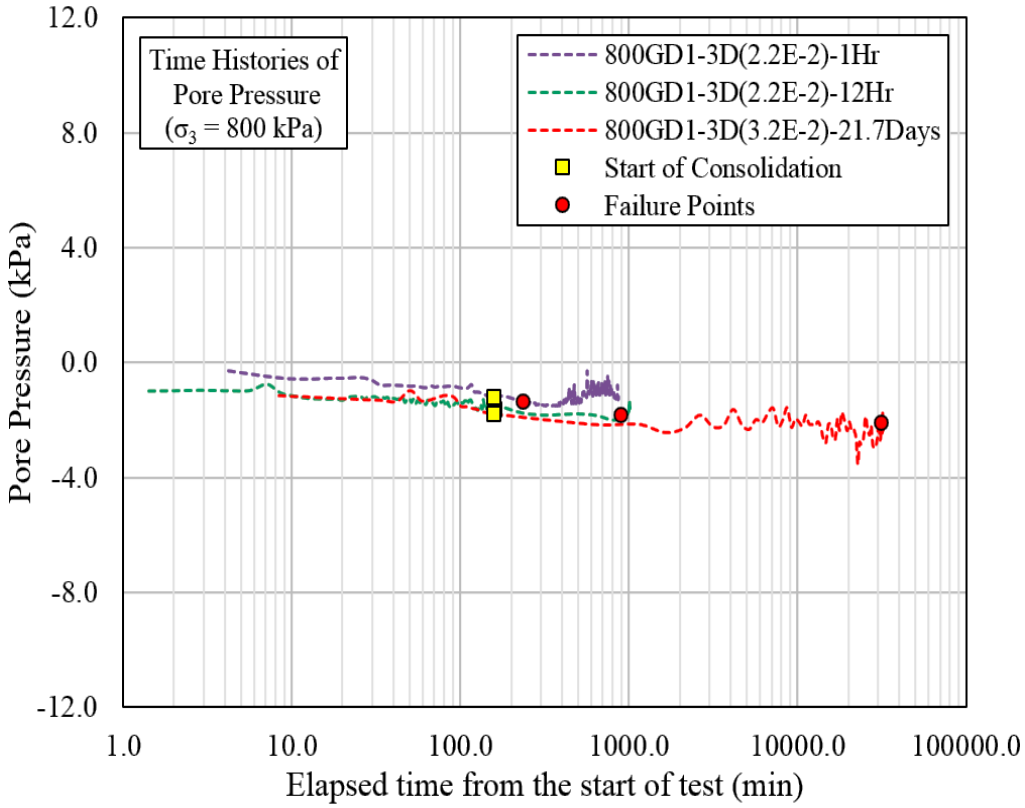

Fig. 7.9. Time histories of pore pressures induced in GMS(MP1(D)-800CDMono-3D)

were isotopically consolidated for 1 hour at targeted confining stress levels, prior to the application of drained monotonic loading. A total of four different loading rates, ranging from 1.6E-3 to 4.5E+0 %/min, were selected for drained monotonic loading, and the axial strains presented onwards were computed from the start of drained monotonic loading. The results of these tests are tabulated in Table 7.2, along with the details of loading conditions.

The stress-strain and normalized stress-strain response of GMS specimens tested at a confining stress of 400 kPa are plotted in Fig. 7.10 and 7.11 respectively. Noticeable effects of loading rate on the peak strength and pre-peak stiffness of these GMS specimens were observed. For instance, 400GD1-3D (4.5E+0)-D01 tested at an average strain rate of 4.5 E+0 %/min failed at a deviator stress of 4882 kPa, and this value reduced to merely 2353 kPa for specimen tested at an average strain rate of 1.6E-3 %/min, as evident in Fig. 7.10. Moreover, the effects of loading rate on the stress-strain (or normalized stress-strain) response of GMS are identical in the pre-peak regions for confining stress values of 400 and 800 kPa, as shown in Figures 7.10 to 7.13.

Table 7.2. Test results of consolidated drained triaxial monotonic tests on GMS(MP1)

Series & Batch ID	Test ID	Bulk Unit Weight Before Testing	Moisture Content After Testing	Average Strain Rate During Monotonic Loading	Confining Pressure	Pore Pressure at Failure	q at Failure	Failure Strain		Failure Time
								EDT	Avg. LDT	
		(kN/m^3)	(%)	(%/min)	(kPa)	(kPa)	(kPa)	(%)	(%)	(min)
GMS(MP1(D)-400(1Hr)CDMono-3D) Batch-D	400GD1-3D (4.5E+0)-D01	18.6	34.0	4.5E+00	400	-0.7	4882	0.561	0.260	0.1
	400GD1-3D (2.1E-1)-D02	18.5	33.2	2.1E-01		-0.1	4430	0.617	0.308	1.5
	400GD1-3D (2.2E-2)-D03	18.6	32.9	2.2E-02		-0.6	3791	0.696	0.426	19.6
	400GD1-3D (1.6E-3)-D04	18.6	32.4	1.6E-03		0.1	2353	1.102	0.868	554
GMS(MP1(D)-800(1Hr)CDMono-3D) Batch-D	800GD1-3D (4.0E+0)-D05	18.5	33.9	4.0E+00	800	0.6	5043	0.541	0.228	0.1
	800GD1-3D (1.7E-1)-D06	18.6	32.4	1.7E-01		-1.9	4773	0.566	0.282	1.7
	800GD1-3D (2.2E-2)-D07	18.5	28.1	2.2E-02		-1.4	3868	0.654	0.427	19.7
	800GD1-3D (1.8E-3)-D08	18.5	28.7	1.8E-03		-0.4	2199	1.983	1.783	1041

In comparison with the normalized stress-strain relationships of GMS under unconfined monotonic loading [7, 8] presented in Fig. 5.2 of Chapter No. 5, the effects of loading rate are generally quite similar on stress-strain behavior in the pre-peak region of GMS for both unconfined and confined monotonic loading conditions. However, the post-peak behavior of GMS is greatly affected by the confining stress values, and the phenomenon of post-peak strain softening diminishes greatly with increase of confining

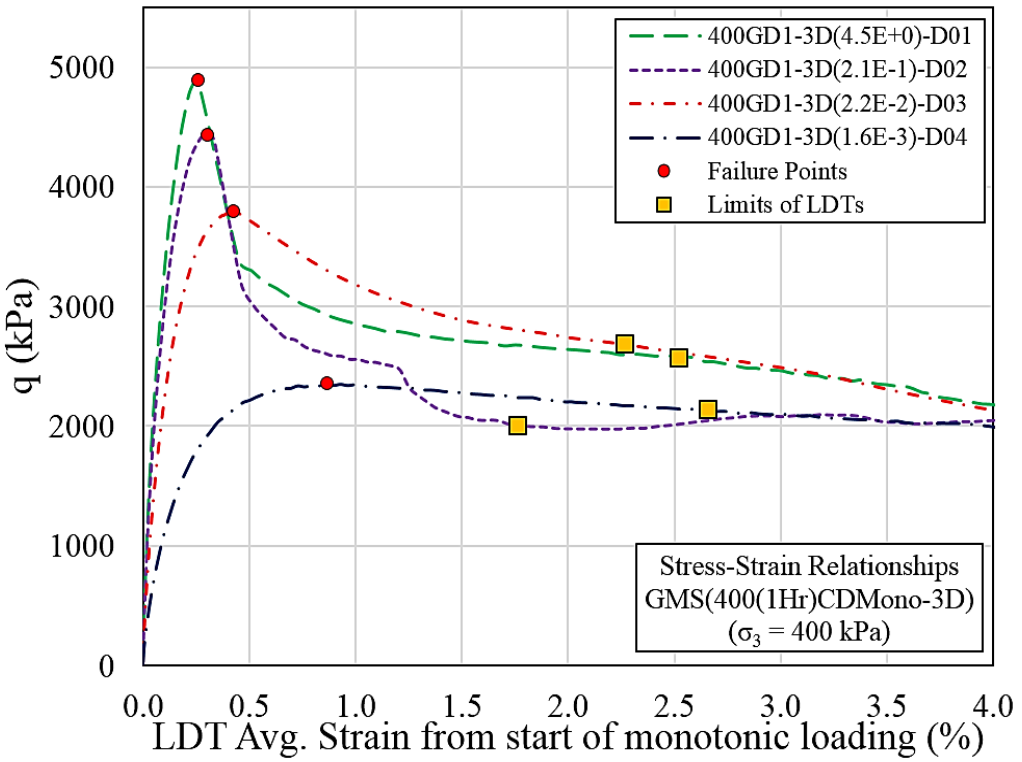

Fig. 7.10. Stress-strain relationships
GMS(MP1(D)-400(1Hr)CDMono-3D)

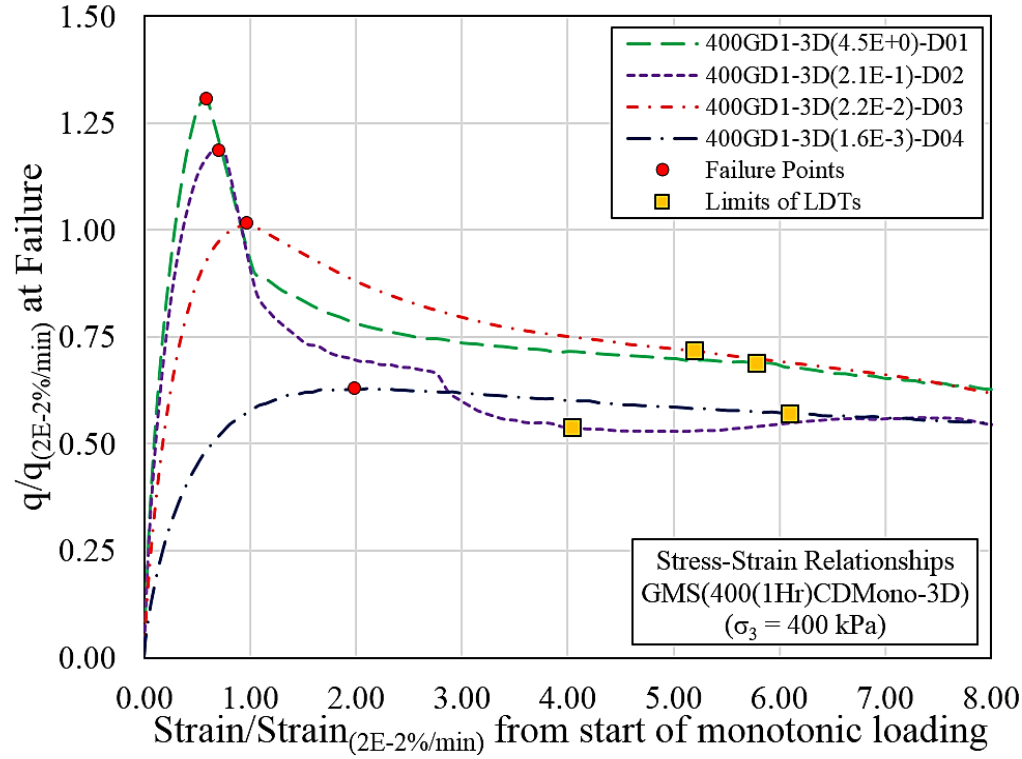

Fig. 7.11. Normalized stress-strain relationships
GMS(MP1(D)-400(1Hr)CDMono-3D)

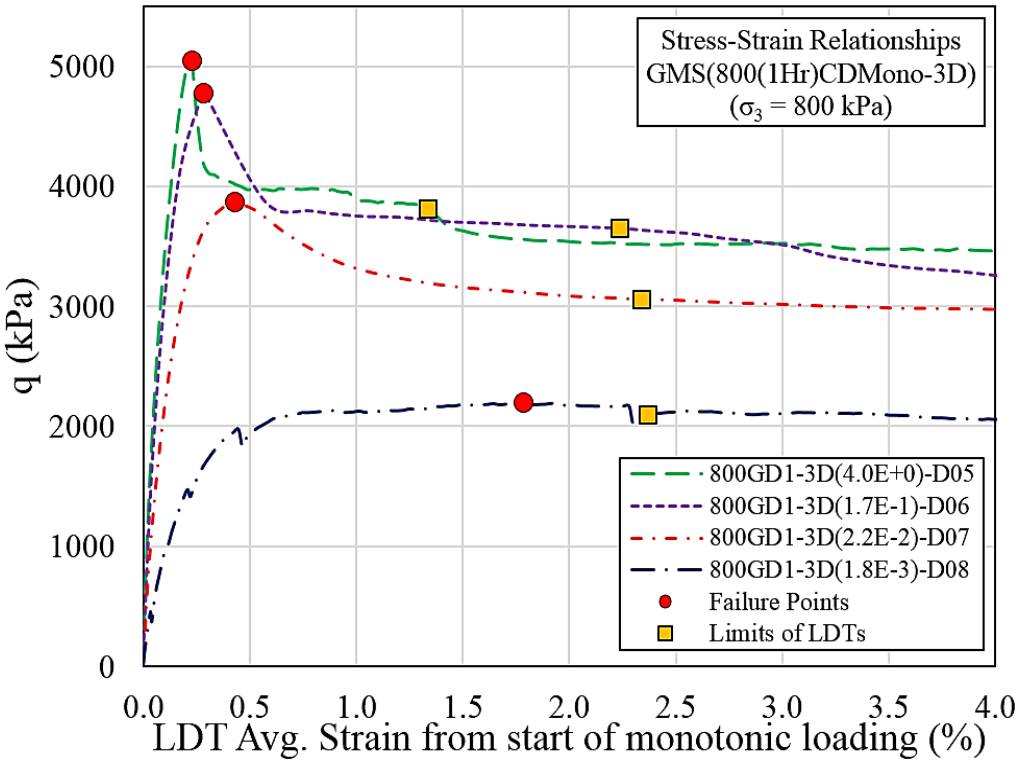

Fig. 7.12. Stress-strain relationships
GMS(MP1(D)-400(1Hr)CDMono-3D)

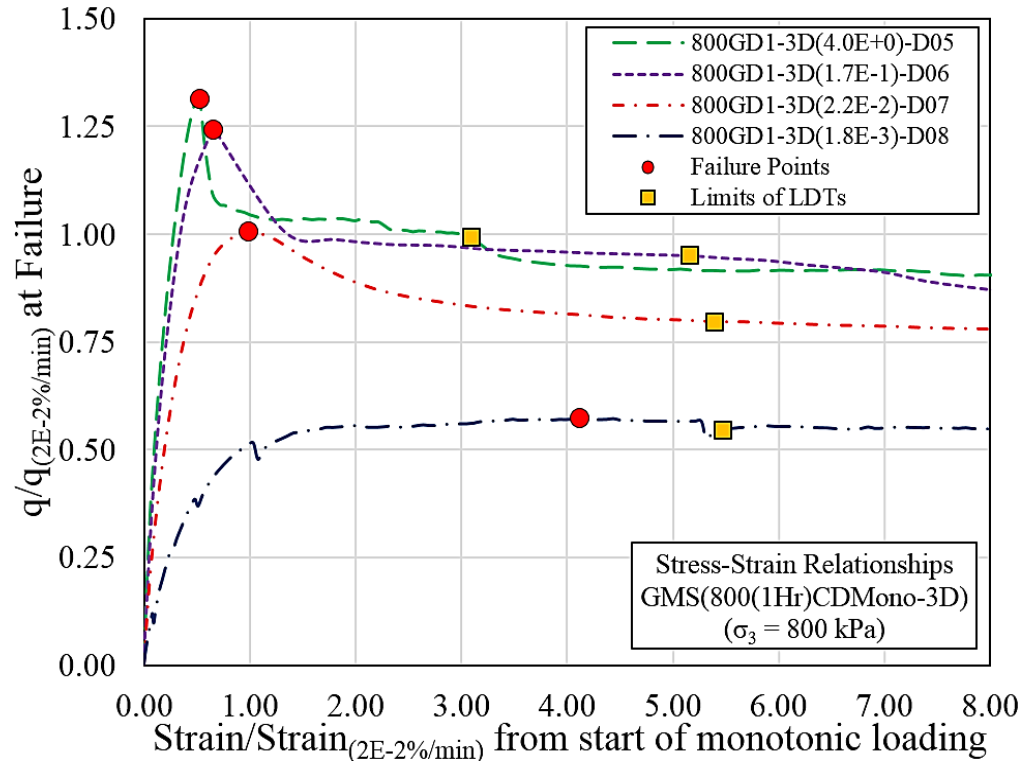

Fig. 7.13. Normalized stress-strain relationships
GMS(MP1(D)-400(1Hr)CDMono-3D)

stress, as evident in Figures 5.2, 7.11 and 7.13. In case of 800GD1-3D(2.2E- 2)-D07 tested at confining stress of 800 kPa and strain rate of 2.2E-2 %/min, the normalized deviator stress dropped merely around 20% at normalized strain value of 5.0%, as shown in Fig. 7.13. However, normalized deviator stress reduction of about 80% was witnessed at normalized strain of 5.0% for GD1-3D(2.4E-2)-D05, tested under unconfined monotonic loading at 2.4E-2 %/min., as shown in Fig. 5.2.

The effects of confining stress on the absolute and normalized values of peak deviator stress of GMS(MP1) specimens are shown in Figures 7.14 and 7.15 respectively. The effects of confining stress are quite trivial on the strength characteristics of GMS(MP1), as a maximum increase of merely 20% in the normalized deviator stress at failure was observed even at confining stress of 800 kPa for specimen subjected to highest strain rates, as shown in Fig. 7.15. In general, the absolute and normalized values of peak deviator stress increase slightly with the increase of confining stress for specimens tested at average strain rates higher than 2.3E-02 %/min., as evident in Figures 7.14 and 7.15. However, no noticeable effects of confining stress can be observed at strain rate of 1.7E-03 %/min, as shown in Figures 7.14 and 7.15.

Owing to the fact that strength of GMS is greatly affected by loading rate [7, 8], the results presented in Figures 7.14 and 7.15 only incorporates the absolute values of confining stress for specimens having significantly different peak strength at unconfined conditions. Therefore, it was deemed indispensable that the combined effects of loading rate and confining stress on the strength characteristics of GMS can rationally be compared by considering the normalized values confining stress instead of the absolute ones, as shown in Figures 7.16 and 7.17. Based on these normalized plots, it can be confidently concluded that the effects of confining stress on the strength characteristics of GMS(MP1) are relatively prominent at higher loading rates, and become relatively insignificant with the decrease of loading rate.

The dependency of peak strength and normalized peak strength of GMS on loading rate at different confining stress levels is summarized in Figures 7.18 and 7.19. Although the values of deviator stress at failure of specimens tested under confined conditions are generally somewhat higher than unconfined conditions especially at higher loading rates (Fig. 7.17), but the overall loading rate dependency of GMS is independent

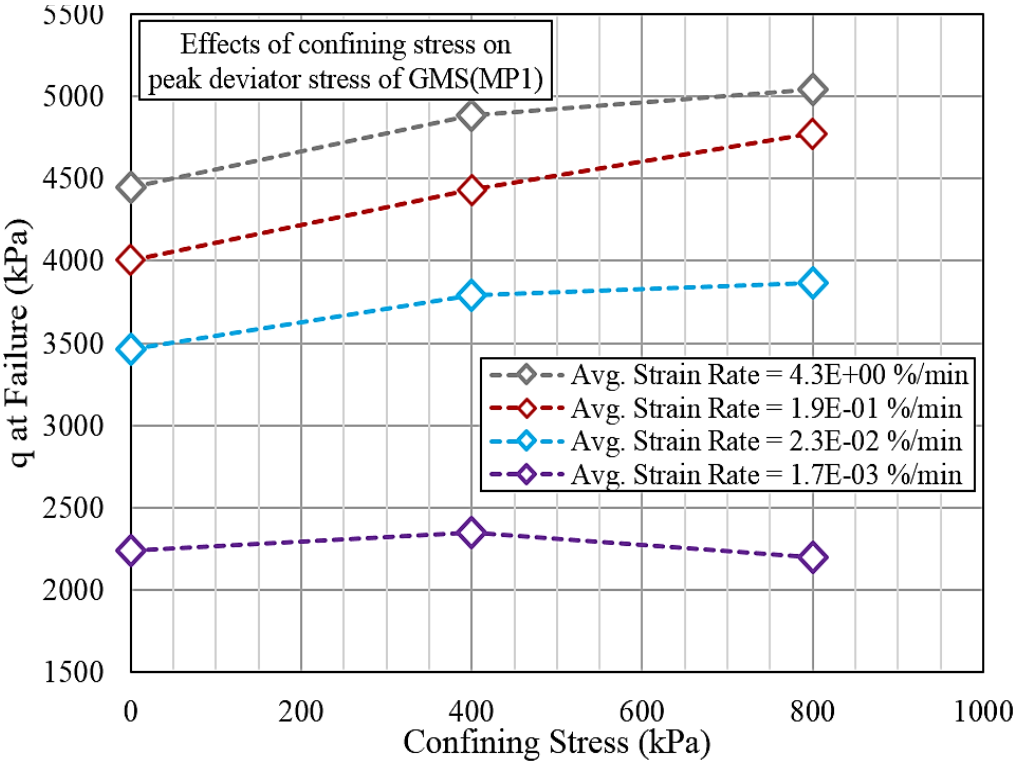

Fig. 7.14. Effects of confining stress on the peak deviator stress of GMS(MP1) tested at different strain rates

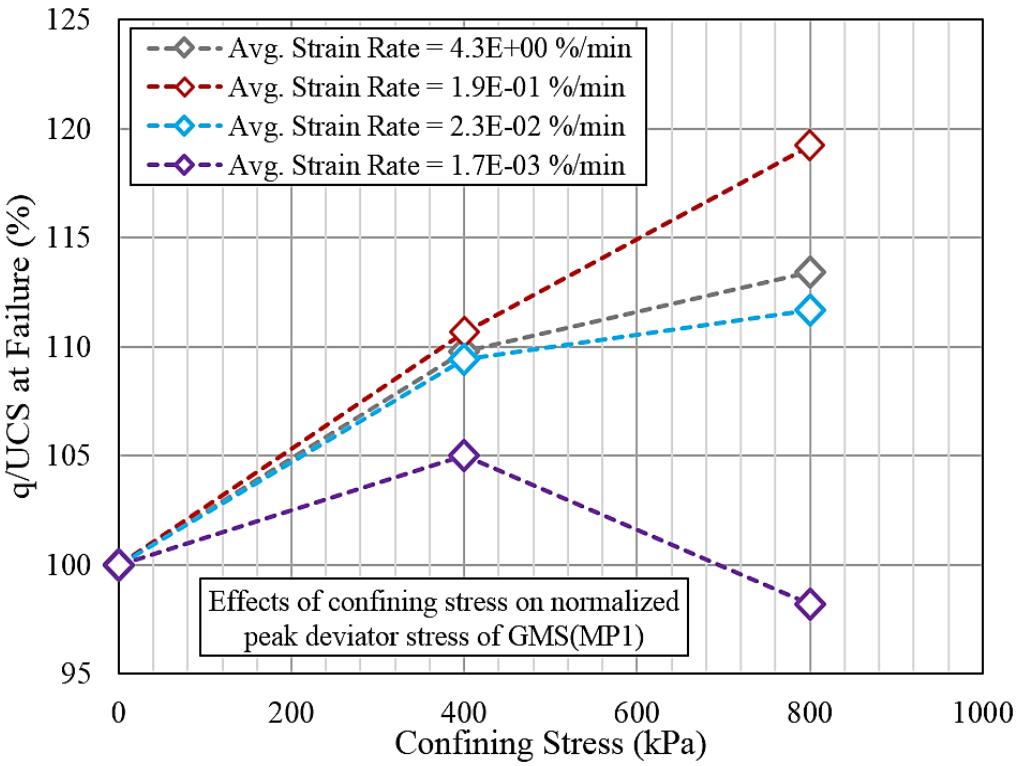

Fig. 7.15. Effects of confining stress on the normalized peak deviator stress of GMS(MP1) tested at different strain rates

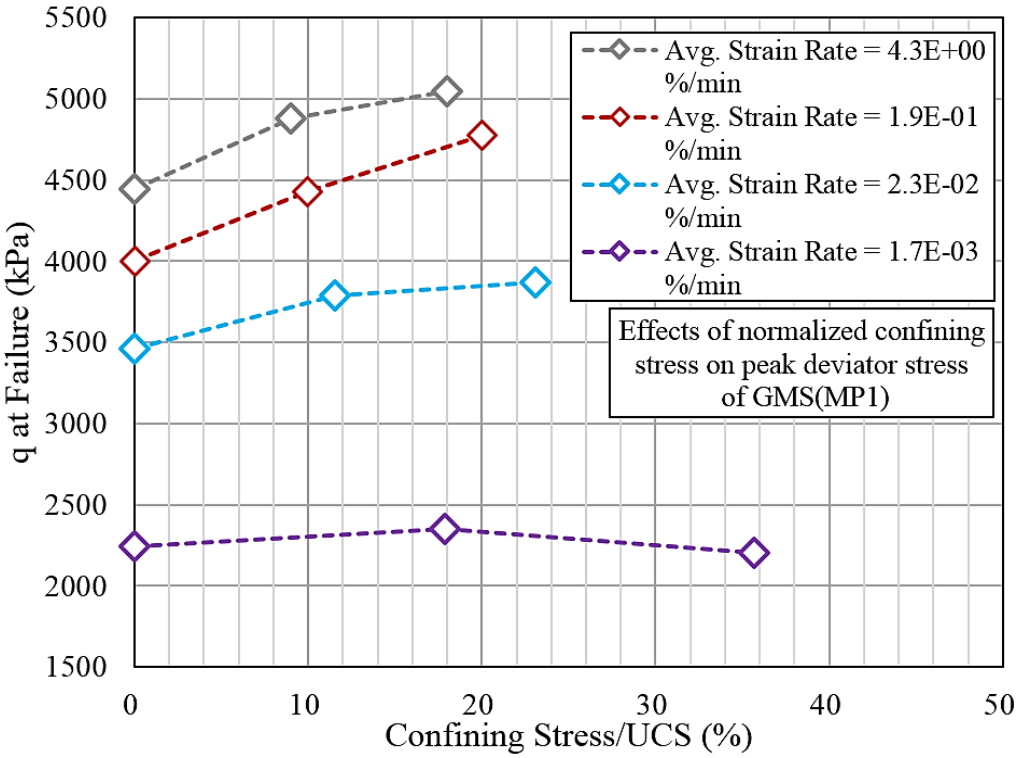

Fig. 7.16. Effects of normalized confining stress on the peak deviator stress of GMS(MP1) tested at different strain rates

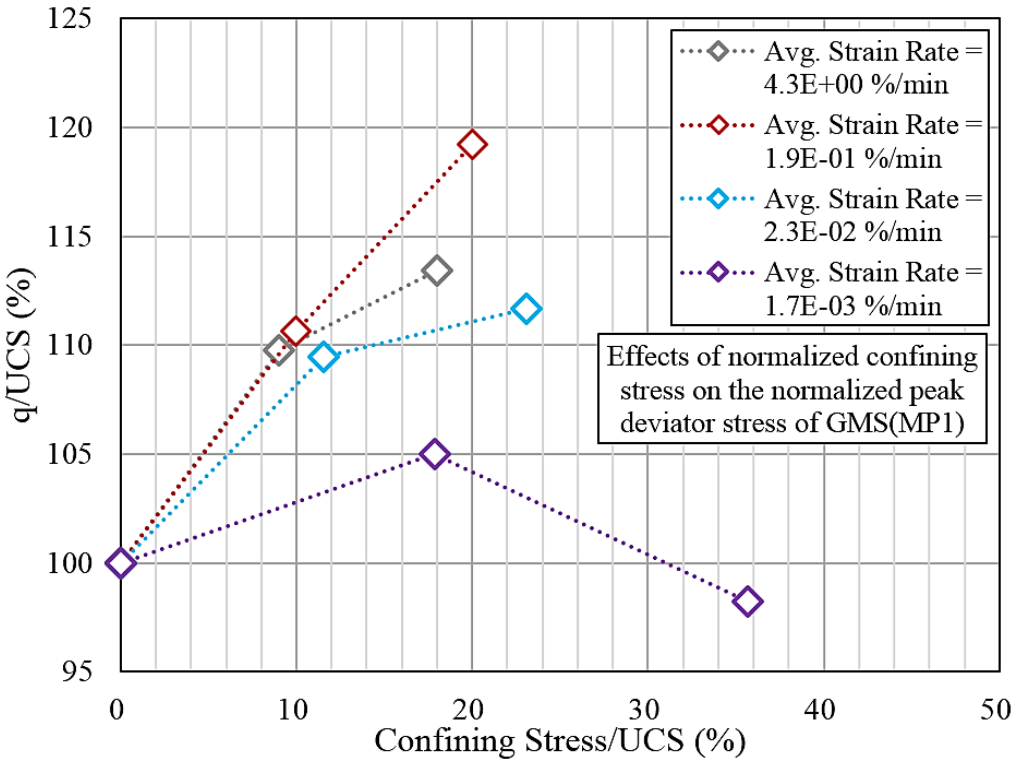

Fig. 7.17. Effects of normalized confining stress on the normalized peak deviator stress of GMS(MP1) tested at different strain rates

of the confining stress, as evident in Fig. 7.19. In other words, the effects of loading rate on the normalized strength of GMS under different confining stress conditions are indubitably comparable with each other.

Similar conclusions can also be inferred for the values of failure strain (and normalized failure strain) observed at different confining stress levels, as shown Fig. 7.20 and 7.21. However, the only noticeable exception is of 800GD1-3D (1.8E-3)-D08 which failed at relatively higher value of axial strain compared to the rest of the specimens. Under the confining stress of 400 and 800 kPa, no noticeable differences of the failure pattern of GMS specimens tested at different strain rate higher than 2.0E-2 %/min was witnessed, as evident in Figures 7.22 (a-c) and 7.23 (a-c). However, only bulging was observed for specimens tested at strain rates lesser than 2.0E-2% at confining stress of 400 and 800 kPa was observed, and no visible cracks or shear band were observed on visual inspection after testing, as shown in Figure 7.22(d) and 7.23(d).

The time histories of pore pressure induced within specimens tested during drained monotonic loading at confining stress of 400 and 800 kPa are shown in Figures 7.24 and 7.25. In general, no definite changes in the pore pressure induced within specimens were observed during drained monotonic loading, as evident in Figures 7.24 and 7.25. Moreover, the values of pore pressure are rather negligible compared with the applied confining stress during monotonic loading, and varies roughly between -3.0 to 3.0 kPa.

7.5 LOADING RATE DEPENDENCY OF SHEAR STRENGTH PARAMETERS OF GMS(MP1)

In the field of geotechnical engineering and rock mechanics, Mohr-Coulomb failure criterion is often employed to model the behavior of isotropic materials defined in terms of two parameters [9, 10], viz. cohesion (c) and angle of internal friction (ϕ). These parameters are collectively known as shear strength parameters [2], and the failure criterion is expressed typically by a linear envelop obtained by plot between shear strength (on vertical axis) and normal strength (on horizontal axis) of targeted materials [9, 10]. The present section aims to quantify the effects of loading rate on these shear strength parameters of bounded geomaterials. The generalized form of Mohr-Coulomb failure criterion [10] is presented in Eq. (7.1).

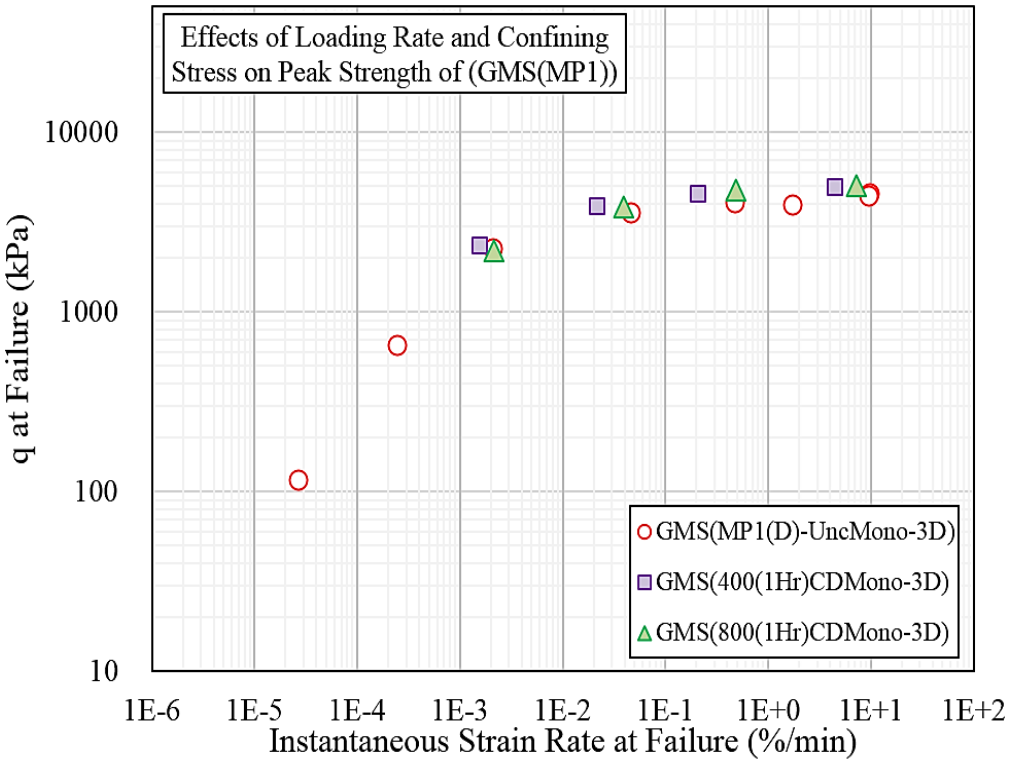

Fig. 7.18. Relationship between peak strength and instantaneous strain rate at failure of GMS(MP1) at different confining stress levels

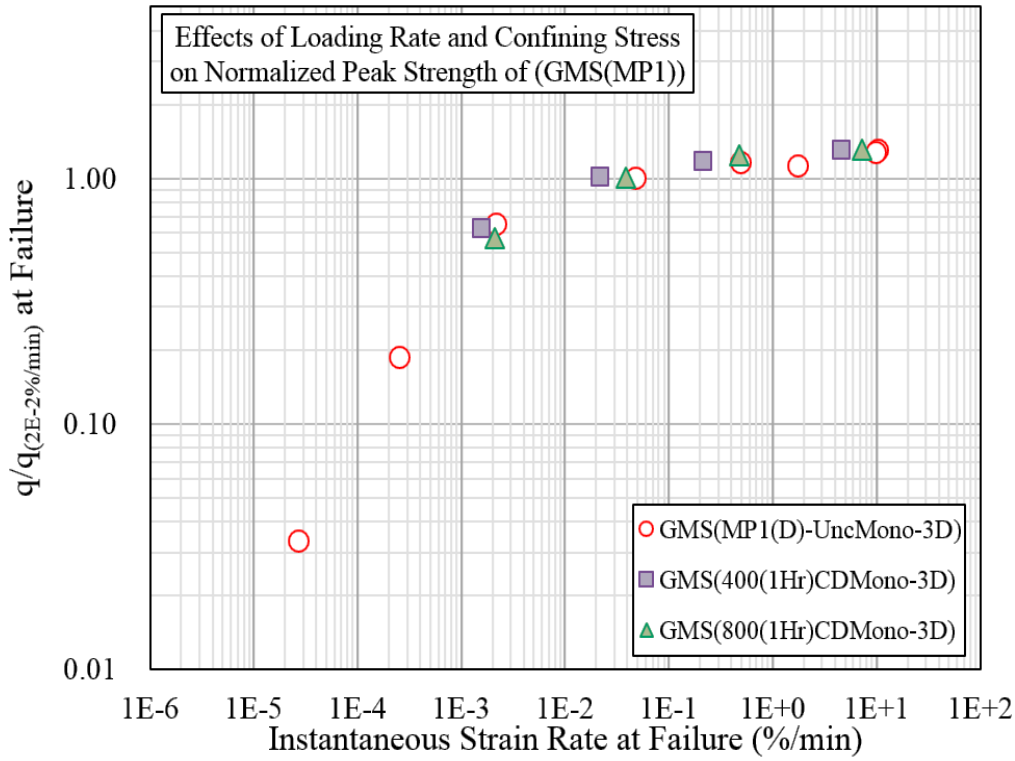

Fig. 7.19. Relationship between peak strength and instantaneous strain rate at failure of GMS(MP1) at different confining stress levels

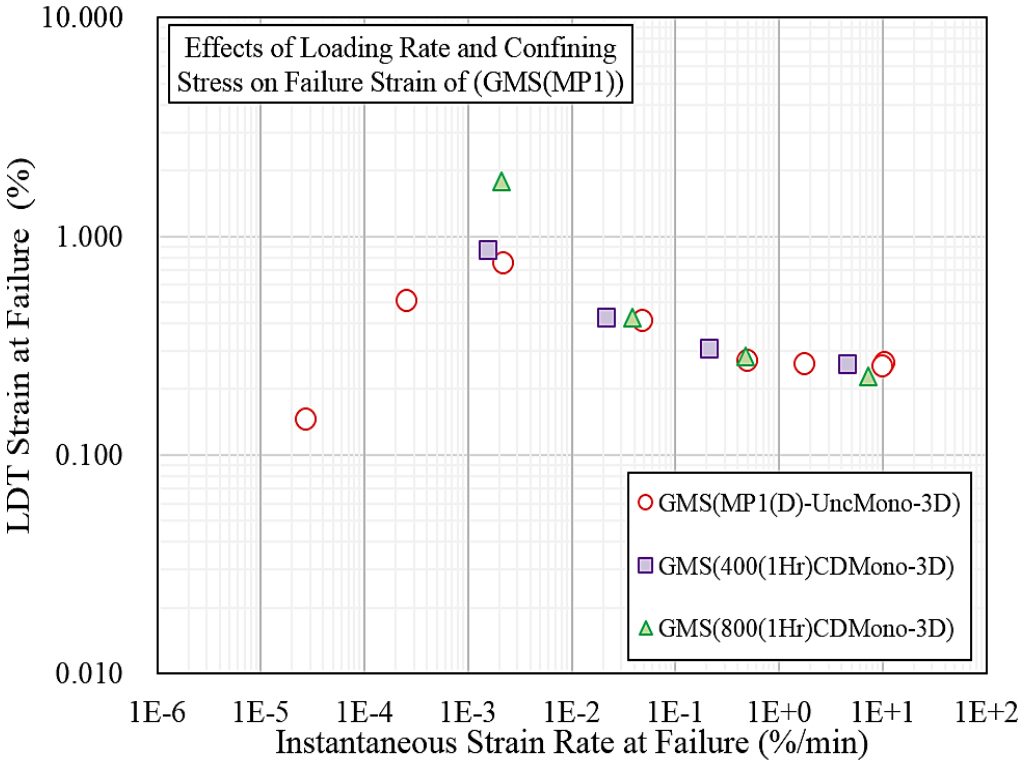

Fig. 7.20. Relationship between failure strain and instantaneous strain rate at failure of GMS(MP1) at different confining stress levels

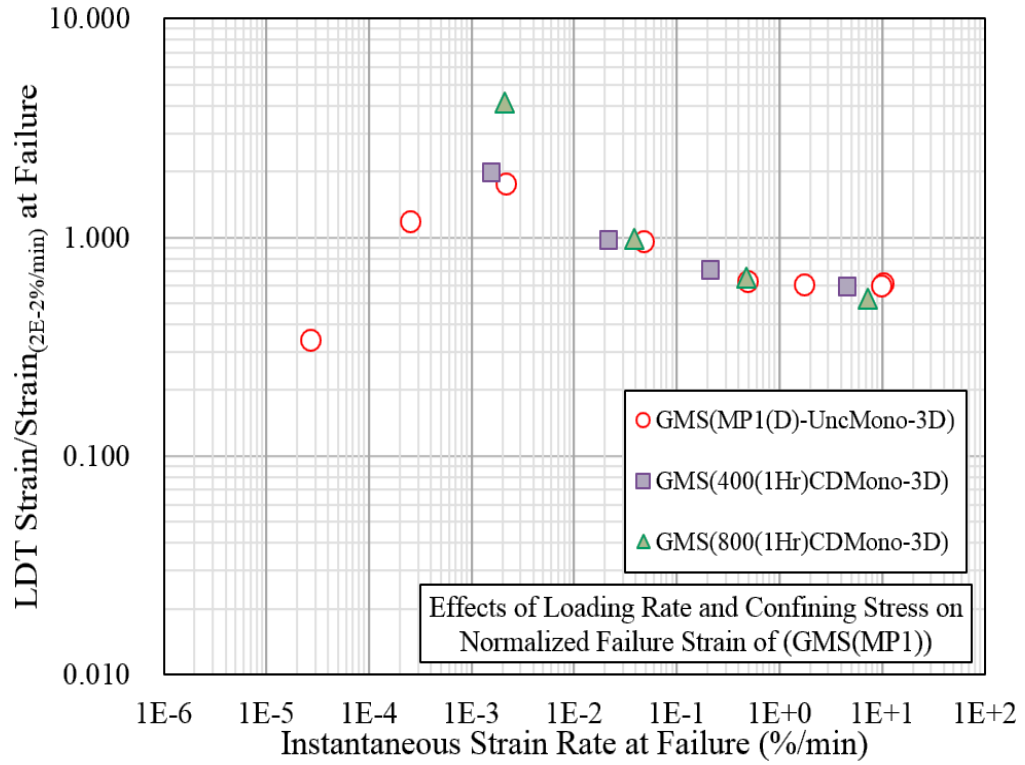

Fig. 7.21. Relationship between normalized failure strain and instantaneous strain rate at failure of GMS(MP1) at different confining stress levels

(a) 400GD1-3D(4.5E+0)-D01

(b) 400GD1-3D(2.1E-1)-D02

(c) 400GD1-3D(2.2E-2)-D03

(d) 400GD1-3D(1.6E-3)-D04

Fig. 7.22. Failure pattern of GMS(MP1(D)-400(1Hr)CDMono-3D) specimens

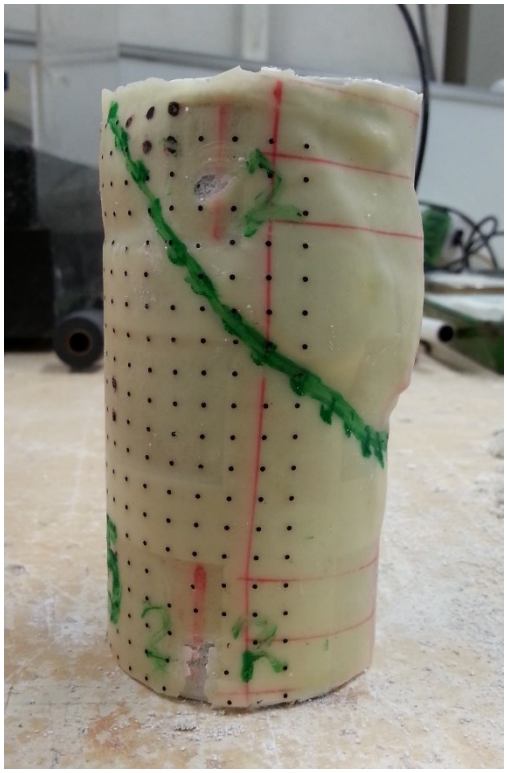

(a) 800GD1-3D(4.0E+0)-D05

(b) 800GD1-3D(1.7E-1)-D06

(c) 800GD1-3D(2.2E-2)-D07

(d) 800GD1-3D(1.8E-3)-D08

Fig. 7.23. Failure pattern of GMS(MP1(D)-800(1Hr)CDMono-3D) specimens

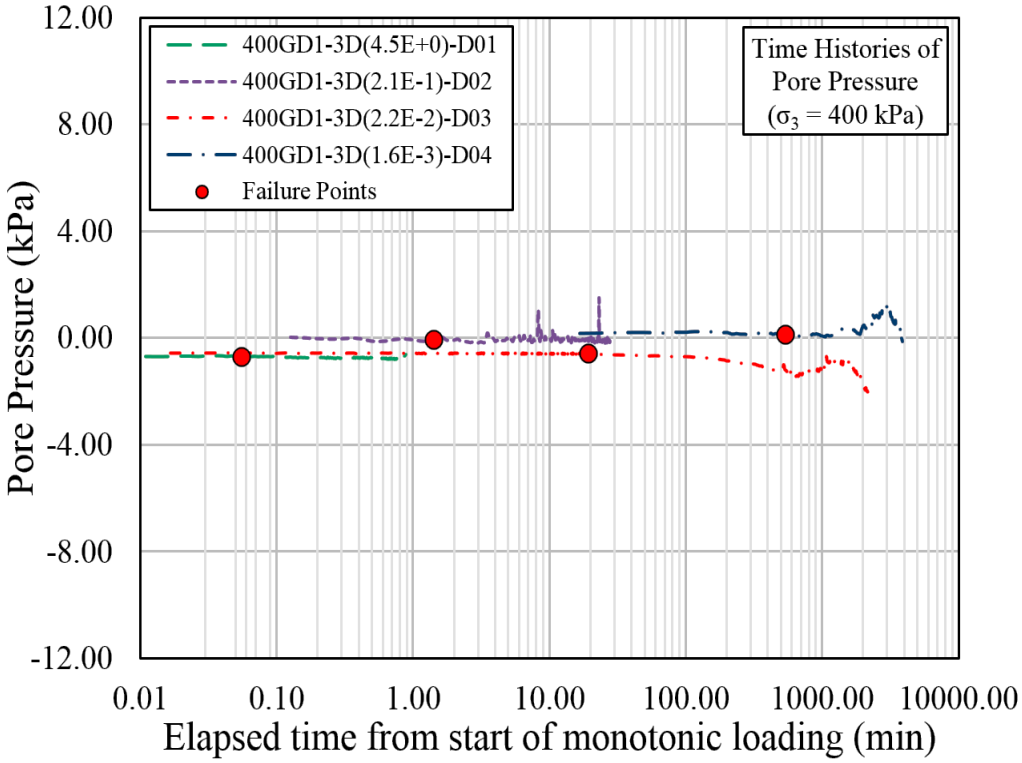

Fig. 7.24. Time histories of pore pressure induced in GMS(MP1(D)-400CDMono-3D) during drained monotonic loading

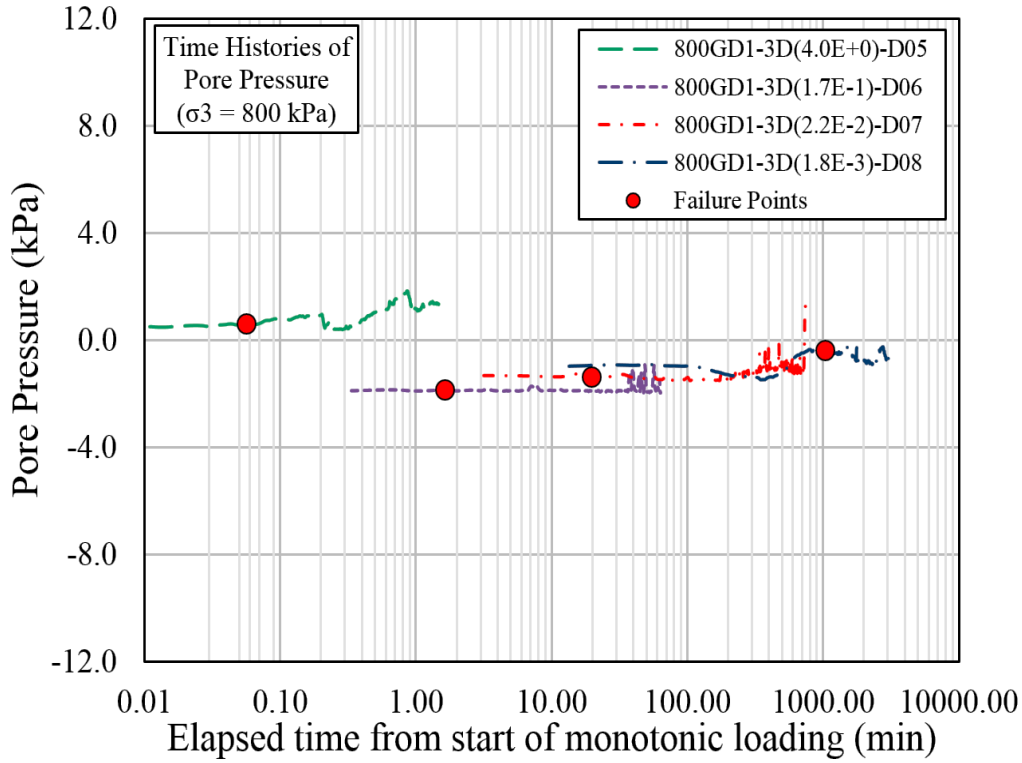

Fig. 7.25. Time histories of pore pressure induced in GMS(MP1(D)-800CDMono-3D) during drained monotonic loading

$$\tau = \sigma \tan \phi + c \tag{7.1}$$

Where:

τ = shear strength

σ = normal stress

c = cohesion

ϕ = angle of internal friction

Additionally, Eq. (7.1) can also be articulated in terms of principal major stress (σ_1) and principal minor stress (σ_3) as follows [10]:

$$\left(\frac{\sigma_1 - \sigma_3}{2}\right) = \left(\frac{\sigma_1 + \sigma_3}{2}\right) \text{Sin}\phi + c\,\text{Cos}\phi \tag{7.2}$$

Where:

σ_1 = major principal stress

σ_3 = minor principal stress

In order to ease the estimation of shear strength parameters, Eq. (7.2) can be simplified by defining a pair of variables [11] as follows:

$$t = s\,\text{Sin}\phi + c\,\text{Cos}\phi \tag{7.3}$$

Where:

$$s = \left(\frac{\sigma_1 + \sigma_3}{2}\right) \tag{7.4}$$

$$t = \left(\frac{\sigma_1 - \sigma_3}{2}\right) \tag{7.5}$$

In the present study, the values of c and ϕ were estimated by considering the slope and intercept of the s-t plot [11] as shown in Equations 7.6 and 7.7 respectively. Schematic illustration of the procedure to compute c and ϕ values from s-t plot is shown in Fig. 7.26.

$$\phi = \text{Sin}^{-1}(m_{(s-t)}) \tag{7.6}$$

$$c = \frac{c_{(s-t)}}{\text{Cos}\phi} \tag{7.7}$$

Where:

$m_{(s-t)}$ = slope of s-t plot

$c_{(s-t)}$ = intercept of s-t plot

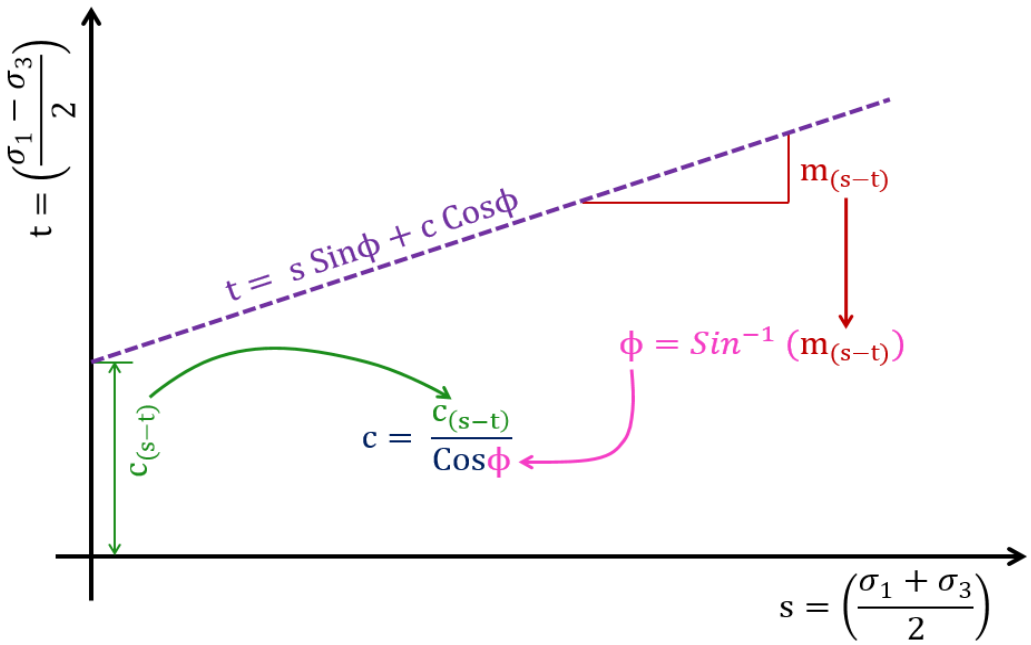

Fig. 7.26. Schematic Illustration of the procedure for the computation of shear strength parameters from s-t plot.

In order to further examine the effects of confining stress at different strain rates, Mohr circles of stresses [12] at failure are plotted for GMS specimens at four different strain rates, as shown in Figures 7.27 to 7.30. As discussed earlier in Section 7.3, these plots also delineate that the effects of confining stress on the strength characteristics of GMS are comparatively noticeable at higher strain rates, and diminishes with the decrease of loading rates. For instance, marked increase in the radius of Mohr circles, i.e. deviator stress at failure, with the increase of confining stress can be undoubtedly witnessed at an average strain rate of 4.3+00 % min, as shown in Fig. 7.27. However, the Mohr circles of stresses for GMS specimens tested at different confining stresses are virtually identical at an average strain rate of 1.7E-03 %/min, as shown in Fig. 7.30.

This aspect is also discernable in the s-t plots [11] of GMS specimens belonging to different strain rates, as shown in Fig. 7.31. For specimens tested at strain rates of 4.3E+00 and 1.9E-01 %/min, the trends of s-t relationships are quite comparable with each other, and the values of coefficient of determination, viz. R2, are fairly close to unity. However, the inclination of s-t relationship decrease with the decrease in strain rate, and is almost horizontal, viz. R^2 = 0.0302, for specimens tested at an average strain rate of 1.7E-03 %/min., indicating almost negligible effects of confining stress on strength characteristics of GMS at slower loading rates, as evident in Fig. 7.31.

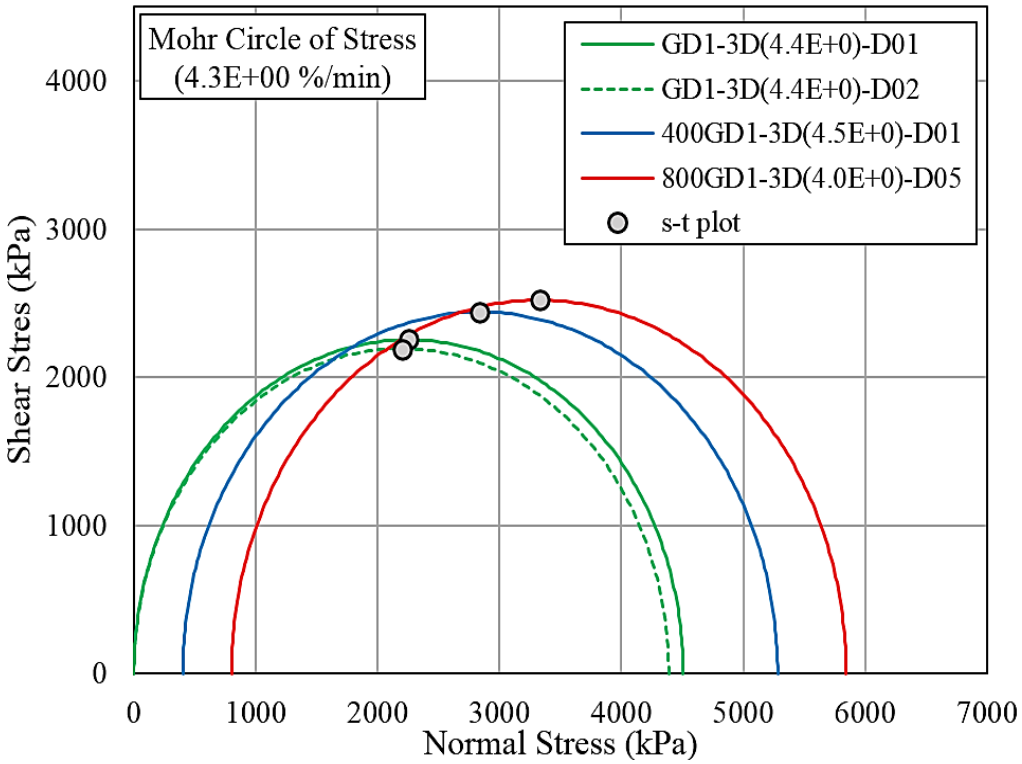

Fig. 7.27. Mohr circle of stress of GMS specimens tested at an average strain rate of 4.3E+00 %/min

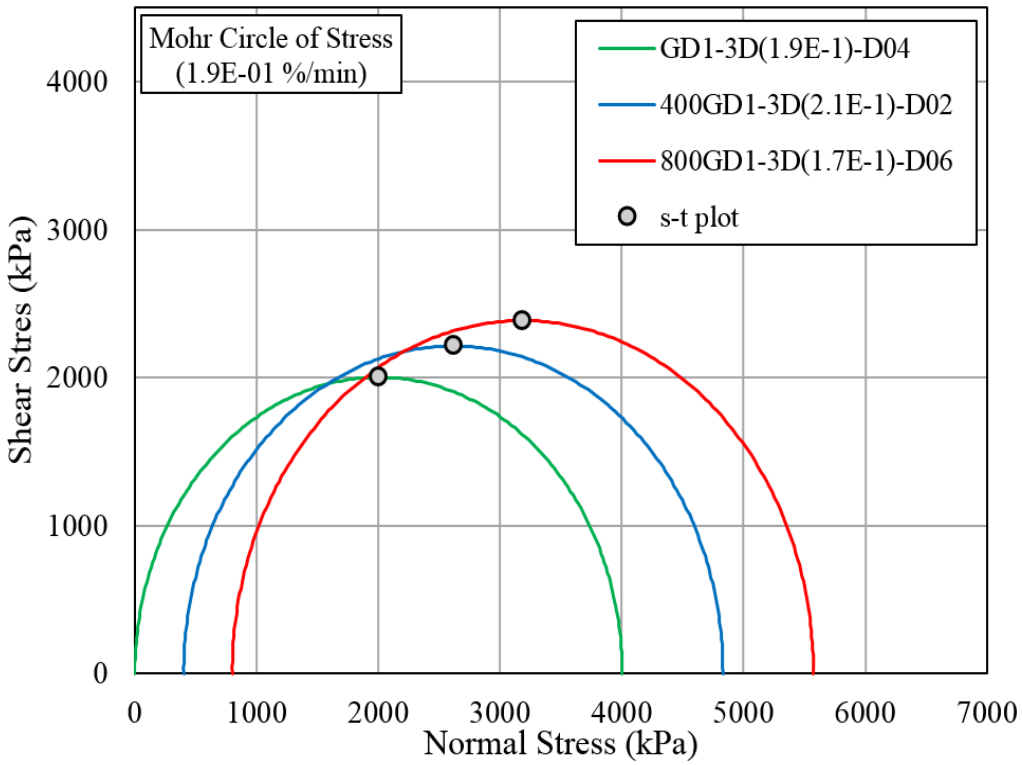

Fig. 7.28. Mohr circle of stress of GMS specimens tested at an average strain rate of 1.9E-01 %/min

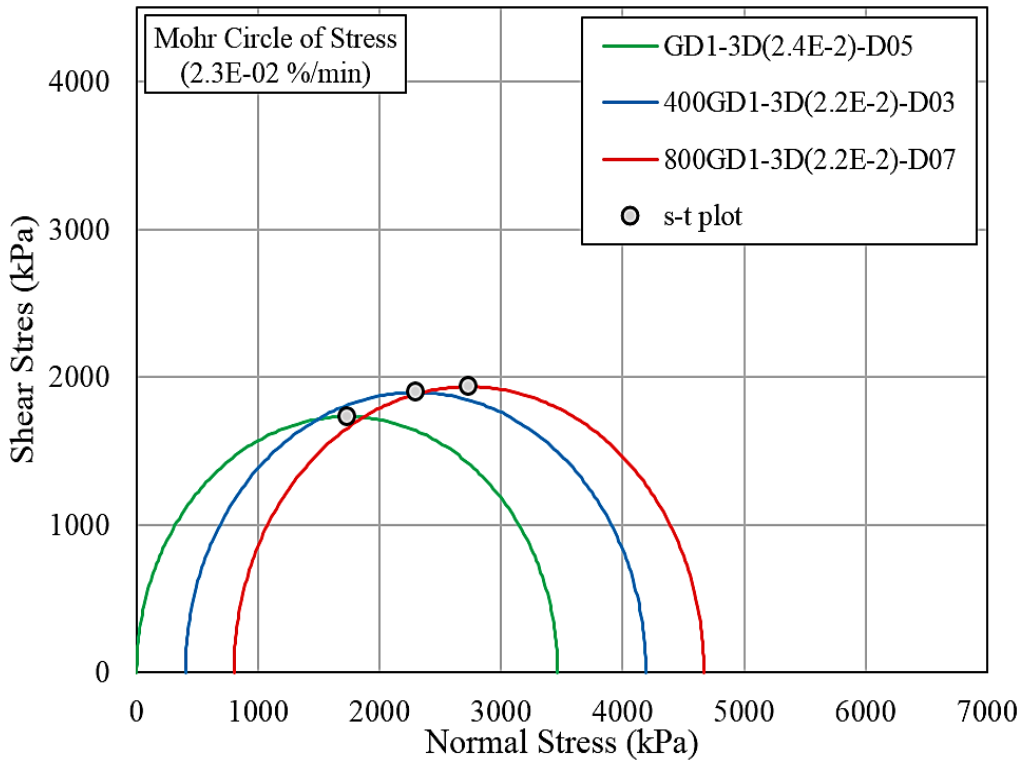

Fig. 7.29. Mohr circle of stress of GMS specimens tested at an average strain rate of 2.3E-02 %/min

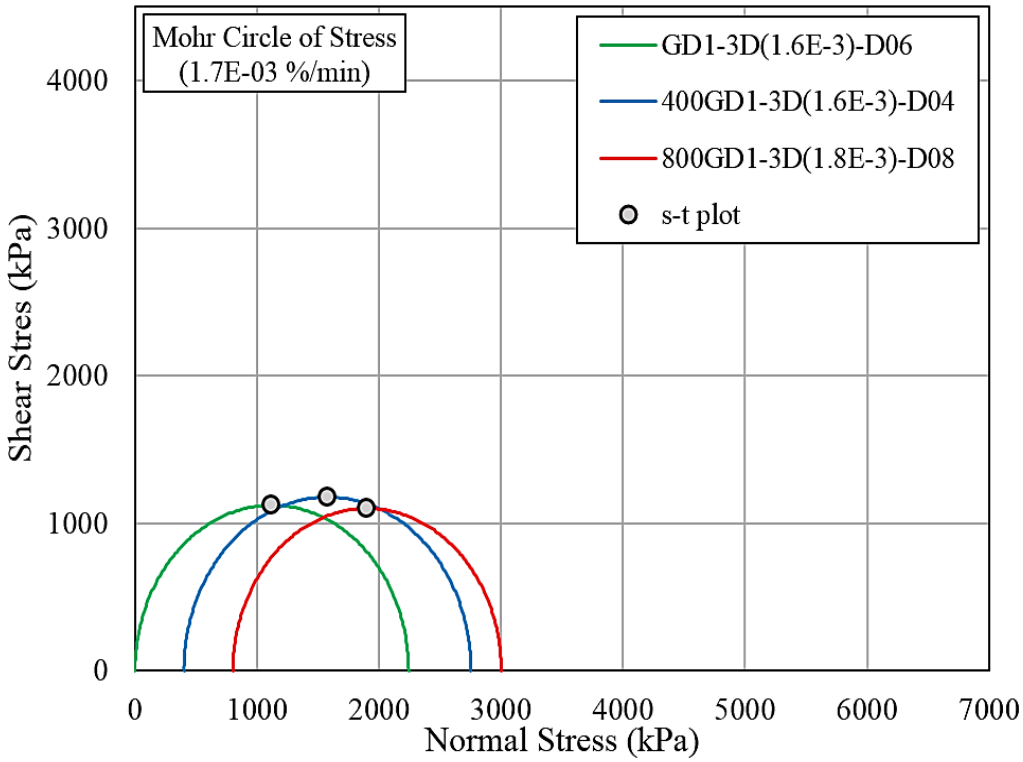

Fig. 7.30. Mohr circle of stress of GMS specimens tested at an average strain rate of 1.7E-03 %/min

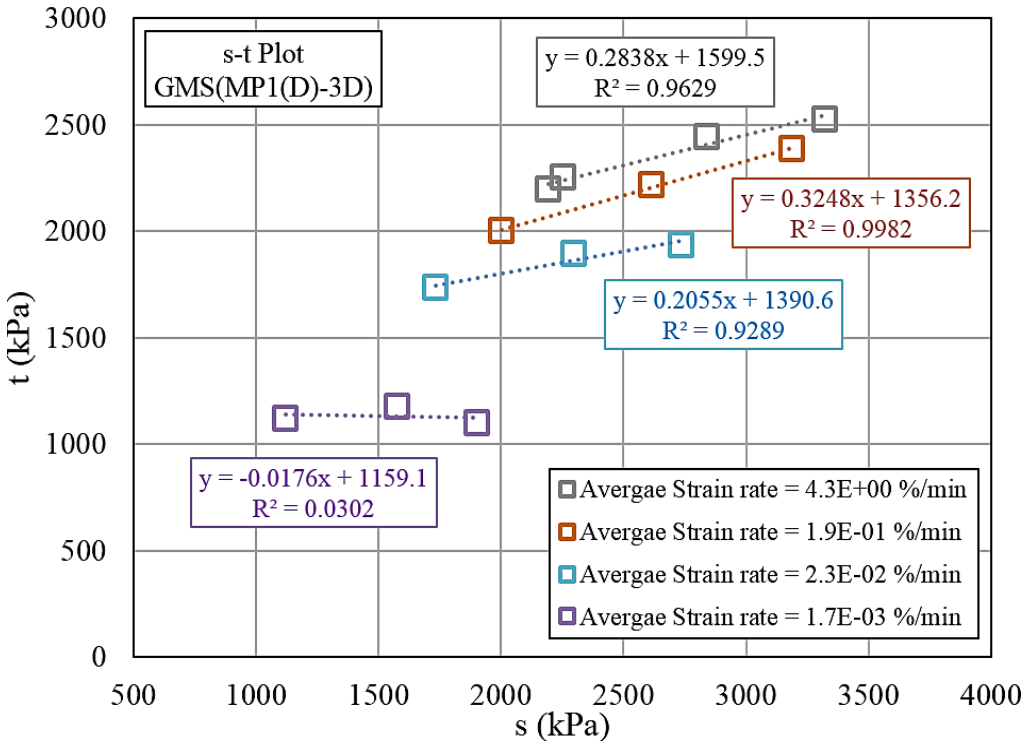

Fig. 7.31. s-t plot of GMS specimens tested at different strain rates and different confining stress levels.

Based on these s-t plots, the values of c and ϕ at peak strength of GMS specimens were computed at different strain rates and the results are plotted in Figures 7.32 and 7.33 respectively. In general, an increasing trend of values of cohesion of GMS specimens with the increase of strain rate can be throughout the tested range, as shown in Fig. 7.32. On the other hand, the values of angle of internal friction of GMS increase with the increase of strain rate up to an instantaneous strain rate of 2.3E-1 %/min (Zone-2), and no effects of loading rate on the values of angle of internal friction of GMS specimens were observed for specimens tested at strain rates higher than 2.3E-1 %/min. (Zone-1), as evident in Fig. 7.29.

7.6 SUMMARY OF FINDINGS

- The results of consolidated drained triaxial compression tests performed on GMS(MP1) specimens consolidated for different periods of isotropic drained consolidation showed that the values of peak strength and failure strains are approximately comparable for specimens consolidated for 1 and 12 hours, suggesting no noticeable effects of duration of consolidation up to 12 hours. However, an increase in peak strength and failure strain was observed for

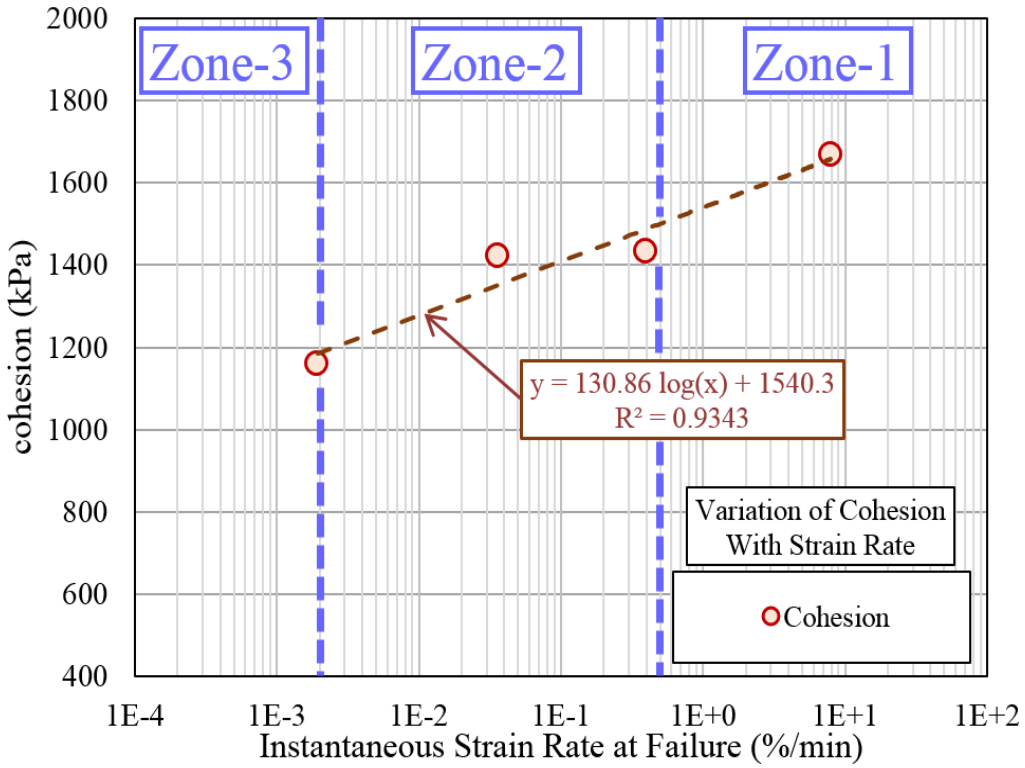

Fig. 7.32. Effects of loading rate on the cohesion values of GMS(MP1) specimens

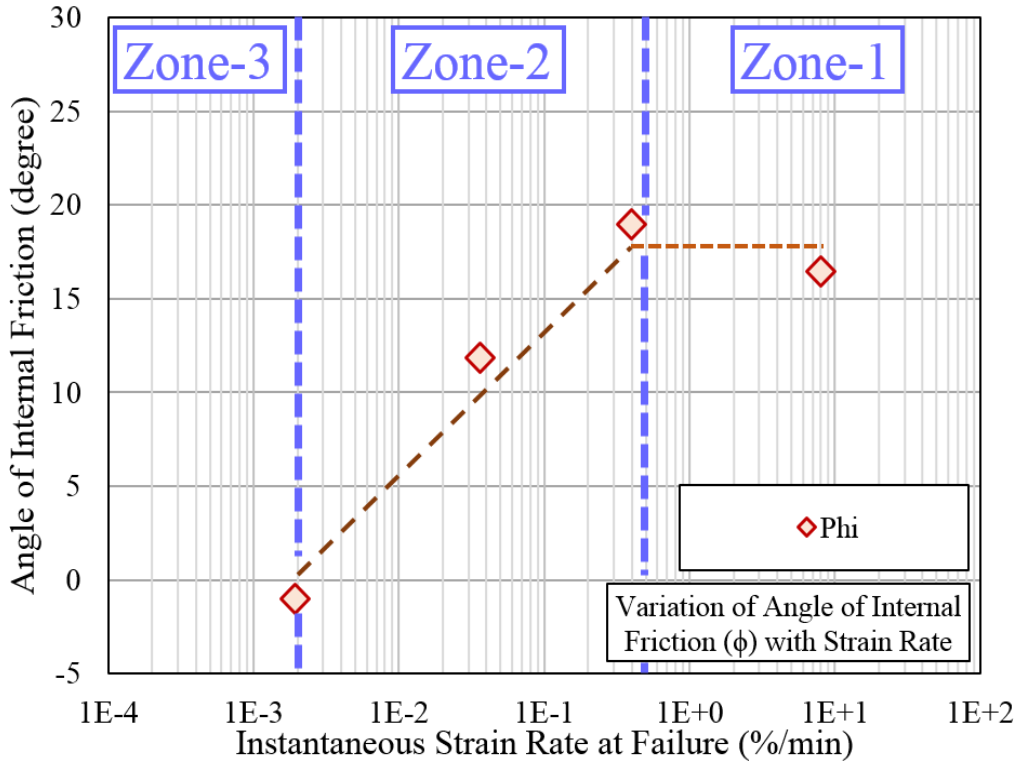

Fig. 7.33. Effects of loading rate on the values of angle of internal friction of GMS(MP1) specimens

consolidated for 21.7 days.

- The stress-strain response of specimens consolidated for 1 and 12 hours are almost identical to each other, and no prominent effects of consolidation were observed within this duration period of consolidation.
- GMS specimens exhibit an increasing trend of axial strain accumulation with the increase of consolidation duration, and approximately 3.0% of externally measured axial strain was witnessed for specimen consolidated for 21.7 days.
- The results suggest that curing at higher confining stress level enhances the strength characteristics of GMS, and it is also likely that a relatively denser and stronger microstructure was rather achieved during consolidation at higher confining stresses.
- Based on the results of consolidated drained monotonic tests performed at four different loading rates under confining stress of 400 and 800 kPa, it was concluded that the effects of loading rate are generally quite similar on stress-strain behaviour in the pre-peak region of GMS for both unconfined and confined monotonic loading conditions.
- The post-peak behavior of GMS is greatly affected by the confining stress values, and the phenomenon of post-peak strain softening diminishes greatly with increase of confining stress.
- The effects of confining stress are quite trivial on the strength characteristics of GMS(MP1), as a maximum increase of merely 20% in the normalized deviator stress at failure was observed even at confining stress of 800 kPa for specimen subjected to highest strain rates.
- The absolute and normalized values of peak deviator stress generally increase slightly with the increase of confining stress for specimens tested at average strain rates higher than 2.3E-02 %/min. However, no noticeable effects of confining stress can be observed at strain rate of 1.7E-03 %/min.
- The combined effects of loading rate and confining stress on the strength characteristics of GMS was rationally compared by considering the normalized values confining stress instead of absolute ones. . Based on these normalized plots, it can be confidently concluded that the effects of confining

stress on the strength characteristics of GMS(MP1) are relatively prominent at higher loading rates, and become relatively insignificant with the decrease of loading rate.

- In spite of the fact that the values of deviator stress at failure of specimens tested under confined conditions are generally somewhat higher than unconfined conditions especially at higher loading rates , but the overall loading rate dependency of GMS is independent of the confining stress. Therefore, the effects of loading rate on the normalized strength of GMS under different confining stress conditions are indubitably comparable with each other.
- Similar conclusions can also be inferred for the values of failure strain (and normalized failure strain) observed at different confining stress levels. However, the only noticeable exception was observed for specimen tested at 1.8E-3 %/min under confining stress of 800 kPa, which failed at relatively higher value of axial strain compared to the rest of the specimens.
- Under the confining stress of 400 and 800 kPa, no noticeable differences of the failure pattern of GMS specimens tested at different strain rate higher than 2.0E-2 %/min was witnessed. However, only bulging was observed for specimens tested at strain rates lesser than 2.0E-2% at confining stress of 400 and 800 kPa was observed, and no visible cracks or shear band were observed on visual inspection after testing.
- In general, no definite changes in the pore pressure induced within specimens were observed during drained monotonic loading. Moreover, the values of pore pressure are rather negligible compared with the applied confining stress during monotonic loading, and varies roughly between -3.0 to 3.0 kPa.
- The Mohr circle of stresses of GMS specimens plotted at failure stress levels also delineated that the effects of confining stress on the strength characteristics of GMS are comparatively noticeable at higher strain rates, and diminishes with the decrease of loading rates. Additionally, the Mohr circles of stresses for GMS specimens tested at different confining stresses are virtually identical at an average strain rate of 1.7E-03 %/min

- The values of cohesion and angle of internal frictions of GMS specimens tested at different strain rates and confining stress conditions were estimated by considering the slope and intercept of the s-t plot.
- For specimens tested at strain rates of 4.3E+00 and 1.9E-01 %/min, the trends of s-t relationships are quite comparable with each other, and the values of coefficient of determination, viz. R^2, are fairly close to unity. However, the inclination of s-t relationship decrease with the decrease in strain rate, and is almost horizontal, viz. $R^2 = 0.0302$, for specimens tested at an average strain rate of 1.7E-03 %/min., indicating almost negligible effects of confining stress on strength characteristics of GMS at slower loading rates.
- In general, an increasing trend of values of cohesion of GMS specimens with the increase of strain rate can be throughout the tested range.
- On the other hand, the values of angle of internal friction of GMS increase with the increase of strain rate up to an instantaneous strain rate of 2.3E-1 %/min (Zone-2), and no effects of loading rate on the values of angle of internal friction of GMS specimens were observed for specimens tested at strain rates higher than 2.3E-1 %/min. (Zone-1).

7.7 REFRENCES

1. Haimson, B. and Chang, C. (2000), "A new true triaxial cell for testing mechanical properties of rock, and its use to determine rock strength and deformability of Westerly granite," *International Journal of Rock Mechanics and Mining Sciences*, **37(1-2)**, 285-296.

2. Gan, J. K. M., Fredlund, D. G. and Rahardjo, H. (1988), "Determination of the shear strength parameters of an unsaturated soil using the direct shear test," *Canadian Geotechnical Journal*, **25(3)**, 500-510.

3. Chiu, H. K., Johnston, I. W. and Donald, I. B. (1983), "Appropriate techniques for triaxial testing of saturated soft rock," *International Journal of Rock Mechanics and Mining Sciences & Geomechanics Abstracts*, **20(3)**, 107-120.

4. Maqsood, Z. and Koseki, J. (2015), "Behavior of gypsum mixed sand under unconfined monotonic and cyclic loading conditions," *GeoKanto, Japanese Geotechnical Society*, Japan.

5. Goto, S., Tatsuoka, F., Shibuya, S., Kim, Y., and Sato, T. (1991), "A simple gauge for local small strain measurements in the laboratory," *Soils and Foundations*, **31(1)**, 169-180.

6. Kongsukprasert, L., and Tatsuoka, F. (2005), "Ageing and viscous effects on the deformation and strength characteristics of cement-mixed gravelly soil in triaxial compression", *Soils and Foundations*, **45(6)**, 55-74.

7. Maqsood, Z., Koseki, J. and Kyokawa, H. (2019), "Effects of loading rate on strength and deformation characteristics of gypsum mixed sand", *7th International Symposium on Deformation Characteristics of Geomaterials*, Glasgow.

8. Maqsood, Z. and Koseki, J. (2019), "Time dependent strength and deformation characteristics of bounded geomaterials", *9th Asian Young Geotechnical Engineering Conference*, Pakistan (submitted)

9. Jaeger, J. C., Cook, N. G. and Zimmerman, R. (1979), "Fundamentals of rock mechanics," 3rd edition, John Wiley & Sons.

10. Labuz, J. F. and Zang, A. (2012), "Mohr–Coulomb failure criterion," *Rock mechanics and rock engineering*, **45(6)**, 975-979.

11. Gue, S. S. and Wong, S. Y. (2009), "Slope engineering design and construction practice in Malaysia," *CIE-IEM Joint Seminar on Geotechnical Engineering*, Taiwan.

12. Parry, R. H. (2004), "Mohr circles, stress paths and geotechnics," CRC Press.

EFFECTS OF LOADING RATE ON STRAIN LOCALIZATION CHARACTERISTICS

8.1 PREAMBLE

As discussed earlier in Chapter No. 5, loading rate not only dictates the strength characteristics of GMS but also affects the failure pattern of specimens. Based on the visual inspection of GMS specimens after testing, visible and distinct shear band formation was witnessed at loading rates higher than 2.0E-2 %/min., and this tendency vanishes with the decrease of loading rate. At strain rates lesser than around 2.0E-4 %/min, only bulging with no visible shear band formation was observed visually. This aspect has further studied in the present chapter by performing Particle Image Velocimetry (PIV) based image analysis [1] of GMS specimens tested at wide range of loading rates. The distributions of vertical and maximum shear strains in GMS specimens at different loading rates are presented, and significance of loading rate on strain localization characteristics of GMS is discussed.

8.2 PROCEDURE OF IMAGE ANALYSIS

In order to capture the deformation of specimens, a grid of black latex dots, having uniform spacing of 5 mm, is pasted on the rubber membrane before the initiation of loading, as shown in Fig. 8.1. A digital camera is used to take images of the grid of black dots at regular interval of time, and the time interval between the successive images was decided considering the targeted loading rate. Based on these captured image, the movement of around 170 dots was tracked during monotonic loading by using a commercial software, viz. Move-Tr2D [2]. Before analyzing the movements of dots, the setting of origin of coordinates, coordinate axis and scale on the reference image (captured prior to the onset of loading) was established, as shown in Fig. 8.2. For scaling, the real distance of 5 mm between two neighboring dots was used, and the center points

of black dots are assigned with coordinates.

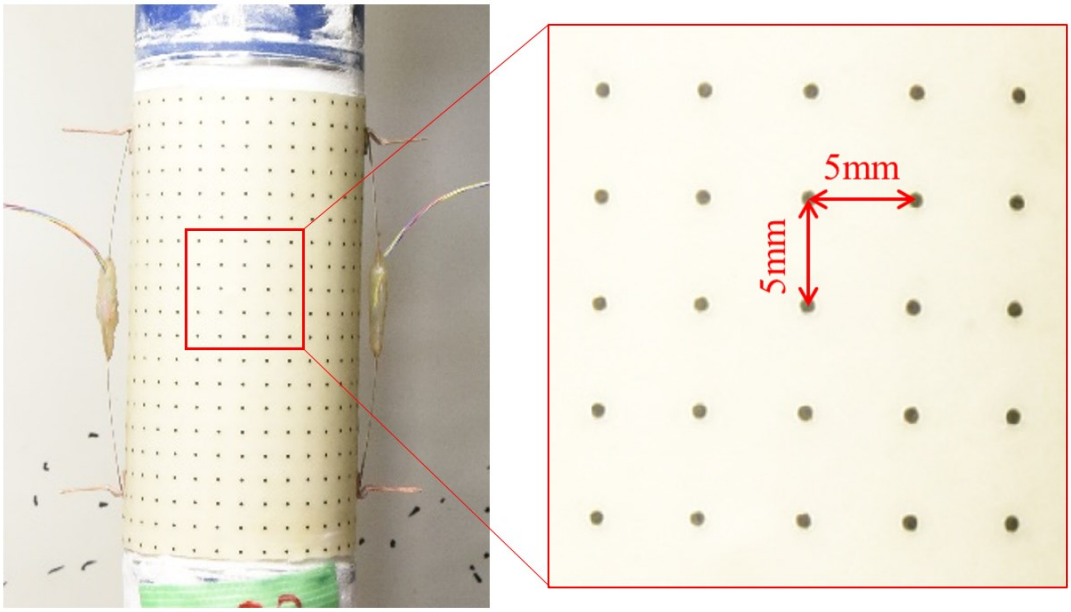

Fig. 8.1. A grid of black latex dots pasted on the rubber membrane at a uniform spacing of 5mm

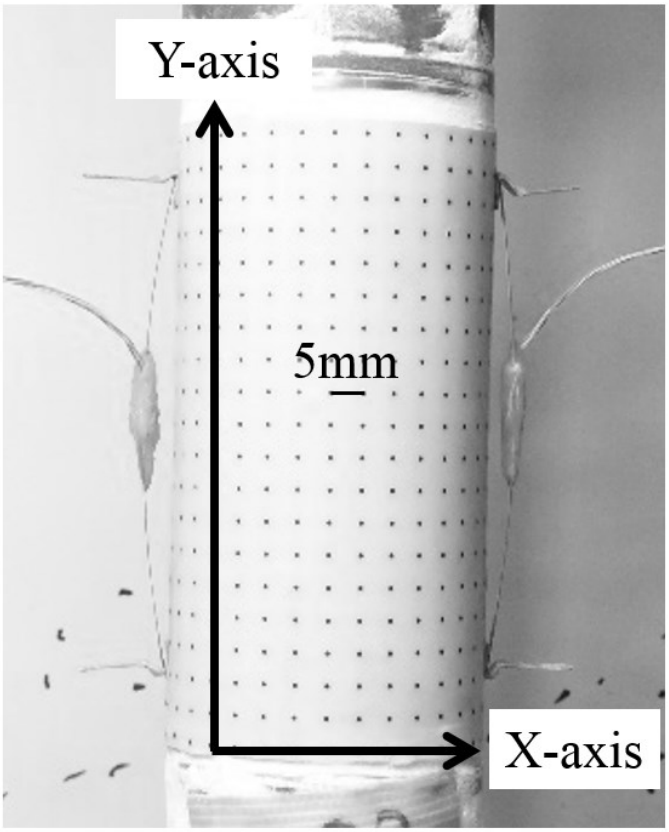

Fig. 8.2. Illustration of setting of coordinate axis and scale setting on reference image (undeformed)

The tracking was done by considering the gray pattern of the dots, and each of these dots are first manually selected on the reference image in the software, as shown in Fig. 8.3. The selected pattern of dots is than searched in the subsequent images by defining a search area. The schematic illustration of selected pattern of an individual dot and targeted search area is shown in Fig. 8.3. Moreover, a fixed reference point is also selected in the reference image, and the coordinates of dots in each image are computed with reference to this fixed point. Finally, the coordinates of each of the selected dots for all the analyzed images were saved and were used to compute strain distribution during loading.

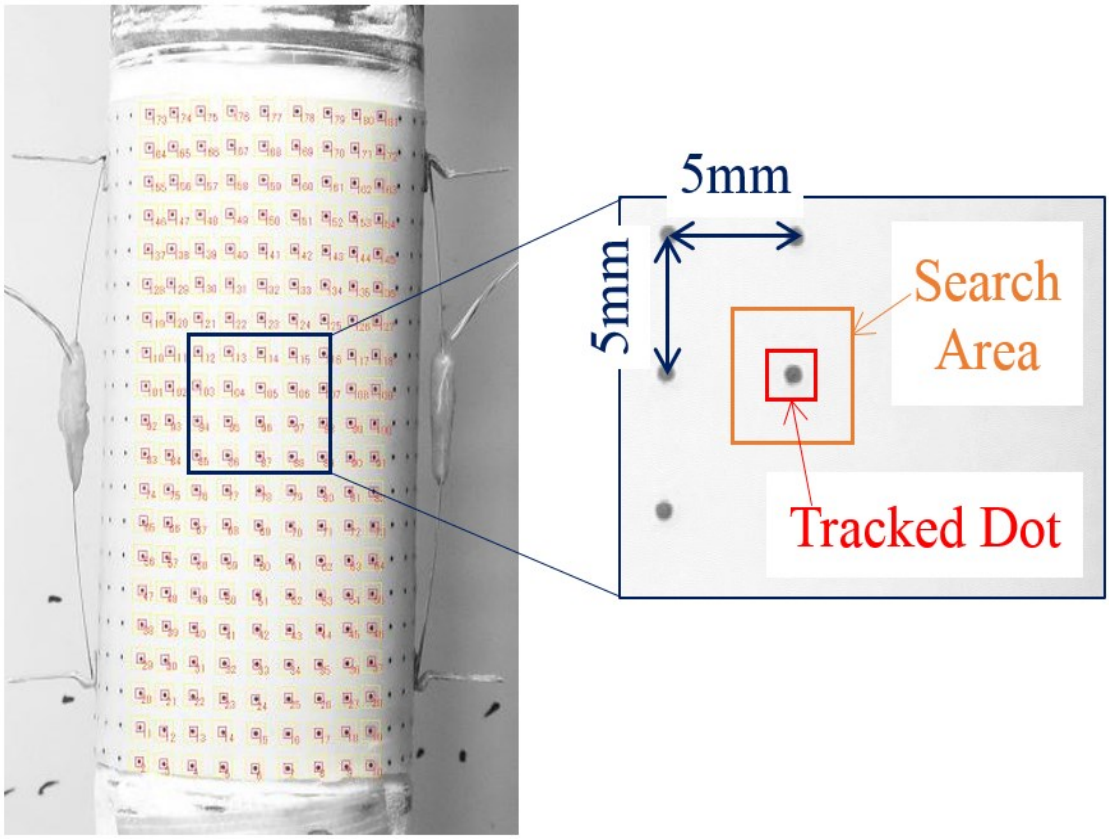

Fig. 8.3. Schematic illustration of tracked dots and assigned search areas in reference image to capturing the movements of selected dots

8.3 CALCULATION OF STRAINS

After acquiring the coordinates of tracked dots, the next step is to estimate the strains based on these coordinates. The schematic illustration to estimate strains in an element using horizontal and vertical displacement is presented in Fig. 8.4, and the average value of strain is assigned to the element [3]. Additionally, this element is mapped

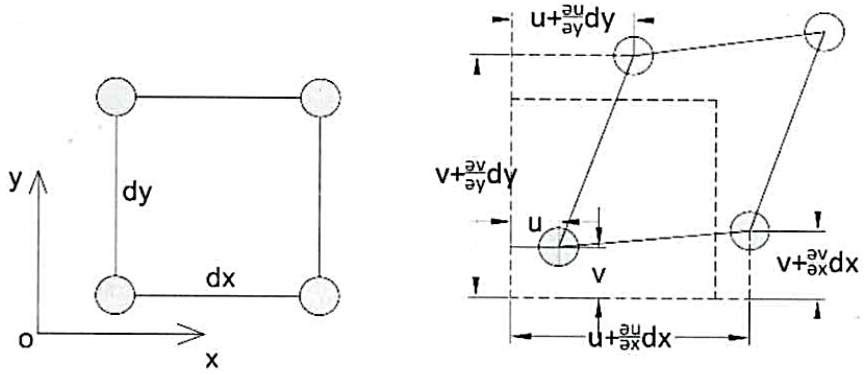

Fig. 8.4. Schematic illustration for estimation of strains in an element using horizontal and vertical displacement [3]

into a local natural coordinate system (ξ, η) for iso-parametric mapping, as shown in Fig. 8.5, and the generalized shape function for the element is presented in Eq. (8.1) based on Lagrange interpolation [3-5].

$$N_i = \frac{1}{4}(1 + \xi\xi_i)(1 + \eta\eta_i) \tag{8.1}$$

Where: ξ_i and η_i are the nodal values in natural coordinate system

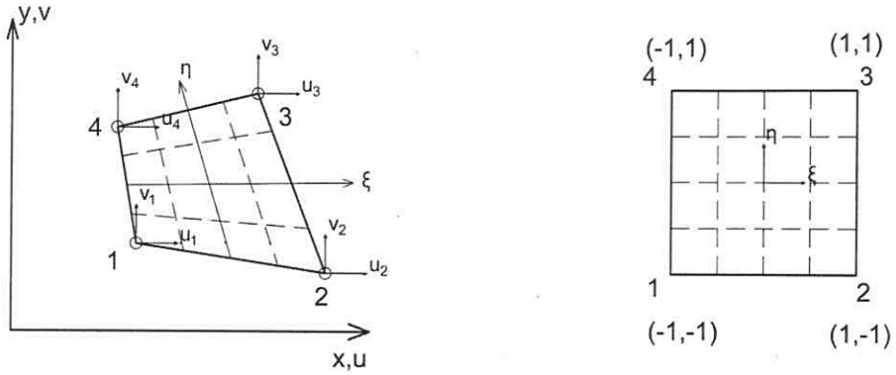

Fig. 8.5. Schematic illustration of Cartesian and natural local coordinate system [3]

The horizontal, vertical and shear strains are computed by the following expressions [3, 6]:

$$\varepsilon_x = -\frac{\partial u}{\partial x} \tag{8.2}$$

$$\varepsilon_y = -\frac{\partial v}{\partial y} \tag{8.3}$$

$$\gamma_{xy} = -\left(\frac{\partial u}{\partial y} + \frac{\partial v}{\partial x}\right) \tag{8.4}$$

In order to compute differential of Cartesian plane with respect to local natural coordinate plane (ξ, η), Jacobian of two-dimensional transformation is necessary [7], and is present in Eq. (8.5) and Eq. (8.6).

$$\begin{bmatrix} dx \\ dy \end{bmatrix} = \begin{bmatrix} \frac{\partial x}{\partial \xi} & \frac{\partial x}{\partial \eta} \\ \frac{\partial y}{\partial \xi} & \frac{\partial y}{\partial \eta} \end{bmatrix} \begin{bmatrix} d\xi \\ d\eta \end{bmatrix} = J^T \begin{bmatrix} d\xi \\ d\eta \end{bmatrix} \tag{8.5}$$

$$\begin{bmatrix} d\xi \\ d\eta \end{bmatrix} = \begin{bmatrix} \frac{\partial \xi}{\partial x} & \frac{\partial \xi}{\partial y} \\ \frac{\partial \eta}{\partial x} & \frac{\partial \eta}{\partial y} \end{bmatrix} \begin{bmatrix} dx \\ dy \end{bmatrix} = J^{-T} \begin{bmatrix} dx \\ dy \end{bmatrix} \tag{8.6}$$

In Eq. (7.2), J^T is the Jacobian matrix of Cartesian coordinate plane (x, y) in terms of local natural coordinate plane (ξ, η). On the other hand, J^{-T} is the Jacobian matrix of local natural coordinate plane (ξ, η) in terms of Cartesian coordinate plane (x, y). The expression to compute strains using Jacobian matrix and Eq. (8.2) to Eq. (8.3) is expressed by the following expression [3, 6]:

$$\begin{bmatrix} \frac{\partial u}{\partial x} & \frac{\partial v}{\partial x} \\ \frac{\partial u}{\partial y} & \frac{\partial v}{\partial y} \end{bmatrix} = [J]^{-1} \begin{bmatrix} \frac{\partial N_1}{\partial \xi} & \frac{\partial N_2}{\partial \xi} & \frac{\partial N_3}{\partial \xi} & \frac{\partial N_3}{\partial \xi} \\ \frac{\partial N_1}{\partial \eta} & \frac{\partial N_2}{\partial \eta} & \frac{\partial N_3}{\partial \eta} & \frac{\partial N_4}{\partial \eta} \end{bmatrix} \begin{bmatrix} u_1 & v_1 \\ u_2 & v_2 \\ u_3 & v_3 \\ u_4 & v_4 \end{bmatrix} \tag{8.7}$$

In Eq. (7.7), the values of u and v are the horizontal and vertical deformations, and can be computed by tracking the movements of dots. Moreover, strains are computed at the center points of the elements, and the values of ξ and η are zero because of this approach [3, 6]. Finally, the values of principal stains were computed by the Eq. (8.8) to Eq. (8.10) [3, 6], and strain contours are plotted in MATLAB using Delaunay triangulation interpolation techniques [8].

$$\varepsilon_1 = \frac{1}{2}\left(\varepsilon_x + \varepsilon_y\right) + \sqrt{\frac{1}{4}\left(\varepsilon_x - \varepsilon_y\right)^2 + \left(\frac{\gamma_{xy}}{2}\right)^2} \tag{8.8}$$

$$\varepsilon_2 = \frac{1}{2}\left(\varepsilon_x + \varepsilon_y\right) - \sqrt{\frac{1}{4}\left(\varepsilon_x - \varepsilon_y\right)^2 + \left(\frac{\gamma_{xy}}{2}\right)^2} \tag{8.9}$$

$$\gamma_{max} = \varepsilon_1 - \varepsilon_2 \tag{8.10}$$

8.4 EFFECTS OF LOADING RATE ON STRAIN LOCALIZATION CHARACTERISTICS OF GMS

The distribution of vertical and maximum shear strain of GMS specimens tested at strain rate higher than 4.0E+0 %/min (belonging to Zone-1) under unconfined condition, along with the stress-strain relationships are presented in Figures 8.6 and 8.7. The distribution of strains are computed at different stages of tests, and are marked on the prospective stress strain curves. Additionally, the shear bands witnessed on the visual inspection of these specimens are also highlighted on the captured images of these specimens. It is clearly evident from these figures that the formation of shear band under higher loading rates is of progressive nature, and is formed immediately after the pre-peak strain softening.

Additionally, the vertical strains are localized at a relatively smaller region of specimen even at the earlier stages of residual strength, viz. S3, and major portion of specimen is intact. For instance, the vertical strains induced within GD1-3D(4.4E+0)-D01 is restricted to a very thin upper region, and no noticeable vertical strain accumulation can be witnessed for the rest of the specimen, as shown in Fig. 8.7. Additionally, this finding was also confirmed by the visual inspection of failed specimen after testing, and no micro-cracking or damage was visually observed in the intact portion. Moreover, the distribution of maximum shear strain in these figures also suggest that shearing of specimens in the post-peak region is primarily due to the sliding of intact portions along the failure surface of specimen.

The negligible amount of vertical strain accumulation in major portion of specimen indicates that limited damage of the microstructure of GMS occurred at higher strain rates. Therefore, these findings also support the concept that major portion of the total strain energy stored with the specimen at higher loading rate is recoverable (elastic) energy due to large hysteresis between crack formation and successive increment of loading [9-11]. In spite of the fact that the specimens were cured for different periods, the general pattern of strain localization characteristics are almost comparable up to the beginning to residual stress levels, viz. S3, as evident in Figures 8.6 and 8.7. Moreover, the failure patterns of specimens observed visually coincides unerringly with the results of image analysis, consequently endorses the reliability of the adopted methodology.

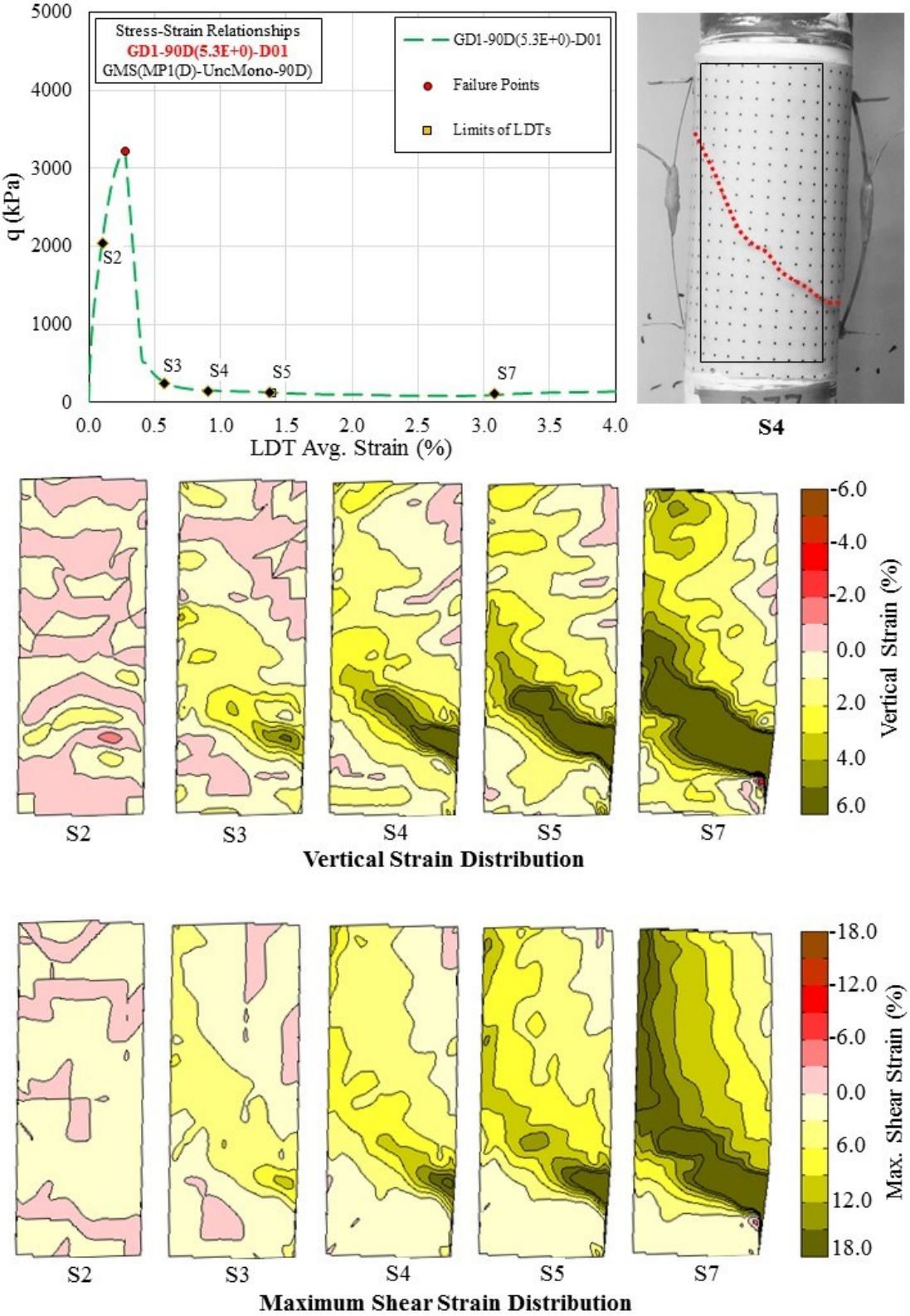

Fig. 8.6. Distribution of vertical and maximum shear strain
in GD1-90D(5.3E+0)-D01 (Curing Time = 90Days, 5.3E+0%/min)

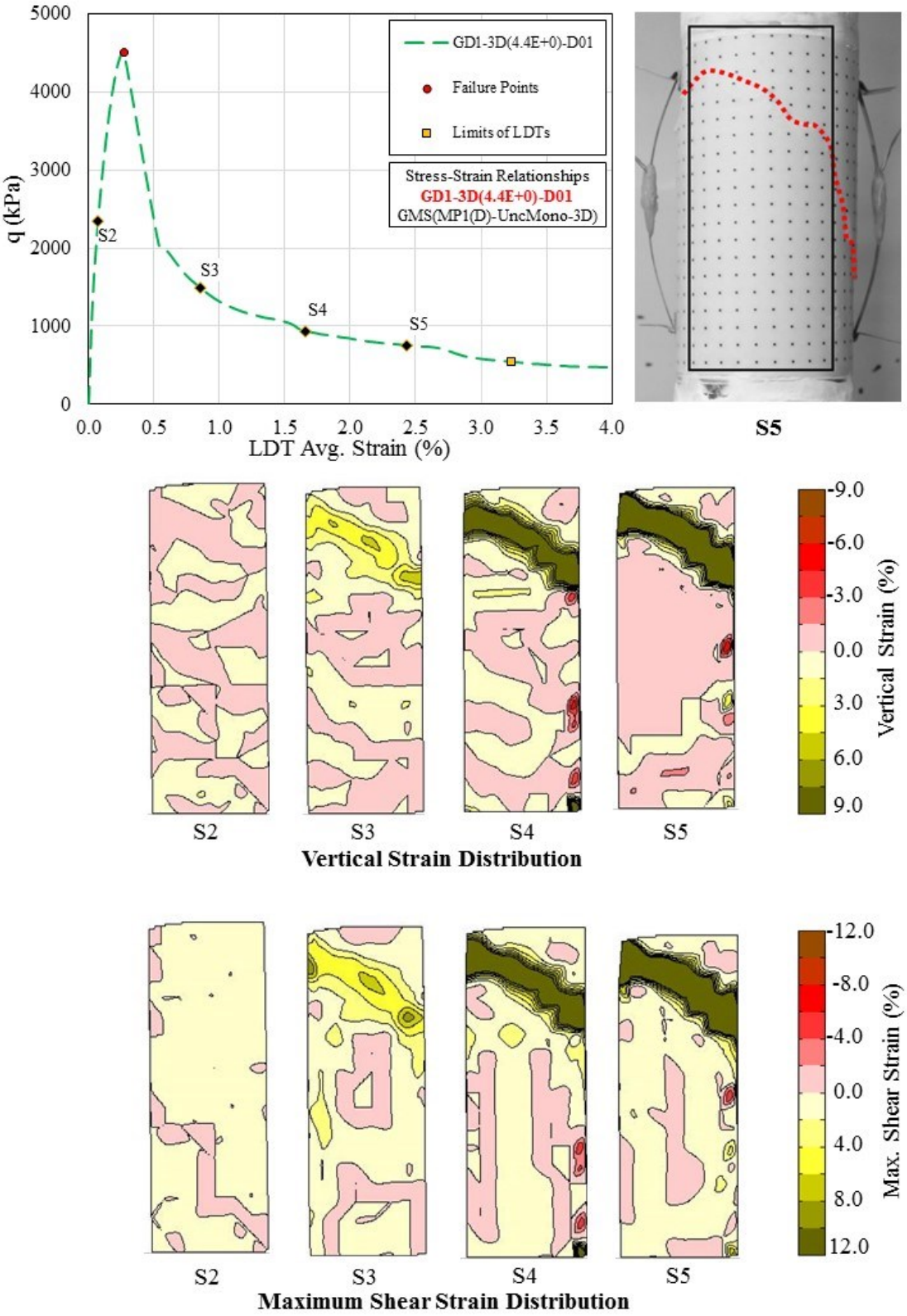

Fig. 8.7. Distribution of vertical and maximum shear strain
in GD1-3D(4.4E+0)-D01 (Curing Time = 3Days, 4.4E+0%/min)

By adopting the same procedure, the strain distribution of specimens tested at strain rates of 2.4E-2 and 1.7E-3 %/min (belonging to Zone-2) are presented in Figures 8.8 and 8.9. In case of GD1-90D(2.4E-2)-D03, vertical strain accumulated in almost entire specimen during the post-peak strain softening (i.e. up to S7), as evident in Fig. 8.8. The onset of shear band formation can also be witnessed at this stage, as indicated by the relatively higher values of shear strain in Fig. 8.8. The residual strain of this specimen is achieved at about 2.5%, and a fully evolved shear band can easily be observed at the beginning of residual state (i.e. up to S120).

It is noteworthy that the general strain distributions of GD1-90D(2.4E-2)-D03 specimen are relatively more diffuse at this loading rate compared with the results presented in Figures 8.6 and 8.7, especially up to the beginning of residual state. Therefore, a relatively higher portion of total absorbed energy is consequently consumed for the formation of micro cracks and permanent damage to the microstructure of GMS at this relatively slower loading rate. As a result, the strength value is relatively lesser for GD1-90D(2.4E-2)-D03 compared to GD1-90D(5.3E+0)-D01.

At a strain rate of 1.7E-3 %/min, it can be easily observed that an almost uniform distribution of vertical and maximum shear strain can be witnessed at the peak strength (i.e. at S81), as shown in Fig. 8.9. Afterwards, the strains accumulated at the middle lower portion of the specimen, and no clear indication of distinct shear band can be observed from these results. However, a relatively diffused pattern of multiple shear bands was visually observed in the specimen, along with noticeable bulging. Such a diffuse pattern of strain accumulation has also been reported for gypsum treated geomaterials under plane strain conditions, and was stated that uniform accumulation of strain at slower loading rates is credited to ample time available for distribution of strains [12].

The strain localization characteristics of specimens tested at strain rates of 2.0E-4 %/min, (i.e. belonging to Zone-3) are presented in Figures 8.10. Based on these results, it is evident that some sort of strain localization in a limited region is apparent in the pre-peak region (i.e. up to S34). Besides, a well uniform distribution of vertical strain is observable near the peak state (S261) and the vertical strains accumulate throughout the specimen in the post-peak region. It is noteworthy that no shear band or cracks were observed in the failed specimen with visual inspection. However, the distribution of shear

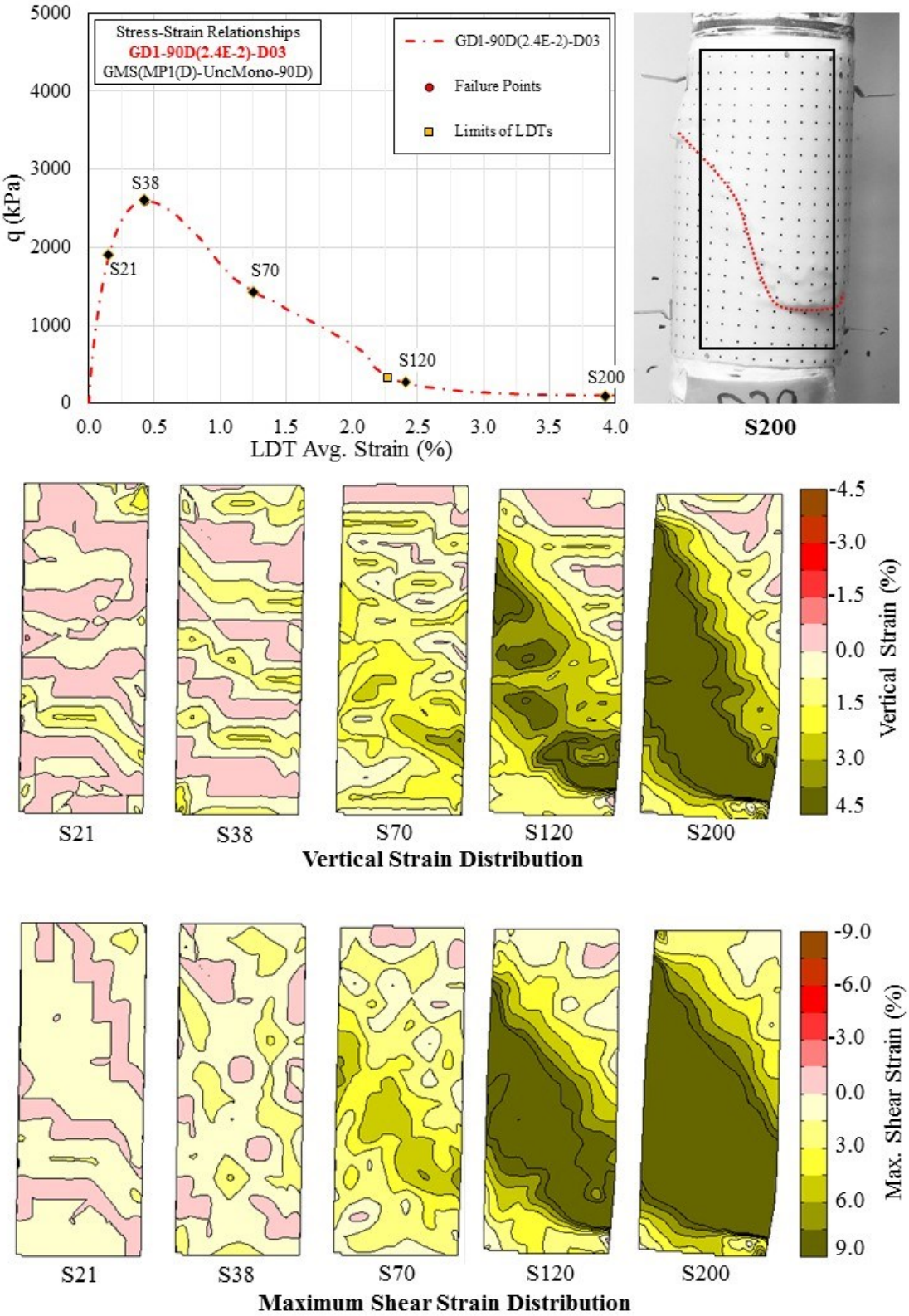

Fig. 8.8. Distribution of vertical and maximum shear strain
in GD1-90D(2.4E-2)-D03 (Curing Time = 90Days, 2.4E-2%/min)

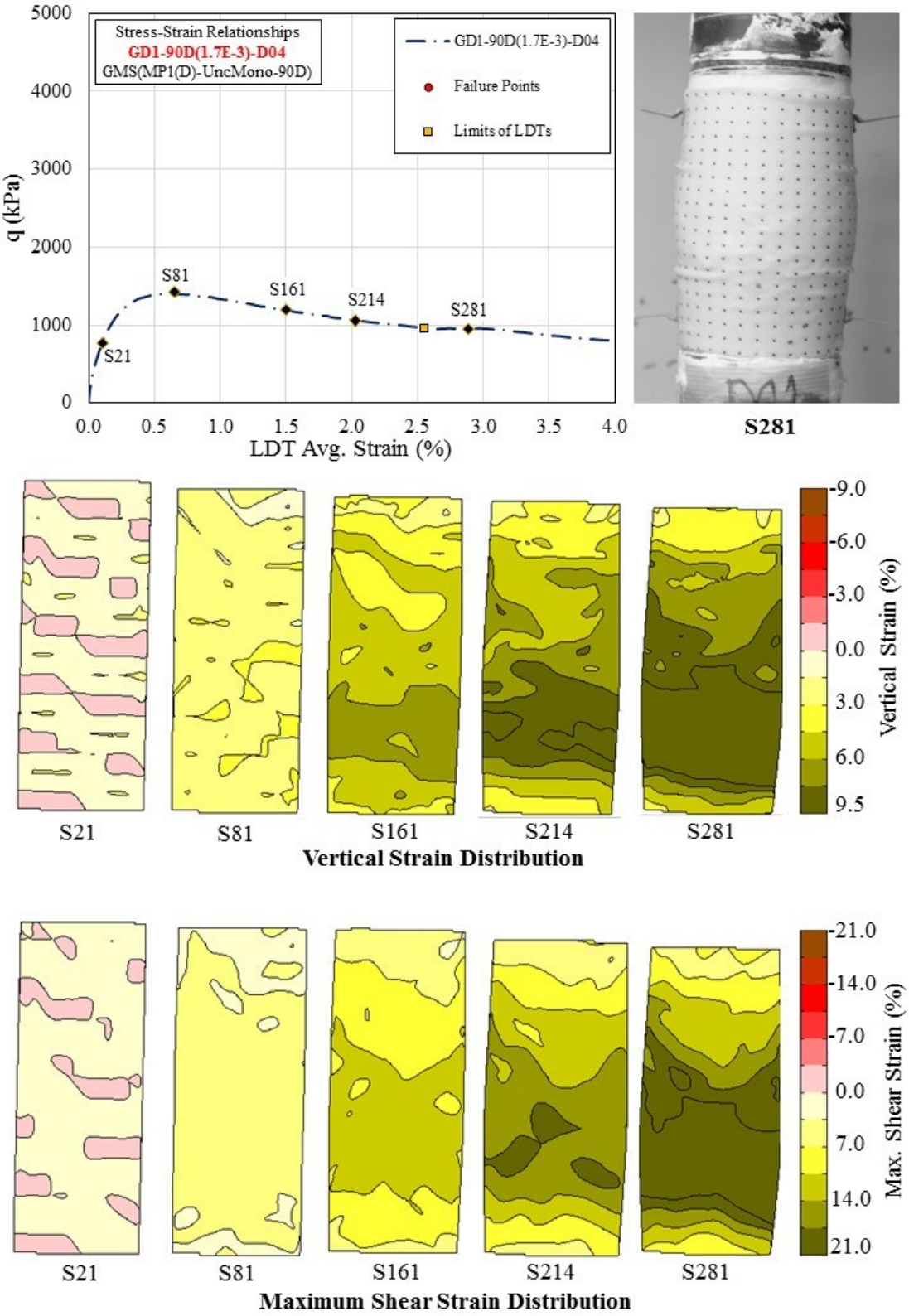

Fig. 8.8. Distribution of vertical and maximum shear strain
in GD1-90D(1.7E-3)-D04 (Curing Time = 90Days, 1.7E-3%/min)

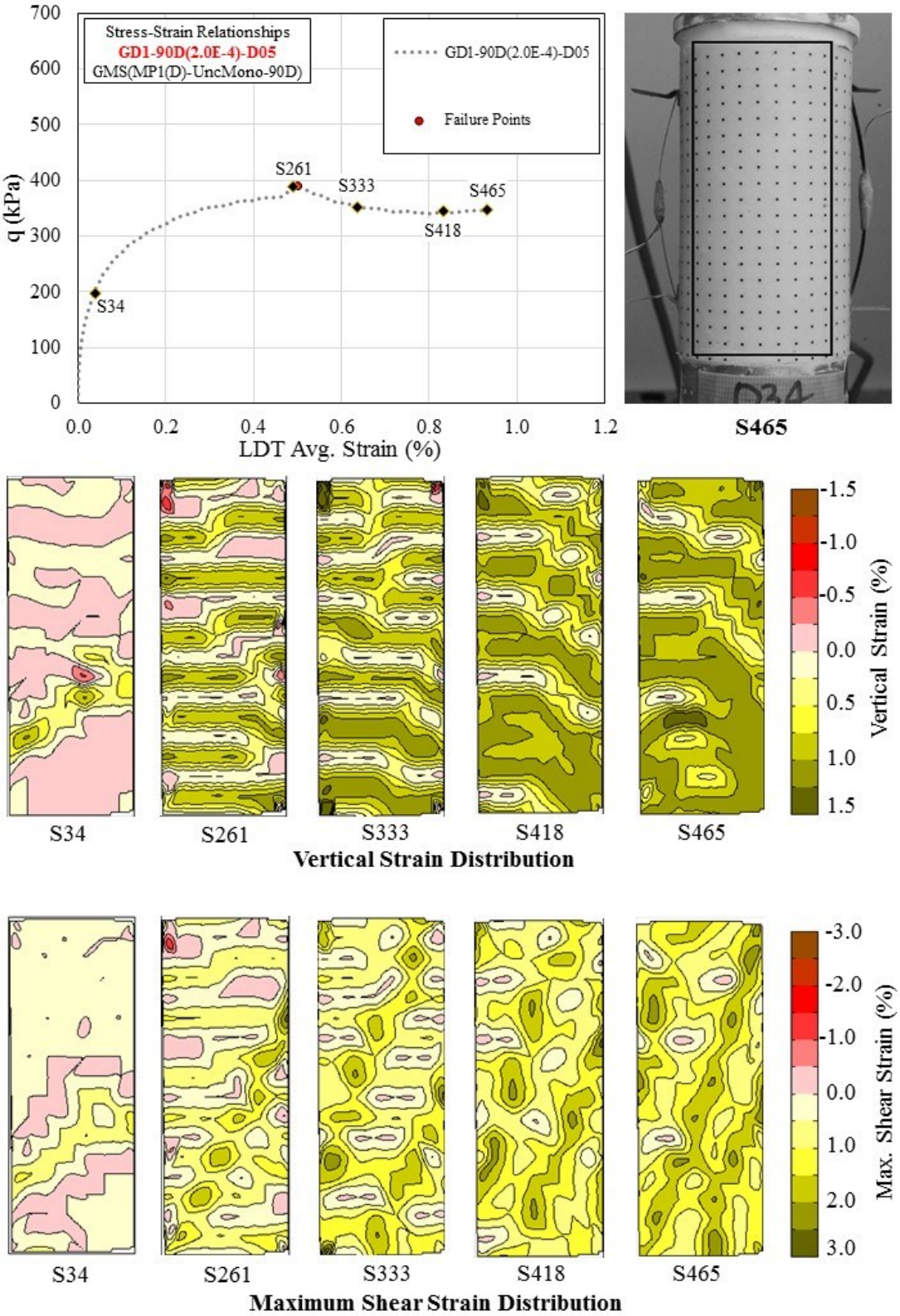

Fig. 8.10. Distribution of vertical and maximum shear strain
in GD1-90D(2.0E-4)-D05 (Curing Time = 90Days, 2.0E-4%/min)

strains shows the possible existence of multiple zones of strain localization. It is believed that there may exist minor non-visible micro-cracking patterns developed under very slow loading rate, and ultimately contributed to significant reduction in peak strength.

8.5 SUMMARY OF FINDINGS

- In case of GMS specimens tested at higher loading (Zone-1), formation of shear band specimens was found to of progressive nature, and was formed immediately after the pre-peak strain softening.
- Additionally, the vertical strains were localized at a relatively smaller region of specimen even at the earlier stages of residual strength. The negligible amount of vertical strain accumulation in major portion of specimen indicates that limited damage of the microstructure of GMS occurred at higher strain rates.
- The findings stated above also support the concept that major portion of the total strain energy stored with the specimen at higher loading rate is recoverable (elastic) energy due to large hysteresis between crack formation and successive increment of loading.
- The strain distribution at strain rates of 2.4E-2 %/min (middle range of Zone-2) showed that vertical strain accumulated in almost entire specimen during the post-peak strain softening. Moreover, fully evolved shear bands was observed at the beginning of residual state.
- The results of another specimen belonging to lower range of Zone-2 (1.7E-3 %/min) showed significant vertical and maximum strain accumulated at the middle lower portion of the specimen, and no clear indication of distinct shear band were observed from these results. Such an accumulation was due to presence of a relatively diffused pattern of multiple shear bands revealed after visual inspection.
- In spite of the fact that no visible shear bands were observed for specimen tested at strain rates lesser than 2.0E-4 %/min (Zone-3), the results of maximum shear strain distribution showed the possible existence of multiple zones of strain localization which contributed to strength reduction at lower loading rates.

8.6 REFRENCES

1. Raffel, M., Willert, C. E., Scarano, F., Kähler, C. J., Wereley, S. T., and Kompenhans, J. (2013). "Particle image velocimetry: a practical guide," *Springer*.
2. Move-Tr/2D, 2D-Motion Analysis cited from http://www.library-japan.com/pro_1.html dated July 25, 2019.
3. Zaho C. (2017), "Direct and indirect local deformation measurements of sand specimen in undrained cyclic triaxial and torsional shear tests," *PhD Thesis, The University of* Tokyo, Japan, 59-78.
4. Ergatoudis, I., Irons, B. M., and Zienkiewicz, O. C. (1968), "Curved, isoparametric, "quadrilateral" elements for finite element analysis," *International Journal of Solids and Structures*, **4(1)**, 31-42.
5. Huebner, K. H., Dewhirst, D. L., Smith, D. E., and Byrom, T. G. (2008), "The finite element method for engineers," *John Wiley & Sons*.
6. Monge, R. S. (2002), "Effects of large amplitude cyclic loading on deformation and strength peroperties of cement treated sand," *Master's Thesis, The University of Tokyo, Japan*.
7. Felippa, C. A. (2004), "Introduction to finite element methods," *Department of Aerospace Engineering Sciences, University of Colorado at Boulder.*
8. MathWorks®, Documentation of Delaunay triangulation cited from https://www.mathworks.com/help/matlab/ref/delaunay.html dated July 25, 2019.
9. Mahanta, B., Singh, T. N., Ranjith, P. G. and Vishal, V. (2018), "Experimental investigation of the influence of strain rate on strength; failure attributes and mechanism of Jhiri shale," *Journal of Natural Gas Science and Engineering*, **58**, 178-188.
10. Liang, C., Wu, S., Li, X. and Xin, P. (2015), "Effects of strain rate on fracture characteristics and mesoscopic failure mechanisms of granite," *International Journal of Rock Mechanics and Mining Sciences*, **76**, 146-154.

11. Liang, W. G., Zhao, Y. S., Xu, S. G. and Dusseault, M. B. (2011), "Effect of strain rate on the mechanical properties of salt rock," *International Journal of Rock Mechanics and Mining Sciences*, **1(48)**, 161-167.

12. Bhandari, A. R. (2005), "Experimental study of strain rates effects on strain localization characteristics of soft rocks," Soils and Foundation, **45(1)**, 125-140.

CONCLUSIONS AND FUTURE RECOMMENDATIONS

9.1 PREAMBLE

The prime emphasis of the present study is to rational evaluation of the loading rate dependent mechanical behavior of artificially bounded geomaterials, viz. GMS and CTS, under different loading conditions. Although detailed findings are discussed at end of each of the chapters of this dissertation, the present chapter focuses on comprehending these findings in a more coherent manner to deduce prolific conclusions about the loading rate dependency of these geomaterials. Additionally, the recommendations to extend the scope of this research topic in future are also highlighted in the latter half of this chapter.

9.2 CONCLUSIONS

Based on the results obtained during this research endeavor the following conclusions can be drawn:

9.2.1 Reproduction and curing of GMS and CTS specimens

The method adopted for the laboratory production of GMS and CTS specimens proved to be viable and efficient. Compared with moist tamping or static compaction techniques, the adopted method not only meet the extensive production demand but also reduced the physical labor associated with specimen preparation. Although different techniques of curing were considered at the earlier stages but the selected polythene sheet curing proved to be reasonably feasible enough to cure large number of specimens for longer duration of time.

9.2.2 Reliability assessment criterion

In spite of the fact that substantial undesirable variations in UCS values of GMS specimens were observed under similar testing conditions. The proposed reliability

criterion using local strain measurements played a key role to assess the reliability of test results. Therefore, it can be concluded that such an approach is lucrative to enhance the consistency of results under similar testing condition, and can provide enough assurance to draw authentic conclusions from the scrutinized results.

9.2.3 Significance of impurities and additives in commercial gypsum

Under similar testing conditions, GMS-MP1 specimens prepared by using different batches of gypsum showed significant differences in peak strength. This variability in strength is potentially associated with the presences of different impurities and additives, such as soluble calcium sulphate anhydrite, calcium sulphate dihydrate and potassium sulphate etc. Therefore, it is essential to consider the role of these substances while evaluating the mechanical behavior of gypsum treated geomaterials for practical applications.

9.2.4 Effects of ageing on the mechanical behavior of GMS

The effects of ageing on the strength and deformation behavior of GMS-MP1 were only found to be noticeable in the earlier first month of curing, and no significant effects of ageing were observed afterwards up to 9 months. Importantly, a perceptible reduction (around 20%) in peak strength of GMS-MP1 was observed during the first month of curing, potentially due to the volume expansion associated with the delayed formation of dihydrate crystals. Considering the practical application of gypsum as a cementing agent, such an early strength reduction is very fundamental to rationally evaluate the long-term performance and serviceability of gypsum treated geomaterials.

9.2.5 Effects of ageing on the mechanical behavior of CTS

In contrast to GMS, a continuous increase in the peak strength values of CTS was observed in the first month of curing, and no further effects of curing on the UCS values were witnessed up to 6 months. In addition, significant increase in pre-peak stiffness and post-peak strain softening with curing time was also witnessed during the first month of curing. However, the effects of ageing on stress-strain response were practically insignificant between curing periods of 1 to 6 months.

9.2.6 Loading rate dependency of GMS under unconfined conditions

Significant effects of loading rate on UCS and stress-strain responses of GMS were witnessed for GMS. An increasing trend of UCS and pre-peak stiffness was observed with the increase in loading rate, and the effects of loading rate on the mechanical behaviour of GMS were divided into three distinct zones of strain rates, viz. Zones 1, 2 and 3. In general, the effects of loading rate on strength and defamation characteristics of GMS were found to be relatively trivial for specimens having instantaneous failure strain rates higher than approximately 5.0E-1 %/min, viz. Zone-1.

However, substantial reduction in peak strength and pre-peak stiffness of GMS specimen with the decrease in strain rate was observed for specimens tested at strain rates lesser than 2.0E-3 %/min, viz. Zone-3. Moreover, the effects of different gypsum batches, gypsum content (G/S = 80% to 40%) and curing conditions are negligible on the loading rate dependency of GMS.

Such a prominent loading rate dependency of GMS is believed to be linked with the micromechanical peculiarities of GMS. Among these peculiarities is the inherent viscosity of the dihydrate crystals possibly due to the weak intermolecular forces. Additionally, the porous nature of interlocked needle-shape mass is also believed to induced relatively lesser frictional forces for crack propagation under slower loading rates.

The estimated relationship between dissipated and recoverable strain energies of specimens tested at different loading rates also showed a tendency of significant damage to the microstructure of GMS under relatively slower loading rates. Considering these aspects, it is essential to rationally evaluate the in-situ loading conditions for gypsum treated geomaterials as their mechanical behavior is very sensitive to loading rates, especially at strain rates lesser than 2.0E-3%.

9.2.7 Loading rate dependency of CTS under unconfined conditions

The effects of loading rate on the peak strength values and stress-strain response of CTS are relatively limited compared with GMS. The effects of loading rate on the total strain energy per unit volume of CTS specimens are relatively trivial compared with GMS. Moreover, the approximated normalized elastic and dissipated strain energies are also not

significantly affected by the loading rates, and the peak strength of CTS was consequently not greatly dictated by the loading rate.

9.2.8 Behavior of GMS under unconfined creep and cyclic loading

The behavior of GMS(MP1) under unconfined creep loading is very unpromising, as a small normalized creep load of mere 32% is sufficient enough to cause a creep failure within a relatively shorter duration of time, viz. about 9 days. Moreover, an increasing trend of axial strain accumulation with the decrease of creep load was witnessed, and an axial strain accumulation of 9.157% was observed for GMS specimen tested at normalized creep load of 32%.

In case of cyclic loading conditions, the effects of cyclic amplitude on axial strain accumulation during cyclic loading are quite marginal, as the values of failure strains are generally approximately similar in different tests. Besides, the results of unconfined creep and cyclic loading tests also indicated that the values of failure strain in cyclic and creep tests are principally governed by the maximum compressive stress induced during cyclic and creep loading respectively.

For both cyclic and creep tests, almost linear trend of axial strain accumulation with elapsed time was witnessed on full-logarithmic plot, followed by a rapid increase in axial strain values after the onset of failure. Moreover, the trends of axial strain accumulation during creep and cyclic loading are practically identical to each other. The anticipated justification for the identical strain accumulation characteristics of GMS was attributed to the intrinsic natures of different types of loading and viscous behavior of GMS.

A unique relationship between the normalized failure stress and instantaneous failure strain rate of GMS specimens tested under unconfined creep and cyclic loading, and the behavior of GMS under unconfined creep and cyclic loading conditions are similar to each other and distinctively different than unconfined monotonic tests.

Based on these aspects, it is concluded that GMS is very weak against creep/cyclic loading, and long-term in-situ performance of GMS under such loading conditions is expected to be inauspicious compared with other bounded geomaterials. Moreover,

exceptionally large values of creep induced deformations in GMS are also susceptible to deteriorate the long-term serviceability of gypsum treated geomaterials.

9.2.9 Behavior of CTS under unconfined creep loading

The performance of CTS under unconfined creep loading conditions was found to be considerably superior to GMS. Moreover, creep induced axial strain accumulation was witnessed to be significantly lesser in CTS compared with GMS. The instantaneous strain rates induced during creep in CTS specimens were noticeably lesser than the GMS specimens subjected to equivalent normalized loads, but the trends of variation of instantaneous strain rate in both CTS and GMS were quite identical.

9.2.10 Behavior of GMS under isotropic drained consolidation

GMS specimens exhibit an increasing trend of axial strain accumulation with the increase of isotropic consolidation duration, and approximately 3.0% of externally measured axial strain was witnessed for specimen consolidated for 21.7 days at 800kPa. The results suggest that curing at higher confining stress level enhances the strength characteristics of GMS, and it is also likely that a relatively denser and stronger microstructure was rather achieved during consolidation at higher confining stresses.

9.2.11 Combined effects of loading rate and confining stress on the mechanical behavior of GMS

The effects of confining stress are quite trivial on the strength characteristics of GMS(MP1), as a maximum increase of merely 20% in the normalized deviator stress at failure was observed even at confining stress of 800 kPa for specimen subjected to highest strain rates. However, no noticeable effects of confining stress can be observed at strain rate of 1.7E-03 %/min.

Based on the results of consolidated drained monotonic tests performed at four different loading rates under confining stress of 400 and 800 kPa, it was concluded that the effects of loading rate are generally quite similar on stress-strain behaviour in the pre-peak region of GMS for both unconfined and confined monotonic loading conditions. The effects of loading rate on the normalized strength of GMS under different confining stress conditions are indubitably comparable with each other. .However, the post-peak behavior of GMS is greatly affected by the confining stress values, and the phenomenon

of post-peak strain softening diminishes greatly with increase of confining stress.

In general, an increasing trend of values of cohesion of GMS specimens with the increase of strain rate was observed throughout the tested range. On the other hand, the values of angle of internal friction of GMS increase with the increase of strain rate up to an instantaneous strain rate of 2.3E-1 %/min (Zone-2), and no effects of loading rate on the values of angle of internal friction of GMS specimens were observed for specimens tested at strain rates higher than 2.3E-1 %/min. (Zone-1).

9.2.12 Effects of loading rate on the strain localization characteristics of GMS

In case of GMS specimens tested at higher loading (Zone-1), formation of shear band specimens was found to of progressive nature, and was formed immediately after the pre-peak strain softening. The negligible amount of vertical strain accumulation in major portion of specimen indicated that limited damage of the microstructure of GMS occurred at higher strain rates. This also supports the concept that major portion of the total strain energy stored with the specimen at higher loading rate is recoverable (elastic) energy due to large hysteresis between crack formation and successive increment of loading.

At relatively lower strain rate of 1.7E-3 %/min (lower range of Zone-2), GMS specimen showed significant vertical and maximum strain accumulated at the middle lower portion of the specimen, and no clear indication of distinct shear band were observed from these results. However, such an accumulation was due to presence of a relatively diffused pattern of multiple shear bands revealed after visual inspection.

In spite of the fact that no visible shear bands were observed for specimen tested at strain rates lesser than 2.0E-4 %/min (Zone-3), the results of maximum shear strain distribution showed the possible existence of multiple zones of strain localization which contributed to strength reduction at lower loading rates.

9.3 FUTURE RECOMMENDATIONS

Owing to the highly viscous behavior of GMS observed in the present study, it is thus not recommended to use as a cementing agent alone for practical purposes, especially under slower or sustained loading conditions. The study also confirms the promising

long-term performance of cement treated geomaterials under slow loading rates and creep. Hence, it is highly anticipated that the treated soils using mixture of other conventional cementing agents, such as cement or lime etc., and gypsum will positively showed relatively reliable long-term performance. The less viscous cementing agents will compensate for the high viscous behavior of gypsum, and a required composite of gypsum and other cementing agents can be improvised depending upon the desired long-term performance under different loading conditions. Therefore, these aspects can be further explored in future to figure out the potential applications of gypsum in the field of geotechnical engineering.

Although the long-term performance of GMS is not commendable, but gypsum can be used for temporary strength enhancement. One of the typical example could be the mixing of gypsum with highly non-workable waste dredged clay. These dredged clays are often considered as waste product of dredging and a high cost is associated with the disposal of these clays due to their poor workability. The addition of gypsum in such soils can reduce the water content and provide a workable mixture with desired strength. Afterwards, these improved soils may be moved to the desired destinations, and can also be used as a potential aggregate for practical applications.

In the light of the fact that GMS showed significantly large amount of strain accumulation during creep, it is expected that by introducing some sort of recycled plastic resins or fibers in gypsum treated geomaterials may provide additional resistance against crack propagation during creep and slow loading conditions. Therefore, it is recommended to study the enhancement of micromechanical characteristics of gypsum treated geomaterials by the addition of these substances.

The highly porous hardened dihydrate mass comprising of needle-shape crystals is believe to be a one of the pivotal reason for the highly viscous behavior of GMS. The addition of different fillers such as silica fume, fly ash or rice husk etc, in gypsum treated geomaterials can also potentially enhance the microstructure. Thus, such aspects can also be explored in future to enhance the time-dependent strength and deformation behavior of gypsum treated geomaterials.

In the present study, the long-term performance of GMS was studied at natural

water content to avoid any possible chemical changes. However, there may exist a plentiful in-situ conditions were gypsum treated geomaterials may come in contact with ground water or other substances, and the effects of chemical weathering on the long-term behavior of gypsum treated geomaterials still needs to be studied thoroughly. Finally, the environmental hazards associated with the use of gypsum, such as release of H_2S and associated contamination of ground water or atmosphere, should also be studied in depth to successfully used gypsum for field applications.

APPENDIX-A

A.1 Calibration of Load Cell (Unconfined Compression Machine)

Calibration Results of Load Cell (Unconfined Compression Machine)	
CAL Value	4000 με
b-Value	4.8378 N/με
Physical Value	19351.2 N

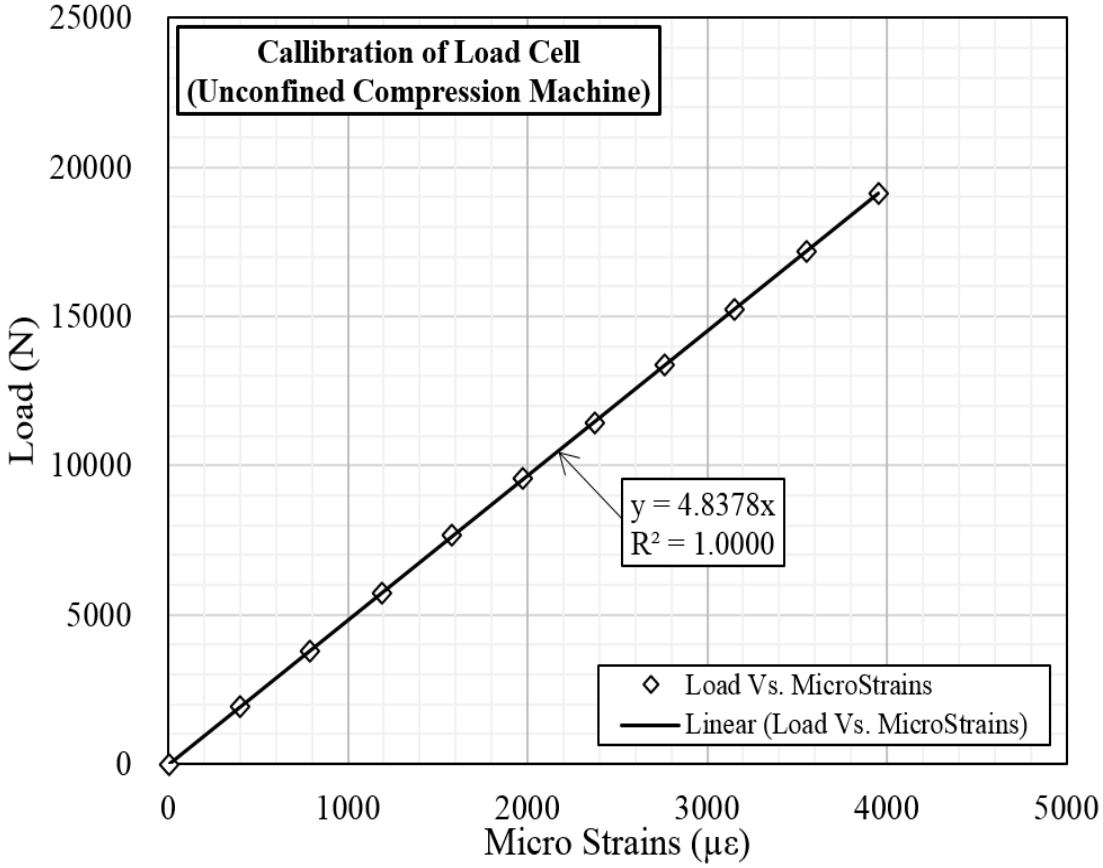

Fig. A.1. Calibration Results of Load Cell
(Unconfined Compression Machine)

A.2 Calibration of Load Cell (Triaxial Compression Machine)

Calibration Results of Load Cell (Triaxial Compression Machine)	
CAL Value	3700 με
b-Value	3.2528 N/με
Physical Value	12035.4 N

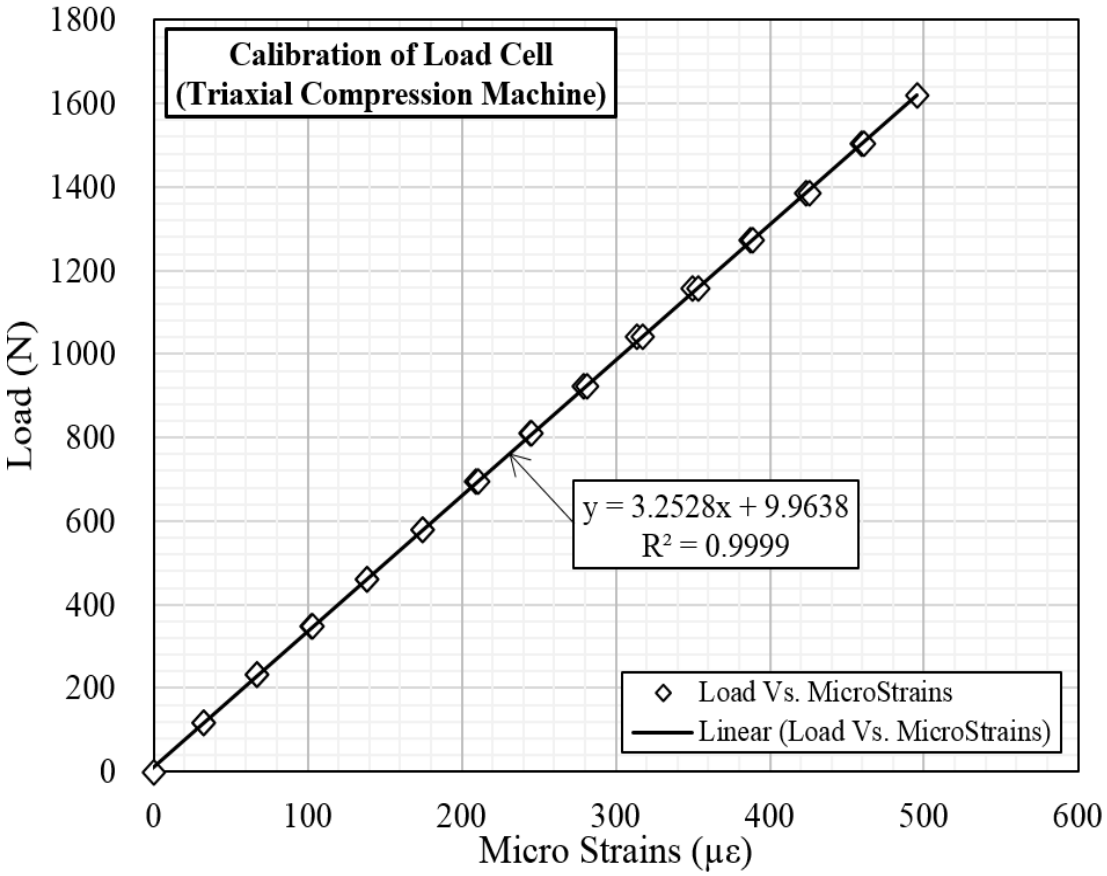

Fig. A.2. Calibration Results of Load Cell
(Triaxial Compression Machine)

A.3 Calibration of EDT (Unconfined Compression Machine)

Calibration Results of EDT (Unconfined Compression Machine)	
CAL Value	9999 με
b-Value	0.0020 mm/με
Physical Value	19.998 mm

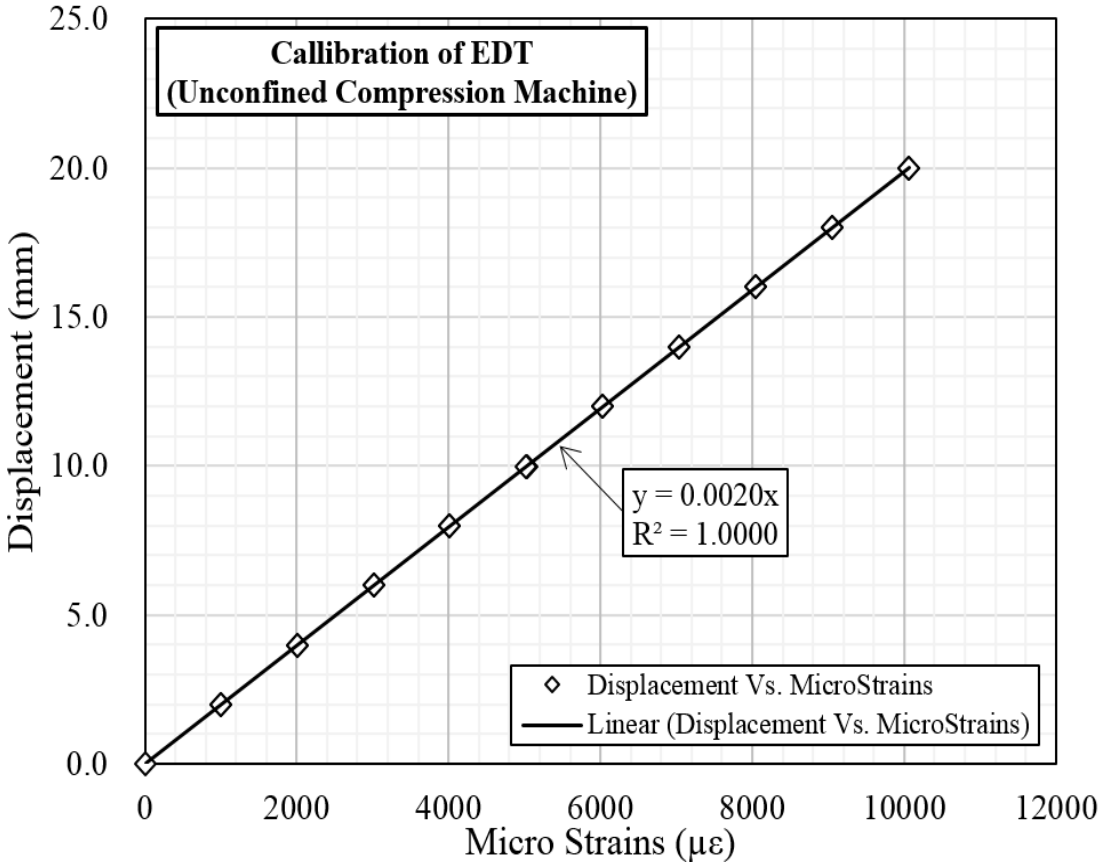

Fig. A.3. Calibration Results of EDT
(Unconfined Compression Machine)

A.4 Calibration of EDT (Triaxial Compression Machine)

Calibration Results of EDT (Triaxial Compression Machine)	
CAL Value	9999 με
b-Value	0.0050 mm/με
Physical Value	49.995 mm

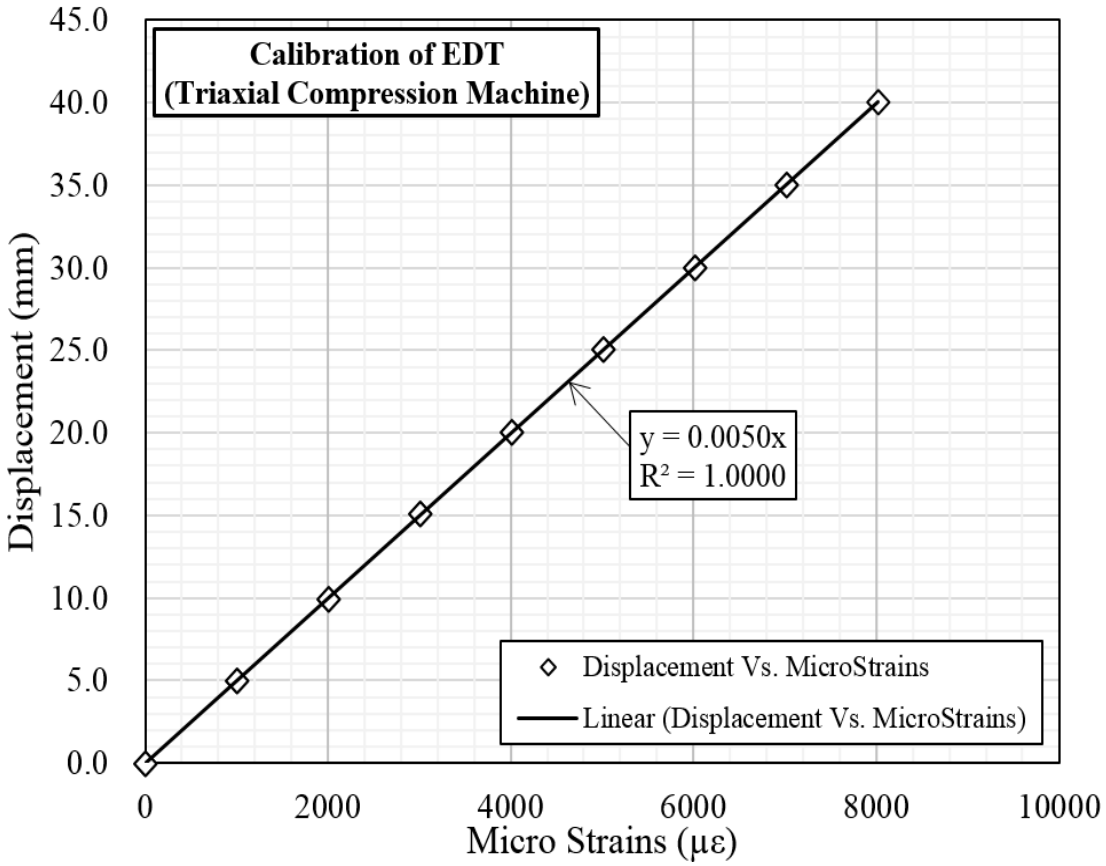

Fig. A.4. Calibration Results of EDT
(Triaxial Compression Machine)

A.5 Calibration of Cell Pressure Sensor (Triaxial Compression Machine)

Calibration Results of Cell Pressure Sensor (Triaxial Compression Machine)	
CAL Value	3900 με
b-Value	0.2217 kPa/με
Physical Value	864.63 kPa

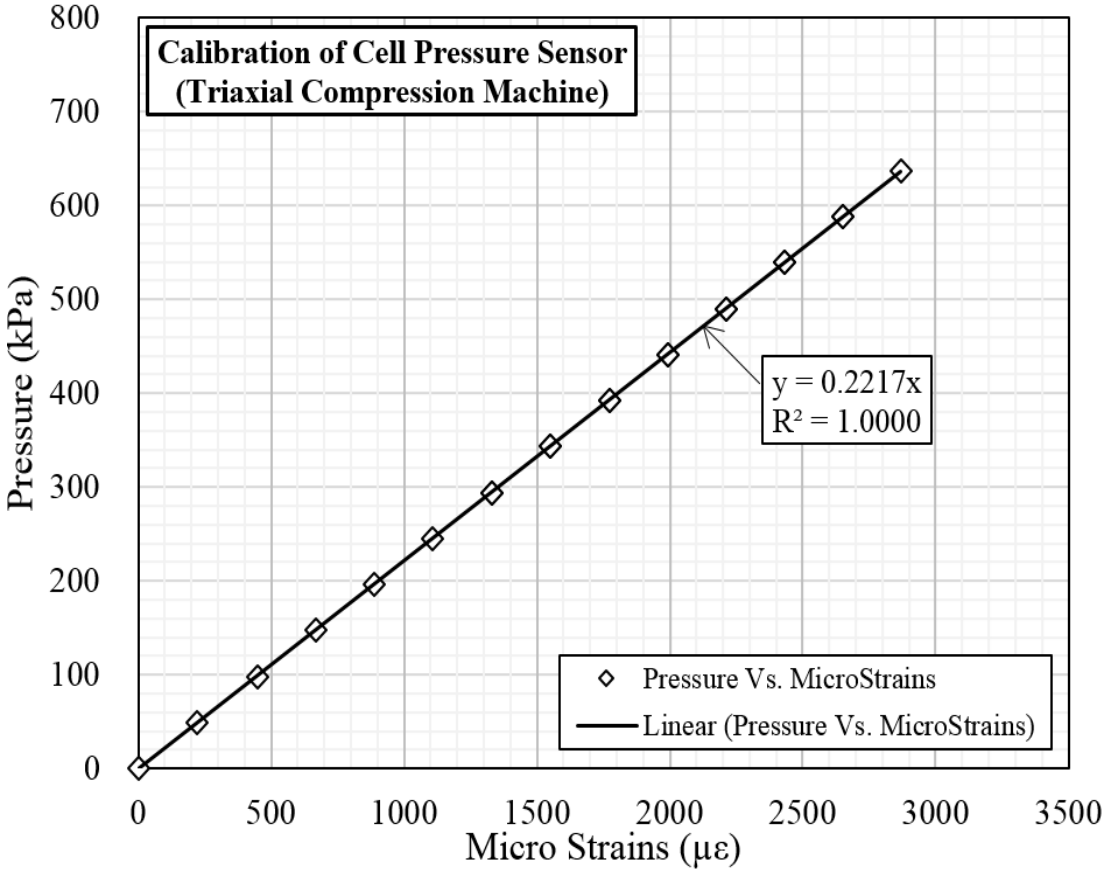

Fig. A.5. Calibration Results of Cell Pressure Sensor
(Triaxial Compression Machine)

A.6 Calibration of Pore Pressure Sensor (Triaxial Compression Machine)

Calibration Results of Pore Pressure Sensor (Triaxial Compression Machine)	
CAL Value	4300 με
b-Value	0.2001 kPa/με
Physical Value	860.43 kPa

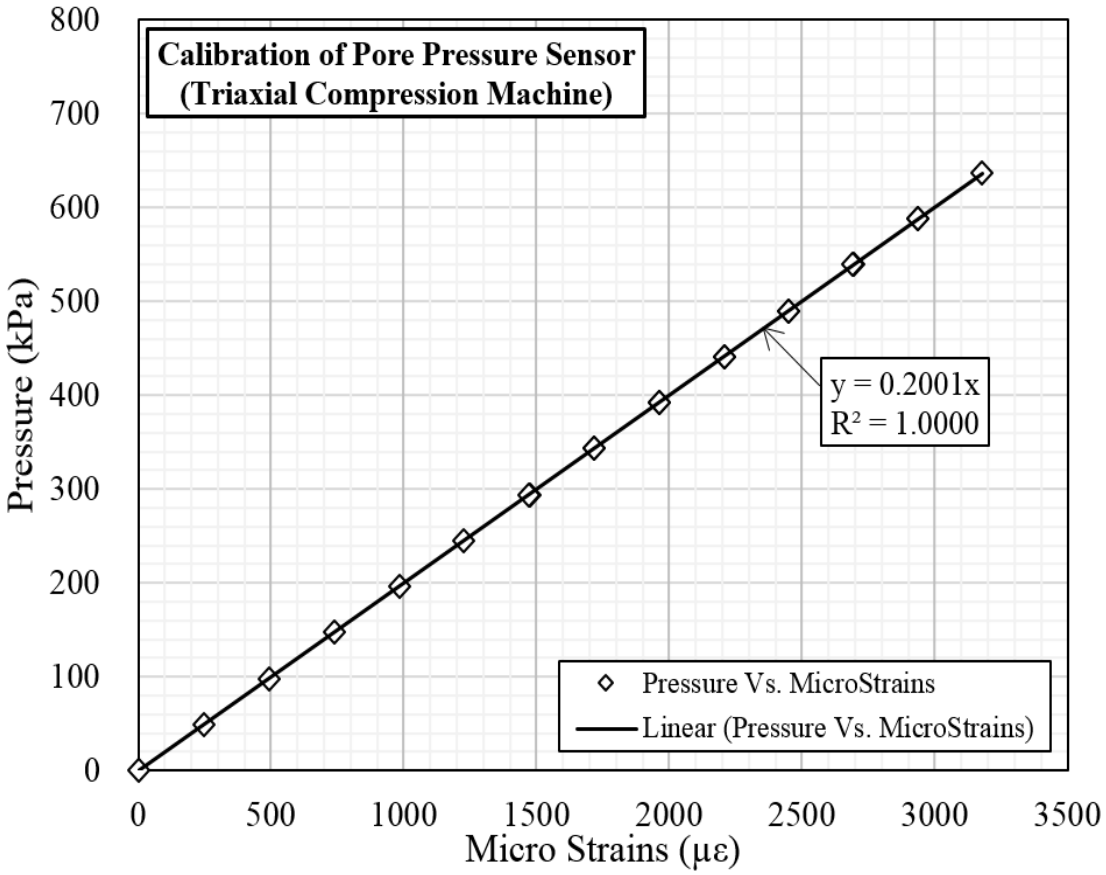

Fig. A.6. Calibration Results of Pore Pressure Sensor
(Triaxial Compression Machine)

A.7 Calibration of LDT-1 (Unconfined Compression Machine)

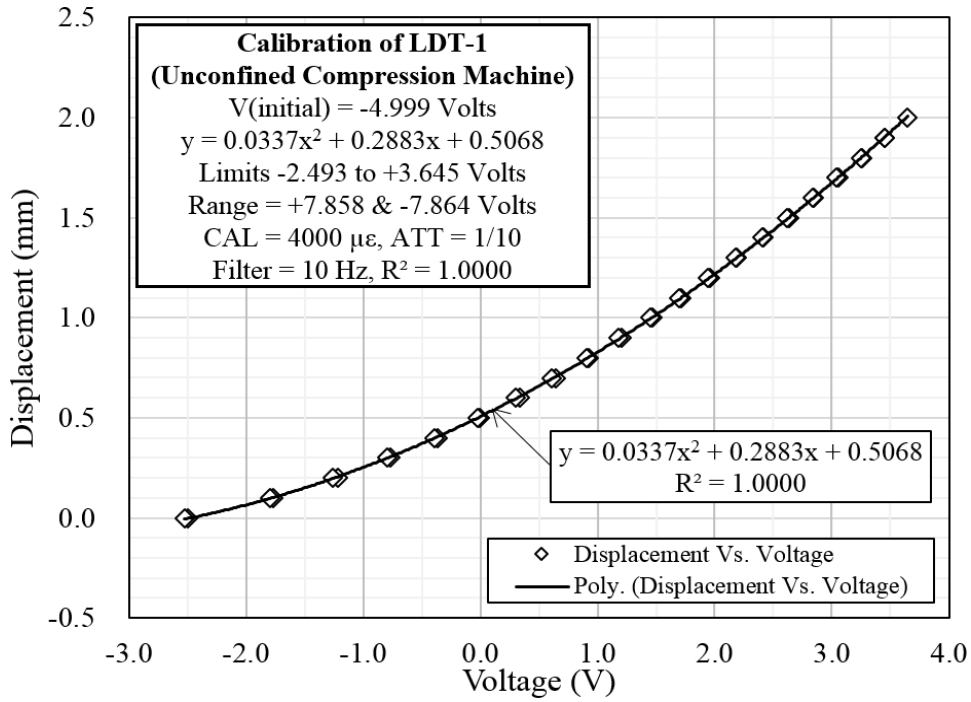

Fig. A.7. Calibration Results of LDT-1
(Unconfined Compression Machine)

A.8 Calibration of LDT-2 (Unconfined Compression Machine)

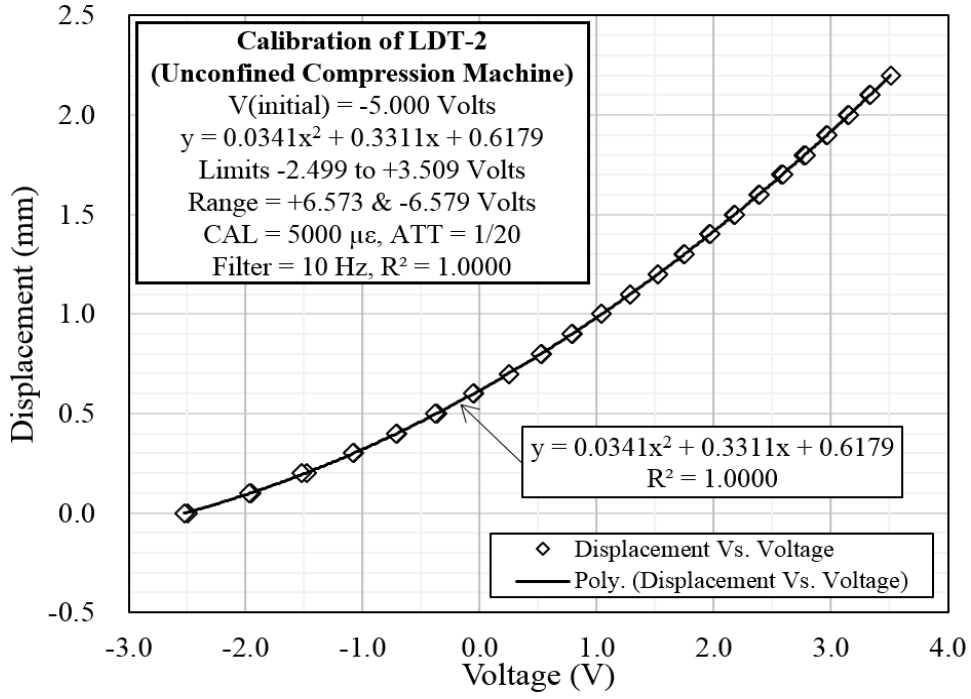

Fig. A.8. Calibration Results of LDT-2
(Unconfined Compression Machine)

A.9 Calibration of LDT-1 (Triaxial Compression Machine)

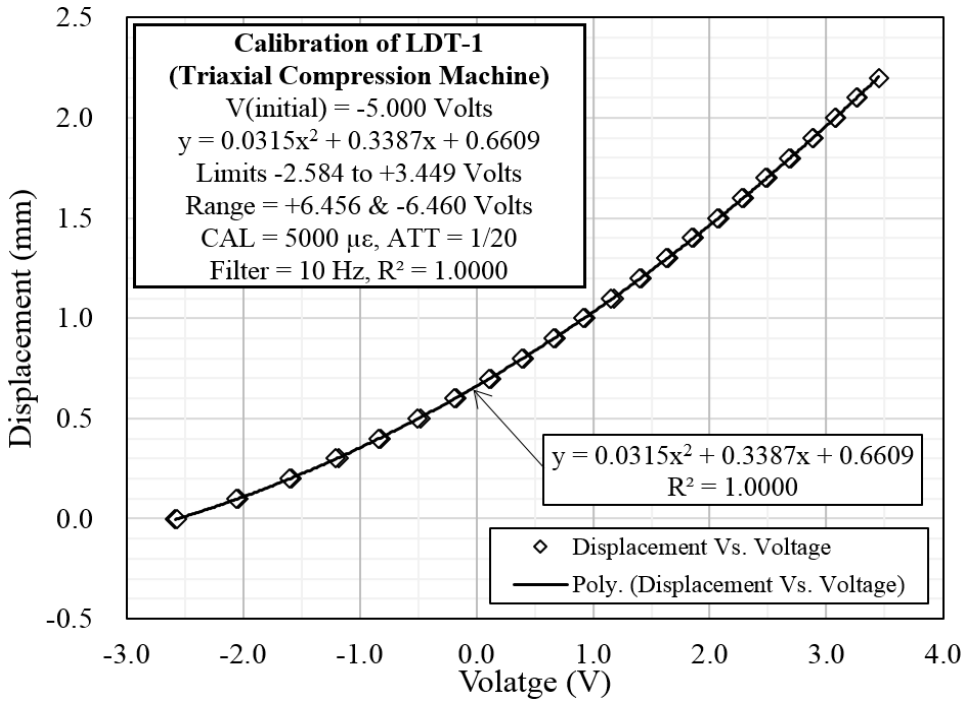

Fig. A.9. Calibration Results of LDT-1
(Triaxial Compression Machine)

A.10 Calibration of LDT-2 (Triaxial Compression Machine)

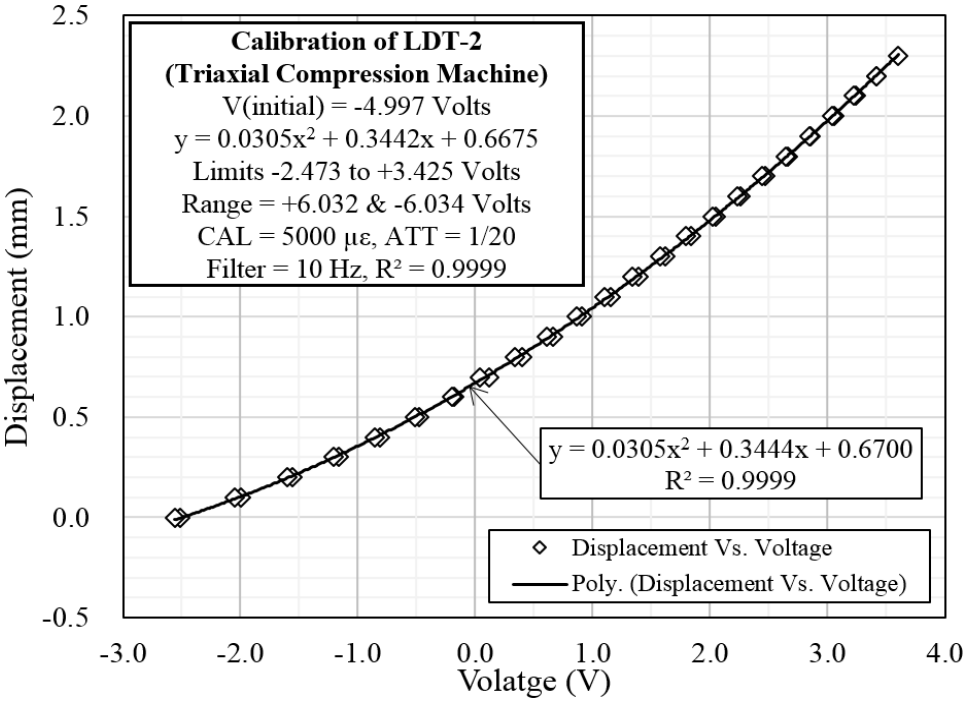

Fig. A.10. Calibration Results of LDT-2
(Triaxial Compression Machine)